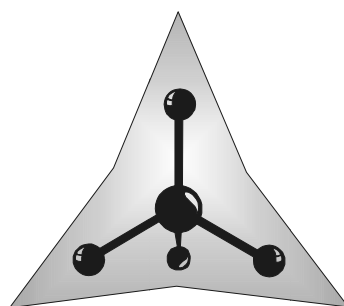


**National Academy of Sciences of Ukraine
Ministry of Education and Science of Ukraine
Scientific Council on the problem
"Physics of Semiconductors and dielectrics" NASU Ukraine
Ukrainian Physical Society
Academy of Sciences of High School of Ukraine
Institute of Physics of NASU
Institute of Semiconductor Physics of NASU
Scientific-Research Company "Carat" (Lviv)
Drohobych Ivan Franko State Pedagogical University**



MATERIALS
OF X INTERNATIONAL CONFERENCE
TOPICAL PROBLEMS
of **SEMICONDUCTOR PHYSICS**
in Memory of Professor Vasyl BOICHUK



**Truskavets, UKRAINE
June 26 – 29, 2018**

PROBLEMS

for discussion

- 1. Quantum-size confinement phenomena.*
- 2. Effects of strong correlation in the systems with electronic and ionic conductivity.*
- 3. Electronic transport, optic, photoelectric and magnetic properties of semiconductor crystals.*
- 4. Impurity and impurity-structural complexes of technological and radiation origin.*
- 5. Structural disordering factor manifestations of basic semiconductor properties. Semiconductor oxide ceramics.*
- 6. Semiconductor metrology, novel techniques and methods.*
- 7. Cluster phase: formation, properties and modeling.*

ORGANIZATORS

National Academy of Sciences of
Ukraine

Ministry of Education and Science
of Ukraine

Scientific Council on the problem
"Physics of Semiconductors and di-
electrics" NASU Ukraine

Ukrainian Physical Society

Academy of Sciences of High School
of Ukraine

Institute of Physics of NASU

Institute of Semiconductor Physics
of NASU

Scientific-Research Company

"Carat" (Lviv)

Drohobych Ivan Franko State Peda-
gogical University

CONFERENCE SPONSORS

LLC "Equipment for Business", Lviv



<http://www.tdb.ua/>

AE "UKRPOL Publishing House", Stryi



<http://ukrpol.ua/>

Digital Equipment Shop "Krapka"
Drohobych



INTERNATIONAL PROGRAM COMMITTEE

Co-chairman: Olexander Belyaev, Academician of NAS of Ukraine, Professor

Co-chairman: Ivan Blonskyi, Corresponding member of NAS of Ukraine, Professor

Co-chairman: Vasyl Boichuk, Professor

MEMBERS:

1. V. Babych (Kyiv, Ukraine)
2. P. Baranskyi (Kyiv, Ukraine)
3. O. Belyaev (Kyiv, Ukraine)
4. M. Brodyn (Kyiv, Ukraine)
5. I. Blonskyi (Kyiv, Ukraine)
6. Yu. Vaksman (Odessa, Ukraine)
7. R. Vysochanskyi (Uzhgorod, Ukraine)
8. V. Hodovanyuk (Chernivtsi, Ukraine)
9. O. Hoxhman (Odessa, Ukraine)
10. M. Dmytruk (Kyiv, Ukraine)
11. H. Zehrya (St. Petersburg, Russia)
12. V. Yemtsev (St. Petersburg, Russia)
13. V. Ivanov-Omskiy (St. Petersburg, Russia)
14. O. Kikinyesi (Debrecen, Hungary)
15. O. Kovalenko (Dnipro, Ukraine)
16. I. Kogoutiuk (Minnesota, USA)
17. D. Korbutyak (Kyiv, Ukraine)
18. Ya. Lepikh (Odessa, Ukraine)
19. V. Lytovchenko (Kyiv, Ukraine)
20. P. Lytovchenko (Kyiv, Ukraine)
21. A. Medvid' (Riga, Latvia)
22. Yu. Malyukin (Kharkiv, Ukraine)
23. M. Raranskyi (Chernivtsi, Ukraine)
24. S. Ryabchenko (Kyiv, Ukraine)
25. V. Shenderovskyi (Kyiv, Ukraine)
26. E. Sheregii (Rzeszów, Poland)
27. I. Stasyuk (Lviv, Ukraine)
28. M. Tkach (Chernivtsi, Ukraine)
29. P. Tomchuk (Kyiv, Ukraine)

COORDINATING COMMITTEE

Chairman: Vasyl Boichuk, Professor
Co-chairmens: Roman Peleshchak, Professor
Coordinator: Ihor Bilynskyy, Associate Professor

MEMBERS:

V. Brytan, Ya. Voronyak, I. Hadzaman, V. Holskyj, O. Dan'kiv, T. Kavetsky, R. Leshko, M. Luchkevych, Yu. Pavlovskyi, R. Pazyuk, L. Pan'kiv, I. Stolyarchuk, Yu. Uhryn, I. Shackleina, I. Shevchuk

QUANTUM-SIZE CONFINEMENT PHENOMENA

EFFECT OF SWITCHING IN THE CONDUCTIVITY OF InGaAs/GaAs HETEROSTRUCTURES WITH TUNNEL-COUPLED QUANTUM WELLS

P.A. Belevskii, M.M. Vinoslavskii*, V.M. Poroshin

*Institute of Physics, National Academy of Sciences of Ukraine, 03028 Kyiv,
Ukraine, *mvinos@iop.kiev.ua*

It is reported about the observation of the effect of switching between states with different conductivities in double tunnel-coupled quantum wells (QW) n-In_xGa_{1-x}As/GaAs under the action of a heating lateral electric field pulse. The effect is explained by the redistribution of carriers between the impurity band in a narrow QW and the lower subband in a wide QW.

Introduction.

Heterostructures with tunnel-coupled quantum wells (HS with TCQW) are used in various devices - field effect transistors, high-frequency oscillation generators, logic elements, and etc. The principle of operation of these devices is based on the tunneling interaction of states in QWs with different conductivity (mobility). In most cases, studies are carried out on samples with three contacts, one of which is the controller (gate). The change in conductivity occurs, for example, in the anti-crossing of the levels of size quantization in the TCQW, which is achieved by changing the gate voltage [1].

In this paper, we report the effect of the lateral (along the heterolayers) conductivity switching in InGaAs/GaAs HS samples with a TCQW with only two current contacts under the action of the pulses of the electric field which is heating carriers.

Technique of the experiment.

The structures grown by the gas-transport epitaxy method contained from 10 to 20 pairs of InGaAs double tunnel-coupled QWs with different widths (80-100 Å and 160-180 Å) separated by GaAs barriers 30-50 Å thick. The QW pairs are separated from each other by GaAs barriers of 700 Å width. The structures with double QWs were δ -doped with Si into narrow QWs. The impurity concentration was $N_d = 1-3 \cdot 10^{11} \text{ cm}^{-2}$ for a period.

The rectangular samples, cleaved from the structure, had In or GeAu strip electrical contacts, the distance between them being 1 to 3 mm. Cooling the samples to a temperature of 4.2 K was carried out in the dark.

To measure the conductivity of the structures, a constant voltage of $\sim 3 \text{ V}$ was applied to the contacts, so that the value of the stabilized current through the sample was of the order of $1 \text{ }\mu\text{A}$. In addition, single voltage pulses of $\sim 0.5 \text{ }\mu\text{s}$ duration and amplitude up to 1000 V were applied to the contacts. After the voltage pulses has finished, the time dependences of the conductivity relaxation (hereinafter in the

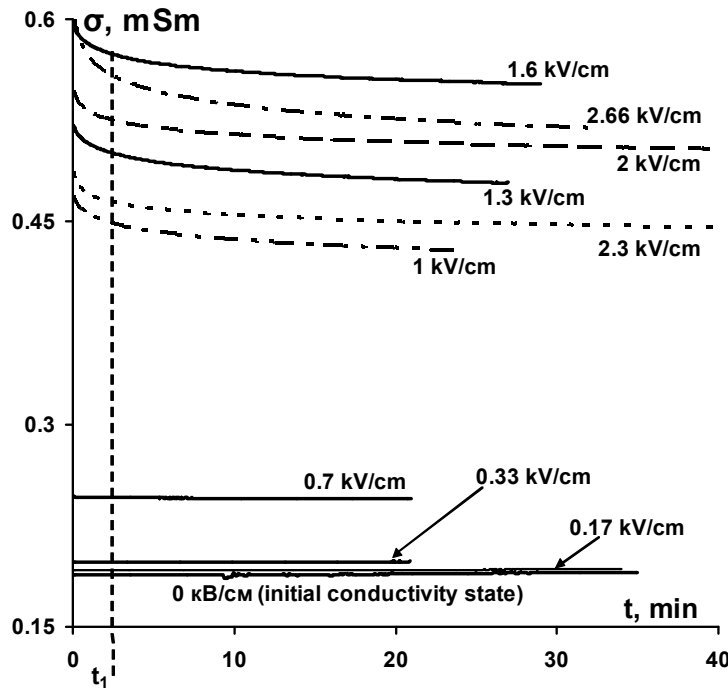


Fig. 1. Time dependence of the residual conductivity of the HS with double QWs after the action of an electric field pulses of various amplitude. t_1 is the conductivity measurement time moment for the curves in Fig. 2 and 3.

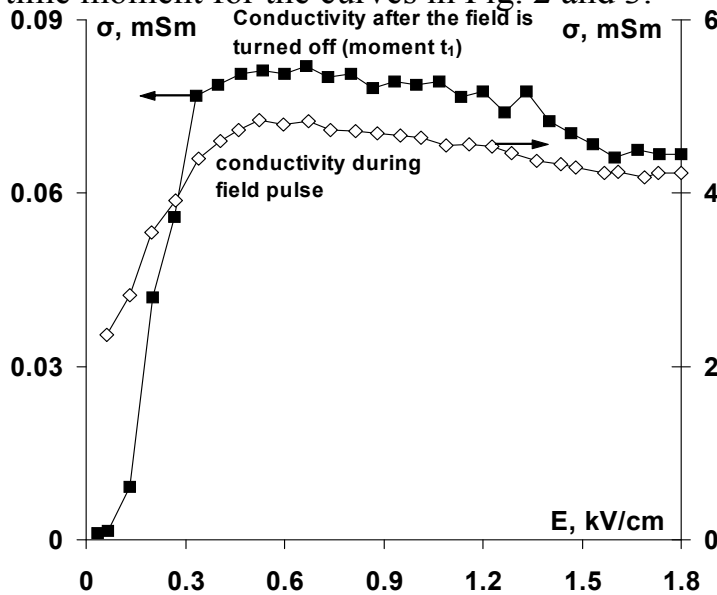


Figure 2. Field dependences of the conductivity of the HS with double QWs during the electric field pulse and after it is turned off

text referred to as the "residual conductivity") of the samples were measured, which usually quickly reached a certain stationary value. In addition, the field dependences of this residual conductivity were measured at a value close to stationary after 1 to 4 minutes after the end of the voltage pulse.

Experimental results.

A typical dependence of the residual conductivity relaxation on time for heterostructures with double QWs is shown in Fig. 1. The dependence of the residual conductivity on the applied field, measured at the time moment t_1 , is shown in Fig. 2.

It has been established that for samples of HS with double QWs δ -doped into narrow QWs, the application of a pulsed electric field $E \geq 0.1$ -1 kV/cm leads to a substantial increase (up to two orders of magnitude) of the residual conductivity, which depends both on the magnitude of the applied pulsed field and the doping level of the QWs (Fig. 3).

The observed strong effect of increasing the residual conductivity in the double QWs structures, δ -doped into a narrow well, is, in our opinion, due

to fact that the conductivity at helium temperatures is carried through two channels: over the lower subband of the wide QW and along the impurity band in the narrow QW [2]. The impurity band is located in energy below the size-quantized subband in this well, but above the bottom of the subband of the wide well (Fig. 4). As follows from the calculations of the energy spectrum, due to the high density of states in the impurity band, even at helium temperature there is a significant

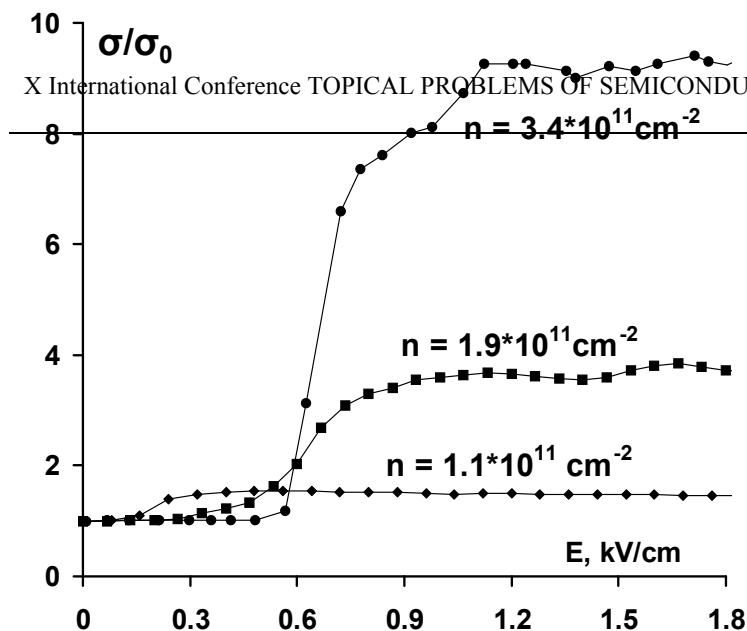


Fig. 3 The field dependences of the residual conductivity of double-well heterostructures (with different levels of δ -doping in a narrow QW) are given after the electric field pulse is turned off: σ_0 is the initial value of the conductivity

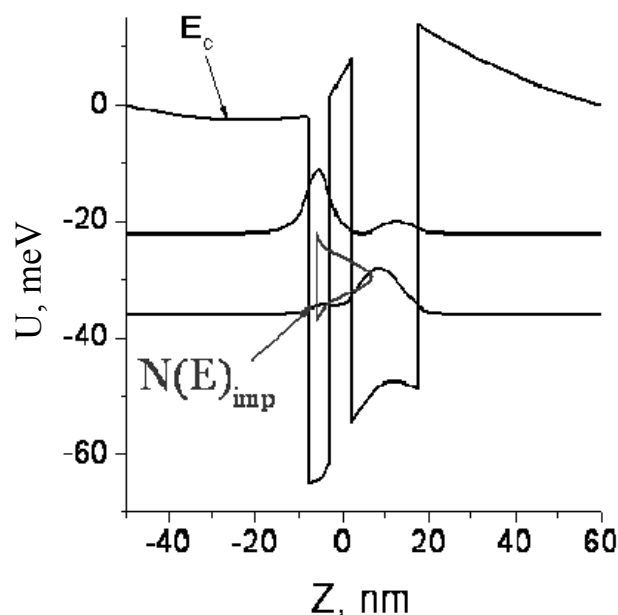


Fig. 4. Calculated profiles of quantum wells, size quantization levels and squares of wave functions on them, as well as the distribution of the density of states in the impurity band in a narrow well.

amount of electrons in it, which is greater for the higher doping. The electron mobility in the impurity band is mainly determined by scattering on the residual impurities and it is much less than the carrier mobility in the lower subband of the wide well. The contribution in the conductivity of the electrons in the impurity band explains the observed relatively low mobility in these structures at helium temperatures. Under the action of the applied high electric field pulse, electrons from the impurity band of a narrow QW tunneling through the barrier to the lower subband at wide QW. As a result the sample conductivity increases. After the field pulse is turned off, the electrons remain in wide wells, since the states of the impurity band are higher in energy and spatially separated from the states of the wide QW subband. As a consequence, a state with high conductivity will be maintained.

We also carried out comparative measurements on single QWs with different types and levels of doping (δ -doping into the barrier, into the well or homogeneous over the period). A common property of such heterostructures was the absence of two channels of conductivity. Respectively to this, the above described switching effects be-

tween them should not be observed. Actually, the maximum change in the residual conductivity obtained by us in these experiments did not exceed 50% and was reached in fields of the order of 2 kV/cm. Moreover, these changes had a complex nature. For example, in addition to an increase of the conductivity, its decrease was observed also. These conductivity changes can be explained by changing the car-

rier concentration due to their capture by various types of barrier-like traps on the QWs interfaces. Ridley pointed out this possibility for the QWs [3]. However, the contribution of such barrier-like states to the change in the conductivity of a HS with double TCQWs under the action of strong electric fields is less importance.

The authors are grateful to N.V. Baidus and B.N. Zvonkov for growing heterostructures.

Reference

1. P. I. Biryulin, A. A. Gorbatshevich, V. V. Kapaev, Yu. V. Kopaev, V. T. Trofimov // *Semiconductors*, November 2001, Volume 35, Issue 11, pp 1300–1304
2. N. V. Baidus, V. V. Vainberg, B. N. Zvonkov, A. S. Pylypchuk, V. N. Poroshin, O. G. Sarbey // *Semiconductors*, May 2012, Volume 46, Issue 5, pp 631–636
3. N. Balkan, B. K. Ridley, A. J. Vickers, and N. A. T. O. S. A. Division, *Negative differential resistance and instabilities in 2-D semiconductors*. Springer, 1993.

OPTICAL PROPERTIES OF THE ARRAYS DIFFERENT FORM QUANTUM DOTS

V.I. Boichuk, I.V. Bilynskiy, R.I. Pazyuk

Physics department

Ivan Franko Drohobych State Pedagogical University

24 Ivan Franko St., Drohobych, 82100, Ukraine, iv.bilynskiy@gmail.com

Investigations of many-dimensional superlattices (spatially ordered) of self-assembled semiconductor quantum dots (QDs) are interesting and potentially practically important in terms of developing fabrication techniques and theory of physical processes of nanosize heterosystems.

Semiconductor quantum dots are local areas of semiconductor material about 2-10 nm in size embedded in a wider energy gap semiconductor matrix. Due to existence of the potential well, charge carriers are confined inside the dots. Because of their small size quantum dots represent the ultimate case of quantum confinement when the movement of carriers is limited in all three directions. A three-dimensional confinement of carriers leads to a strong spectrum modification of electronic states, so that the electronic structure of a quantum dot brings an analogy with a single atom.

We considered conduction band intersubband electron transitions in an array of non-interacting one-dimensional chains of spherical quantum dots in the $GaAs/Al_xGa_{1-x}As$ semiconductor system. The absorption coefficient caused by these transitions was calculated depending on frequency and polarization of incident light, Fermi level position, and temperature. We established the existence of peaks of the absorption coefficient at the edges of the absorption region in consequence of intersubband transitions according to the defined selection rules. The dependence of the absorption coefficient on Fermi level position was found. It is shown that the absorption coefficient reaches its maximal value at the center of the

region between the s -, p -like subbands and slightly varies with temperature. In case of change in the direction of the polarized light wave from perpendicular to parallel the absorption bandwidth increases sharply. It is obtained that the absorption bandwidth also increases with reducing quantum dot radius followed by a simultaneous blue shift. It is demonstrated that the absorption coefficient of light incidence parallel to the quantum dot chain does not depend on the method of polarization (linear or circular), while the change in the direction of polarization (to perpendicular) leads to appearance of the quasi-resonant band within the absorption region. We also analyzed the dependence of the relative absorption coefficient on concentration of aluminum in the $Al_xGa_{1-x}As$ matrix.

TWO ELECTRONIC MOLECULA CONTAINING THREE SPHERICAL QUANTUM DOTS

Boichuk V.I., Holskyj V.B., Leshko R.Ya.

Physics department

Drohobych Ivan Franko State Pedagogical University,

Stryiska Street, 3, Drohobych, 82100, hol.wit@gmail.com

Quantum dots (QD) are often referred to as artificial atoms through their discrete electron spectrum. When several QD are near placing, they begin to interact, resulting in the energy particle levels split [1]. For large influences of tunneling on electronic states, covalent bonds are introduced, as in real molecules [2]. Regardless of whether there is a large effect of tunneling on the formation of coherent molecular-like states, this must be taken into account for the correct description of the system of QD. It has a practical value for quantum computing [3], coherent states for the formation of qubits, and for implementing a SWAP gate for control of qubits [4]. The methods of self-organization that provide the production of molecules and arrays of semiconductor quantum dots are now well developed and continue to be refined [5].

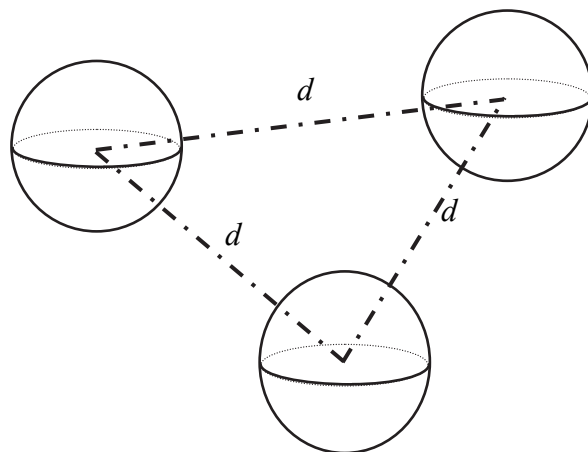


Fig.1.The model of the nanosystem.

The paper considers a molecule of three spherical QDs that are connected with each other due to tunneling effects (Fig. 1). The spectrum of energy states of such a molecule contains the split states of individual QDs. To determine them when there is one electron in such a nanosystem, the wave function is represented as a linear combination of electron wave functions of individual QDs:

$$\Psi(r) = \sum_{i=1}^3 C_i \varphi_{is}(r), \quad i=1, 2, 3, \quad (1)$$

$\varphi_{is}(r)$ is the wave function of the electron ground state, in i -th QD.

To obtain the energy particle levels, a substitution (1) has been made in the stationary Schrödinger equation with Hamiltonian:

$$\hat{H} = -\frac{\hbar^2}{2} \nabla \frac{1}{m} \nabla + U(r), \quad (2)$$

$$U(r) = \begin{cases} U_0, & \text{if } r \text{ in QDs space} \\ 0, & \text{if } r \text{ other} \end{cases}, \quad (3)$$

where m is effective mass of electron for the proper area, $U < 0$.

As a result, a system of linear homogeneous equations is obtained. To calculate the specific energy values a condition is used that the system has a solution when its determinant is zero.

The found energy levels and wave functions were used to determine the energy of the system of two electrons and their wave function for the molecule under study. We considered nine levels of energy, which are described by the following wave functions:

$$\begin{aligned} \Psi^{(1)}(r_1, r_2) &= \Psi_I(r_1) \Psi_I(r_2) \\ \Psi^{(2)}(r_1, r_2) &= \Psi_{II}(r_1) \Psi_{II}(r_2) \\ \Psi^{(3)}(r_1, r_2) &= \Psi_{III}(r_1) \Psi_{III}(r_2) \\ \Psi^{(4,5)}(r_1, r_2) &= \frac{1}{\sqrt{2}} (\Psi_I(r_1) \Psi_{II}(r_2) \pm \Psi_I(r_2) \Psi_{II}(r_1)) \\ \Psi^{(6,7)}(r_1, r_2) &= \frac{1}{\sqrt{2}} (\Psi_I(r_1) \Psi_{III}(r_2) \pm \Psi_I(r_2) \Psi_{III}(r_1)) \\ \Psi^{(8,9)}(r_1, r_2) &= \frac{1}{\sqrt{2}} (\Psi_{II}(r_1) \Psi_{III}(r_2) \pm \Psi_{II}(r_2) \Psi_{III}(r_1)). \end{aligned} \quad (4)$$

The energy of two electrons system is found from the stationary Schrödinger equation with Hamiltonian:

$$\hat{H} = -\frac{\hbar^2}{2} \nabla_1 \frac{1}{m} \nabla_1 - \frac{\hbar^2}{2} \nabla_2 \frac{1}{m} \nabla_2 + \frac{e^2}{\varepsilon |\vec{r}_1 - \vec{r}_2|} + U(r). \quad (5)$$

Consequently, the numerical calculation of the energy spectrum of two electrons in a molecule, formed from three quantum dots of a spherical shape, was performed. The influence of the magnitude of the nanocrystal, the distance between them and the symmetry of the quantum molecule on the energy spectrum of two electrons is investigated. The case of symmetry of an equilateral and an isosceles triangle is considered.

1. Boichuk V.I., Holskyj V.B., Journal of Physical Studies. – 2001. – 46, № 3. – c. 342-345.
2. R. H. Blick, R. J. Haug, J. Weis, D. Pfannkuche, K. v. Klitzing, and K. Eberl, Phys. Rev. B 53, 7899 (1996).
3. D. Loss and D. P. DiVincenzo, Phys. Rev. A 57, 120 (1998).
4. R. Hanson, L. P. Kouwenhoven, J. R. Petta, S. Tarucha, and L. M. K. Vandersypen, Rev. Mod. Phys. 79, 1217 (2007).
5. Ledentsov. N.N.. IEEE J. Select. Topics Quant. Electron., 8. 1015 (2002).

EFFECT OF POLARIZATION TRAPS, DONOR AND ACCEPTOR IMPURITIES ON THE INTRABAND AND INTERBAND LIGHT ABSORPTION OF QUANTUM DOTS

Boichuk V.I., Leshko R.Ya., Karpyn D.S., Ivanchyshyn I.B., Toma I.P.

Physics department

*Drohobych Ivan Franko State Pedagogical University,
Stryiska Street, 3, Drohobych, 82100, leshkoroman@gmail.com*

It is a long period of time that the physics of nanosystems is considered to be a priority direction in the modern development of the materials science and nanoelectronics. Its success is due to the use of nanoobjects such as quantum wells, quantum wires, quantum rings and especially quantum dots (QDs). Due to their unique properties, QDs are widely used in optoelectronics. The narrow spectrum of radiation of monodisperse QDs makes it possible to use QDs in light-emitting diodes (LEDs). They have better spectral characteristics and a higher coefficient of efficiency than LEDs on the basis of the liquid crystals and organics materials.

Today technologies give possibility to product high-quality QDs, but it does not guarantee absence of various defects in them. In the nanocrystal can be at least one impurity atom. Also impurities can passivate the torn ties on the QD surface. In addition, the impurities can purposefully inject into a nanostructures by doping. Therefore, impurities may be in QDs and affect its properties.

An increasing ratio of the number of atoms on the surface to the number of atoms in the nanocrystal volume (QD size becomes small) increases the role of the surface states in the formation of absorption and luminescence bands. It relates to the heterosystem with QDs. Notwithstanding that in QD it is often hard to determine the nature of the surface states, in most cases the red radiation spectrum is caused by electron transition with concern to the surface traps [1]. One of the reasons for the existence of a surface trap is the polarization charges on the interfaces. The value of polarization charges and the potential energy of the electron interac-

tion with polarization charges are defined by the difference of the dielectric permittivity of a heterosystem. A larger difference of the dielectric permittivity of a heterosystem and smaller sizes of QDs increase the role of the polarization trap.

Therefore, there are two important factors which effect on optical properties of the QD: 1) surface states causes by the polarization charges and impurities (especially for small QD); 2) different impurities (for intermediate and large QD). Those two factors leads to presence of the absorption peaks in the long-wavelength region in the interband and intraband light absorption and luminescence.

The calculation of the electron energy in the QD heterosystem with an impurity shows that the reduction of the QD size causes a transformation of the lowest exited states from the inner-dot into the outer-dot states. The outer-dot states are characterised by a weak energy dependence on the QD radius. The probability density of the electron in the space for those states has a maximum value near the QD surface in the matrix [2]. Those states are called “surface electron states”.

Taking into account the polarization charges and the intermediate layer with $\varepsilon = \varepsilon(r)$ on the surface, causes the existence of the electron polarization trap in the matrix near the QD surface. It has been defined that the electron interaction with polarization charges increases the binding energy of the surface states (decreases the electron energy) [3].

Also, we consider 5 types of the QD excitation: the Wanier-Mott exciton and 4 types of exciton-impurity complexes. The dependence of the total absorption coefficient of light on the wavelength for a heterosystem with such types of electron excitation showed that the main absorption band is characterized by two maxima. It is formed by quantum transitions of an electron with the formation of exciton, exciton-ionized donor, exciton-neutral donor, exciton-ionized acceptor. The longwave wing of this band is formed during the formation of the complex exciton-neutral acceptor.

- [1] Romcevic M., Romcevic N., Kostic R., Klopotoski L., Dobrowolski W.D., Kossut J., Čomor M.I., J. Alloys Compd., 2010. V. 497. P. 46, doi:10.1016/j.jallcom.2010.03.072.
- [2] Boichuk V.I., Leshko R.Ya., Karpyn D.S. Condensed Matter Physics, 2017. V. 20. P. 43704:1-8, doi:10.5488/CMP.20.43704.
- [3] Boichuk V.I., Leshko R.Ya., Karpyn D.S. Sensor Electronics and Microsystem Technologies, 2018. V. 15, №1. P. 5-16.

THE JOINED EFFECT OF ELECTRIC AND MAGNETIC FIELD ON THE OPTICAL PROPERTIES OF NANOSTRUCTURE CdS/HgS/CdS/HgS/CdS

V.A. Holovatsky, M.Ya. Yakhnevych, N. Ya. Yakhnevych

Chernivtsi National University. Chernivtsi, Ukraine.

External fields are important mechanism of influence on optical characteristics of quantum dots (QDs). Because of using electric or magnetic fields we can change absorption or radiation spectrums of nanostructures.

There are other works concerning with the simultaneous effect of electric and magnetic fields on the electronic states in QDs [1-5]. Authors of paper [1] investigates the light interband absorption coefficient in parabolic GaAs quantum dot in the presence of codirected electric and magnetic fields. Analytical solutions of Schrodinger equation are gotten. The ground state energy of the exciton in cylindrical quantum dot in the presence of external fields is obtained in [2] by variational method. Influence of electrical and magnetic fields on electron states in multilayered QD is investigated in [4-5] for spherical nanosystems: core-barrier/well/shell and core-well/shell/well correspondently, using the expansion method, which is based on the solutions of Schrodinger equation for electron in nanosystem without external fields.

The semiconductor multilayered spherical QD is considered consisting of core-potential barrier with radius r_0 and two layers forming the potential wells with Δ_1 and Δ_2 respectively, separated by y thin layer-barrier with ρ thickness, placed into the semiconductor matrix-barrier is considered. Directions of magnetic field induction vector and electric field intensity vector coincide with Oz-axis. The effective masses of electron, dielectric constants in potential wells and barriers, and confining potential has forms

$$\begin{aligned}\mu(r) &= \begin{cases} m_0, & r_0 < r \leq r_1, r_2 \leq r \leq r_3 \\ m_1, & r \leq r_0, r_1 < r \leq r_2, r \geq r_3 \end{cases}, \\ \varepsilon(r) &= \begin{cases} \varepsilon_0, & r_0 < r \leq r_1, r_2 \leq r \leq r_3 \\ \varepsilon_1, & r \leq r_0, r_1 < r \leq r_2, r \geq r_3 \end{cases}, \\ U(r) &= \begin{cases} V_0, & r \leq r_0, r_1 < r \leq r_2, r \geq r_3 \\ 0, & r_0 < r \leq r_1, r_2 \leq r \leq r_3 \end{cases}\end{aligned}\tag{1}$$

In order to obtain the energies and wave functions of the electron in nanostructure, which is placed into external fields, we are going to solve the Schrödinger equation with Hamiltonian (2), where \vec{p} is the electron quasi-momentum, \vec{A} - vector potential.

$$H = (\vec{p} - \frac{e}{c} \vec{A}) \frac{1}{2\mu(r)} (\vec{p} - \frac{e}{c} \vec{A}) + V_F(r, \theta) + V^p(r) + U(r) \quad (2)$$

Formula (3) describes electric field potential, where unknown coefficients are gotten as solutions of Poisson equation.

$$V_F(r, \theta) = -eF \cos \theta \begin{cases} a_0 r, & r \leq r_0 \\ a_1 r + \frac{b_1}{r^2}, & r_0 < r \leq r_1 \\ a_2 r + \frac{b_2}{r^2}, & r_1 < r \leq r_2 \\ a_3 r + \frac{b_3}{r^2}, & r_2 < r < r_3 \\ r + \frac{b_4}{r^2}, & r > r_3 \end{cases} \quad (3)$$

The potential $V^p(r)$ is calculated in ref. [6] and has the form

$$\begin{aligned} V^p(r) = & \frac{e^2}{2r_1\epsilon_0} \left(\frac{\epsilon_1 - \epsilon_0}{\epsilon_1 + \epsilon_0} \right) \left\{ \frac{r_1^2}{r_1^2 - r^2} + \left(\frac{r_1}{r} \right)^2 F \left(1, \alpha_1, \alpha_1 + 1, \left(\frac{r_1}{r} \right)^2 \right) \right\} + \\ & + \frac{e^2}{2r_2\epsilon_0} \left(\frac{\epsilon_0 - \epsilon_1}{\epsilon_0 + \epsilon_1} \right) \left\{ \frac{r_2^2}{r_2^2 - r^2} + \frac{\epsilon_0}{\epsilon_1} F \left(1, \alpha_2, \alpha_2 + 1, \left(\frac{r}{r_2} \right)^2 \right) \right\} + \\ & + \frac{e^2}{2r\epsilon_0} \sum_{n=0}^{\infty} \left\{ \left(\frac{r_1}{r} \right)^{2n+1} \frac{(\epsilon_1 - \epsilon_0)n}{(\epsilon_1 n - \epsilon_0(n+1))} - \left(\frac{r}{r_2} \right)^{2n+1} \frac{(\epsilon_0 - \epsilon_1)(n+1)}{(\epsilon_0 n - \epsilon_1(n+1))} - 2 \right\} \frac{1}{Z_n} \end{aligned} \quad (4)$$

$$Z_n = 1 + \left(\frac{r_2}{r_1} \right)^{2n+1} \frac{1}{n(n+1)} \frac{(\epsilon_1 n + \epsilon_0(n+1))(\epsilon_0 n + \epsilon_1(n+1))}{\epsilon_1^2 - \epsilon_0^2}, \quad \alpha_1 = \frac{\epsilon_0}{\epsilon_1 + \epsilon_0}, \quad \alpha_2 = \frac{\epsilon_1}{\epsilon_0 + \epsilon_1}.$$

When nanostructure is placed in electric and magnetic field, wave functions is calculated in following view

$$\psi_{jm}(\vec{r}) = \sum_n \sum_l c_{nl}^j \Phi_{nlm}(\vec{r}) \quad (5)$$

The energy spectrum E_{jm} and expansion coefficients are gotten from solution of the secular equation 6.

$$\left| H_{n'l',nl} - E_{jm} \delta_{n,n'} \delta_{l,l'} \right| = 0 \quad (6)$$

Fig. 1 proves that the degeneration of the energy spectrum with respect to magnetic quantum number is taken off in the magnetic field. The energies of the states with $m \geq 0$ increase when the magnetic field induction becomes bigger. The energies of the states with $m < 0$ at first decrease, and further increase at B increasing. In the fig. 1 one can see the complicated behavior of electron energy spectrum

with the regions of anti-crossing between neighbor energy levels with same magnetic quantum number m . In these regions the electron changes its location tunneling through the finite potential barrier due to the spatial confinement of electron by magnetic field. The role of the ground state is played by the states with $m=0$; -1 ; -2 , alternately, when B increases. The configuration of the ground state changes when the magnetic field changes on the same value ΔB .

The similar behavior of the electron energy spectrum is observed for the quantum rings and is known as the Aharonov-Bohm effect. Fig.1b and fig.1c prove that in case of presence of electric field such effect decreases, and then completely disappears. With electric field intensity 100 kV/sm this effect decreases and with 200 kV/sm effect completely disappeared. Increasing electric field intensity the ground state of the electron doesn't change its magnetic quantum number.

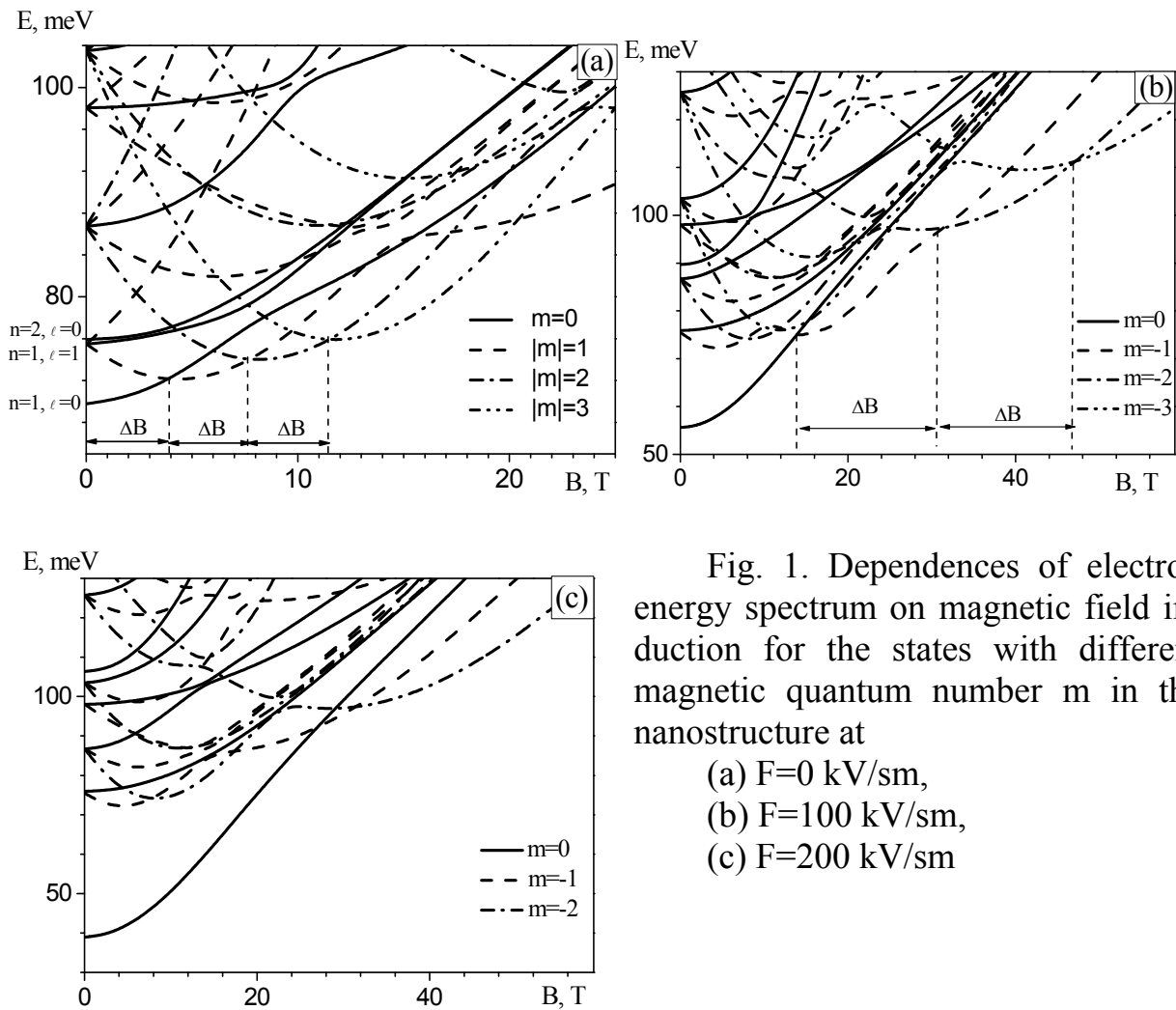


Fig. 1. Dependences of electron energy spectrum on magnetic field induction for the states with different magnetic quantum number m in the nanostructure at

- (a) $F=0\text{ kV/sm}$,
- (b) $F=100\text{ kV/sm}$,
- (c) $F=200\text{ kV/sm}$

With increasing magnetic field induction electron in the ground state gradually tunnels from external potential wall into internal one. In case of presence of electric field intensity tunneling occurs at bigger values of magnetic field induction than at without electric field. When with 0 kV/sm tunneling occurs at 10 T , at 100 kV/sm - 25 T , at 200 kV/sm - 50 T .

In anticrossing area electron changes its localization. This phenomenon is observed because of electron tunneling possibility through finite potential barrier because of spatial restriction charged particle by magnetic field. Change of localization quasiparticle has influence on the optical properties of the nanostructure (especially on the intensity of intraband and interband quantum transitions). Dependence of oscillator strengths are shown on figure 2.

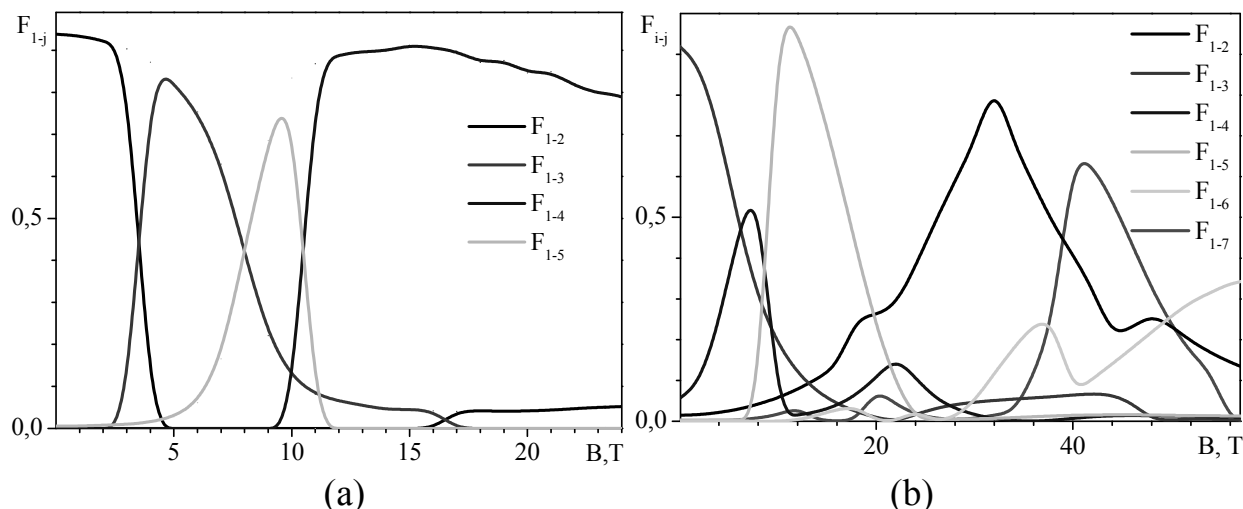


Fig.2. Dependences of oscillator strengths from magnetic field induction at without electric field – (a), and $F=100$ kV/sm – (b)

In case of presence of electric field dependences of oscillator strengths intraband quantum transitions from magnetic field induction becomes more complicated, and transitions such as $1 \rightarrow 6$, $1 \rightarrow 7$ become available. In case of absence of electric field such strengths equal zero.

The properties of electron energy spectrum in the nanostructure under study can be implemented in new magneto-optical devices.

1. M.S. Atoyan, E.M. Kazaryan, H.A. Sarkisyan, *Physica E* **31**, 83–85 (2006).
2. A. Vinolin, A. J. Peter, *e-J. Surf. Sci. Nanotech.* **11**, 29-35 (2013).
3. Guojun Jin, Yongyou Zhang, and Yu-qiang Ma, *J. Appl. Phys.* **105**, 063716 (2009).
4. V. Holovatsky, I. Bernik, *Semiconductor Physics, Quantum Electronics and Optoelectronics* **17**, 7-13 (2014).
5. M.H. Tanhaei, G. Rezaei, *Superlattices and Microstructures*, **98**, 29-36 (2016).
6. V. Boichuk, R. Kubay, I. Bilynskii, *J. Phys. Studies* **3**, 187-191 (1999).

BACGROUND IMPURITIES AND DELTA-DOPED QWs

**O.Fomina¹, V.Tulupenko^{1,2}, R. Demediuk¹, V. Akimov³, C. A. Duque²,
A.L.Morales², and D. Sushchenko¹**

¹ *Donbass State Engineering Academy, Kramatorsk 84313, Ukraine,*

² *Grupo de Materia Condensada, Instituto de Física, Facultad de Ciencias Exactas y Naturales, Universidad de Antioquia-UdeA, Calle 70 No. 52-21, Medellín, Colombia*

³ *Departamento de Ciencias Básicas, Universidad de Medellín, Carrera 87 No. 30-65, Medellín, Colombia,
tvn@laser.donetsk.ua*

We showed recently [1] that ionization of shallow impurities arranged as a delta layer within the quantum well (QW) with relatively small concentration increases their binding energy and changes (also increases) the separation between couples of the first neighboring space-quantized energy levels. Here the term “relatively small” means that we treat impurities as isolated ones or in other words, impurity binding energy (IBE) does really exist. As an upper criterion for such concentration is the critical one N_M for the Mott’s metal-semiconductor transition which can be found from the relation $a_B N_M^{1/2} = 0.37$ ¹. The reason for such phenomena is the fact that (partly) ionized delta layer “digs out” its own electrostatic QW, which is superimposed on the original energy profile created by heterostructure. The Fig. 1 explains these phenomena. Here one can see and compare the original QW with neutral impurities at low temperature – *a*) and compound QW with ionized center-doped – *b*), and edge-doped delta layer – *c*) at elevated temperatures. At low (helium) temperature all the electrons are frozen out to impurities and therefore there are no additional electrostatic QW. In this case the IBE for center-doped QW is approximately twice as large as for edge-doped one (for QW widths not less than three Boron radii – and it is with such QWs that we will deal further). Increased temperature involves ionization of the delta layer. As a result additional electrostatic Hartree potential created by free electrons and ionized donors is added to the original one. Due to the fact that this “digged out” QW is narrower than original one the difference between energy levels here is larger than in wider initial QW, which is shown in the parts *b*) and *c*). Note that for edge-doped QW in the case *c*) the added QW is narrower than in the case *b*). It means that wave function of the first level of the spatial quantization is bigger in magnitude and more concentrated near the impurity atom. All this is followed by an increase in both the IBE [1] and

¹ There are some other values of the right-hand side in the literature, not so much different from each other. We use here the estimate given in [2].

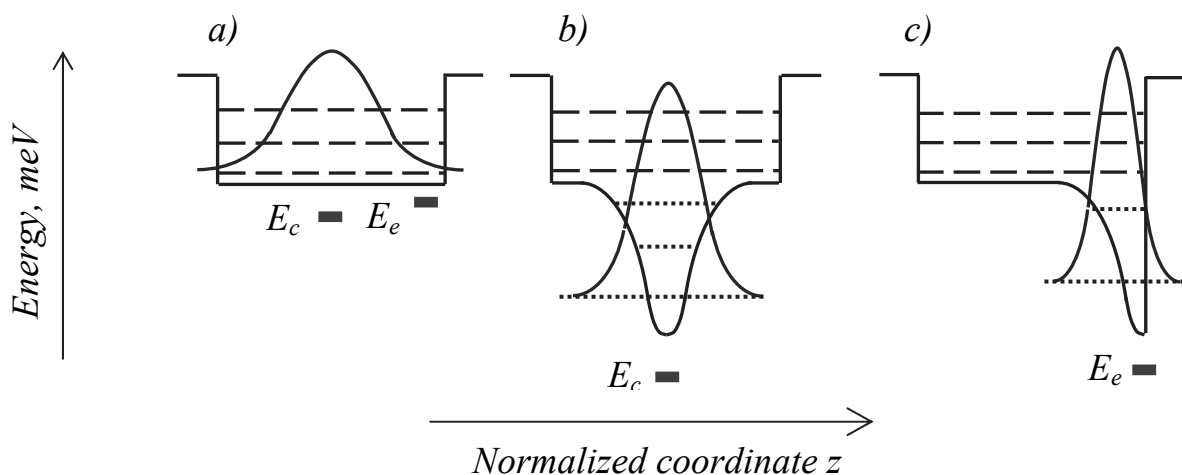


Fig.1. Schematic representation of influence of the ionized delta layer potential on the energy structure and impurity binding energy. Solid lines – energy profiles of the QWs, dashed lines – energy levels of the original QW, dotted lines – energy levels created by the electrostatic (Hartree) potential, blue lines – wave functions of the first energy level. E_c and E_e (short bold red lines) – ground impurity states for center-, and edge-doped QWs accordingly. *a)* – original structure with neutral impurities (at low temperatures), *b)* – structure with center-doped ionized delta layer, *c)* – structure with edge-doped ionized delta layer.

difference between pairs of neighboring energy levels [3]. Meanwhile, it is known that background impurities exist in any QW structure or some impurities can be introduced intentionally into the barriers (for instance as a delta-layer to enlarge mobility and concentration of charge-carriers in the QW – a so-called modulation doping) for some or other reason. But regardless of whether the impurities introduced intentionally or not, they lead to the band bending near interfaces even at zero temperature like it is schematically shown in Fig.2 for an edge-doped QW. In turn this affects the electrical and optical properties of the device as a whole. Therefore our work is focused on the theoretical study of the influence of the band bending on the energy spectrum and, consequently on the impurity binding energy of the partly ionized delta doped QWs. We do it on the example of n-type $\text{Si}_{0.8}\text{Ge}_{0.2}/\text{Si}/\text{Si}_{0.8}\text{Ge}_{0.2}$ QW structure with infinitely long barrier²s, center- or edge-doped with Phosphorus at temperatures $T = 4$ and 300 K. The donor impurity in the barriers is taken as uniformly distributed with concentration of 10^{15} cm^{-3} , 10^{16} cm^{-3} , и 10^{17} cm^{-3} . The energy spectrum of the QW is calculated in two steps. At the beginning, we calculate the band bending and the energy spectrum by a self-consistent solution of the Schrodinger and Poisson equations and with a constant IBE for the impurities of the delta layer, which is equal to the value obtained without background impurities. In the second step we calculate the IBE in the delta layer and the energy spectrum of the QW again by the self-consistent solution

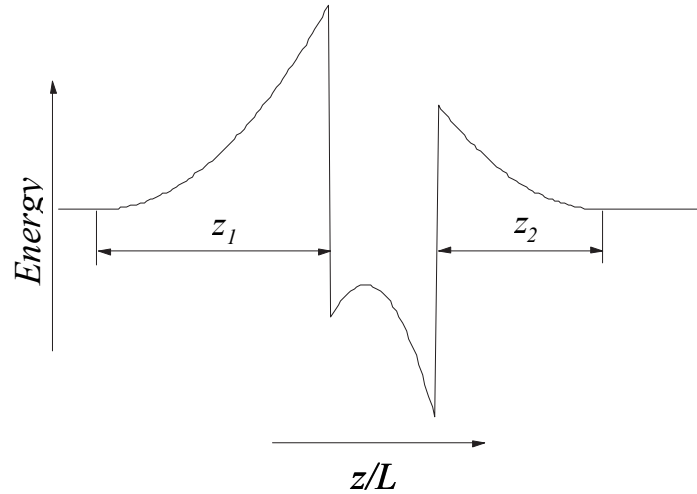


Fig.2. Schematic representation of edge delta-doped QW with residual impurities at elevated temperatures.

of the Schrödinger and Poisson equations with taking into account the energy profile of the structure obtained on the first stage. The procedure is described in our works [1,3, 4]. Some results are shown in the Table 1. In the last column designated with asterisk * we present the results from our work [4] obtained for the absence of background impurities. It is seen that background impurities do not affect much to the IBE for donors in the delta layer but their influence on the separation between neighboring energy levels is more pronounced. Careful analysis shows that IBE in the delta layer and the separation between couples

Table 1. Impurity binding energies E_δ , differences between couples of the first space-quantized energy levels, number of electrons in the QW released from the depletion layers n_b , and from the delta layer n_δ , and a percent content of donors in the delta layer for different concentrations of background impurities N_b for a center-, and an edge-doped QW. Concentration of donors in the delta layer $1.24 \cdot 10^{12} \text{ cm}^{-2}$, temperature $T=300\text{K}$.

$N_b, \text{ cm}^{-3}$	10^{17}		10^{16}		10^{15}		0^*	
Place of doping	Center	Edge	Center	Edge	Center	Edge	Center	Edge
$E_\delta, \text{ meV}$	32.4	32.4	33.4	31.7	33.7	31.6	33.4	30
$\Delta E_{12}, \text{ meV}$	6.1	27.4	11.3	25.8	12.4	25.9	11.1	19.7
$\Delta E_{23}, \text{ meV}$	2.4	17.9	5.8	18.3	6.9	18.8	5.8	11.2
$n_b, 10^{11} \text{ cm}^{-2}$	7.7	7.3	2.0	1.8	0.4	0.3	0	0
$n_\delta, 10^{11} \text{ cm}^{-2}$	7.3	5.6	7.8	6.8	8.1	7.2	8.4	7.8
$N_\delta^+, \%$	61	47	65	57	68	60	70	65

of neighboring energy levels are the result of a shape of the bottom of the QW. This shape, in turn is formed by the competition of the potentials created by

charges released due to the band bending on the one hand, and by the charges obtained by the ionization of the delta layer on the other hand [5]. The results on the number of electrons in the QW (see the last row in the Table 1) show that it is possible to increase them (which can be important for some optoelectronic devices – see, for example, Ref. [6]) by increasing the number of electrons supplied by the depletion layers.

Thus the obtained results allow one to predict the changes in the optical properties depending on the band bending and the level of ionization of impurities in the center- or edge-delta doped QWs.

This work was partly supported by the ministry of education and science of Ukraine.

1. V. Tulupenko, A. Abramov, Ya. Belichenko, V. Akimov, T. Bogdanova, V. Poroshin, and O. Fomina. *J. Appl. Phys.* 109, 064303 (2011).
2. A.G. Kyazym-zade, *Semiconductors* 29 (1995) 10.
3. V. Tulupenko, C.A. Duque, R. Demedyuk, Ya. Belichenko, C.M. Duque, V. Akimov, V. Poroshin, O. Fomina, *Philos. Mag. Lett.* 93 (2013) 42.
4. V. Tulupenko, C.A. Duque, R. Demediuk, V. Belykh, A. Tiutiunnyk, A.L. Morales, V. Akimov, R.L. Restrepo, M.E. Mora-Ramos, V. Poroshin, O. Fomina. *Physica E*, 66 (2015) 162–169.
5. V. Tulupenko, C. A. Duque, A. L. Morales, A. Tiutiunnyk, R. Demediuk, T. Dmytrychenko, O. Fomina, V. Akimov, R. L. Restrepo, and M. E. Mora-Ramos. *Phys. Status Solidi B*, 1–6 (2016).
6. C. A. Duque, V. Akimov, R. Demediuk, V. Belykh, A. Tiutiunnyk, A. L. Morales, R. L. Restrepo, O. Nalivayko, O. Fomina, M. E. Mora-Ramos, and V. Tulupenko, *Superlattices Microstruct.* 87, 5 (2015).

Synthesis of doped NCs CdTe

O.A. Kapush, D.V. Korbutyak, S.I. Budzulyak, N.D. Vakhniak

V.E. Lashkaryov Institute of Semiconductor Physics NAS of Ukraine, Natl. Acad. of Sci. of Ukraine, Kiev, Ukraine.

Luminescent semiconductor nanocrystals (NCs) have gained increasing attention in the past decade due to their unique optical, electronic and magnetic properties that are not available in either isolated molecules or bulk solids. Then NCs are potential candidates for various technical applications such as light-emitting diodes and lasers and biological fields. Recent years have seen considerable research interest in II–VI compound semiconductors, which are promising materials for novel microelectronic devices that take advantage of quantum size effects, missing in bulk materials. Such effects are most pronounced in CdTe, because it has a large Bohr exciton radius ($a_B = 7.5$ nm). Unfortunately, among nanoparticulate cadmium chalcogenides CdTe has been studied least. The reason for this is that colloidal solutions of CdTe are difficult to prepare because many Te (II) compounds have a tendency to decompose and are highly toxic.

Currently, there are many different methods of CdTe NCs obtaining for using in various spheres of science and technology. Physical methods provide a high degree of control system parameters, but they are quite complicated in implementation and require cumbersome and valuable equipment. Chemical methods are simple and economical, more profitable than the others methods of synthesis, thus they allow to obtain CdTe NCs of small sizes, even to several nanometres. Chemical methods are simple and economical, more profitable than the others methods of synthesis, thus they allow to obtain CdTe NCs of small sizes, even to several nanometres. They offer great opportunities to receive and study the properties of low-dimensional systems based on CdTe. It is possible to operate not only the size of the NCs, but also affect on their shape and structure by changing the synthesis conditions.

In this paper we consider an easy way of obtaining a doped CdTe NCs at room temperature. CdTe nanocrystals capped with thioglycolic acid and, thus, carrying a negative charge were synthesized in aqueous medium by the method colloidal synthesis in a semi-periodic reactor. Aqueous solution of 40 ml 0.1 M CdI₂ and 2-15 mmol stabilizer was placed in the reactor to synthesize CdTe NCs. Further we increased the pH to desired value by introducing aqueous solution of 1.25 M NaOH into the mixture; if it is necessary, then overall volume of the solution (250 ml) was topped by adding a solvent. For stabilization of CdTe NCs surface during the synthesis tioglycol acid S(CH₂CO₂H)₂ (99 %) has been used. All chemical reagents have been used without additional purification, and deionized water was taken for the preparation of solutions with resistivity 2.5 MOhm.

To optimize CdTe NC formation parameters, we measured the photoluminescence spectra of colloidal solutions of CdTe NCs and determined the particle

size by calculational techniques and experimentally, using photon correlation spectroscopy.

The alloying of CdTe NCs by ions of the f-group is an interesting and promising task, in particular because their intraatomic transitions lie in the visible and near infrared regions of the spectrum. For example, the maximum of the luminescence of the erbium is observed at a wavelength of 1550 nm, which corresponds to the second window of transparency in fiber optic transmission systems. However, these transitions are prohibited by the rules of selection and the intensity of these lines is very small. Therefore, the implantation of an ion into a nanocrystal characterized by strong absorbing power, and provided by an effective energy transfer occurs, will significantly increase the required luminescence.

From the side of synthesis, the introduction of several impurity atoms in a NC containing only a few hundred atoms can lead to their expulsion to the surface or deteriorate the crystalline structure. Actually this is the creation of highly doped NCs in conditions of strong confinement. Electronic and optical properties in such conditions are not completely studied yet.

ELECTRONIC PROPERTIES OF SURFACE VACANCIES IN CDS NANOCRYSTALS

I.M. Kupchak, N.F. Serpak, O.A. Kapush, D.V. Korbutyak

V. Lashkarev Institute of Semiconductor Physics, NAS Ukraine, 45, Prospect Nauky, Kyiv 03680, Ukraine, kupchak@isp.kiev.ua

Cadmium sulfide (CdS) is a classic direct gap $A^{\text{II}}B^{\text{VI}}$ semiconductor with a band gap of 2.42 eV (515 nm) at room temperature, but remains an interesting material during the long time [1,2]. However, in recent years, this interest has grown significantly due to possible application of CdS nanocrystals (NCs) in micro- and optoelectronics and, particularly, in light-emitting diodes, lasers, sensors, photo-electrical devices, solar cells, memory cells etc. [3-7].

Bulk CdS is a non-stoichiometric semiconductor of n -type, provided by the presence of intrinsic defects, such as sulfur vacancies and interstitial cadmium [8]. However, at the nanoscale, the recombination processes are expected to be affected by the presence of the surface defects due to the smallness of NCs size, resulting mainly in the luminescence characteristics of NCs. In the most of cases PL spectra of such the nanocrystals are determined by the inter-band transitions only, as widely described in the literature [9-11]. Nevertheless, the defect-associated luminescence may be observed in PL spectra of cadmium chalcogenides [12] as well. There is a set of works [13-18] dedicated to the problem of the photoluminescence properties and establishing the mechanism of radiative recombination in CdS nanocrystals. However, many factors remain undefined, particularly, the nature of the recombination centers *have still not been clarified*. There are the assumptions made in many works that the radiation occurs through the $V_{\text{cd}}-V_{\text{S}}$ [14,18] centers, acceptor centers V_{Cd} [15-17] or through the surface defects of unknown nature. In order to make a conclusion which kind of these defects are the most probable center of radiative recombination, we perform the geometry structure and the electronic density of states calculations of the defect-free $\text{Cd}_{33}\text{S}_{33}$ cluster in the charge states $q=-2..2$, as well as of cluster containing the cadmium vacancy V_{Cd}^q with $q=0..-2$ or sulfur vacancy V_{S}^q with $q=0..2$. The vacancies were simulated by removing the single atoms of the corresponding sort - cadmium or sulfur from the NC surface, leading to the general study the properties of $\text{Cd}_{32}\text{S}_{33}$ and $\text{Cd}_{33}\text{S}_{32}$ clusters.

All the calculation have been carried out within the density functional theory, as implemented in GAMESS-US software package [19], with the use of hybrid exchange-correlation functional B3LYP [20-23] and the Hay-Wadt set of basis functions and effective core potentials, known as LANL2DZ basis set [24-26].

We calculated the formation energies E_{form} of neutral and charged vacancies of cadmium and sulfur, ionization energies of defect-free system E_{F}^q and relaxation energies (Franck-Condon shifts) E_{r}^q for charged systems, which are listed in the Table 1.

Table 1.

E , eV	$q=-2$	$q=-1$	$q=0$	$q=1$	$q=2$
E_F^q , eV	-4.283	-3.130	-	7.392	16.965
E_r^q , eV	-1.441	-0.089	-	-0.889	-1.872
$E_{form} V_{Cd}^q$, eV	1.064	2.237	3.727	-	-
$E_{form} V_S^q$, eV	-	-	5.992	4.523	1.877

It is seen from the table, that the largest energy is needed to form the neutral vacancy of sulfur, although all the values of formation energy are positive. It is noteworthy to note, that formation energies of charged vacancies are significantly smaller than for neutral ones: with the increase of ionization energy, the system relaxation becomes larger, leading to increase in Franck-Condone shift. Fig.1 shows the total and partial density of states (PDOS), calculated for neutral and charges vacancies of cadmium and sulfur. PDOS is formed with the states of the

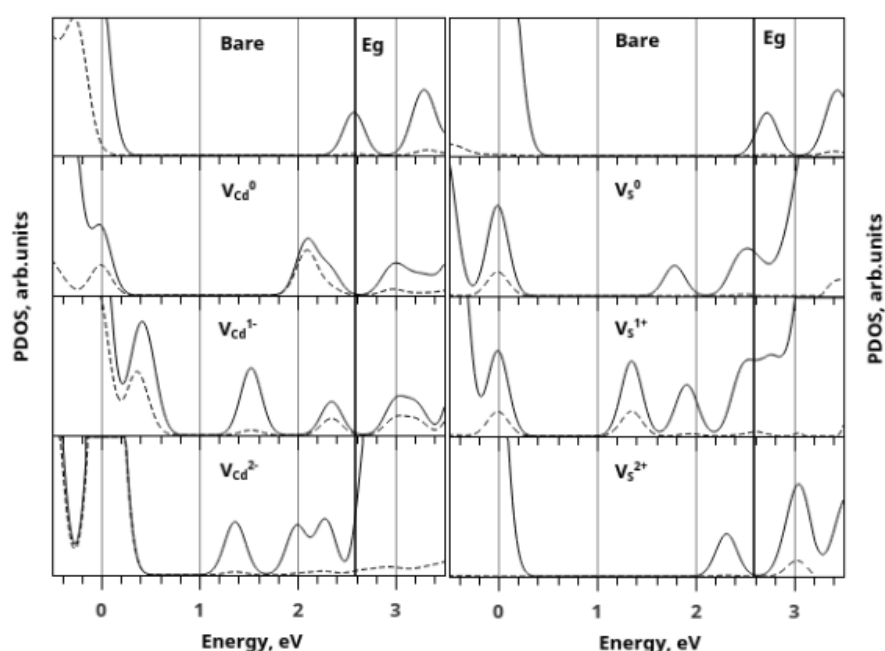


Figure 1. Total (continuous line) and partial (dashed line) DOS of defect-free (bare) NC, containing the neutral and charged vacancies of cadmium and sulfur.

nearest sulfur or cadmium atoms, participating in the vacancy of cadmium and for sulfur vacancy formation, respectively. All spectra are obtained using the Gaussian convolution with a smearing parameter 0.25eV and are aligned over HOMO levels, taken as zero energy for the convenience. It is seen, that the DOS of initial, defect-free NC has a clear gap (the HOMO-LUMO energy distance) of $E_g = 2.6$ eV. For the sulfur vacancy, the states of nearest cadmium atoms appear in the forbidden gap in the vacancy charge state $V_S(q=+1)$ only. Also, they form a clear peak close to the conduction band bottom (LUMO level) in the systems with neutral or $q=+1$ charged vacancy. The rest of peaks, arising in a gap, are related with the general

relaxation of the system. In the case of the singly charged acceptor-type vacancies of cadmium, the well-defined peak in DOS appears on the energy distance of about 0.4 eV far from the valence band top, and during the recharging into state $q=-2$ the nearest sulfur atoms form another peak close to the valence band top. The presence of such well-defined peak in the DOS during the singly charged vacancy formation means that these centers could be responsible for the radiative recombination in CdS NCs. This result is a theoretical confirmation for the assumptions made in experimental works listed above, that the surface singly charged vacancies of cadmium are the centers of luminescence. It is noteworthy to note, that in work [7], two closely located bands in PL spectra of CdS NCs in the region 2.1-2.3 eV are assigned to interstitial sulfur ions. With regards to the results, obtained in this work, we can assume, that one of these bands is related with singly charged cadmium vacancies, and another — with interstitial sulfur ions.

- [1] J. J. Ramsden and M. Grätzel, J. Chem. Soc. Faraday Trans. 1 **80**, 919 (1984).
- [2] A. Dumbrava, C. Badea, G. Prodan, and V. Ciupina, Chalcogenide Lett. **7**, 111 (2010).
- [3] S.V. Sorokin, S.V. Gronin, *et al.*, Fiz.Tehn.Polu. **49**, 342 (2015).
- [4] A. Mukherjee, B. Satpati, S. R. Bhattacharyya, R. Ghosh, and P. Mitra, Phys. E **65**, 51 (2015).
- [5] S. Wang, W. Dong, X. Fang, S. Wu, R. Tao, Z. Deng, J. Shao, L. Hu, and J. Zhu, J. Power Sources **273**, 645 (2015).
- [6] M. Tomakin, M. Altunbaş, E. Bacaksiz, and Ş. Çelik, Thin Solid Films **520**, 2532 (2012).
- [7] Y. Li, S. Q. Yuan, and X. J. Li, Mater. Lett. **136**, 67 (2014).
- [8] C. Wu, L. Wang, Z. Zhang, X. Zhang, Q. Peng, J. Cai, Y. Yu, H. Guo, and J. Jie, Front. Optoelectron. China **4**, 161 (2011).
- [9] T. Inoshita and H. Sakaki, Phys. B **227**, 373 (1996).
- [10] U. Bockelmann and T. Egeler, Phys. Rev. B **46**, 15574 (1992).
- [11] A. V. Fedorov, A. V. Baranov, I. D. Rukhlenko, T. S. Perova, and K. Berwick, Phys. Rev. B **76**, 45332 (2007).
- [12] T. Orii, S. Kaito, K. Matsuishi, S. Onari, and T. Arai, J. Phys. **14**, 9743 (2002).
- [13] G. Y. Rudko, I. P. Vorona, V. I. Fediv, A. Kovalchuk, J. E. Stehr, B. D. Shanina, W. M. Chen, and I. A. Buyanova, Nanoscale Res. Lett. **12**, 130 (2017).
- [14] V.M. Skobeeva, V.A. Smyntina, A.I. Sviridova, D.A. Strutz, and A.V. Tyurin, Journal of Applied Spectroscopy **75**, 556 (2008).
- [15] P. Mandal, S. S. Talwar, S. S. Major, and R. S. Srinivasa, J. Chem. Phys. **128**, 114703 (2008).
- [16] H. Lee, H. Yang, and P. H. Holloway, Phys. B **404**, 4364 (2009).
- [17] S. Q. Yuan, P. F. Ji, Y. Li, Y. L. Song, and F. Q. Zhou, Adv. Optoelectron. **2015**, 1 (2015).
- [18] V. Smyntyna, B. Semenenko, V. Skobeeva, and M. Malushin, Electronics and Information Technologies **45** (2012).

- [19] M. W. Schmidt, K. K. Baldridge, J. A. Boatz, S. T. Elbert, M. S. Gordon, J. H. Jensen, S. Koseki, N. Matsunaga, K. A. Nguyen, S. Su, T. L. Windus, M. Dupuis, and J. A. Montgomery, *J. Comput. Chem.* **14**, 1347 (1993).
- [20] P. J. Stephens, F. J. Devlin, C. F. Chabalowski, and M. J. Frisch, *J. Phys. Chem.* **98**, 11623 (1994).
- [21] S. H. Vosko, L. Wilk, and M. Nusair, *Can. J. Phys.* **58**, 1200 (1980).
- [22] C. Lee, W. Yang, and R. G. Parr, *Phys. Rev. B* **37**, 785 (1988).
- [23] A. D. Becke, *J. Chem. Phys.* **98**, 5648 (1993).
- [24] P. J. Hay and W. R. Wadt, *J. Chem. Phys.* **82**, 299 (1985).
- [25] W. R. Wadt and P. J. Hay, *J. Chem. Phys.* **82**, 284 (1985).
- [26] P. J. Hay and W. R. Wadt, *J. Chem. Phys.* **82**, 27

Ефект негативної диференціальної провідності у 2D напівпровідникових моношарах: теоретична модель

В.Г.Литовченко, А.І.Курчак, М.В.Стріха

Інститут фізики напівпровідників ім.В.Є.Лашкарьова НАН України

Уперше отриманий у 2004 році атомний моношар вуглецю графен є напівметалом, що стало принциповою перешкодою на шляху створення на базі графену елементної бази для нової електроніки. Численні спроби наділити графен напівпровідниковими властивостями виявилися малоуспішними з погляду дальших приладних застосувань. Протягом останніх років, однак, інтенсивно синтезуються й вивчаються інші моношари з напівпровідниковими властивостями (насамперед - халькогеніди перехідних металів). Моношари MoS_2 та WS_2 є прямозонними напівпровідниками з шириною забороненої зони $E_g \sim 1,7$ еВ та 1,8 еВ відповідно і з екстремумами зони провідності й валентної зони, розташованими в точках K , K' гексагональної зони Бріллюена, подібно до того, як це має місце в графені [1].

Спектр зони провідності цих матеріалів містить також бічний екстремум (T -долину) з енергією приблизно на $\Delta E \sim 0,2$ еВ і 0,08 еВ більшою від енергії дна зони, розташований у напрямку від точок K , K' до центру зони Бріллюена Γ . Наявність двох підзон зони провідності, нижчої (1) і вищої (2), у яких для ефективних мас двовимірних електронів виконується співвідношення $m_1 < m_2$ [1], дає підстави очікувати можливості реалізації в 2D моношарах типу WS_2 , MoS_2 ефекту негативної диференціальної провідності [2].

Нещодавно цей ефект було вперше експериментально виявлено в моношарах WS_2 [3]. Показано, що у випадку ненапруженого моношару ефект не відбувається через замалу енергетичну відстань між долинами $\Delta E \sim 0,08$ еВ, бо за кімнатної температури заселення електронами T -долини починається вже при мінімальних значеннях полів між витоком і стоком. Однак при прикладенні двовісного стиску, коли значення $\Delta E \sim 0,1$ еВ і дещо вище, ефект негативної диференціальної провідності починає виразно виявлятися в залежності струму через польовий транзистор від прикладеної напруги.

У рамках напівфеноменологічної моделі, подібної до тієї, яка широко використовується для тривимірних матеріалів [2], нами обчислено польову залежність дрейфової швидкості $v(\varepsilon)$ в WS_2 при температурі $T = 300$ К для різних значень ΔE від 0,03 еВ до 0,27 еВ, а також співвідношення концентрації електронів у верхній T -долині n_2 до загальної концентрації електронів у зоні провідності n від електричного поля. При розрахунках використано значення $\tau_e = 10^{-12}$ с, $\mu_l = 50$ см²/Вс, $m_2/m_1 = 10$. Залежність $v(\varepsilon)$

набуває вигляду кривої з максимумом, а співвідношення n_2/n при полях, що відповідають максимуму, починає зростати (це відповідає інтенсивному заселенню розігрітими електронами верхньої долини зони провідності)

починаючи з певного порогового значення $\Delta E \sim 0,15$ eВ, що якісно відповідає результатам [3]. При нижчих значеннях ΔE електрони інтенсивно переходять до верхньої долини вже при мінімальних значеннях електричного поля ε , й ефект негативної диференціальної провідності відсутній.

Таким чином, уперше адаптована нами до 2D напівпровідникових моношарів типу MoS₂ та WS₂ проста теоретична модель розігріву електронів у системі з двома долинами [6] добре описує наявні експериментальні дані й підтверджує можливість створення на таких структурах нового покоління діодів Ганна. Частоти, які може бути отримано на таких діодах, легко оцінити зі співвідношення $f \sim v/L$, де L – довжина каналу діода. Для значень, що відповідають системі, яка вивчалася в [3] ($v = 4 \cdot 10^6$ см/с, $L = 5$ мкм) отримуємо частоти порядку 10 ГГц, що робить такі діоди потенційно привабливими для низки практичних застосувань.

Викладена в цій роботі модель дозволяє також оцінити перспективність створення Ганнівських діодів на інших 2D напівпровідникових моношарах та тонких квантових ямах, базованих як на традиційних матеріалах електроніки, так і на алотропах вуглецю «між графеном і графітом», що, як було показано нами в [4], також можуть мати корисні напівпровідникові властивості.

1. Xinming Li et all. Graphene and related two-dimentional materials: Structure-property relationship for electronics and optoelectronics. Applied Physics Reviews 4, 021306 (2017).
2. S.M.Sze. Physical devices in semiconductors. John Wiley and Sons, New York (1981).
3. G.He et all. Negative Differential Conductance & Hot-Carrier Avakanching in Monolayer WS₂ FETs. Scientific Reports 7, 11256 (2017).
4. V. Lytovchenko, A. Kurchak, and M. Strikha. The semi-empirical tight-binding model for carbon allotropes “between diamond and graphite”. Journal of Applied Physics 115, 243705 (2014).

EFFECT OF ELECTRIC FIELD ON OPTICAL PROPERTIES OF SEMI-CONDUCTOR QUANTUM RINGS IN INFRARED REGION OF THE SPECTRUM

O.M. Makhanets, V.I. Gutsul

Chernivtsi National University, Chernivtsi, Ukraine

Cylindrical semiconductor quantum rings are intensively studied for a long time [1-5]. Varying the geometrical sizes of nano-rings one can influence the energy spectrum of quasi-particles and obtain the demanded optical properties.

The outer fields essentially affect the spectra of quasi-particles in such nano-structures. For instance, in the papers [2, 3], the effect of magnetic field on energy spectrum of electron and oscillator strengths of intra-band quantum transitions in nano-rings fabricated of semiconductors $GaAs/Al_xGa_{1-x}As$. In particular, it is shown that the electron energy and oscillator strengths of intra-band quantum transitions non-monotonously depend on the magnitude of magnetic field induction (B). In the dependences of energies on induction B one can see the anti-crossing of energy levels of equal symmetry over the magnetic quantum number (Aaronov-Bohm effect). The bright maxima and minima are observed in oscillator strengths as functions of induction B . In the papers [4, 5], the authors studied the influence of homogeneous electric field on optical properties of semiconductor nano-rings. Herein, the model of parabolic potential was used and wave function of electron in electric field was obtained as expansion over the complete set of wave functions of quasi-particle in infinitely deep potential well with further solution of the respective secular equation.

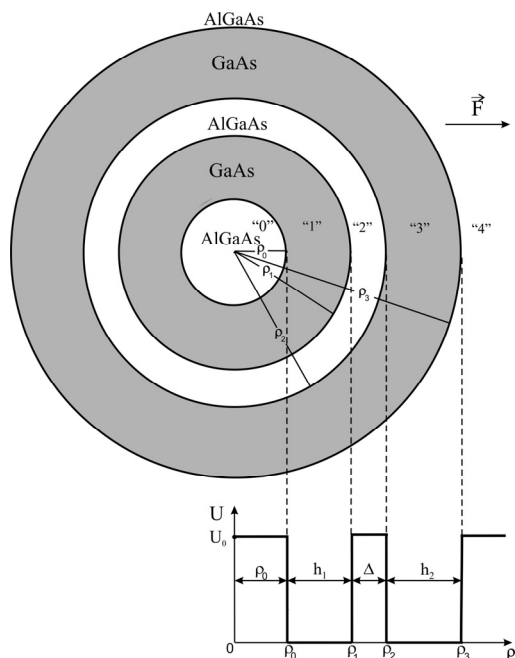


Рис.1 Geometrical and potential energy scheme of nano-structure

In the proposed paper we study the model of the system similar to those ones, observed in the papers [4,5]. However, we use an optimal model of confined potential with the orthonormal set of cylindrical wave functions, obtained in the model of finite potential. The oscillator strengths of intra-band quantum transitions as functions of electric field intensity in double semiconductor nano-rings $GaAs/Al_xGa_{1-x}As$ are analyzed for the first time.

In the paper we study the nano-structure consisting of two concentric rings with a height L (GaAs quantum wells) separated by concentric and tunnel-transparent ring $Al_xGa_{1-x}As$ with the thickness Δ . The inner and outer radii of the first ring are ρ_0 and ρ_1 , respectively (h_1 is the thickness), for the second ring - ρ_2

and ρ_3 (h_2 is the thickness). The cross-section by the plane $z = 0$ and potential energy scheme are shown in fig.1. A vector of electric field intensity \vec{F} is directed along Ox axis of nano-structure.

Taking into account the symmetry of the problem, the further calculations are performed in the cylindrical coordinate system (ρ, φ, z) with Oz axis directed along the axial axis of the rings. The electron effective mass m^* is fixed by the expression

$$\mu(\vec{r}) = \begin{cases} \mu_0, & |z| \leq L/2 \text{ i } \rho_0 < \rho < \rho_1, \rho_2 < \rho \leq \rho_3 \\ \mu_1, & |z| > L/2 \text{ a b o } |z| \leq L/2 \text{ i } 0 \leq \rho \leq \rho_0, \rho_1 \leq \rho \leq \rho_2 \end{cases}. \quad (1)$$

In order to study the electron energy spectrum, we solve the stationary Schrodinger equation

$$\hat{H}\Psi(\rho, \varphi, z) = E\Psi(\rho, \varphi, z) \quad (2)$$

with Hamiltonian

$$\hat{H} = \frac{1}{2\mu(\vec{r})} \left[-\hbar^2 \left(\frac{\partial^2}{\partial \rho^2} + \frac{1}{\rho} \frac{\partial}{\partial \rho} + \frac{1}{\rho^2} \frac{\partial^2}{\partial \varphi^2} + \frac{\partial^2}{\partial z^2} \right) \right] - \frac{\hbar^2}{2\mu(\vec{r})} \frac{\partial^2}{\partial z^2} + U(\vec{r}) - |e|F\rho \cos \varphi. \quad (3)$$

Assuming the fact that the electric field does not influence the energy spectrum when electron moves along Oz axis and that the electron is mostly located in the quantum wells of nano-structure (weakly penetrating into the barriers), the potential energy $U(\vec{r})$ is conveniently written as

$$U(\vec{r}) = U(z) + U(\rho), \quad (4)$$

where

$$U(z) = \begin{cases} U_0, & |z| > L/2, \\ 0, & |z| \leq L/2, \end{cases}, \quad U(\rho) = \begin{cases} U_0, & 0 \leq \rho \leq \rho_0, \rho_1 \leq \rho \leq \rho_2, \\ 0, & \rho_0 < \rho < \rho_1, \rho_2 < \rho \leq \rho_3. \end{cases} \quad (5)$$

If the potential energy has such form, then, z variable is separated in Schrodinger equation. Herein, the energy spectrum (E_{n_z}) and wave function ($f_{n_z}(z)$) of electron moving along Oz axis is easily obtained [3].

The Schrodinger equation with the Hamiltonian (3) is also exactly solved when electric field is absent. As a result, the energy spectrum ($E_{n_\rho m}$) and the radial wave functions ($R_{n_\rho m}(\rho)$) are obtained.

For the electron energy spectrum at $F \neq 0$, we write the unknown wave functions as an expansion over the complete set of wave functions

$$\frac{1}{\sqrt{2\pi}} R_{n_\rho m}(\rho) e^{im\varphi}:$$

$$\Psi_n(\vec{r}) = \frac{1}{\sqrt{2\pi}} \sum_{n_\rho} \sum_m c_{n_\rho m}^n R_{n_\rho m}(\rho) e^{im\varphi}. \quad (6)$$

We should note that the new states of electron are characterized only by one quantum number (n).

Setting the expansion (6) into Schrodinger equation with Hamiltonian (3), we obtain the secular equation:

$$\left| H_{n_p m, n'_p m'} - E_n \delta_{n_p, n'_p} \delta_{m, m'} \right| = 0, \quad (7)$$

where the matrix elements $H_{n_p m, n'_p m'}$ are the following:

$$H_{n_p m, n'_p m'} = E_{n_p m} \delta_{n_p, n'_p} \delta_{m, m'} + (\delta_{m', m+1} + \delta_{m', m-1}) \frac{eF}{2} \int_0^\infty R_{n_p m}(\rho) R_{n'_p m'}(\rho) \rho^2 d\rho. \quad (8)$$

Finally, the problem of obtaining of energy spectrum (E_n) and wave functions ($\psi_n(\vec{r})$) is reduced to the calculation of eigenvalues and eigenvectors of this matrix.

These electron energies and wave functions give opportunity to evaluate the oscillator strengths of intra-band optical quantum transitions, using the formula [15]

$$F_n^{n'} \sim (E_{n'} - E_n) \left| M_n^{n'} \right|^2, \quad (9)$$

where

$$M_n^{n'} = \int \psi_n^*(\vec{r}) e \rho \cos(\varphi) \psi_{n'}(\vec{r}) d\vec{r} \quad (10)$$

is a dipole momentum of the transition.

In this paper we analyze the electron energies and oscillator strengths of intra-band quantum transitions as functions of electric field intensity.

1. T. Mano, T. Kuroda, S. Sanguinetti, T. Ochiai, T. Tateno, J. Kim, T. Noda, M. Kawabe, K. Sakoda, G. Kido, N. Koguchi, *Nano Lett.* **5**, 425 (2005).
2. F.J. Culchac, N. Porras-Montenegro, J.C. Granada, A. Latge, *Microelectronics Journal* **39**, 402–406 (2008).
3. O.M. Makhanets, V.I. Gutsul, A.I. Kuchak, *Journal of Nano- and Electronic Physics* **9**, 06015 (2017).
4. C.M. Duque, Ruben E. Acosta, A.L. Morales, M.E. Mora-Ramos, R.L. Restrepo et al., *Optical Materials* **60**, 148-158 (2016).
5. H.M. Baghrmian, M.G. Barseghyan, D. Laroze, A.A. Kirakosyan, *Physica E* **77**, 81–89 (2016).
6. M. Masale, *Physica B* **292**, 241 (2000).

PROPERTIES OF ELECTRON QUASI-STATIONARY STATES IN DOUBLE-BARRIER NANOSTRUCTURE WITHIN THE MODEL OF POSITION DEPENDENT EFFECTIVE MASS

J.O. Seti, M.V. Tkach, O.M. Voitsekhivska

Yuriy Fedkovych Chernivtsi National University, 2, Kotsyubinsky Str., 58012, Chernivtsi, Ukraine, j.seti@chnu.edu.ua

The theory of position-dependent effective mass and potential energy of quasiparticles became actual after the appearance of the unique unipolar nano-devices – quantum cascade lasers and quantum cascade detectors. The theory, which explains the tunneling of electrons through the resonant-tunneling structures (RTS), being the cascades of the abovementioned devices, is very important for the correct optimization of their operating parameters. Such theory demands use of the models with rather realistic position-dependent effective mass. The physical considerations prove that, due to not perfect hetero interfaces between structure layers, there exist the near-interface regions, where the effective mass of quasi-particle differs from that in the contacting crystals, being the linear function of coordinate in the first approximation.

We should mention that due to the mathematical difficulties arising at the solution of Schrodinger equation, in the majority of theoretical papers [1, 2], the electronic tunneling through the multi-layered RTS was studied within the simple step-like models for the electron potential energy and effective mass at hetero interfaces.

In the proposed paper, we develop the theory and investigate the properties of spectral parameters of electron quasi-stationary states (QSS) within the smooth position-dependent effective mass. The plane open double-barrier RTS is studied using the model of rectangular potential profile of electron and its position-dependent effective mass, being the linear function of coordinate z (fig.1)

$$m(z) = m_w \begin{cases} 1, & 0 \leq |z| \leq z_{\pm 1}, z_{\pm 6} \leq |z| \leq \infty; \\ 1 + \delta m \frac{|z| - z_{\pm 1}}{2\Delta_1}, & z_{\pm 1} \leq |z| \leq z_{\pm 3}; \\ \frac{m_b}{m_w} - \delta m \frac{|z| - z_{\pm 4}}{2\Delta_2}, & z_{\pm 4} \leq |z| \leq z_{\pm 6}; \\ \frac{m_b}{m_w}, & z_{\pm 3} \leq |z| \leq z_{\pm 4}, \end{cases} \quad (1)$$

where Δ_1 and Δ_2 are the sizes of near-interface regions between wells and barriers of RTS and m_w , m_b are the electron effective masses in wells and barriers, respectively, $\delta m = (m_b - m_w) / m_w$.

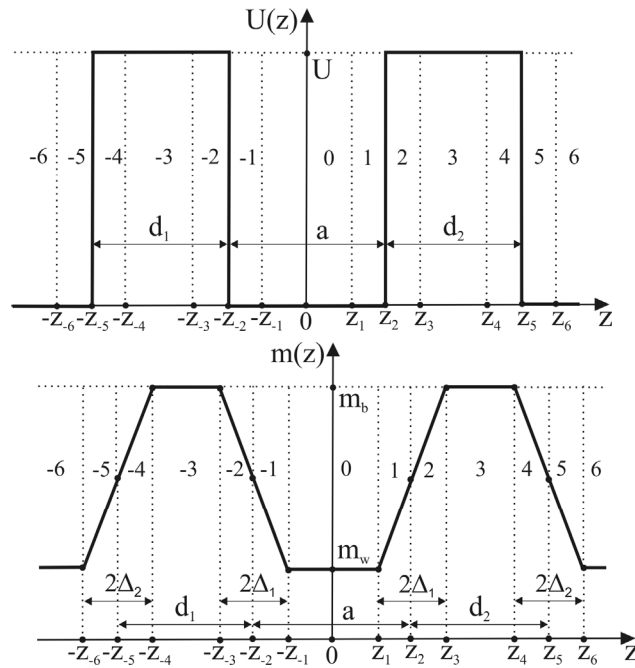


Fig.1. Rectangular potential profile (U) as function of coordinate (z) and linearly-dependent effective mass (m) of electron in double-barrier RTS

The solutions of Schrodinger equation for the electron [3]

$$\left[-\frac{\hbar^2}{2} \frac{d}{dz} \left(\frac{1}{m(z)} \frac{d}{dz} \right) + U(z) \right] \Psi(z) = E \Psi(z), \quad (2)$$

are obtained using two well-known quantum-mechanical approaches: transmitting coefficient (D -method) or scattering matrix (S -method). In both methods (D and S), they must satisfy the fitting conditions, which can be written in compact form:

$$\Psi_{\pm(p-1)}^{D,S}(z_{\pm p}) = \Psi_{\pm p}^{D,S}(z_{\pm p}), \quad \left. \frac{d\Psi_{\pm(p-1)}^{D,S}(z)}{dz} \right|_{z=z_{\pm p}} = \left. \frac{d\Psi_{\pm p}^{D,S}(z)}{dz} \right|_{z=z_{\pm p}}, \quad (p=1-6) \quad (3)$$

In the regions of RTS where the electron effective mass is constant, the solutions of equation (2) are known [2], and in D -method are the following:

$$\Psi_{\pm p}^D(z) = A_{\pm p}^D e^{iK_{\pm p}z} + B_{\pm p}^D e^{-iK_{\pm p}z}, \quad (p=0, 3, 6) \quad (4)$$

and in S -method

$$\Psi_{\pm p}^S(z) = A_{\pm p}^S e^{iK_{\pm p}z} + B_{\pm p}^S e^{-iK_{\pm p}z}, \quad (p=0, 3) \quad (5)$$

$$\Psi_{\pm 6}^S(z) = A_{\pm 6}^S (e^{\mp ikz} - S e^{\pm ikz}), \quad (p=6) \quad (6)$$

where

$$K_{\pm p} = \sqrt{(-1)^p} \begin{cases} k = \hbar^{-1} \sqrt{2m_w E}, & p=0, 6, \\ \chi = \hbar^{-1} \sqrt{2m_b (U - E)}, & p=3. \end{cases} \quad (7)$$

S is the scattering matrix.

In the near-interface regions of RTS where the electron effective mass is linearly dependent of coordinate, equation (2) in D - and S -methods also has the exact solutions [4], written as linear superpositions of the derivatives of Airy functions

$$\Psi_{\pm p}^{D,S}(\xi_{\pm p}) = A_{\pm p}^{D,S} \text{Ai}'(\xi_{\pm p}) + B_{\pm p}^{D,S} \text{Bi}'(\xi_{\pm p}), \quad (p=1, 2, 4, 5) \quad (8)$$

where

$$\xi_{\pm p}(\eta) = 2m(\eta) \begin{cases} \left(-\frac{m_w a_0^2 d^2 Ry \varepsilon}{\delta m^2 \hbar^2} \right)^{1/3}, & p=1, 5, \\ \left(\frac{m_w a_0^2 d^2 Ry (V - \varepsilon)}{\delta m^2 \hbar^2} \right)^{1/3}, & p=2, 4. \end{cases} \quad (9)$$

Now, using the known procedure [2], from the system of fitting conditions (3), one can obtain the transfer matrix. Its elements define the scattering matrix and transmitting coefficient for the double-barrier RTS. The functions $D(E)$ and $S(E)$ make possible to calculate the resonance energies (E_n) and widths (Γ_n) of electron QSS in both approaches and to study their behavior at the varying sizes of near-interface regions (Δ_1, Δ_2).

The high accuracy numeric calculations were performed for the double-barrier RTS with $\text{In}_{0.53}\text{Ga}_{0.47}\text{As}$ wells and $\text{In}_{0.52}\text{Al}_{0.48}\text{As}$ barriers, being the basic elements of modern quantum cascade lasers and detectors [5]. Thus, the geometrical parameters for wells and barriers were taken typical, varying from several to dozen nano-meters (as for the cascades of nano-devices).

The calculations prove that the differences between the resonance energies of sub-barrier electron QSS, obtained within the exact S -method and approximated D -method, do not exceed one per cent and that of resonance widths – several per cents. It is shown that the spectral parameters of electron QSS strongly depend on the size (Δ_1) of near-interface regions between the inner potential well and barriers of double-barrier RTS and are almost independent of the size (Δ_2) of outer near-interface regions.

It is established that in the ranges of physically correct Δ_1 size (till one lattice constant), the resonance energies of sub-barrier electron QSS differ from that obtained in the well-known simplified abrupt model for the effective mass, not more than at 0.5%, while the resonance widths – not more than at 5%. Herein, the resonance energies in abrupt model are always smaller than that obtained in the realistic model with linearly-dependent effective mass. The difference between the resonance energies of electron QSS in both models not big. However, it can be either positive or negative depending of the size of quantum well and number of the state.

1. C. Jirauschek, T. Kubis, Appl. Phys. Rev. 1, 011307 (2014).
2. N. V. Tkach, Yu. A. Seti, Low Temp. Phys. 35, 556 (2009).
3. D. J. BenDaniel, C. B. Duke, Phys. Rev. 152, 683 (1966).
4. M. Tkach, J. Seti, O. Voitsekhivska, Superlattices Microstruct. 109, 905 (2017).
5. B. Schwarz et al., Appl. Phys. Lett. 107, 071104 (2015).

Effect of Polarization Phonons on Electron, Hole and Exciton States in Spherical Quantum Dots of Cubic Lattice Structure

I. S. Shevchuk

*Department of Physics
Ivan Franko Drohobych State Pedagogical University*

In recent years quantum dot structures attract increasing attention due to their interesting quantum mechanical phenomena and unique perspectives to apply them in electronic and optoelectronic devices [1]. In view of their size-dependent optical properties QDs can be used in biological and biomedical researches [2]. In these systems there exists a strong 3D quantum confinement effect on electron, hole and exciton states arising from the energy gap difference between materials. The localization of charged particles (electrons, holes) and excitons in quantum dots leads to increasing interaction between particles. Electron-phonon interaction in QD is different from the interaction in bulk material. It considerably increases with reducing dimensionality of the system, a number of polarization oscillating branches, which interact with electrons and holes, rises: there exist confined and interface (surface) optical phonon types [3]. It is found that the electron-optical phonon interaction cannot be neglected, and near the surface the interaction of an electron with surface optical phonons can be compared by magnitude to that with confined longitudinal optical phonons [4]. A strong electron-phonon interaction results in arising of polaron states in QDs based on materials with a high degree of ionicity. Polaron states show themselves in a quite noticeable change of electron and hole quantizing energy in the quantum dot.

In [1] the effect of electron-phonon interaction on impurity electron energy in a ZnSe spherical QD, placed in a non-polar matrix, is investigated by variation technique. In [4] electron and hole polaron energies are found in a spherical quantum dot with an infinite potential barrier by unitary transformation method. The interaction of longitudinal optical phonons and surface optical phonons with conduction electrons and donor-type excitons in polar spherical quantum dots placed in a glass matrix (calculated for CdSe and CuCl QDs) is considered. A quantum-size effect is described with the infinite potential well in the two non-degenerate band model in the envelope function approximation. The interaction of charged carriers with phonons is considered in the adiabatic approach. The ground state energy of donor-type exciton is calculated by variation technique using a one-parameter probe envelope function considering the electron-hole interaction. The data show that for a donor-type exciton in a quantum dot centre, the lattice polarization effect leads to reducing of the energy for all values of a QD radius.

Optical transition energies of the lowest states of an electron-hole pair in CdSe QDs placed in glass are determined in [5]. The comparison of experimental data obtained by different methods is made; a general dependence of energy on QD size is established.

In [6] bulk CdSe band parameters in magneto-optic measurements of super-thin samples are found. Absorption spectra for a CdSe QD system located in planes in a ZnSe matrix are obtained. A theoretical model to describe energy spectra and exciton behaviour is proposed. Theoretical calculations allow predicting of structure parameters necessary for the relevant carrier localization and oscillator strength enhancement.

In [7] the dependence of CdSe nanocrystal optical transitions in the many-body approximation on the basis of one-particle wave functions for a pseudo-potential on presence of the so-called “observers” – electrons and holes is calculated. Because of the difference in localization of electron and hole wave functions, absorption lines are shifted in a certain manner when an electron or a hole goes into a quantum dot. The lowest emission line is significantly shifted in the direction of the long wavelength region of spectrum with respect of the lowest allowed absorption line.

In [8] the dependence of exciton ground state energy and oscillator strength in a spherical quantum dot made of crystal with a high ionization degree in case of infinite potential barriers is investigated. A strong interaction of an exciton with optical phonons using the effective potential between an electron and a hole is taken into consideration. The comparison is made between exciton ground state energy values calculated with this potential and the results where the interaction of an exciton with confined and surface phonons is considered separately. A very good agreement of these calculated results is observed. In comparison with two simpler exciton models, it is seen that a strong confinement in small QDs decreases the polaron shift effect on exciton properties. The electron-hole interaction is reduced. The conclusion is made that the oscillator strength is less dependent on the form of the effective interaction with reducing quantum dot size. The exciton formation energy is defined for materials with a high ionization degree such as CdSe, GaN, ZnO, and CuCl.

I. P. Ipatova et al [9] found electron and hole polaron energies in spherical QDs considering the valence band degeneracy. The adiabatic approach is used. However, the electron-phonon interaction Hamiltonian is chosen in the form similar to that of the bulk crystal.

Therefore, the general analysis shows that in spite of a rather wide study of polaron effects and their influence on electron, hole and exciton states a significant number of questions need to be solved. In particular, in ionic semiconductor QD nanoheterosystems the question of partial contribution of different polarization phonon modes in the hole and exciton energy renormalization is insufficiently studied when a complex semiconductor band spectrum and different-type polarization phonon effects on exciton Stokes shift are considered. This work highlights the above-mentioned problems.

In the paper the dielectric continuum approximation to the study of the effect of polarization phonons on renormalizing of the energy of electron, hole and exciton states in spherical quantum dots of cubic lattice structure is employed taking into account degenerate valence bands. The role of interface and confined polarization phonons in formation of the electron-, hole-, and exciton-polaron energy for

various quantum dots is defined. The proposed theoretical formalism was used to analyse the energy spectra of *GaAs*, *CdSe*, *CdTe* quantum dots. The resonant Stokes shift both without and with account for polaron effects at different radii of quantum dots is one of the theoretical results of this work. Qualitative agreement between our results and the results obtained in [3] gives hope that our approach can be accepted for further study of optical properties of such nanostructures.

- [1] D.V.Melnikov, W.B. Fowler, Phys. Rev.B, 2001, **63**, 165302.
- [2] R. Zeng, T. Zhang, J. Liu et al, Nanotechnology, 2009, **20**, 095102.
- [3] I.P. Ipatova, A.Yu. Maslov, O.V. Proshina, Phys. Low-Dim. Structur., 1996, **4-5**, 1.
- [4] Z.J. Shen, X.Z. Yuan, G.T. Shen, and B.C. Yang. Phys. Rev.B, 1994, **49**, 11035.
- [5] U. Woggon, O. Wind, F. Gindele, E. Tsitsishvili, M. Muller. Journal of Luminescence, 1996, **70**, 269.
- [6] G.N. Aliev, A.D. Andreev, R.M. Datsiev et al, Journal of Crystal Growth, 1998, **184/185**, 315.
- [7] A. Franceschetti, A. Zunger, Phys. Rev.B, 2000, **62**, R16287.
- [8] R. T. Senger, K.K. Bajaj, Phys. Rev.B, 2003, **48**, 045313.
- [9] I.P. Ipatova, A.Yu. Maslov, O.V. Proshina, Fiz. Tverd. Tela, 1999, **33**, 832.
- [10] I.M. Kupchak, D.V. Korbutyak, S.M. Kalytchuk, Yu.V. Kryuchenko, A.Y. Shkrebtiiy, Journal of Physical Studies, 2010, **14** 2701.

SYNTHESIS OF NANOCOMPOSITE POLYMER FILMS WITH THE EMBEDDED CIS NANOCRYSTALS AND THEIR OPTICAL PROPERTIES

**V. Tokarev¹⁾, O. Shevchuk¹⁾, H. Ilchuk¹⁾, N. Bukartyk¹⁾, R. Petrus¹⁾, S. Tokarev¹⁾, D. Korbutyak²⁾, S. Budzulyak²⁾, O. Kapush²⁾, V. Ermarov²⁾, S. Kalytchuk²⁾
N. Vakhnyak²⁾**

¹⁾ *Lviv Polytechnic National University (Lviv, Ukraine)*

²⁾ *V.E. Lashkaryov Institute of Semiconductor Physics, NAS of Ukraine (Kyiv, Ukraine)*

Due to the increasing demand for semiconductor nanocrystals (NCs) that a last time found many applications, particularly in consumer electronic devices, in medicine etc., the task of developing novel materials that does not contain toxic compounds, first of all heavy metals, becomes crucial [1,2]. One of the possible and promising alternative to semiconductors containing toxic elements (Cd, Pb, Se) is less toxic copper indium disulfide CuInS_2 semiconductors (CIS), which is a direct wide-band semiconductor. Recently a special attention has been paid to CIS nanocrystals, since they are characterized by high absorption coefficients (extinctions) over a wide range of wavelength within visible spectrum, high efficiency of luminescence under different types of excitation, the ability to significantly change the width of their bandgap, the values of the Stokes shift, and the radiation field.

In situ synthesis of CIS nanocrystals embedded in cross-linked polymer films on a solid support and their optical properties are the main topics of this presentation.

The cross-linked polymer films based on the reactive peroxide copolymers (RC) and polyethyleneglycol (PEG-200) have been used as polymeric matrices for *in situ* synthesis of CIS NCs. The mixtures of these two polymeric components (RC and PEG-200) have several benefits as matrices for synthesis of mineral NCs, the most important among which are the following: i) these matrices can easily form the cross-linked polymer films; ii) this process is accompanied by the formation of nanopores of controllable size, where synthesis of NCs takes a place; iii) these matrices can tether the metal ions by forming ionic and coordination chemical bonds.

The AFM image, the roughness profile and the nano-porosity distribution of the cross-linked polymer film, obtained at thermal treatment of the mixture of RC with PEG-200 spin-cast on a glass slide, are shown in Figure 1 a-c.

No phase separation of the initial polymer components (RC and PEG-200) is observed in the cross-linked polymer film (Figure 1 a); its roughness is rather small, on average 2-4 nm (Figure 1 b); unimodal size distribution of nano-pores with the average size of 7.7 nm has been found (Figure 1 c). These pores can serve as nano-reactors for *in situ* synthesis of semiconductor NCs. By controlling the size of pores, it is possible to control the size of NCs obtained [3].

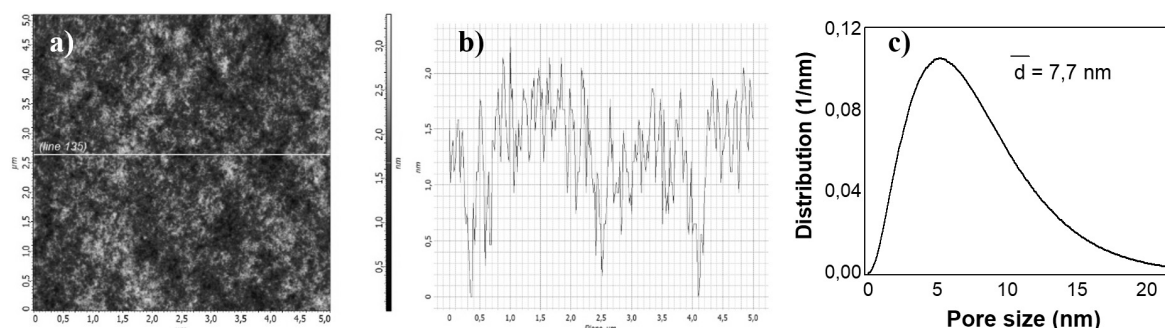


Figure 1. AFM image (a), the roughness profile along the line in the left image (b) and distribution of nanopores determined by Small-Angle X-ray Scattering (c) in the polymer film comprised RC and PEG-200, which was spin-cast and cross-linked on a glass slide.

Copper acetate monohydrate $\text{Cu}(\text{CH}_3\text{COO})_2 \cdot \text{H}_2\text{O}$ and Indium acetate $\text{In}(\text{CH}_3\text{COO})_3$ have been used as precursors for synthesis of CIS NCs. These salts at their various ratios have been initially mixed with the polymer components in a joint solvent before spin-casting on glass slides to form polymer films containing metal ions. Afterwards these films have been heated at $T=120^\circ\text{C}$ for 1.5 h to cross-link followed by exposure to gaseous H_2S at $T=60^\circ\text{C}$ for 12 h to form CIS NCs directly in the polymer films. It should be noted that prior to exposure to H_2S these films were completely transparent and colorless. They become colored only after exposure to gaseous H_2S while remaining completely transparent, despite a high enough content of CIS semiconductor particles (theoretically 20%). This is possible only if CIS particles formed are of nanometer size. In our case, the size of CIS NCs is about 5 nm that is somewhat less than the size of nanopores in the polymer matrix.

Absorption spectra in the visible region of the nanocomposite films with embedded CIS NCs are shown in Figure 2 a.

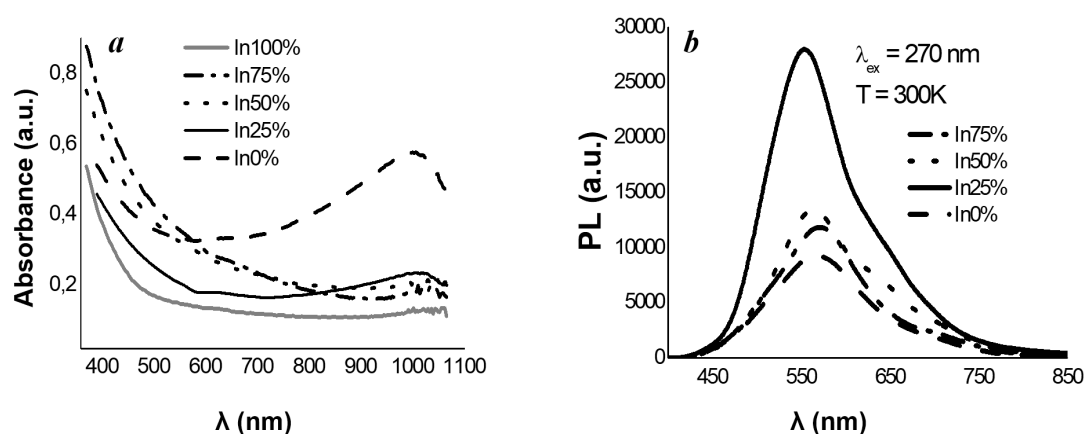


Figure 2. Absorption spectra (a) and photoluminescence spectra (b) of the nanocomposite films with embedded CIS NCs obtained at various initial ratios of Cu to In ions in the cast solutions as it is indicated in the legend.

It is clearly seen that the shape of absorption spectrum (Figure 2 a) depends strongly on the Cu:In ratio. An introduction of In ions (25%) brings about initially a sharp decrease in absorption intensity in the region of $\approx 1000 \text{ nm}$ attributed to ab-

sorption of CuS NCs, which almost completely disappears with a further increase of In content ($\geq 50\%$). For the film with NCs based on 100% In, no absorption is observed in this region. That evidences rather in favour of formation of tertiary semiconductor NCs with various composition $\text{Cu}_x\text{In}_{(1-x)}\text{S}_2$ depending on the Cu:In ratio taken.

Photoluminescence (PL) spectra of the nanocomposite films with embedded CIS NCs have been recorded on an automated setup at excitation wavelength of 270 nm, at temperature 300K (Figure 2 b).

Broad bands are observed in the photoluminescence (PL) spectra of $\text{Cu}_x\text{In}_{(1-x)}\text{S}_2$ NCs in the wavelength range 450-750 nm (Figure 2 b); these bands are structured and composed of at least two closely spaced bands. Broad PL band with a large Stokes shift is characteristic for the CIS semiconductor nanocrystals [4], while the origin of this phenomenon remains unclear and is still not understood. The energy position of the maxima of these bands ($\lambda \approx 550$ nm) depends weakly on the elemental composition of the $\text{Cu}_x\text{In}_{(1-x)}\text{S}_2$ NCs. This means that luminescence of the nanocrystals synthesized is determined by their own structural defects inside the NCs and by those located on the boundary between nanocrystal and polymeric matrix. Characteristically, the integrated PL intensity of $\text{Cu}_x\text{In}_{(1-x)}\text{S}_2$ NCs depends on the elemental composition of the NC not monotonically, reaching a maximum at $x = 0.75$. This can mean that at such a ratio of Cu / In in the $\text{Cu}_x\text{In}_{(1-x)}\text{S}_2$ NCs, the concentration of radiating centers is maximal.

Acknowledgement

This work was supported by the State foundation for basic research of Ukraine, Grant No $\Phi 76/24 - 2018$.

1. Phosphors, Up Conversion Nano Particles, Quantum Dots and their Applications. Volume 2 / Ed. Ru-Shi Liu. – Springer Science+Business Media, Singapore – 2016, 882 p.
2. Aldakov D., Lefrançois A., Reiss P. Ternary and quaternary metal chalcogenide nanocrystals: synthesis, properties and applications. J. Mater. Chem. C, 2013, 1, 3756-3776.
3. Tokarev V., Shevchuk O., Ilchuk H., Tokarev S., Kusnezh V., Korbutyak D., Budzulyak S., Kalytchuk S., Bukartyk N. Thin polymer films with embedded CdS nanocrystals. Colloid. Polym. Sci., 2015, 293, 1159-1169.
4. Leach A. D. P., Macdonald J. E. The Optoelectronic Properties of CuInS_2 Nanocrystals and their Origin. J. Phys. Chem. Lett., 2016, 7, 3, 572-583.

ON REARRANGMENT OF THE ENERGY SPECTRUM OF DELTA-DOPED QUANTUM WELLS IN THE THZ RANGE

**V. Tulupenko^{1,2}, R. Demediuk¹, V. Akimov³, C. A. Duque², A. L. Morales²,
D. Sushchenko¹, and O. Fomina¹.**

¹ *Donbass State Engineering Academy, Kramatorsk 84313, Ukraine,*

² *Grupo de Materia Condensada, Instituto de Física, Facultad de Ciencias Exactas y Naturales, Universidad de Antioquia-UdeA, Calle 70 No. 52-21, Medellín, Colombia*

³ *Departamento de Ciencias Básicas, Universidad de Medellín, Carrera 87 No. 30-65, Medellín, Colombia,*

Scientists dealing with optics always have a dream of having in hands easy in operation and convenient tools for changing the frequency (wavelength) of radiation. Since the times when Max Planck and Albert Einstein introduced the formula for differences between j -th and i -th energy levels $\Delta E_{ij} = E_j - E_i = h\nu_{ij}$, with h and ν being the Planck's constant and light frequency correspondingly, and it became clear that light is emitted (absorbed) due to electron transitions between these levels³, this problem has been transformed into a problem of changing the energy difference between the energy levels⁴. That is particularly important for those who work in the field of development of photodetectors and lasers. By the time of the nanotechnology era, people have only dealt with the energy levels supplied by nature and it was extremely difficult to change the original spacing between these levels although they always wanted to do that. Development of nanotechnology opened new possibilities for controlling the distance between energy levels provided by new objects such as quantum wells, quantum wires, quantum dots, quantum rings and graphene-based layered structures of different shapes and dimensions, which can potentially lead to the creation of new tunable devices on their base. And one of the most important things in such devices is the fact that the structure of their energy levels is controlled by their shapes and dimensions. It gives the exiting possibility to plan desirable working frequency of the apparatus on the early stage of designing the structure. And of course, different kinds of nanostructures became to be studied on the subject of changing the operating frequency in already having been fabricated devices. Among many others there is such exotic suggestion [1] as to use microscopic heaters (!), and authors of the works [2] for the same purpose use the external emission to change optical properties of the cladding layers, which leads to the tunability of the device. We give these examples to underline the importance of the problem and that people are seeking any possibility for tunability of the devices. But it is obviously that for the ordinary user the most convenient way of tuning the working frequency of the device is using a small electric field. And similar works have always been and will be in focus of researchers working in the field of various types of

³ We do not touch here the light emission mechanisms associated with accelerated or relativistic (Cherenkov effect) movement of electrons.

⁴ We put aside the problem of selection rules and matrix elements for a while.

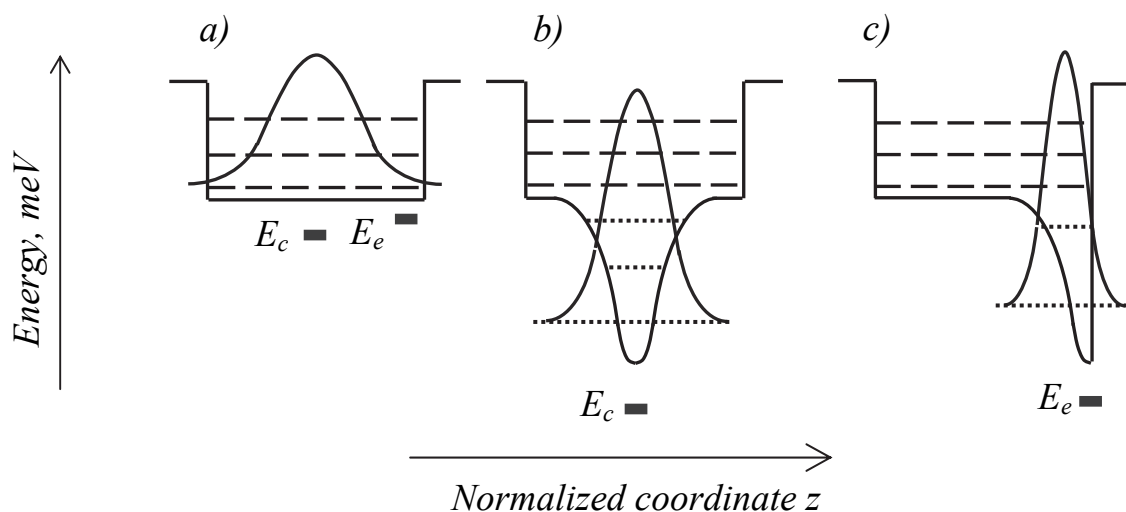


Fig.1. Schematic representation of influence of the ionized delta layer potential on the energy structure and impurity binding energy. Solid lines – energy profiles of the QWs, dashed lines – energy levels of the original QW, dotted lines – energy levels created by the electrostatic (Hartree) potential, blue lines – wave functions of the first energy level. E_c and E_e (short bold red lines) – ground impurity states for center-, and edge-doped QWs accordingly. *a)* – original structure with neutral impurities (at low temperatures), *b)* – structure with center-doped ionized delta layer, *c)* – structure with edge-doped ionized delta layer.

optoelectronic devices. Therefore each such new idea about easy broadband tuning of the wavelength deserves to be examined as it can find its own potential users. And this article is devoted to review of our works [3 - 8] considering one of such ideas about tuning of the frequency by a small electric field in such specific and important now spectral range as a THz one, which got a tremendous development during last two decades due to very important for human life application of THz radiation. We can mention here only few of them, which are, in our opinion, the most important. They are the medical application, including localization [9] and even treatment of a cancer tissue [10]. Another important area of using THz radiation is security [11] and antiterrorism activity, which became especially important after terrorist attacks in the United States on September, 11, 2001. And very important thing concerning THz radiation is that it is harmless to the staff and surrounding people due to a small energy of a THz quantum. Therefore in many developed countries the special programs on the THz science and its application were adopted. And tunability of the THz devices one of the most important topics of researches. Here, however we must say that we do not consider the time domain THz generation and detection techniques in spite of the fact that most of the remarkable applications of THz radiation were obtained by this technique in scientific laboratories around the world. We suppose that such complicated method is not intended for the ordinary user and the modern trend in development of the THz science is

creation of cheap, miniature, which means nanostructure-based, and easy in operation devices like that presented in the work [12]. And our proposal of using rectangular delta doped with shallow impurities QW lies in the way of this trend. We consider the idea using the example n-type delta-doped QW, although p-type QWs can also be used. Important thing is that in this case impurity concentration must be small enough in order one can speak about impurity levels rather than about impurity bands. At low temperatures all the electrons are frozen out to impurities and we have the ordinary rectangular QW – see Fig.1a. Increased temperature is followed by the ionization of impurities in the delta layer and additional potential (Hartree potential) created by ionized donors and free electrons in the subbands of spatial quantization appears. This situation is shown in Fig.1b and Fig.1c for center-, and edge-doped QWs. Thus it is became possible to change the potential by varying temperature or at fixed temperature – by a small electric field as we remember that impurities are shallow! Again, using a small electric field one has the possibility to change the deep of the v-shaped QW and therefore the number of energy levels and separation between them.

In the report we discuss the various aspects of the above described picture on the base of our works on the topic.

This work was partly supported by the ministry of education and science of Ukraine.

1. Alfredo Bismuto, Yves Bidaux, Camille Tardy, Romain Terazzi, Tobias Gresch, Johanna Wolf, Stephane Blaser, Antoine Muller and Jerome Faist, OPTICS EXPRESS, 23, 29715 (2015).
2. Shanshan Song, Scott S. Howard, Zhijun Liu, Afusat O. Dirisu, Claire F. Gmachl, and Craig B. Arnold, Appl. Phys. Lett., 89, 041115 (2006).
3. V. Tulupenko, A. Abramov, Y. Belichenko, V. Akimov, T. Bogdanova, V. Poroshin and O. Fomina, J. Appl. Phys. 109 (2011) p.064303.
4. V. Tulupenko, C.A. Duque, R. Demedyuk, Ya Belichenko, C.M. Duque, V. Akimov, V. Poroshin, O. Fomina, Philos. Mag. Lett. 93 (2013) 42.
5. V. Tulupenko, C.A.Duque, R.Demediuk, V.Belykh, A.Tiutiunnyk, A.L.Morales, V. Akimov, R.L.Restrepo, M.E.Mora-Ramos, V.Poroshin, O.Fomina. Physica E, 66 (2015) 162–169.
6. V. Tulupenko, C.A.Duque, V.Akimov, R.Demediuk, V.Belykh a, A.Tiutiunnyk, A.L.Morales, R.L.Restrepo, M.E.Mora-Ramos, O.Fomina. Physica E 74 (2015) 400–406.
7. C. A. Duque, V. Akimov, R. Demediuk, V. Belykh, A. Tiutiunnyk, A. L. Morales, R. L. Restrepo, O. Nalivayko, O. Fomina, M. E. Mora-Ramos, and V. Tulupenko, Superlattices Microstruct. 87, 5 (2015).
8. C.A. Duque, V. Akimov, R. Demediuk, V. Belykh, A. Tiutiunnyk, A.L. Morales, R.L. Restrepo, O. Nalivayko, O. Fomina, M.E. Mora-Ramos, V. Tulupenko. Superlattices and Microstructures 87,125 (2015).

9. O. Mitrofanov, M. Lee, J. W. P. Hsu, I. Brener, R. Harel, J. F. Federici, J. D. Wynn, L. N. Pfeiffer and K. W. West, IEEE J. Sel. Top. Quantum Electron. 7, 600 (2001).
10. A. J. Fitzgerald, V. P. Wallace, M. Jimenez-Linan, L. Bobrow, R. J. Pye, A. D. Purushotham, D. D. Arnone, Radiology 239, 533(2006).
11. By Hai-Bo Liu, Hua Zhong, Nicholas Karpowicz, Yunqing Chen, and Xi-Cheng Zhang, Proceedings of the IEEE, 95, 1514 (2007).
12. Kazuue Fujita, Masahiro Hitaka, Akio Ito, Tadataka Edamura, Masamichi Yamanishi, Seungyong Jung, and Mikhail A. Belkin. APPLIED PHYSICS LETTERS 106, 251104 (2015).

OBTAINING AND OPTICAL PROPERTIES OF ZnS, ZnS:Fe NANOCRYSTALS

Yu.F.Vaksman, Yu.A.Nitsuk

*I.I.Mechnikov Odesa National University, Dvoryanskaya str. 2, Odesa, 65082
Ukraine*

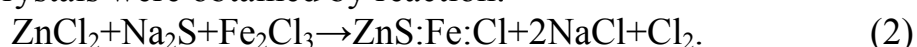
Semiconductor compounds of the A_2B_6 group doped with transitional elements, are of considerable interest as effective phosphors in the near infrared wavelength range. Nanocrystals of this compound can be used as luminescent markers in medicine. The emission of such markers should be localized in the range of maximum transparency of biological tissues (0.65-1.5 μm). Investigation of the semiconductor ZnS:Fe single crystals [1,2] indicates a photoluminescence broad band of (0.5-0.8 μm), which makes their use in medicine promising.

The goals of this study is to develop a synthesis technique for the preparation of ZnS:Fe nanocrystals having a photoluminescence spectrum in the near infrared region. In order to compare the obtained results, the optical properties of ZnS and ZnS, ZnS:Fe single crystals are presented.

Preparation of nanocrystals. ZnS, ZnS: Fe nanocrystals were prepared by chemical synthesis in a polyvinyl alcohol or gelatin medium. Pure zinc sulfide nanocrystals were prepared by the reaction:



Iron-doped ZnS nanocrystals were obtained by reaction:



After the synthesis reaction, the solution was dried on a glass substrate. As a result, ZnS, ZnS: Fe nanocrystals were obtained in a transparent solid polymer matrix. For comparison, in some cases liquid samples were obtained in an aqueous solution..

Optical absorption spectra. Optical absorption spectra of undoped single and nanocrystals are shown in Fig.1. The band gap width of undoped single crystals of zinc sulfide is 3.6 eV. The obtained nanocrystals are characterized by values of the band gap of 5.2, 5.1 and 4.9 eV at concentrations of Na_2S and ZnCl_2 equal to 5, 10, 20%, respectively.

Optical absorption spectra of ZnS:Fe nanocrystals indicate the absorption edge shift toward smaller energies than undoped samples (Fig. 2). This shift is 0.44 eV, with an increase of 0.2 to 0.5% Fe_2Cl_3 . The latter may be due to an increase in iron concentration in the samples, or an increase in the nanocrystals size. According to studies of the absorption edge of ZnS:Fe single crystals with iron concentration of $2 \cdot 10^{18} \text{ cm}^{-3}$, the band gap shift is reduced by 40 meV and is 3.2 eV. Thus, an increase of nanocrystals size is the main reason for ZnS:Fe band gap width decreasing during iron doping.

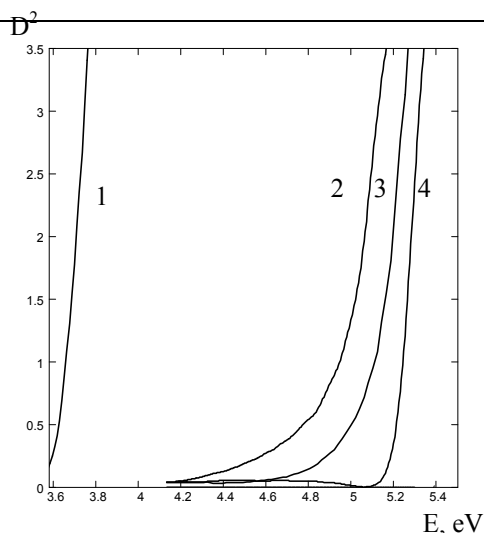


Fig.1. Optical absorption spectra of ZnS (1) single and (2-4) nanocrystals.

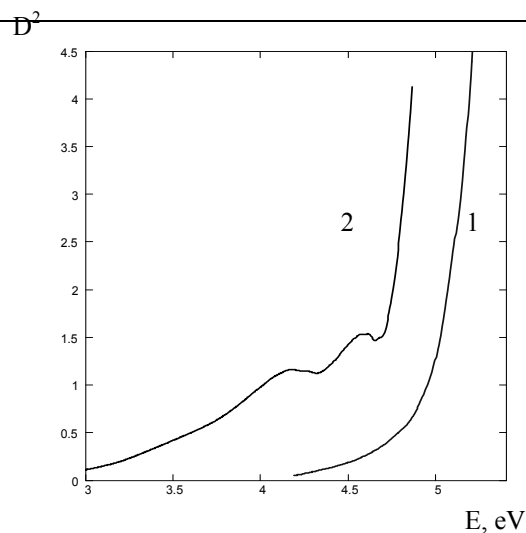


Fig.2. Optical absorption spectra of (1) ZnS and (2) nanocrystals.

Fig. 3 shows the optical absorption spectra of ZnS: Fe nano- and single crystals at the range 1.6 - 3.0 eV. Comparison of these spectra allows us to estimate the iron concentration in nanocrystals of order 10^{17} - 10^{18} cm $^{-3}$.

The calculation nanocrystals sizes was carried out on the magnitude of the difference between their band gap width and bulk single crystals using a well-known ratio [3]:

$$R = \frac{h}{\sqrt{8\mu\Delta E_g}}, \quad (3)$$

where h is the Planck constant, $\mu = ((m_e)^{-1} + (m_h)^{-1})^{-1}$ – reduced mass, $m_e = 0.27m_0$,

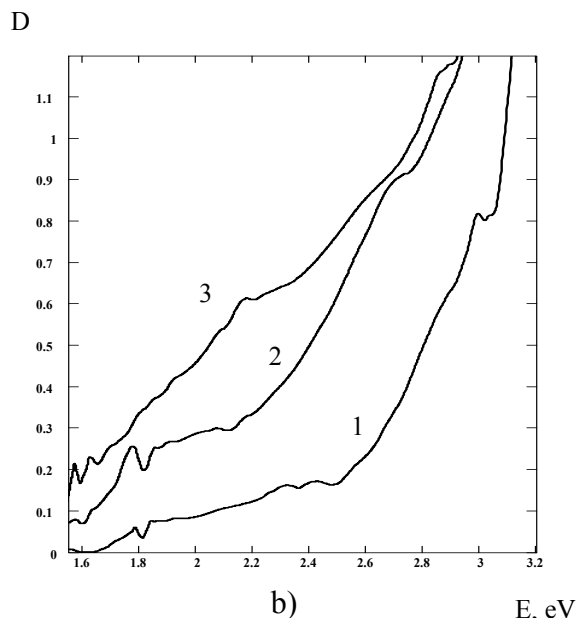
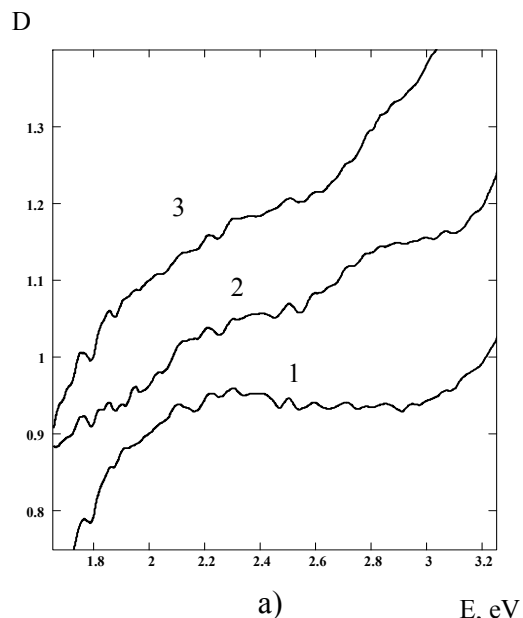


Fig.3. Optical density spectra of ZnS:Fe (a) bulk and (b) nanocrystals with different iron concentration: a) 1 – $2 \cdot 10^{17}$, 2 – $7 \cdot 10^{17}$, 3 – $9 \cdot 10^{18}$ cm $^{-3}$, b) Fe $_2$ Cl $_3$ 1 – 0.2%, 0.3%, 0.5%.

sulfide, m_e is the mass of the free electron; ΔE_g is the difference between the width of the band gap in the nanoparticle and the bulk crystal of ZnS (3.6 eV) or ZnS:Fe (3.33 eV for iron concentration equal 10^{18} cm^{-3}). The results of nanocrystal sizes calculations are presented in the table.

Table. The results of ZnS, ZnS:Fe nanocrystals sizes calculations under different preparation conditions of the samples.

Concentration, %	E_g, eV	$\Delta E_g, \text{eV}$	R, nm
5% $\text{CdCl}_2, \text{Na}_2\text{S}$	5.2	1.6	3.3
10% $\text{CdCl}_2, \text{Na}_2\text{S}$	5.1	1.5	3.4
20% $\text{CdCl}_2, \text{Na}_2\text{S}$	4.9	1.3	3.7
10% $\text{CdCl}_2, \text{Na}_2\text{S}$, 0.2% Fe_2Cl_3	4.66	1.06	4.1
10% $\text{CdCl}_2, \text{Na}_2\text{S}$, 0.3% Fe_2Cl_3	4.52	0.92	4.3
10% $\text{CdCl}_2, \text{Na}_2\text{S}$, 0.5% Fe_2Cl_3	4.4	0.8	4.7

Photoluminescence spectra. In undoped ZnS single crystals, luminescence in the 1.6-2.8 nm region was not observed. Doping ZnS single crystals with iron leads to the formation of a broad structured photoluminescence band in the region of 1.6-2.8 nm (Fig. 4, a). A narrower structured band of photoluminescence is observed in ZnS:Fe nanocrystals (Fig. 4, b). With increased of iron concentrations, the luminescence spectrum shifts toward smaller energies. At the Fe_2Cl_3 concentration equal to 2%, the luminescence band maximum is 1.8 eV (690 nm).

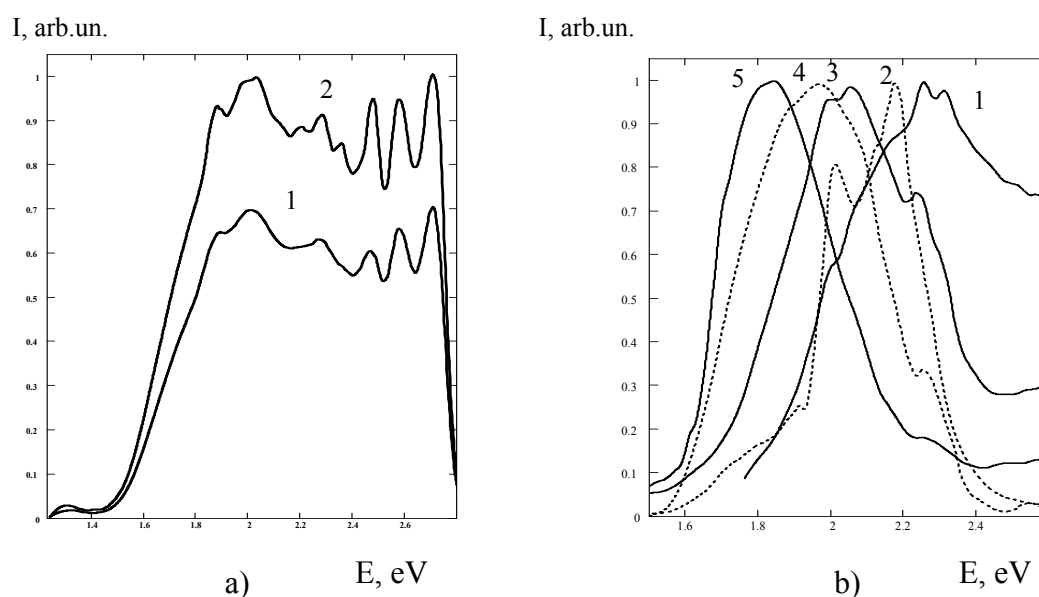


Fig.4. Photoluminescence spectra of ZnS:Fe (a) bulk and (b) nanocrystals with different iron concentration: a) 1 – $2 \cdot 10^{17}$, 2 – $7 \cdot 10^{17} \text{ cm}^{-3}$, b) Fe_2Cl_3 1 – 0.2%, 2 – 0.3%, 3 – 0.5%, 4 – 1%, 5 – 2%. $E_{ex} = 3.1 \text{ eV}$.

Conclusions. The nanocrystals of zinc sulfide doped with iron are obtained. A comparative analysis of optical absorption and photoluminescence spectra of pure and doped by iron zinc sulfide nano and single crystals is carried out.

ZnS:Fe nanocrystals have a photoluminescence spectrum, which corresponds to the range of biological tissues transparency. This allows the use of ZnS:Fe nanocrystals as fluorescent markers in medical diagnostics.

1. Nitsuk Yu.A., Vaksman Yu.F., Yatsun V.V., Purtov Yu.N. Optical absorption and diffusion of iron in ZnS single crystals// Functional Materials.-2012.-V.19, No.2.-p.182-186.
2. Ваксман Ю.Ф., Ницук Ю.А., Яцун В.В., Насибов А.С., Шапкин П.В. Влияние примеси железа на люминесценцию и фотопроводимость кристаллов ZnSe в видимой области спектра// ФТП.-2011.-Т.45, В.9.-С.1171-1174.
3. Гусев А.И., Ремпель А.А. Нанокристаллические материалы.-М:Физматлит.-2000.-С.224.

ELECTRONIC TRANSPORT, OPTIC, PHOTOELECTRIC AND MAGNETIC PROPERTIES OF SEMICONDUCTOR CRYSTALS

SPATIO-TEMPORAL TRANSFORMATION OF INFRA-RED FEMTO-SECOND LASER PULSES IN CRYSTAL SILICON

Ivan Blonskyi^a, Viktor Kadan^a, Svitlana Pavlova^a, Ihor Pavlov^{a,b}, Andriy Rybak^a, Laurent Calvez^c, Oleh Shpotyuk^{d,e}

^a*Institute of Physics of NASU, Prospect Nauky 46, 03680 Kyiv, Ukraine;*

^b*Middle East Technical University, Ankara, Turkey;*

^c*UMR-CNRS 6226, Université de Rennes 1, 35042 Rennes Cedex, France;*

^d*Vlokh Institute of Physical Optics, Dragomanov str. 23, 79005 Lviv, Ukraine;*

^e*Institute of Physics of Jan Dlugosz University, al. Armii Krajowej 13/15, 42200 Czestochowa, Poland*

Ultra-short temporal width and ultrahigh power, of femtosecond (fs) laser pulses, make them an attractive instrument for micro-machining and micro-modification of photonics materials, among which perhaps, crystal silicon (c-Si) is the most important. In this report we present the results of our experimental study of transformation of femtosecond laser pulses at 1550 nm wavelength propagating in crystal silicon (c-Si). Nonlinear temporal dynamics of the fs pulses have been revealed in their spatio-temporal and spectral transformation.

To perform this study, we designed and built a pump-probe microscopy setup, working both in polarographic and shadowgraphic modes at 1550 nm wavelength (Fig. 1). Using this setup, we recorded instantaneous polarographic pictures of spatio-temporal transformation of the laser pulse itself, propagating inside c-Si plate at 1550 nm wavelength. In the shadowgraphy mode, the resulting picture is formed by interplay of TPA and Kerr- and plasma-induced modifications of refractive index. Both polarographic and shadowgraphic microscopy reveals temporal widening of the axial part of the propagating pump pulse, which at least partially, can be caused by TPA.

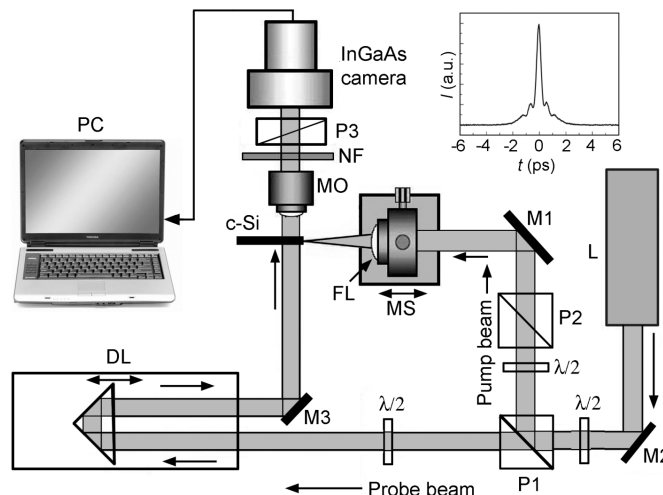


Fig. 1. Pump-probe microscopy setup. The inset shows autocorrelation trace of the output laser pulses of 2 μ J energy at 250 kHz repetition rate.

The polarization microscopy pictures obtained with crossed polarizers P3 and P4, are shown in Fig. 2a. The axial intensity of the pump pulse is maximum at

small τ up to 0.95 ps, while at longer time delays it decreases, and starting from $\tau = 3.26$ ps, transversal pulse splitting becomes perceptible.

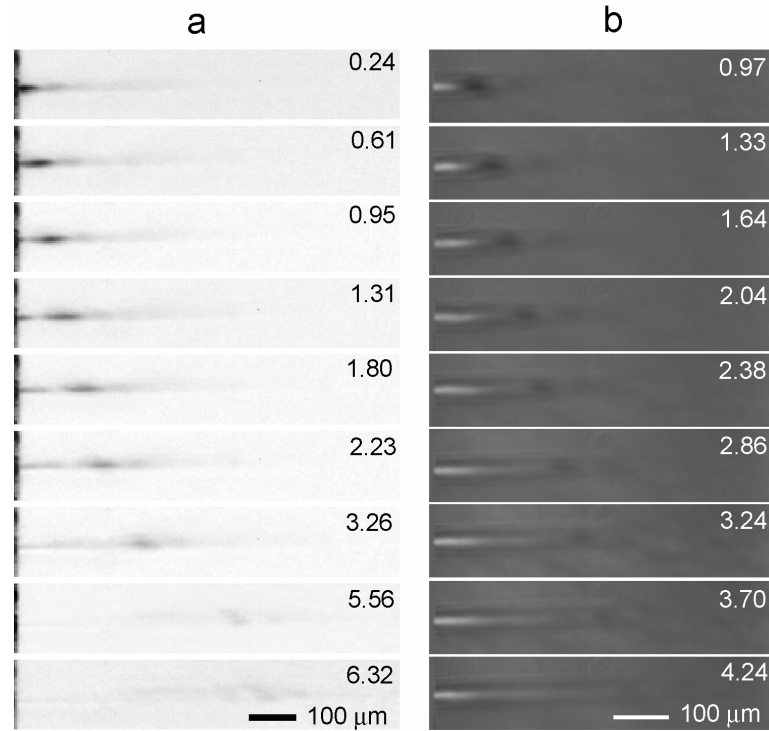


Fig. 2. Laser pulses propagating in 0.5 mm-thick c-Si sample under the f_s excitation at the 1550 nm wavelength, $f = 250$ kHz repetition rate and single pulse energy $E_p = 1.14$ μ J. The time delays τ in picoseconds are indicated at the upper right corner of each panel. Polarization microscopy (a). Shadowgraphy (b).

The time-resolved shadowgraphic pictures are presented in Fig. 2b. Plasma of free carriers generated by the pump beam through two-photon absorption (TPA), forms the tail, which follows the propagating laser pulse in Fig 2b. Both in polarization and transmission time-resolved microscopy broadening of the axial component of the pulse is observed. So, temporal dynamics of the f_s laser pulse at 1550 nm propagating in c-Si has been for the first time recorded using methods of time-resolved microscopy. It is suggested that TPA is the main factor responsible for the increase of on-axis time width of the laser pulse during the first 1.5 picoseconds of its propagation.

In frequency domain the temporal dynamics manifests itself as Kerr- and plasma induced self-phase modulation (SPM), which non-symmetrically widens the frequency band of the laser pulse (Fig. 3). The laser pulses of different energies E_p up to 1.3 μ J at 1.55 μ m wavelength with repetition rate $f = 250$ kHz, and temporal width $\Delta t_p = 450$ fs were focused into a 0.5 mm-thick c-Si plate with aspherical lens L of 35 mm focal distance, as is shown in Fig. 3a. The comparison of figures 3b and 3c reveals significant temporal dynamics of the f_s laser pulse in nonlinear propagation mode at $E_p = 1.3$ μ J, which manifests itself as a widening of the output IR spectrum in Fig. 3c.

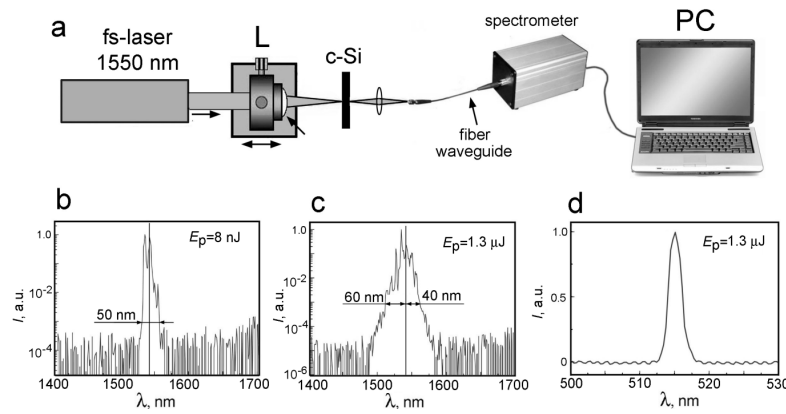


Fig. 3. IR spectra of the laser pulses, exiting the 0.5 mm-thick c-Si plate at the pulse energies $E_p=8$ nJ (b) and $E_p=1.3$ μ J (c). Visible output spectrum at $E_p=1.3$ μ J (d).

Third harmonic generation (THG), visible by naked eye has also been observed in c-Si, despite very small (~ 1 μ m) absorption length at 516 nm in this semiconductor (Fig.4). According to the spectral measurements (Fig. 3d), the green emission wavelength is centered at $\lambda_{TH} = 516$ nm, suggesting its origin as third harmonics of the pump laser band.

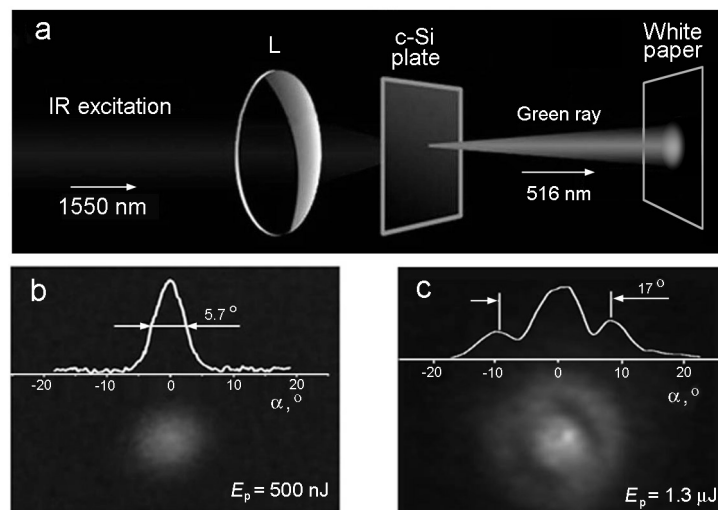


Fig. 4. THG in c-Si. Experimental scheme (a). Picture and angular profile of the TH beam generated in 0.5 mm thick c-Si plate at $E_p=500$ nJ (b). Picture and angular profile of the TH beam generated in 8 mm thick c-Si plate at $E_p=1.3$ μ J (c).

The authors acknowledge support from the STCU-NASU (project 6174).

Bimetallic nanocatalysts PtCu and PtNi for fuel cells.

Chernikova O.M.^{*}, Ogorodnik Y.V.^{}**

^{*} *Kyryviy Rih National University,* ^{**} *Radiation Monitoring Devices, inc. USA*

We review the physical mechanisms of heterogeneous catalytic oxidizing reactions methanol oxidation with using bimetallic film layered mechanically strained PtNi and PtCu-based catalysts. The main research methods are theoretical calculations based on the density functional theory and the "ab initio" pseudopotential method. The work illustrates that the mechanical stress and the presence of dissociated oxygen have the greatest impact on increasing electron bimetallic catalyst activity during the oxidation of methanol with using bimetallic layered mechanically strained PtNi and PtCu-based catalysts. The compression of the platinum film pushes the electron density outside the film and it gives the density an elongated form and increases the chemical and absorption activity of the film.

Introduction

Of particular interest are fuel cells (PEs), which are an integral part of energy devices. As a catalytic component in PE, as a rule, use platinum. Its main disadvantages include degradation during long-term work in the PE, as well as high cost. The solution of these problems is associated with the development of multi-component catalytic systems based on platinum with the inclusion of other metals. The strategies of their development really depend on a detailed understanding of the mechanisms of oxidation of fuel and the recovery of oxygen [1].

The direct relationship between activity on Pt-based RVC catalysts and Pt-M catalysts from the distances between the immediate Pt-Pt layers has been described in many papers. The smaller the distance, the stronger is the catalytic activity relative to the RVC [2].

Methods and objects of computing

The basic states of the alimentary-nuclear systems were manifested by a self-consistent solution of the Konan-Shema equations, since only electronic changes were determined with fixed atomic bases. Following Cona and Shema, the electron density was recorded in terms of occupied orthonormal single-particle wave functions:

$$n(\vec{r}) = \sum_i |\psi_i(\vec{r})|^2 \quad (1)$$

The point on the surface of the potential energy in the Born-Oppenheimer approximation was determined by a minimum in relation to the wave functions of the energy functional:

$$E[\{\psi_i\}, \{R_j\}, \{\alpha_v\}] = \sum_i \int_{\Omega} d^3r \psi_i^*(\vec{r}) \left[-\frac{\hbar^2}{2m} \nabla^2 \right] \psi_i(\vec{r}) + U[\{n(\vec{r})\}, \{R_j\}, \{\alpha_v\}] \quad (2)$$

where $\{R_j\}$ - the coordinates of atomic shafts, $\{\alpha_v\}$ - all possible external influences on the system.

Due to the fact that the calculation algorithm implies translational symmetry in the investigated atomic system, an artificial super-lattice of the tetragonal type

was originally created. To obtain the film structure, the lattice parameters along the axes OZ, OX, OY had a ratio of 2: 1: 1. The parameters of the super-lattice and the atomic basis are determined by the object of the study.

The parameters of the platinum lattice are larger than those of nickel and copper, which allows the process to create compressed layers Pt, either by the epitaxial build-up of the layers Pt on the substrate Ni or Cu or the cultivated (synthesized) alloy of a given composition ($\text{Pt}_x\text{Ni}_{1-x}$, $\text{Pt}_x\text{Cu}_{1-x}$).

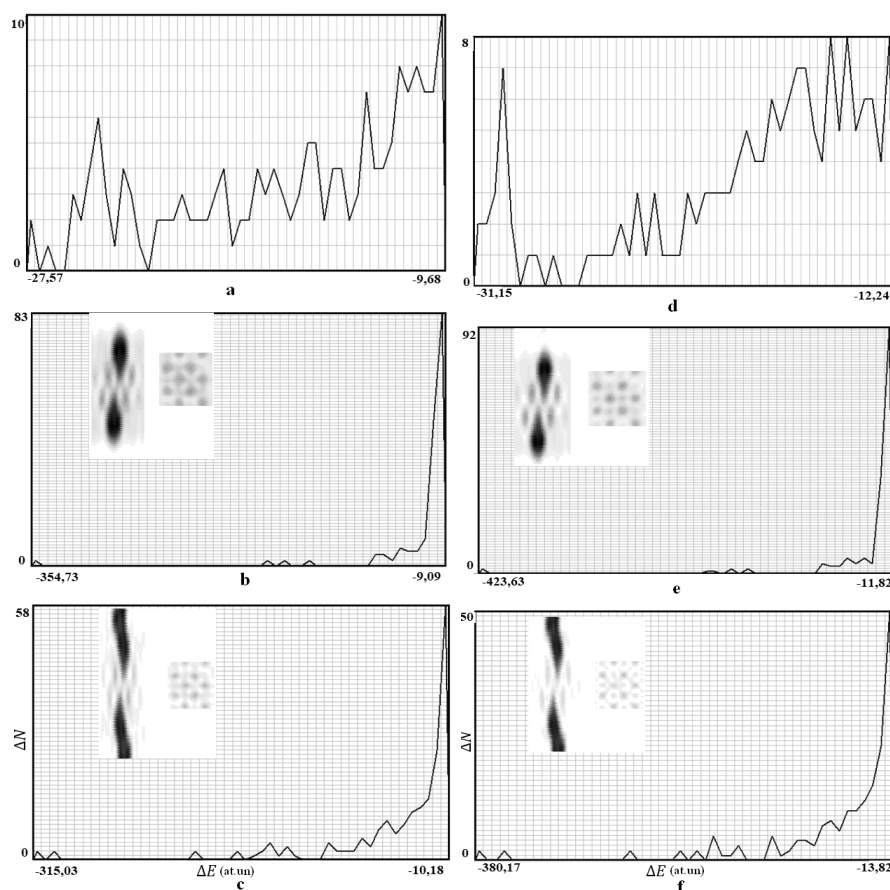


Fig. 1 Electronic spectra of the valence electrons for 4 layers film PtCu (a, b, c) with lattice Cu ($a = 3,615 \text{ \AA}$) and PtNi (d, e, f) with lattice Ni ($a = 3,524 \text{ \AA}$) with absorption atoms on the surface: a) 4 layers film PtCu; b) 4 layers film PtCu adding atom O; c) 4 layers PtCu with atom O and molecule of methanol; d) 4 layers film PtNi; e) 4 layers film PtCu adding atom O; f) 4 layers PtNi with atom O and molecule of methanol.

To study the physical mechanisms of the methanol oxidation reaction on platinum-containing catalysts for the comparative analysis, three groups of nano objects with a thickness of 4 atomic layers containing 32 atoms in the base, which in the first group are divided into objects: film Pt; film Cu; film Ni; film heterostructure consisting of two atomic layers of nickel or copper coated on two sides on one platinum layer.

Next, the atomic systems described above, supplemented by two oxygen atoms, were located in the interstate positions of the surface layers Pt and alloys $\text{Pt}_x\text{Ni}_{1-x}$, $\text{Pt}_x\text{Cu}_{1-x}$.

The third model group was based on the second group of objects with addition on the surface of methanol molecules. In addition, for the possibility of evaluating changes in atomic systems, an isolated methanol molecule and two-layer platinum films were additionally calculated.

Results of calculation

According to the results of calculations using the author's software code [3], the spectral characteristics of the developed model atomic systems, the spatial distributions of the density of valence electrons and their intersection were determined.

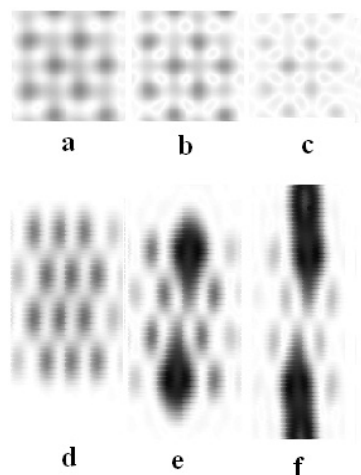


Fig. 2 Intersections of spatial density distributions of valence electrons in planes (110) and (100) 32-atoms film Cu atom of methanol on the surface (the center of the molecule is located above void between atoms on surface layer of catalyst) and the oxygen atom of the molecule of O₂ is dealt face up in the position between the surface atoms of Cu catalysts: (a, d) film Cu; (b, e) film Cu with the addition of the atom O; (c, f) Cu film with atom O and molecule of methanol.

Figure 1 shows the distributions of electrons in energy areas for the g point super lattice Brillouina zone above the described systems. In the analysis of distributions that meet the 4 layers brief films PtCu and PtNi, with added oxygen atoms and molecules of methanol, it is evident that there is a significant difference in electronic properties of systems, analyzed above for adding the atomic the oxygen in the system. The character of the distribution of the electrons as the energies and space changing from uniform to the inherent systems with internal electric fields and energy barriers: the emerging spatial area with locally higher charge in the neighborhood of the oxygen atoms, and the distribution (sorting) of electrons to energies on the distribution of the dominant maximum energy near the Fermi, thereby increasing the catalytic activity of the films.

Conclusions

The methods of the functional of electron density and pseudopotential from the first principles obtained distributions of the density of valence electrons and electronic energy spectra of bimetallic catalysts on the basis of Pt to determine the mechanisms of their increased catalytic activity. It was found that mechanical stresses and the presence of dissociated oxygen play the greatest influence on the increase of the electronic activity of the catalyst.

References

1. Yoshiyuki Show, Yutavo Ueno Formation of platinum catalyst on carbon black using on in-liquid plasma method for fuel cells// J. Nanomaterials, 2017, V.7, pp. 31-40.
2. Kuln S., Strasser P. Oxygen electrocatalysis on dealloed Pt nanocatalysts // Springer Catalysis J., 2016, V. 59, pp. 1628-1637.
3. Balabay RM, Grishchenko N.V. A complex of programs for calculations of ab initio solid-state structures // Photoelectronics. 1998. №8, pp. 25-29.

LOW FREQUENCY RAMAN SPECTRA OF $\text{As}_x\text{S}_{100-x}$ GLASSES AND LOW FREQUENCY QUASI-LOCALIZED VIBRATIONS OF SOFT AND RIGID As_nS_m NANOCLOUDS DEPENDING ON NUMBER OF FIXED POINTS

R. Holomb^{*}, V.Mitsa^{*}, L.Himics^{**}, M.Veres^{**}

^{*}*Uzhhorod National University, Pidhirna 46 Str., 88000 Uzhhorod, Ukraine*

^{**}*Wigner Research Centre for Physics of the Hungarian Academy of Sciences, Budapest, Hungary*

ABSTRACT

The effect of the structural interconnection of the clusters on their vibrational mode frequencies was modeled by attaching different numbers of heavy dummy terminated atoms to the dangling bonds of a branchy- $\text{As}_{2+4/3}\text{S}_5$ and 12-membered ring-like $\text{As}_6\text{S}_{6+6/2}$ nanoclusters. It was found that the vibrational mode frequencies have a U-shaped dependence on the level of interconnection, which correlates with experimental findings on compositional dependence of the Boson peak position in $\text{As}_x\text{S}_{100-x}$ glasses.

INTRODUCTION

One of the most important and intriguing fundamental phenomenon in the physics of non-crystalline solids is the excess contribution to the low-frequency (LF) vibrational states with respect to the predictions of the Debye squared-frequency theory [1]. Inelastic (neutron, Raman) scattering studies reveal a broad peak (usually referred to as the Boson peak (BP)) in the 2-10 meV energy range, the intensity of which is being proportional to the density of states ($g(\omega)$) in scale $g(\omega)/\omega^2$ [2-6]. There are two different prevailing hypotheses in this field [7,8]. According to the first, the excess vibrational states are due to the localization of the high energy vibrational modes induced by the static disorder in the non-crystalline state. In this work the contribution of different (ring-, branchy- and cage-like) As_nS_m nanoclusters' vibrations to the experimental LF Raman spectra of $\text{As}_x\text{S}_{100-x}$ glasses is investigated and discussed.

METHODS

The low-frequency Raman spectra of As-S glasses were measured using the triple grating Dilor-XY800 spectrometer. The As_nS_m nanocluster models consists three different geometry topologies namely branchy-, ring- and cage-like. The DFT method with the revised Becke hybrid B98 functional by was applied for geometry optimizations and Raman spectra calculations similar as in [5,6]. The Pople's basis set with the polarization functions on heavy atoms (6-311+G(3df)) was used for the As, S and H atoms and heavy terminated.

RESULTS AND DISCUSSION

Fig. 1A shows that the spectrum of the sample with highest sulfur content has well distinguishable peaks at 7, 33, 41 and 81 cm^{-1} superposed onto the broad band serving as their background. The modes at 33, 41 and 81 cm^{-1} can be assigned

to the vibrations of S_8 rings of crystalline sulfur. The following four compositions between $As_{22}S_{78}$ and $As_{45}S_{55}$ have very similar spectra consisting of a broad peak with maximum between 20 and 30 cm^{-1} and a shoulder at 7 cm^{-1} . The spectrum of the sixth structure is dominated by the 7 cm^{-1} peak and has some other narrow features sitting on the background of the broad band in the 6-100 cm^{-1} region.

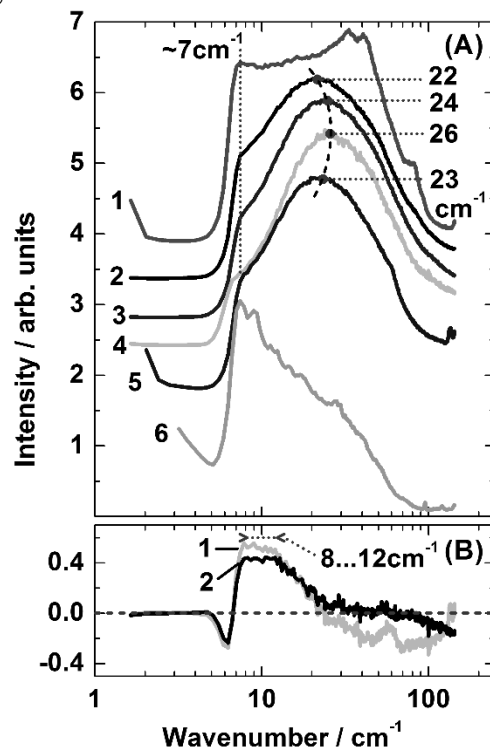


Fig. 1 (A) Depolarized LF Raman spectra of As_xS_{100-x} glasses measured at 632.8 nm laser excitation: As_6S_{94} (1), $As_{22}S_{78}$ (2), $As_{28.6}S_{71.4}$ (3), $As_{40}S_{60}$ (4), $As_{45}S_{55}$ (5) and $As_{60}S_{40}$ (6); (B) Differential LF Raman spectra of $As_{45}S_{55}$ (1) and $As_{28.6}S_{71.4}$ (2) glasses relative to g- $As_{40}S_{60}$

It can be seen from Fig. 1A that the peak at 7 cm^{-1} is characteristic for all the investigated As-S samples. Another common feature is the broad band the maximum of which shows an inverted U-shape behavior with the increase of the As content of the glass structure. The peak position increases from 22 cm^{-1} ($As_{22}S_{78}$ sample) to 26 cm^{-1} ($As_{40}S_{60}$) and then decreases to 23 cm^{-1} ($As_{45}S_{55}$). Presumably the structures with lowest and highest As content also fit well into this tendency, however due to the overlapping narrow peaks it is hard to determine the maximum of the broad band in their case.

Figure 1B shows the differential Raman spectra of $As_{45}S_{55}$ and $As_{28.6}S_{71.4}$ glasses relative to the stoichiometric g- $As_{40}S_{60}$. It can be seen that in spite of the fact that one composition ($As_{28.6}S_{71.4}$) has deficiency and the other ($As_{45}S_{55}$) surplus of As content compared to the stoichiometric composition, the two differential spectra behave similarly. A relatively strong excess scattering contribution can be observed between 7 and 20 cm^{-1} in the spectrum of both compositions, having a plato-like maximum between 8-12 cm^{-1} in both cases.

The stoichiometric $As_{40}S_{60}$ structure is a distinguished one: it has the highest BP position and the lowest Raman scattering contribution in the 7-20 cm^{-1} region. The position of LF Raman modes of soft branchy- and ring-like As-S nanoclusters are in accordance with the position of BP in the experimental Raman spectra of

$\text{As}_x\text{S}_{100-x}$ glasses. As we showed earlier [15,16] the branchy- or chain-like clusters build of more than one AsS_3 units have LF vibrational modes that are mostly of torsional type in nature and these vibrations are in the BP region of the Raman spectra. It was found also that the increase of the cluster size causes a red shift of the lowest frequency modes.

The calculated vibrational mode frequencies was performed on free-standing nanoclusters, where the dangling As and S bonds were terminated first with hydrogen atoms. However, these vibrations are affected by the surrounding of the nanoclusters and their interconnection could have a crucial impact on the vibrational mode frequencies. Additional calculations were performed on models containing extra heavy ($\sim 10^{20}$ a.u.) terminal atoms in order to investigate the effect of the level of interconnection of the structure and the spectral behavior of LF Raman modes of nanoclusters fixed in space. The results show that the position of LF Raman modes calculated for these models is red and/or blue shifted in comparison with those calculated for the free-standing As-S nanoclusters. Also, it was established that the frequency shift is depending on number of fixed points.

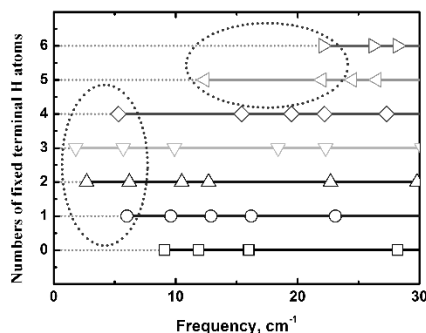


Fig. 2 Distribution of calculated LF vibrational modes of 12-membered ring (cluster $\text{As}_6\text{S}_{6+6/2}$) depending on the number of fixed points

Calculations on the LF vibrational modes were performed on the $\text{As}_6\text{S}_{6+6/2}$ nanocluster attached to different number of fixed points (heavy dummy atoms), the number of which was ranging from 0 (free-standing cluster) and 6. The results of the simulations are presented in Fig. 2. It can be seen that as the number of fixed points increases, the LF vibrational mode frequencies shift to lower wave numbers and its energy position correlate with position of “plato” in low-temperature thermal conductivity of $\text{g-As}_2\text{S}_3$ [9]. This behavior is in accordance with the expectations, since from two objects of the same structure the heavier (in this case that has more fixed points) will have lower vibrational frequencies then the lighter one. However, the tendency stops at the nanocluster with 3 fixed points, and then the LF mode frequencies shift towards higher wavenumbers as the number of fixed points increases from 3 to 6 and the nanocluster at 6 is arranged into a totally fixed configuration as in fully connected glassy matrix. These observations point on a U-shaped behavior in the dependence of the LF vibrational frequency on the number of fixed points. The latter represents the interconnection of the cluster with the surrounding matrix, and these results suggests, that this is an important factor affecting the features of the Boson peak in $\text{As}_x\text{S}_{100-x}$ glasses of different compositions.

CONCLUSIONS

The position of BP of glass-forming As-S composition show non-linear composition dependence with the maxima for $\text{As}_{40}\text{S}_{60}$ glass with mean coordination number $z=2.4$. Deviation from stoichiometric composition lead to shift of BP position to lower wavenumber.

The branchy- and ring-like As_nS_m nanoclusters contribute to the formation of super low frequency of quasi-elastic (relaxation) and the central parts of low frequency peak. Calculations show that when the transition from the "soft" free to partially rigid (partially fixed in space) As-S nanoclusters is taking place the anomalous super low-frequency Raman active modes start to appear in the calculated vibrational spectra. These modes are localized below 10 cm^{-1} and its frequencies are strongly dependent from number and position of fixed points. For the totally rigid structures the frequency position of calculated low frequency Raman modes of As_nS_m nanoclusters are in excellent accordance with the position of BP (26 cm^{-1}) in the experimental Raman spectra of g- As_2S_3 ($\text{As}_{40}\text{S}_{60}$) with the fully connected structural network matrix.

ACKNOWLEDGEMENTS

V. Mitsa gratefully acknowledge support from the Hungarian Academy of Sciences within the Domus Hungarica Scientiarum et Artium and DFFD found of Ukraine.

REFERENCES

- [1] Buchenau U, Zhou HM, Nuker N, Gilroy KS, Phillips A (1986), Low-frequency modes in vitreous silica. *J. Phys. Rev.* 34:5665. <https://doi.org/10.1103/PhysRevB.34.5665>
- [2] Phillips WA (1981) *Amorphous Solids: Low-temperature Properties*. Springer, New York
- [3] Naumis GG, Romero-Arias JR (2010) The problem of glass formation and the low frequency vibrational modes anomalies. *Revista mexicana de física* 56(2): 97–105
- [4] Mitsa V., Feher A., Petretskyi S., Holomb R., Ihnatolia P., Laver A (2017) Hysteresis of Low-Temperature Thermal Conductivity and Boson Peak in Glassy (g) As_2S_3 : Nanocluster Contribution *Nanoscale Research* 12, 345-351 <https://DOI.org/10.1186/s11671-017-2125-6>
- [5] Holomb R and Mitsa V (2004) Boson peak of $\text{As}_x\text{S}_{1-x}$ glasses and theoretical calculations of low frequencies clusters vibrations. *Solid State Commun.* 129:655. <https://doi.org/10.1016/j.ssc.2003.11.025>
- [6] Holomb R, Mitsa V, Johansson P, Veres M (2010) Boson peak in low-frequency Raman spectra of $\text{As}_x\text{S}_{100-x}$ glasses: nanocluster contribution. *Phys. Status Solidi C* 7, No. 3–4:885–888. <https://doi.org/10.1002/pssc.20098282>
- [7] Gurevich VL, Parshin DA, Pelous J, Schober HR (1993) Theory of low-energy Raman scattering in glasses. *Physical Review B* 48:16318. <https://doi.org/10.1103/PhysRevB.48.16318>
- [8] Martin AJ, Brenig W (1974) Model for Brillouin Scattering in Amorphous Solids. *Physica Status Solidi B* 64:163-172. <https://doi.org/10.1002/pssb.2220640120>

GENERATION OF ELECTRONIC EXCITATIONS IN SEMICONDUCTORS UNDER THE ACTION OF CHEMICAL REACTION ON THE SURFACE

V.P. Grankin, D.V. Grankin

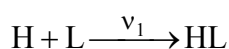
Pryazovskyi State Technical University, Mariupol

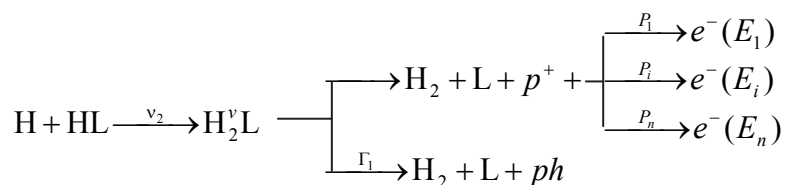
Energy dissipation processes in gas–surface interactions which are also referred to as accommodation processes are the essential part of the modern surface chemistry and physics [1]. The exothermic chemical reaction, as well as the action of photons on the surface, leads to electronic excitation of the crystal provided that most of the chemical energy is converted during a short (femtoseconds) time interval, before the adiabatic energy dissipation occurs as a result of the generation of thermal lattice vibrations (picoseconds) [2]. The surface chemiluminescence, observed in some cases, and the so called exoelectron emission are also unambiguous evidences of chemical energy to semiconductor electrons transfer. Phenomena indicated give the examples of nonadiabatic processes in gas–surface collisions.

At the same time, for semiconductors and dielectrics, as well as for metals, there is no reliable data on the probability of accommodation of the reaction energy via an electronic channel on the energy of the electronic transition in a solid. A method for determining the rate constant for the accommodation of the reaction energy via the electronic channel from the energy of the electronic transition in a solid is proposed in [3]. It is based on the simultaneous measurement of thermoluminescence during linear heating of a sample irradiated with UV light, the intensity of heterogeneous chemiluminescence upon exposure to a pulsed flow of atoms H and the stored light sum on traps of different depths. It is established [3] that the rate constant of electron excitation by atomic hydrogen of the investigated samples ZnS; ZnS,CdS-Ag increases exponentially with decreasing energy of the electronic transition in a solid in the wide range of electron transition energies $E = 0.2\text{--}3.7$ eV. This provides a basis for calculating the effectiveness of nonadiabatic chemo-electronic energy conversion in semiconductor heterostructures.

The goal of the work is to determine the probability of accommodation of the energy of a chemical reaction via the electronic channel from the energy of the electronic transition in a solid and the yield of nonadiabatic chemo-electronic energy conversion in semiconductor heterostructures.

Electronic excitation of the crystal arises when a large number of exothermic chemical reactions occur on its surface (oxidation of hydrogen, natural gas, carbon monoxide, recombination of hydrogen atoms, deuterium, oxygen, etc.). Recombination of hydrogen atoms on the surface leads to the appearance of a highly excited reaction product, vibrationally excited hydrogen molecules, the relaxation of which is accompanied by electronic excitation of the surface. With this in mind, the kinetic model that describes the excitation of e^-p^+ pairs in the semiconductor as a result of reaction interactions of atomic hydrogen with the surface, has the form:





Here HL is adsorbed hydrogen atom, L is the surface of the catalyst which is free of adsorbed particles, $e^-(E_i)$ is excited due to the reaction electron in the conduction band of a p-semiconductor with the energy E_i relative to the top of the valence band, ph is a phonon generated by reaction in a solid, p^+ is a hole in the valence band, H_2^vL is a vibrationally excited hydrogen molecule formed during the recombination of H atoms, P_i is the probability of an electron generation with the energy E_i in the act of recombination of H atoms on the surface. Above the arrows are indicated: ν_1, ν_2 are the probabilities of adsorption and recombination of H atoms on the catalyst, respectively, Γ_1 is the probability of relaxation of H_2^vL via the phonon channel.

We introduce the notation: $[\text{HL}] \rightarrow N_1$, $[\text{L}] \rightarrow N$, $[\text{H}_2^v\text{L}] \rightarrow N_2^v$, $e^-(E_i) \rightarrow n_i$. From the kinetic model:

$$\begin{aligned}
 n_1 &= P_1 \nu_2 N_1 \\
 &\dots\dots\dots \\
 n_i &= P_i \nu_2 N_1 \\
 \hline
 n &= \sum n_i = P \nu_2 N_1
 \end{aligned} \tag{1}$$

where n_i is the number of electrons with energy E_i , that are generated to the conduction band due to the reaction on 1 cm^2 of the surface in a second, n is the total number of high-energy electrons generated by the reaction on 1 cm^2 of the surface in a second. In (1) it is taken into account that $\sum_{i=1}^n P_i = P$. From (1), the value of $P_i = n_i/\omega$, where $\omega = \nu_2 N_1$ is the reaction rate on the surface. Due to the fact that the energy levels in the conduction band are located quasi-continuously, the probability dP of electron generation, which have energy in the range dE in the vicinity of the energy value E is calculated by the formula $dP = f(E)dE$, where $f(E)$ is the function of the energy distribution of electrons in the semiconductor that are generated in the conduction band in an exothermic chemical reaction on the surface. In [3], for the first time, a dependence was found experimentally for the probability of generation of high-energy electrons in a solid (systems H–ZnS, CdS–Ag; H–ZnS) by the energy of an exothermic heterogeneous chemical reaction (of recombination of hydrogen atoms), which has the form:

$$f(E) = A \exp(-E/\Theta_{char}) \tag{2}$$

and the value of Θ_{char} is found for these systems: $\Theta_{char} = 0.173 \text{ эВ}$. Here E is the transition energy of an electron in a semiconductor, Θ_{char} is the characteristic energy of the reaction, A is the pre-exponential factor. We find A from the normalization condition and taking into account the experimental dependence (2):

$$P(E_g \rightarrow 0) = \int dP = \int_0^{\infty} f(E) dE = \int_0^{\infty} A \cdot \exp(-E/\Theta_{char}) dE = 1, \quad A = 1/\Theta_{char}.$$

Then the probability of relaxation H_2^vL via the electronic channel is:

$$P(E \geq E_g) = \int_{E_g}^{\infty} f(E) dE = \exp(-E_g/\Theta_{char}). \quad (3)$$

From the kinetic model and taking into account expression (3), the yield of electrons with $E \geq E_g$ is equal to:

$$\alpha = P/(P + \Gamma_1) = \frac{\exp(-E_g/\Theta_{char})}{\exp(-E_g/\Theta_{char}) + \Gamma_1}. \quad (4)$$

Consider two limiting cases. Suppose that $\Gamma_1 \gg P$. Then, taking into account the fact that $P + \Gamma_1 = 1$, the value of $\alpha = \exp(-E_g/\Theta_{char})$ is described by an exponential dependence and decreases rapidly with increasing E_g . The value of α is as greater as greater the value of Θ_{char} . For example, at $E_g = 1.0$ eV and $\Theta_{char} = 0.25$ eV the value of $\alpha = 1.8 \cdot 10^{-2}$, and at the same value of $E_g = 1.0$ eV, but at $\Theta_{char} = 0.15$ eV the value of $\alpha = 1.3 \cdot 10^{-3}$, i.e. an order of magnitude smaller.

In case if $\Gamma_1 \ll P$, i.e. when there is no phonon channel of the accommodation of the energy of the reaction, then from (4) $\alpha \approx 1$ and each act of reaction interaction should result in the generation of an e^-p^+ pair, regardless of the width of the forbidden band, since in this case the relaxation of H_2^vL is possible only via the electronic channel.

Until recently, there was a gap in the knowledge of the laws and mechanisms of energy exchange (the accommodation of the energy of a chemical reaction) in gas-surface reaction collisions involving the electronic subsystem of a crystal. The transfer of vibrational energy found in direct experiments using the molecular beam method in the collisions of gas-phase vibrationally excited molecules with a surface to electronic states in a dielectric, semiconductor, or metal shows that the electronic subsystem in a crystal is a full participant in relaxation processes in the gas-surface system [4]. The obtained results indicate the possibility of using semiconductor heterostructures for constructing devices for direct conversion of the energy of the chemical reaction to the electric energy and show the direction of work on the creation of efficient current generators for hydrogen power engineering based on the chemo-electronic conversion of energy in them.

1. B. I. Lundqvist, A. Hellman, I. Zoric, in: E. Hasselbrink, B. I. Lundqvist (Eds.), Hand-book of Surface Science, vol. 3, Elsevier, Amsterdam, 2008.
2. J. C. Tully, Annu. Rev. Phys. Chem. 51 (2000) 153.
3. В. П. Гранкин, Д. В. Гранкин, ЖФХ 90, 950 (2016).
4. J. D. White, J. Chen, D. Matsiev et al., Nature 433, 503 (2005).

OPTICAL PROPERTIES OF PMMA NANOCOMPOSITES IMPLANTED BY LIGHT AND HEAVY IONS

**T.S. Kavetsky^{1,2}, M. Trzciński², M.M. Kravtsiv¹, K.V. Zubrytska¹,
O.R. Mushynska¹, A.L. Stepanov^{3,4}**

¹*Drohobych Ivan Franko State Pedagogical University, 82100 Drohobych, Ukraine*

²*The John Paul II Catholic University of Lublin, 20-950 Lublin, Poland*

³*Kazan Physical-Technical Institute, Russian Academy of Sciences, 420029 Kazan, Russia*

⁴*Kazan Federal University, 420008 Kazan, Russia
E-mail: kavetsky@yahoo.com*

Ion implantation is a powerful tool for structural modification of polymers and changes of their physico-chemical properties. Investigation of depth profiles of light and heavy ions implanted into organic polymers [1] has stimulated a progressive interest to newly attained functionality of modified surface layer with absolutely new properties. One of the significant changes observed in physical properties of ion-implanted polymers is increasing absorbance in the course of ion implantation to be interpreted as the signature on the formation of carbonaceous clusters [2]. Recently, dose dependences of the optical band gap energy of boron-ion-implanted layer $E_g^{\text{opt,B}}$ and a number of carbon atoms in carbonaceous clusters N in PMMA nanocomposite films formed by ion implantation of boron have been systematically studied [3]. It has been found the existence of three regions of ion doses (1) $6.25 \times 10^{14} \div 3.13 \times 10^{15} \text{ B}^+/\text{cm}^2$, (2) $3.75 \times 10^{15} \div 6.25 \times 10^{15} \text{ B}^+/\text{cm}^2$, and (3) $1.25 \times 10^{16} \div 2.5 \times 10^{16} \text{ B}^+/\text{cm}^2$, showing thresholds in the estimated $E_g^{\text{opt,B}}$ and N values as a function of ion dose and, consequently, ion-induced structural evolution towards formation of carbon nanostructures within these thresholds has been suggested [3].

In the present work, the optical band gap and carbon clusters behaviors as a function of ion dose are examined for the 40 keV light (B^+ and He^+) and heavy (Xe^+) ion-implanted PMMA at the same ion doses of 3.13×10^{15} , 6.25×10^{15} , 1.25×10^{16} , and $2.5 \times 10^{16} \text{ ions}/\text{cm}^2$. The thickness d of the implanted layer was estimated by SRIM code, not exceeding a maximum penetration depth $R_{\text{max}}^{\text{ion}}$ (Table 1 [4]).

Figure 1 shows UV-visible absorption spectra and the optical absorption coefficient $\alpha(h\nu)$ of implanted samples at different doses and thicknesses d of the implanted layer [5]. The values of E_g^{opt} and N^{ion} were compared and analyzed. The effect of ion mass on the carbonization processes in PMMA nanocomposite films formed by ion implantation of boron, helium, and xenon as revealed from optical absorption measurements was considered. It was established that He^+ implantation into PMMA leads to dramatic changes of the optical band gap and the number of

carbon atoms in carbonaceous clusters N^{He} in comparison with B^+ implantation, while the effect of Xe^+ implantation is negligible.

Table 1. SRIM simulation results for ion implantation into PMMA at energy of 40 keV (^adata from the work [2]; ^bdata from www.webelements.com; ^cdata are estimated with error ± 5 nm) [4].

Ion	^b Atomic weight	^c $R_{\text{max}}^{\text{Ion}}$, nm	$R_{\text{p}}^{\text{Ion}}$, nm	$\Delta R_{\text{p}}^{\text{Ion}}$, nm	$R_{\text{max}}^{\text{V}}$, nm	R_{p}^{V} , nm
^a B^+	10.81	400	253	58	380	220
He^+	4.0026	880	593	102	820	560
Xe^+	131.29	90	56	10	90	30

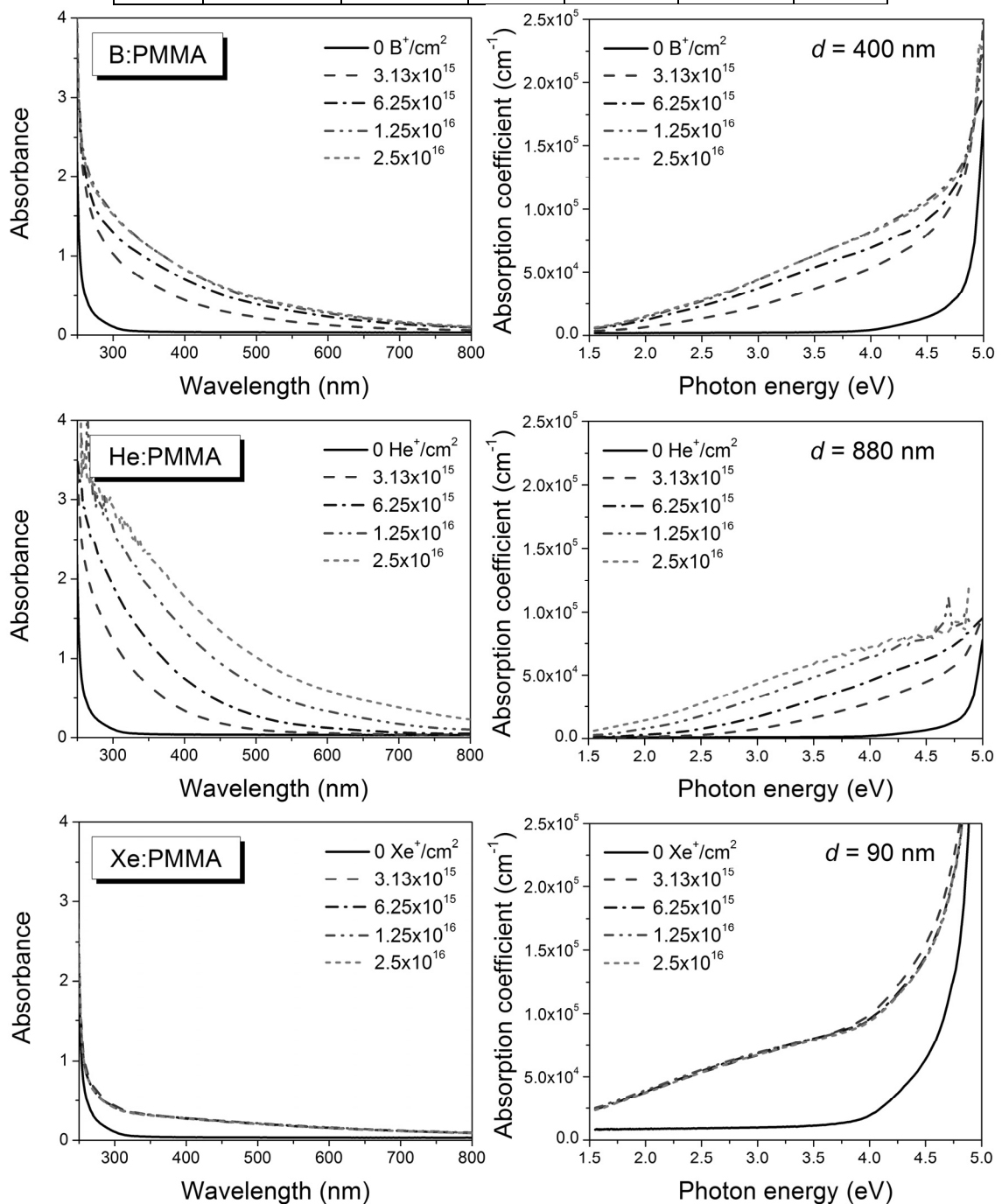


Fig. 1. UV-visible absorption spectra (left) and optical absorption coefficient $\alpha(h\nu)$ of implanted layers (right) for B:PMMA, He:PMMA, and Xe:PMMA samples at different ion doses and thicknesses d of the implanted layer as revealed by SRIM simulations [4,5].

Acknowledgments

This work was financially supported in part by the Ministry of Education and Science of Ukraine (projects #0116U004737 and #0118U000297 to TSK, and #0117U007142 for Young Scientists to MMK, KVZ, ORM) and by the Russian Foundation for Basic Research (projects #15-48-02525 and #17-08-00850 to ALS).

References

- [1] D. Fink, J.P. Biersack, J.T. Chen, M. Städele, K. Tjan, M. Behar, C.A. Olivieri, F.C. Zawislak, *J. Appl. Phys.* **58** (1985) 668.
- [2] T. Kavetsky, V. Tsmots, A. Kinomura, Y. Kobayashi, R. Suzuki, H.F.M. Mohamed, O. Šauša, V. Nuzhdin, V. Valeev, A.L. Stepanov, *J. Phys. Chem. B* **118** (2014) 4194.
- [3] M. Trzcinski, T. Kavetsky, G. Telbiz, A.L. Stepanov, *J. Mater. Sci. Mater. Electron.* **28** (2017) 7115.
- [4] T.S. Kavetsky, A.L. Stepanov, In: “Radiation Effects in Materials” (W.A. Monteiro, ed.), Rijeka: InTech, 2016, Chapter 11, P. 287-308.
- [5] M. Trzciński, T.S. Kavetsky, A.L. Stepanov, In: NATO Science for Peace and Security Series B: Physics and Biophysics “Advanced Nanotechnologies for Detection and Defence Against CBRN Agents” (P. Petkov, D. Tsiulyanu, C. Popov, W. Kulisch, eds.), Dordrecht: Springer, 2018, Chapter 7, DOI: 10.1007/978-94-024-1298-7_7.

FABRICATION OF PHOTONIC CRYSTAL BY ION IMPLANTATION: POSSIBILITY TO USE A CHALCOGENIDE FILM SUBSTRATE

**T.S. Kavetsky^{1,2}, K.V. Zubrytska¹, A.V. Stronski³, L.I. Pan'kiv¹, P. Petkov⁴,
V.I. Nuzhdin⁵, V.F. Valeev⁵, A.M. Rogov⁶, Y.N. Osin⁶, A.S. Morozova^{5,6},
A.L. Stepanov^{5,6}, J. Ruan⁷, H. Tao⁷, X. Zhao⁷**

¹*Drohobych Ivan Franko State Pedagogical University, 82100 Drohobych, Ukraine*

²*The John Paul II Catholic University of Lublin, 20-950 Lublin, Poland*

³*V.E. Lashkarev Institute of Semiconductor Physics, National Academy of Sciences of Ukraine, 03028 Kyiv, Ukraine*

⁴*University of Chemical Technology and Metallurgy, 1756 Sofia, Bulgaria*

⁵*Kazan Physical-Technical Institute, Russian Academy of Sciences, 420029 Kazan, Russia*

⁶*Kazan Federal University, 420008 Kazan, Russia*

⁷*State Key Laboratory of Silicate Materials for Architectures, Wuhan University of Technology, 430070 Wuhan, China*

E-mail: kavetsky@yahoo.com

Recently, a fabrication of submicron chalcogenide glass ($\text{As}_{40}\text{Se}_{40}\text{Te}_{20}$) photonic crystal using resist-free nanoimprint lithography has been reported in [1]. Namely, the period of the prepared photonic crystal structure was 600 nm and the height of the rods in the imprinted structure was about 150 nm.

The present work shows a possible fabrication of a chalcogenide photonic crystal by 30 keV Ag ion implantation through a nickel grid mask with square holes in a $(\text{GeSe}_5)_{80}\text{B}_{20}$ chalcogenide film (thickness 500 nm) [2]. The results obtained (the period of grating is about 25 μm , the step height about 170-200 nm as shown in Figure 1) were similar with the above mentioned literature results using thermal nanoimprint lithography. The observed difference in the period of fabricated photonic crystal structures is due to the difference in the sizes of the stamp in the case of the nanoimprint lithography and the square holes in the case of the ion implantation technique.

Therefore, the low-energy ion implantation technique, progressively used for the surface modification of materials and the formation of PMMA nanocomposite thin films with carbon nanostructures and metal nanoparticles [3-8], oxide materials with metal nanoparticles [9-11], porous silicon [12,13] and porous germanium [14], periodic diffractive structure in silica glass [15], PMMA [16] and diamond [17], could be also used as alternative approach instead of nanoimprint lithography in the fabrication of photonic crystal structures with certain grating parameters in the case of chalcogenide glasses. From a practical point of view, such diffraction gratings could be utilized in elements of optical communication, for the improvement of solar cells as well as in biomedical research as active substrates for the registration of biomolecules through a heterogeneous method in surface-enhanced Raman scattering and surface plasmon resonance of metal nanoparticles.

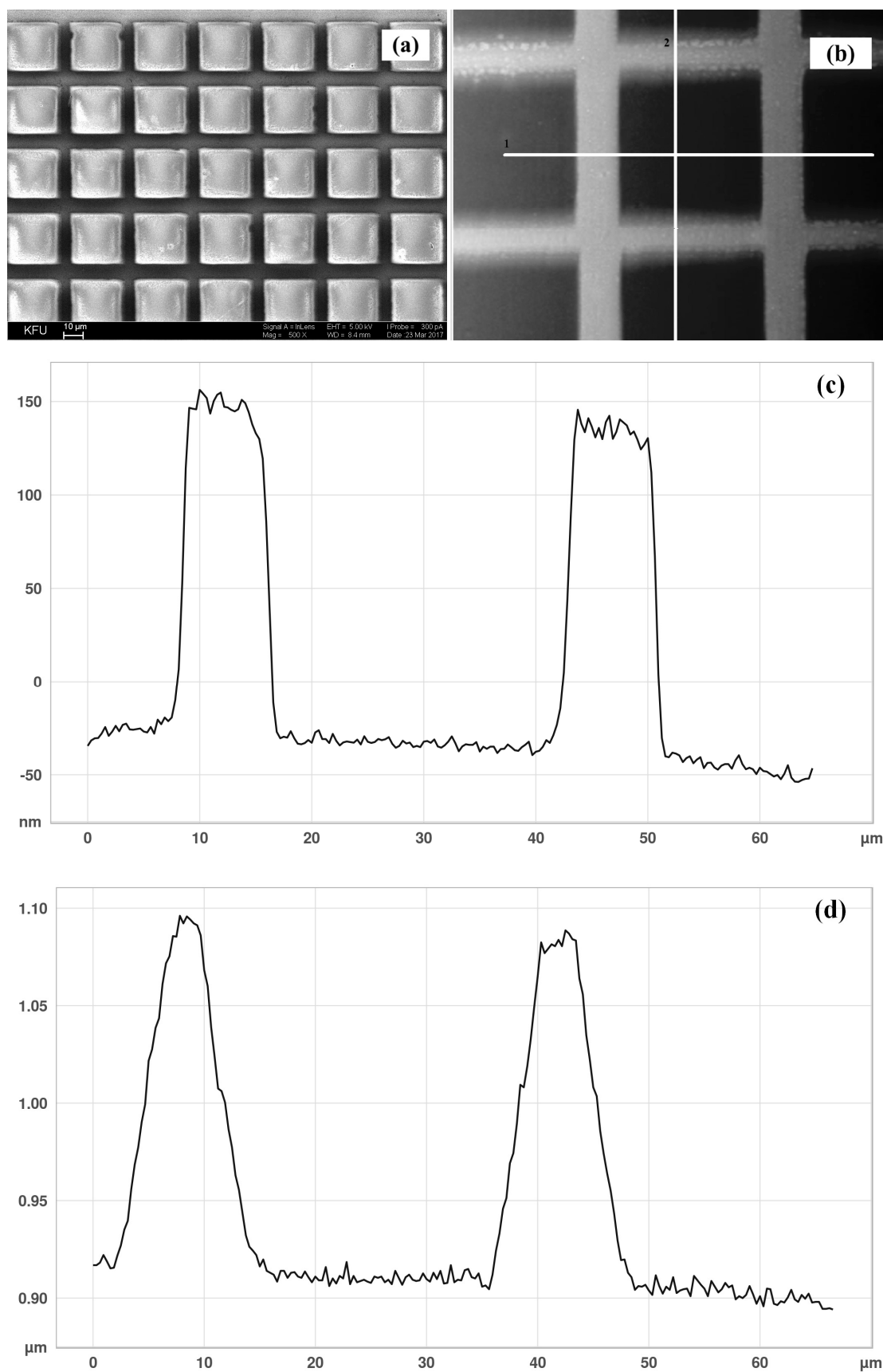


Fig. 1. (a) and (b) SEM images of the chalcogenide film implanted by 30 keV Ag ions through a nickel grid mask; (c) and (d) AFM cross-sections along the lines 1 and 2 shown in (b) [2].

Acknowledgments

This work was financially supported in part by the Ministry of Education and Science of Ukraine (projects #0116U004737 to TSK, #0117U007142 for Young Scientists to KVZ, and #0117U007143 to TSK), and by the Russian Foundation for Basic Research (project #17-08-00780 to ALS).

References

- [1] J. Zeng, Q. Zhang, P. Zhang, J. Tang, Y. Xu, F. Chen, X. Shen, S. Dai, *Appl. Phys. A* **123** (2017) 579.
- [2] T.S. Kavetsky, K.V. Zubrytska, A.V. Stronski, L.I. Pan'kiv, P. Petkov, V.I. Nuzhdin, V.F. Valeev, A.M. Rogov, Y.N. Osin, A.S. Morozova, A.L. Stepanov, In: *NATO Science for Peace and Security Series B: Physics and Biophysics "Advanced Nanotechnologies for Detection and Defence Against CBRN Agents"* (P. Petkov, D. Tsiulyanu, C. Popov, W. Kulisch, eds.), Dordrecht: Springer, 2018, Chapter 6, DOI: 10.1007/978-94-024-1298-7_6.
- [3] T.S. Kavetsky, V. Tsmots, A. Kinomura, Y. Kobayashi, R. Suzuki, H.F.M. Mohamed, O. Šauša, V. Nuzhdin, V. Valeev, A.L. Stepanov, *J. Phys. Chem. B* **118** (2014) 4194.
- [4] T. Kavetsky, J. Nowak, J. Borc, J. Rusnák, O. Šauša, A.L. Stepanov, *Spectrosc. Lett.* **49** (2016) 5.
- [5] T. Kavetsky, K. Iida, Y. Nagashima, A. Kuczumow, O. Šauša, V. Nuzhdin, V. Valeev, A.L. Stepanov, *J. Phys. Conf. Ser.* **791** (2017) 012028.
- [6] M. Trzcinski, T. Kavetsky, G. Telbiz, A.L. Stepanov, *J. Mater. Sci. Mater. Electron.* **28** (2017) 7115.
- [7] T.S. Kavetsky, A.L. Stepanov, in: W.A. Monteiro (Ed) *Radiation Effects in Materials*, Rijeka: InTech, 2016, p. 287.
- [8] A.L. Stepanov, *Tech. Phys.* **49** (2004) 143.
- [9] A.L. Stepanov, *Rev. Adv. Mater. Sci.* **26** (2010) 1.
- [10] A.L. Stepanov, *Rev. Adv. Mater. Sci.* **27** (2011) 115.
- [11] A.L. Stepanov, X. Xiao, F. Ren, T. Kavetsky, Y.N. Osin, *Rev. Adv. Mater. Sci.* **34** (2013) 107.
- [12] A.L. Stepanov, A.A. Trifonov, Y.N. Osin, V.F. Valeev, V.I. Nuzhdin, *Optoelectron. Adv. Mater. – Rapid Commun.* **7** (2013) 692.
- [13] T.S. Kavetsky, A.L. Stepanov, in: P. Petkov, D. Tsiulyanu, W. Kulisch, C. Popov (Eds) *Nanoscience Advances in CBRN Agents Detection, Information and Energy Security*, Dordrecht: Springer, 2015, p. 35.
- [14] A.L. Stepanov, Yu.N. Osin, V.I. Nuzhdin, V.F. Valeev, V.V. Vorob'ev, *Nanotechnol. Russ.* **12** (2017) 508.
- [15] T.S. Kavetsky, M.F. Galyautdinov, V.F. Valeev, V.I. Nuzhdin, Yu.N. Osin, A.B. Evlyukhin, A.L. Stepanov, *Tech. Phys. Lett.* **39** (2013) 591.
- [16] M.F. Galyautdinov, V.I. Nuzhdin, Ya.V. Fattakhov, B.F. Farrakhov, V.F. Valeev, Yu.N. Osin, A.L. Stepanov, *Tech. Phys. Lett.* **42** (2016) 182.
- [17] A.L. Stepanov, V.I. Nuzhdin, M.F. Galyautdinov, N.V. Kurbatova, V.F. Valeev, V. V. Vorobev, Yu.N. Osin, *Tech. Phys. Lett.* **43** (2017) 104.

STRUCTURE AND PHYSICO-CHEMICAL PROPERTIES OF GRAPHENE-LIKE NANODOTS

Karpenko O.S., Demianenko E.M., Lobanov V.V., Kartel M.T.

*O.Chuika Institute of Surface Chemistry of NAS of Ukraine,
General Naumov Str., 17, 03164 Kyiv, Ukraine, karpenkooksana@ukr.net*

Experimental confirmation of the possible existence of isolated or deposited on the substrate of graphene planes allowed to consider the properties of many carbon materials from an uniform position, i.e., starting from the properties of a two-dimensional net of hexagons of carbon atoms. These materials reveal many unusual and unexpected properties, among them the most important in the applied aspect is the adsorption of atomic and molecular hydrogen.

The paper presents the results of calculations, using the density functional theory with the exchange-correlation potential B3LYP and the basis set 6-31G** on the properties of carbon nanodots (CND) of a hexagonal form bounded by six zigzag-shaped edges, that is, boundaries of the same type.

The optimization of the spatial structure of CND C_6 – C_{216} with predefined multiplicity (M) showed the ground electronic state (GES) of the clusters C_6 and C_{24} to be singlet, while for others the lowest-energy ones were high-spin states – triplet and quintet.

From Fig. 1, which shows the dependence of atomization energy ($E_{at}^\#$) related to a single carbon-carbon bond, calculated for the GES of CND C_6 – C_{216} , it is clear that for the first representatives of this series (C_6 – C_{54}) it is almost exponentially decreasing with an increase in the number of carbon atoms. For others, starting from C_{96} , this value changes almost linearly with the size of the cluster. The choice of the $E_{at}^\#$ parameter for the characteristic that determines the size of the cluster, sufficient to reproduce adequately the properties of all representatives of the series C_6 – C_{216} , allowed to select the CND C_{96} ; its spin state energies are shown in Table. 1.

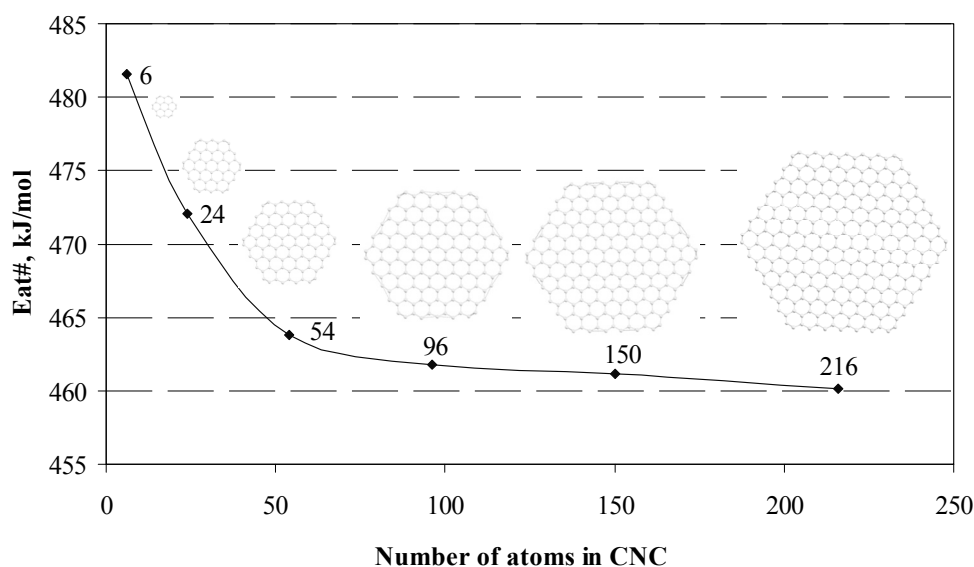
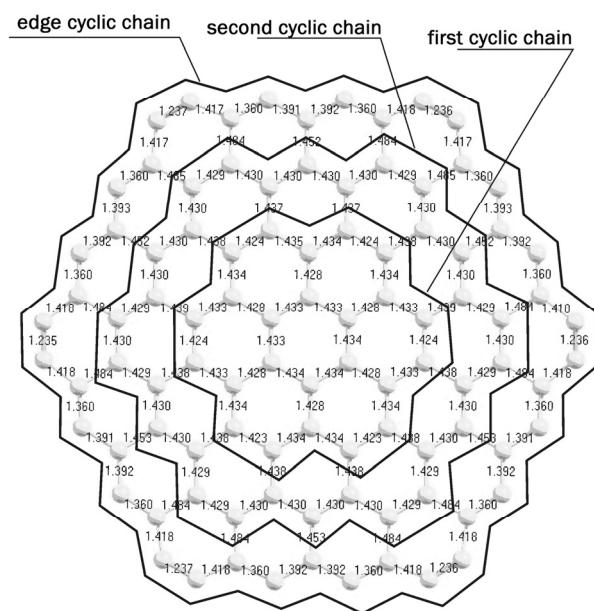


Fig. 1. Atomization energy averaged over all the C–C bonds in a C_6 – C_{216} cluster as a function of the cluster size

Table 1. Energy values (eV) of some selected nanoclusters of varying size (C_6 – C_{216}) and different spin states

Electronic state multiplicity	Carbon nanodots					
	C_6	C_{24}	C_{54}	C_{96}	C_{150}	C_{216}
1	0	0	5.60	7.66	12.18	13.56
3	1.17	2.74	0	1.65	0	0.39
5	2.14	2.96	0.70	0	1.57	0
7	-----	7.64	2.12	1.05	2.81	0.80

From Fig. 2 it is seen that all bond lengths C–C of the central hexagon of CND C_{96} ($M=5$) are 1.433–1.434 Å (in the benzene molecule 1.399 Å). The equality of the lengths of the central hexagon is also typical for all representatives of the considered series of CND, which for GES's are: C_{24} ($M = 1$) – 1.451; C_{54} ($M=3$) – 1.432; C_{150} ($M=3$) – 1.429; C_{216} ($M=5$) – 1.427 Å. There is a clear tendency to shorten the bonds for the GES's considered by the CND with the increase in the number of atoms in them. The central hexagon in CND C_{96} is framed by the first cyclic chain of carbon atoms, where it is noticeable that the bond lengths vary from 1.424 to 1.434 Å, which fall into the interval between the bond lengths C–C in ethane (1.534 Å) and ethylene (1.337 Å).

**Fig. 2.** C–C bond lengths of the equilibrium structure of the C_{96} ($M=5$) carbon nanocluster in the ground electron state

Each of the six identical edges of CND contains seven carbon atoms, two of them at junctions with similar edges participate in the formation of almost triple carbon-carbon bonds, their lengths are 1.236 Å (in acetylene 1.212 Å). Quite substantially is that the atoms of the boundary chain are bound to atoms of the cyclic chain II with sufficiently long bonds (from 1.452 to 1.484 Å), which significantly exceed the bond length in benzene (1.399 Å). Therefore, we can assume that the $2p_z$ -atomic orbitals of the boundary carbon atoms are rather poorly involved in conjugation with the $2p_z$ -orbitals of the other part of the CND C_{96} and the π -system

of edge-chain should be regarded as relatively isolated from the π -system of the central part of the cluster.

Fig. 3 shows the spectrum of the one-electron energy levels (ε_i) of the GES CND C_{96} , which has a somewhat non-typical view of molecular systems with a singlet ground electron state, which consists in the fact that the energies of several lower vacant MO's fall into the energy intervals of the upper occupied MO's. For α -subsystems there are four ($\alpha 291$ – $\alpha 294$) such MO's are, and for β -subsystems ($\beta 287$ – $\beta 293$) – seven. The implementation of such a filling scheme is determined, in our opinion, by the need to meet two very contradictory requirements. The first one is obvious – first of all, those MO's that provide the minimum energy of the entire system are filled. The second requirement is due to the specifics of the object under consideration, namely, the presence of twice-coordinated boundary carbon atoms with uncompensated bonds, each of them is related to a one-electron state.

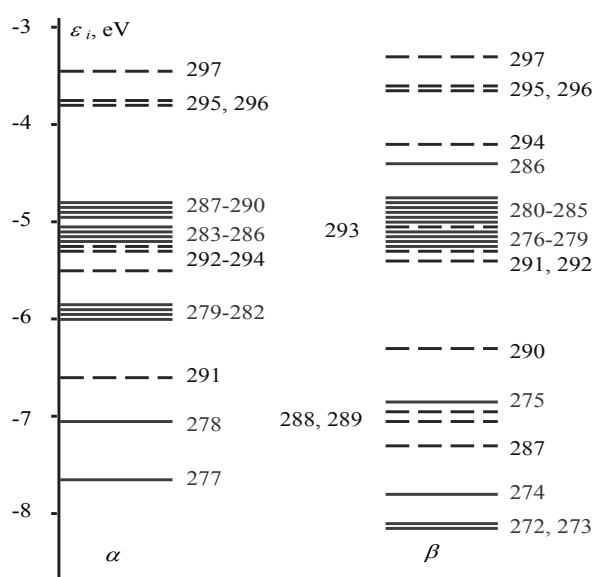


Fig. 3. Single-electron energy levels of the frontier MO's of the α - and β -subsystems of the CND C_{96} nanodot in the ground state (solid lines: occupied MO's, dotted lines-unoccupied MO's)

To find out the effects of various kinds of vacancies on the multiplicity of the GEC, on the spectrum of the single-electron energy levels, and on the structural properties of the carbon nanoclusters of hexagonal form, the equilibrium configurations and the corresponding total energies of carbon clusters obtained by removing single ($C_{96-1(1)}$) or two non-adjacent ($C_{96-2(1)}$) carbon atoms from the CND C_{96} . The results of calculations are shown in Table 2, from which it can be seen that the GES of CND, which contains vacancies of various types, is not singlet.

Table 2. Energy (eV) of the considered systems for various spin states

Electronic state multiplicity (M)	System		
	C_{96}	$C_{96-1(1)}$	$C_{96-2(1)}$
1	7.66	8.01	8.95
3	1.65	0	0
5	0	0.63	0.93
7	1.05	--	--

The calculations have shown that the removal of one atom from the CND C_{96} is related to an energy consumption of 1572.4 kJ/mol, which is calculated

as referred to one of the three broken bonds of 524.1 kJ/mol. Formation of the $C_{96-2(1)} (M=3)$ from the cluster $C_{96-1(1)} (M=3)$ occurs with an energy effect of 1342.6 kJ/mol, which, when referred to a single broken bond, gives a value of 320.9 kJ/mole.

In CND C_{96} , the carbon atoms occupy several non-equivalent positions, their substitution with a nitrogen atom leads to the obtaining of different CND-N isomers. In the literature devoted to the calculations of the shifts of the core energy levels of the atoms, depending on their chemical environment, when comparing the theoretically obtained values with the experimentally measured ones, usually scaling factors for each type of atoms and orbitals are usually introduced separately to compensate various types of errors in quantum-chemical methods. In our case, a factor of 1.026 was used to reproduce the state density in the energy region of the level $N1s$, which is obtained by dividing the empirical value for methylamine (399 eV) by 389.01 eV, calculated theoretically for this compound. Similarly, the conversion factor of the energy scale in the vicinity of the core level $C1s$ was calculated. This ratio is 1.024.

The plot with a maximum of -400.8 eV corresponds to the distribution of energy of the core level $N1s$, and in the range from -286.7 to -284.5 eV that of the energy distribution of the core level $C1s$. The complicated structure of the spectrum at this site is due to the different chemical environments of carbon atoms in the $C_{95}N$ CND. The third section relates to the one-electron energy levels of molecular orbitals.

Thus, the results obtained suggest that:

- the GES of CND $C_{54}-C_{216}$ of ideal hexagonal form, despite the even number of electrons in them, is not singlet. Their spatial structure is such that the orbitals of boundary cyclic chain forms a conjugate system, weakly connected with that of the central part of the cluster, which allows it to be regarded as relatively independent;
- the magnetic moment of clusters with only zigzag-shaped edges is determined by the presence of two-fold coordinated carbon atoms with highly localized on them electronic states.
- the maximum of the line of core level $N1s$ in clusters $C_{95}N$ is characterized by a positive chemical shift relative to the position of this line in the reference molecule for nitrogen-containing compounds – methylamine;
- the value of the chemical shift of the core level $N1s$ is the smallest for the pyridine-like arrangement of the nitrogen atom and increases with the distance of the graphite-like nitrogen atom from the zigzag edge, at corresponds to the experimentally elucidated regularity of its connection with the effective charge on the nitrogen atom.

First-principles study of the conductivity of $\text{In}_x\text{Tl}_{1-x}\text{I}$ solid solutions of substitution

Kashuba A.I., Franiv A.V., Solovyov V.V.

Ivan Franko National University of Lviv, Faculty of Physics, Cyryl and Metody str. 8a, 79005 Lviv, Ukraine

Introduction: For a long time the attention of scientists is being focused on the searching new materials with the controlled changes of physical properties. In particular, these properties can be obtained by introducing impurities into the already known crystals or by creating solid solutions based on them. Also, the stability of materials and their production costs are of importance.

Among the recently synthesized new mixed semiconductors of the $\text{A}^{\text{II}}\text{V}^{\text{VII}}$ group the three-component crystals $\text{In}_x\text{Tl}_{1-x}\text{I}$ represent a continuous series of solid solutions of substitution (SSS). Their band gap E_g vary within the range 2.01 - 2.84 eV [1 - 2]. These crystals possess a layered structure and in contrast to typical layered crystals of the $\text{A}^{\text{II}}\text{V}^{\text{VII}}$ and $\text{A}^{\text{III}}\text{V}^{\text{VI}}$ (PbI_2 , CdI_2 , HgI_2 , GaSe , InSe) groups [3, 4], in which the van der Waals interlayer gaps are formed by the corresponding anions, in these SSS $\text{In}_x\text{Tl}_{1-x}\text{I}$, this region of the weakest chemical bonding is created by the nearest cations of indium and thallium.

Investigations of the crystals $\text{In}_x\text{Tl}_{1-x}\text{I}$ is of the interest due to the possibility of samples creation that combine the properties of InI and TlI ones. The prospect of these compounds is associated with their practical application as working elements in the ionizing radiation detectors and optical modulators of CO_2 laser. Thallium iodide crystallizes in a rhombic structure at the temperatures up to 178 °C, but at higher temperatures, it transforms into the CsCl structure of the cubic symmetry. Information on the corresponding structural phase transition is presented in Ref. [5]. In halides of indium, no phase transitions occur except in InCl . In Ref. [6], a possibility of forming the InI structure as a matrix for the TlI quantum dots inclusion is discussed. The crystals InI and TlI cleave perpendicularly to the crystallographic b -axis [2]. Smooth controlled changes of the energy parameters (e.g. band gap E_g), mechanical and photovoltaic characteristics and spectral range of the recombination radiation may be realized in them. Results of investigation of the band structure (BS) and photoconductivity with change of the indium vs thallium content of the crystals $\text{In}_x\text{Tl}_{1-x}\text{I}$ are presented in the recent study [2].

The presents study is based on the first principles calculations of the band structure and conductivity spectra of the nominally pure $\text{In}_x\text{Tl}_{1-x}\text{I}$ crystal for $x = 0.125, 0.25, 0.375, 0.5, 0.625$.

Method of calculations: In order to determine the band structure of $\text{In}_x\text{Tl}_{1-x}\text{I}$ SSS we used the density functional theory (DFT) first principles method based on the nonlocal pseudopotentials. The calculation method used is described in details in Refs. [7].

Results and discussion: The band structure calculations were carried out at the points of Brillouin zone (BZ) along the line containing the high symmetry

points Γ , F, Q, and Z (Fig. 1). The band structures of $\text{In}_x\text{Tl}_{1-x}\text{I}$ SSS without any vacancies or interstitials were obtained and studied in [2] (Fig. 2).

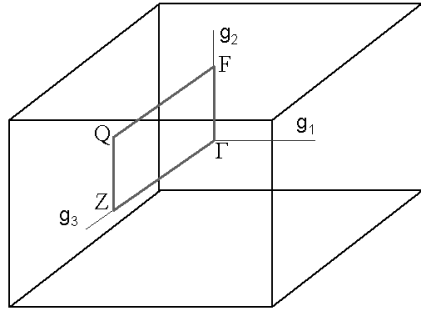


Fig. 1. BZ for orthorhombic $\text{In}_x\text{Tl}_{1-x}\text{I}$ SSS and high symmetry points Γ , F, Q and Z

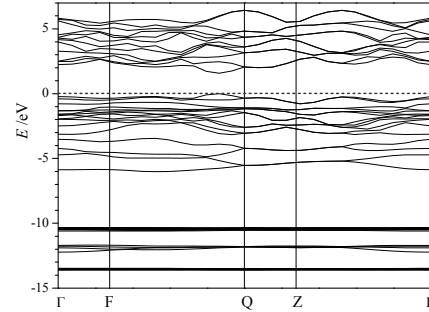


Fig. 2. Band structures of $\text{In}_{0.5}\text{Tl}_{0.5}\text{I}$ crystal

It is seen from Fig. 2 that substantial nonzero energy gap ($E_g \approx 1.5$ eV) takes place between the Fermi level and lowest conduction bands. As a result, no metal-like conductivity is expected in this case.

According to our results, the direct band gap E_g of $\text{In}_{0.5}\text{Tl}_{0.5}\text{I}$ is not localized at the Γ -point of BZ (Fig. 2). This is true for all compounds of the $\text{A}^{\text{II}}\text{V}^{\text{VII}}$ class, both cubic and orthorhombic, and it follows, mainly, from the electronic configuration of these ten-electrons compounds with an excess of the s electron pairs of metal.

The effective electron mass m^* is usually defined by the following relation from the band structure calculations [8, 9],

$$\frac{1}{m^*} = \frac{4\pi^2}{h^2} \frac{d^2 E(\mathbf{k})}{d\mathbf{k}^2}, \quad (1)$$

where h is the Planck constant, $E(\mathbf{k})$ is the dependence of the band energy E on the electron wave vector \mathbf{k} . For the case of $\text{In}_x\text{Tl}_{1-x}\text{I}$ SSS, the effective electron mass m^* was calculated at the minimum of the conduction band energy located between the high symmetry Z and Γ points of BZ. At this \mathbf{k} -point, the smallest energy gap between the valence and conduction bands (E_g) of $\text{In}_x\text{Tl}_{1-x}\text{I}$ SSS also takes place. We have found that the higher the doping concentration of thallium ($1-x$) in the non-defective $\text{In}_x\text{Tl}_{1-x}\text{I}$ SSS, the larger the corresponding effective electron mass m^* (Fig. 3).

The choice of the \mathbf{k} -point for the theoretical determination of the effective electron mass is caused by the fact that experimental determination of m^* using the edge luminescence is possible only from the minimum of conduction band as an initial energy state at this \mathbf{k} -point. Similar experimental studies of the effective electron mass on the basis of other minima of the band energy dependences $E(\mathbf{k})$ are not known.

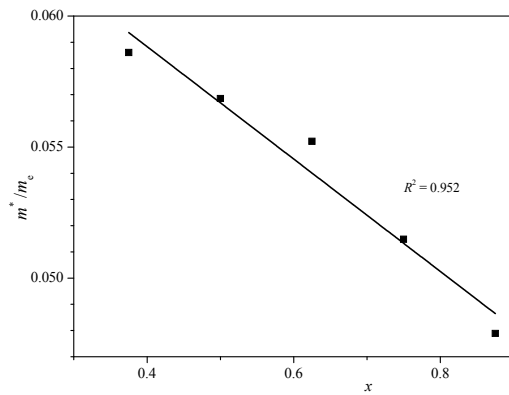


Fig. 3. Dependence of the effective electron mass m^* of non-defective $\text{In}_x\text{Tl}_{1-x}\text{I}$ SSS, calculated at the minimum of the conduction band energy located between the high symmetry Z and Γ points of BZ, on the indium vs thallium content x . R^2 is the coefficient of determination for the linear fit

According to the semiconductor theory [8, 9] the specific conductivity σ of a material is dependent on the charged particles mobility μ ,

$$\sigma = n \cdot q \cdot \mu. \quad (2)$$

Here q is the particle's charge and n is the charged particles concentration. That is why the dependence of the electron mobility μ on the indium vs. thallium content x of $\text{In}_x\text{Tl}_{1-x}\text{I}$ SSS is of interest also for the probable practical applications of the material. It is known also that for the case of the high doped semiconductors, the heating effects might be neglected in the conductivity process in comparison to the electron scattering by the ionized impurities, which becomes a dominating factor [9].

The electron mobility μ_i associated with an impurity of the i -type may be presented by the following relation [9],

$$\mu_i = \frac{q\tau_i}{m^*}. \quad (3)$$

where τ_i is the relaxation time, which is inversely proportional to the ionized impurity concentration n_i ,

$$\tau_i \sim n_i^{-1} T^{3/2}. \quad (4)$$

Here T is the thermodynamic temperature. Then, for two different impurity concentrations of thallium, n_1 and n_2 ($n_2 > n_1$), one can obtain the following relation,

$$\frac{\mu_2}{\mu_1} = \frac{\tau_2 q m_1^*}{\tau_1 q m_2^*} = \frac{n_1 m_1^*}{n_2 m_2^*} \approx 0.16. \quad (5)$$

The ratio $\mu_2/\mu_1 = 0.16$ corresponds to the electron mobilities μ_2 in $\text{In}_{0.375}\text{Tl}_{0.625}\text{I}$ and μ_1 in $\text{In}_{0.875}\text{Tl}_{0.125}\text{I}$ SSS.

According to the relation (2), the ratio of conductivities corresponding to two different doping concentrations n_2 and n_1 of thallium may be estimated as,

$$\frac{\sigma_2}{\sigma_1} = \frac{n_2 \mu_2}{n_1 \mu_1} = \frac{m_1^*}{m_2^*} \approx 0.82. \quad (6)$$

Here, σ_1 is the specific electron conductivity for $\text{In}_{0.875}\text{Tl}_{0.125}\text{I}$ SSS, and σ_2 for $\text{In}_{0.375}\text{Tl}_{0.625}\text{I}$.

One however should remember that the above estimations of the values μ_2/μ_1 and σ_2/σ_1 have been obtained at two simplifications: (1) the charge concentrations n_1 and n_2 for the impurity electrons (see Eq. 2) are identified as the corresponding impurity concentrations of thallium atoms; (2) the value of m_1^*/m_2^* corresponds to the non-defective $\text{In}_x\text{Tl}_{1-x}\text{I}$ SSSs, where the electric charges associated

with interstitials of thallium atoms are absent. In the real case, two kinds of thallium atoms may exist in $\text{In}_x\text{Tl}_{1-x}\text{I}$: (1) thallium substituting indium in its crystal symmetry positions and (2) interstitial thallium. The above mentioned simplifications may cause the values μ_2/μ_1 and σ_2/σ_1 to be a bit larger but they can't change the final conclusion that the electron conductivity of $\text{In}_x\text{Tl}_{1-x}\text{I}$ SSS is decreasing with increase of the doping concentration of thallium.

Conclusions: First principles calculations of the band electronic structure and optical conductivity spectra, based on the density functional theory, have been performed for the non-defective and defective (with anion vacancies and cation interstitials) solid state solutions of $\text{In}_x\text{Tl}_{1-x}\text{I}$ ($x = 0.125, 0.25, 0.375, 0.5, 0.625$). On the basis of the band structures obtained the effective electron mass and consequently the electron mobility and conductivity have been calculated. It was found out that the static (total) electrical conductivity of the non-defective $\text{In}_x\text{Tl}_{1-x}\text{I}$ SSS decreases with increasing the thallium content.

References:

1. Blonskij I.V./ Influence of static lattice disordering on optical properties of $\text{In}_x\text{Tl}_{1-x}\text{I}$ crystals / I.V. Blonskij, M.I. Kolinko, Yu.O. Lun, A.V. Franiv // Proceedings of SPIE - The International Society for Optical Engineering. — 1995. . — Vol. 2647. . — P. 452-454.
2. Kashuba A.I. Specific features of content dependences for energy gap in $\text{In}_x\text{Tl}_{1-x}\text{I}$ solid state crystalline alloys / A.I. Kashuba, M. Piasecki, O.V. Bovgyra, V.Yo. Stadnyk, P. Demchenko, A. Fedorchuk, A.V. Franiv and B. Andriyevsky // Acta Physica Polonica A. — 2018. — Vol. 133, №1. — P. 68-75.
3. Brodin M.S. Dynamical properties of excitons in layer crystals of PbI_2 / M.S. Brodin, I.V. Blonskii, B.M. Nitsovich, A.S. Krochuk, A.V. Franiv // physica status solidi (b). — 2001. — Vol. 111, № 2. — P. 625-630.
4. Zallen R. Inter-polytype conversion and layer-layer coupling in PbI_2 / Zallen R., Slade M.L. // Solid State Communications. — 1975. — Vol. 17, № 12. — P. 1561-1566.
5. Lowndes R.P. Molecular structure and anharmonicity in thallium iodide / R.P. Lowndes, C.H. Perry // J. Chem. Phys. — 1973. — Vol. 58, № 1. — P. 271-278.
6. Franiv A.V. Temperature behavior of thermal expansion and birefringence of $\text{In}_x\text{Tl}_{1-x}\text{I}$ - substitution solid solutions/ A.V. Franiv, V.Y. Stadnyk, A.I. Kashuba, R.S. Brezvin, O.V. Bovgyra, A.V. Futei // Optics and Spectroscopy. — 2017. — Vol. 123, № 1. — P. 177-180.
7. Kolinko M.I. Optical constants of indium bromide / M.I. Kolinko, O.V. Bovgyra, M. Piasecki // Low temperature physics. — 2001. — Vol. 27, № 2. — P. 153-157.
8. P.Y. Yu, M. Cardona, *Fundamentals of Semiconductors: Physics and Materials Properties*. Springer, 2010, p. 205.
9. Qingyu Hou. Study on the effect of high V doping on the conductivity of anatase TiO_2 / Qingyu Hou, Wencai Li, Zhenchao Xu, Chunwang Zhao // International Journal of Modern Physics B.— 2016. — Vol. 30. — P. 1650001(9).

RADIATION-INDUCED CREATION OF ATOMIC CLUSTERS IN POLYATOMIC CRYSTALS

A. E. Kiv, N. A. Mykytenko, Yu. V. Bondaruk, I. I. Donchev

South-Ukrainian national pedagogical university after K. D. Ushinskij

26, Staroportofrankovskaya Str., Odessa, 65 020 Ukraine

Email: kiv@bgu.ac.il

It is known that mechanisms of formation of radiation defects depend significantly on the energy of incident particles. The particles penetrate into material with initial energy, E_0 , which is dissipated throughout the particle trajectory to zero. In the conditions of the long-term irradiation as a rule a stationary energy distribution of incident particles is set. In each interval of energy spectrum specific mechanisms of defect formation are realized. The final radiation effect is determined by the superposition of radiation effects caused by incident particles at different intervals of the energy spectrum. Therefore to decrypt the mechanisms of radiation defect formation it is important to clarify the nature of radiation-stimulated processes in different intervals of the energy spectrum of incident particles.

We developed a new approach for molecular dynamics (MD) method that allows studying radiation stimulated processes in the selected range of energy spectrum of incident particles. To simulate the effect of particles collisions in the selected interval of the energy spectrum the striking forces (F_s) acting on the lattice atoms are introduced [1].

The standard expression for the total force in the Verlet algorithm is written as:

$$\vec{F}_i^n = -\sum \frac{\partial U(\vec{r}_{ij})}{\partial x_i} + F_s \quad , \quad (1)$$

The second term in (1) is the introduced striking force, U is the interatomic potential.

To choose the lattice atom and parameters of F_s the random functions [2] are used.

$$x_{n+1} = (x_n + x_{n-k})|m| \quad , \quad (2)$$

where k and module m are positive integers, $x_1 \dots x_n$ are arbitrary numbers. Each $n+1$ member depends on the previous one n . The function (2) provides: selection of an atom to kick, choice of the energy value in a given energy interval, choice of the direction of kick.

The developed approach is particularly useful in the case when the compound under irradiation consists of atoms with significantly different masses. By irradiation of such compounds with mono-energy ion beam and changing the energy of ions it is possible to obtain specific defect structures that can be used in electronics.

Let's say we want to study the effect of the particles in the energy range (E_1, E_2).

In the case of the irradiation with ions of mass m_{ion} the energy transferred in elastic collisions to the lattice atom of mass M is:

$$\varepsilon_{1,2} = \frac{m_{ion}}{M} \cdot E_{1,2} \quad , \quad (3)$$

It means that the random function chooses the energy value in the interval $(\varepsilon_1, \varepsilon_2)$. Now the scaling of the force F_s is necessary in order to determine the kinetic energy, transferred to atom.

As a reference point we can use the energy (E_d) that is necessary for the elastic displacement of lattice atom to interstitial position.

$$\frac{(Fst)^2}{2M} = E_d, \quad (4)$$

In (4) t is duration of the action of the force pulse in one kick. In computer experiment we gradually increase the value of the force F_s to the point where the atoms begin to move irreversibly to interstitial positions. This value of the force F_s corresponds to $E_d \approx 25 - 30$ eV. Thus we can define the interval F_s that corresponds to interval $(\varepsilon_1, \varepsilon_2)$ and respectively to (E_1, E_2) .

The approach was applied to study the cluster defects formation in PbS crystals under ion irradiation. PbS is a material with significantly different masses of atoms. The mass of S is ~ 6.5 times less in comparison with the mass of Pb . The model crystal was constructed according to the usual method [1].

In a certain interval (E_1, E_2) of radiation energies one may expect an intensive displacement of S atoms from their lattice sites accompanied by formation of vacancies. Proceeding from the mean value of $E_d = 30$ eV for S and Pb and using (3) we obtain for the case of bombardment of the target by nitrogen ions: $E_1 \geq 67$ eV and $E_2 < 443$ eV. In this energy interval the radiation-induced displacements of Pb atoms do not occur.

Computer program allows fixing the time from the onset of exposure to the moment of the first Pb cluster formation (τ). It is clear that $1/\tau$ is proportional to the probability of cluster formation. The result shown in Figure 1 leads to conclusion that a simultaneous disordering of two sublattices does not lead to the formation of clusters of atoms of the same type. To get such clusters we should use the ion beams with energy. We note also the role of the radiation stimulated diffusion of Pb atoms under the bombardment of particles with energy less than the threshold energy of the atoms displacement.

Figure 2 illustrates the kinetics of formation of clusters of Pb atoms. This Figure clearly demonstrates the transition region from clusters with two atoms to clusters with three atoms.

References

1. A. Kiv, N. Mykytenko, D. Fuks, I. Dahan, L. Meshi, Molecular Dynamics probing of the energy spectrum of particles in radiation stimulated processes, *International Journal of Advanced Computer Technology*, Vol. 4, No. 6, 2016, pp. 81-86.
2. J. Honerkamp, Statistical Physics: An Advanced Approach with Applications, 3rd edition, Springer, 2012, 554 p.

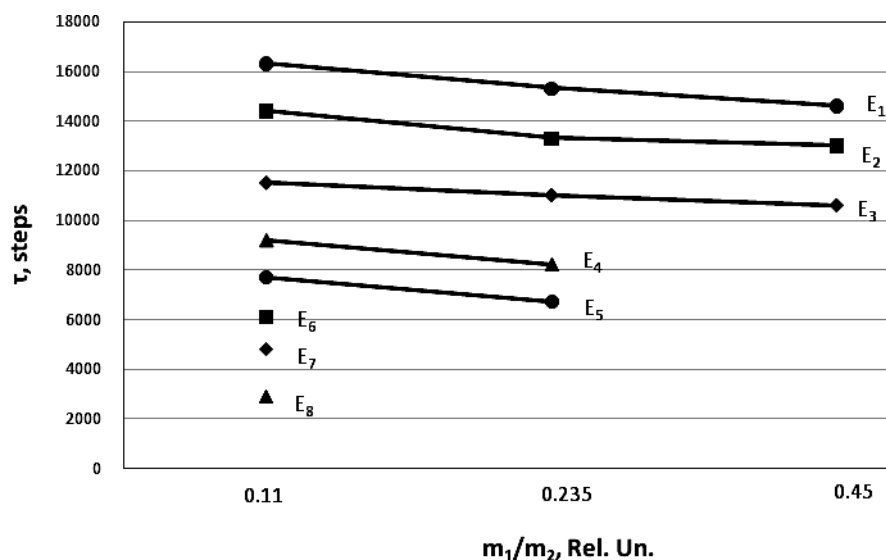


Figure 1. Dependence of τ on the mass ratio of the light atom (m_1) and the heavy atom (m_2): The energies of bombarding ions are $E_1 = 70$ eV, $E_2 = 85$ eV, $E_3 = 107$ eV, $E_4 = 150$ eV, $E_5 = 205$ eV, $E_6 = 300$ eV, $E_7 = 350$ eV, $E_8 = 425$ eV.

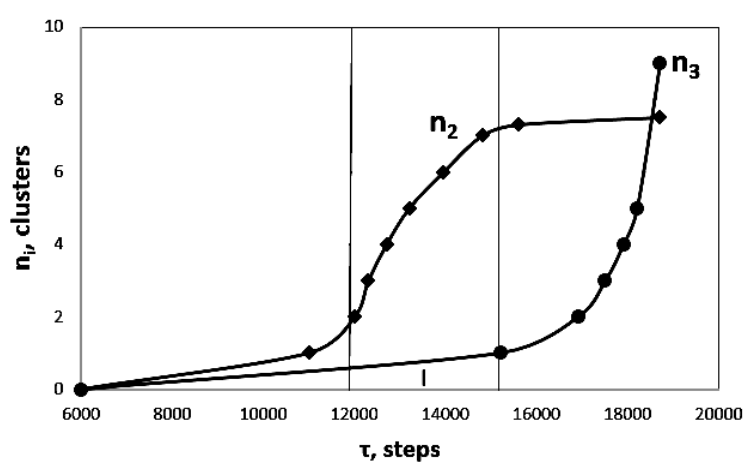


Figure 2. The kinetics of accumulation of Pb clusters containing 2 (n_2) and 3 (n_3) atoms. n_2 and n_3 are in relative unites.

PARTICULARITIES OF ZnO:Mn NANOCRYSTALS DOPING AT THEIR SYNTHESIS BY AEROSOL SPRAY PYROLYSIS METHOD

A.V. Kovalenko, V.Yu. Vorovsky, M.F. Bulaniy, O.V. Khmelenko

*Dnepropetrovsk National University named after Oles Honchar,
Gagarin Avenue, 72, 49010, the city of Dnepr, Ukraine.*

In recent years, diluted magnetic semiconductors (DMS) draw particular attention of researchers due to their potential for use in spintronics [1]. A great number of studies were concerned with research of DMS prepared by ZnO doping with the transition metals. This is due to the fact that the study [2] theoretically predicts ferromagnetic properties of nanocrystals (NC) of Mn-doped ZnO at the room temperature. The experimental validation of this prediction was presented in the study [3]. Results obtained by us [4] show as well that sample ZnO:Mn NCs synthesized by the aerosol spray pyrolysis (AP) method have ferromagnetic properties at the room temperature. These properties disappeared after the sample annealing in air at $T = 800^{\circ}\text{C}$ and varied depending on the synthesis process conditions.

The AP method has an obvious advantage over all other DMS preparation methods in that it is simple and allows nanomaterial preparation in form of both powder and film. This method is based on the thermal decomposition of initial solution aerosol droplets when these pass through the thermal zone. Feature of NC synthesis by the AP method is that NCs are formed during the short period of time within the micro-droplet volume under the nonequilibrium conditions. This results in occurrence of great number of defects in the NC, which materially affect physical properties of the synthesis product. Thus, important is investigation of NC doping capability with admixtures for the short time under the nonequilibrium crystallization conditions during the synthesis.

This paper presents results of research of properties of ZnO:Mn NCs prepared by the AP method in as-synthesized and as-annealed state.

Sample ZnO:Mn NCs were prepared by the AP method from solutions of zinc and manganese nitrates in accordance with the technique described in the work [5]. Prepared samples had Mn concentration of 2 and 4at.%. These also were subject to annealing in air at temperature $T_1 = 550^{\circ}\text{C}$ and $T_2 = 850^{\circ}\text{C}$ for 1 hour. Samples were investigated by the X-ray diffraction (XRD) analysis and electronic paramagnetic resonance (EPR) methods.

Investigation of sample ZnO:Mn NC with manganese concentration of 4at.% by XRD method (fig. 1a) showed that its crystalline structure was of wurtzite type. The synthesized sample has homogeneous composition, but after annealing at $T_1 = 550^{\circ}\text{C}$, Mn_2O_3 admixture phase occurs therein. Conclusion is made that this phase was in the amorphous state before the sample annealing and its identification XRD by method was infeasible. After the annealing at temperature $T_2 = 850^{\circ}\text{C}$, admixture phase disappears because Mn forms solid solution with ZnO at this temperature and dissolves in it. This fact is supported by the research results presented in

the Table 1, which demonstrate that values of crystalline lattice parameters (a,c) and elementary

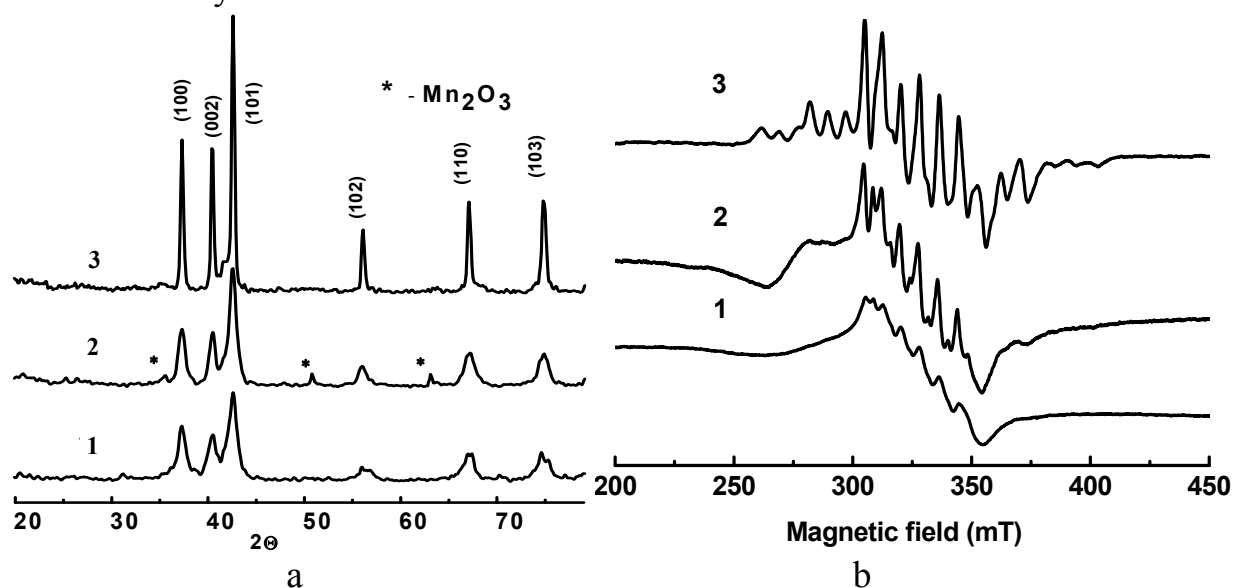


Fig. 1 X-ray diffraction patterns of sample ZnO:Mn NC (4at%) (a) and its EPR spectra (b): 1 – before annealing, 2 – after annealing at $T_1 = 550^\circ\text{C}$, 3 – after annealing in air at $T_2 = 850^\circ\text{C}$ for 1 hour. Symbol '*' – Mn_2O_3 phase.

cell volume (V) of samples before and after annealing at $T_1 = 550^\circ\text{C}$ are scarcely different from such values of non-doped ZnO NC [5]. Increase in these parameters after the high-temperature sample annealing at $T_2 = 850^\circ\text{C}$ shows that under these conditions, process of volumetric ZnO NC doping occurs by substitution of zinc ions Zn^{2+} with manganese ions Mn^{2+} having larger ionic radius (in wurtzite structure, ionic radius of Mn^{2+} makes 0.83\AA , and that of Zn^{2+} makes 0.74\AA).

Table 1 – ZnO and ZnO:Mn NCs crystalline lattice parameters (a,c), average crystal size (d), elementary cell volume (V).

Sample	Mn concentration 2.0at%				Mn concentration 4.0at%			
	d, nm	a, \AA	c, \AA	V, \AA^3	d, nm	a, \AA	c, \AA	V, \AA^3
ZnO, pyrolysis [5]	a = 3.2389, c = 5.1932, V = 47.12							
before annealing	35.8	3.2352	5.1951	47.08	33.6	3.2395	5.1873	47.14
annealing at 550°C	38.6	3.2389	5.2014	47.19	34.9	3.2396	5.1876	47.15
annealing at 850°C	93.7	3.2525	5.2105	47.73	104.2	3.2403	5.1917	47.21

Investigation of sample ZnO:Mn NC with manganese concentration of 4at.% by EPR method (Fig. 1b) also confirmed that high-temperature sample annealing is

required for its doping with Mn. Amplitude of EPR spectrum hyperfine structure (HFS) lines after annealing at temperature $T_2 = 850^\circ\text{C}$ is considerably increased, which is due to the considerable increase in Mn^{2+} ion concentration in ZnO NC volume. These studies also showed that EPR spectrum after the sample annealing at $T_1 = 550^\circ\text{C}$ had additional peaks (Fig. 1.b). Assumption is made that existence of these peaks is caused by the existence in the sample of Mn^{2+} ions in other local environment. Supposedly, the Mn_2O_3 admixture phase formation contributes in it (Fig. 1a). In addition, increase in amplitude of EPR spectrum HFS lines after the sample annealing at $T_1 = 550^\circ\text{C}$ is found. Most probably, some portion of Mn admixture being in the amorphous state diffuses in the ZnO NC surface layer during the sample annealing thus increasing the Mn^{2+} ions concentration, while other portion of this admixture crystallizes forming Mn_2O_3 phase.

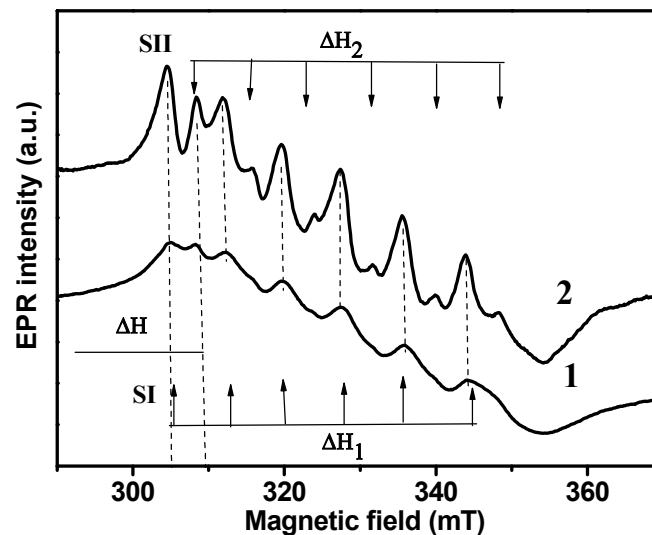


Fig. 2 EPR spectra of the sample ZnO:Mn NC with manganese concentration of 4at%: 1 – before annealing, 2 – after annealing at $T_a = 550^\circ\text{C}$

Performed analysis of EPR spectra of sample ZnO:Mn NC with Mn concentration of 4at% (Fig. 2) shows that peaks of basic sample spectrum HFS lines before (1) and after annealing (2) coincide (line group SI). Peaks of supplemental HFS lines (line group SII) in sample after annealing at temperature $T_1 = 550^\circ\text{C}$ (2) are shifted in relation to the basic HFS line peaks by $\Delta H = 3.9\text{mT}$. SI and SII line groups width values for all EPR spectra are the same and equal to $H_1 = H_2 = 39.5\text{mT}$. Calculation of mean values of the EPR spectrum hyperfine structure constants shows that these are approximately the same and equal to $A_1 = A_2 = A_3 \sim 7.9\text{mT}$. This value is close to the value $A = 7.6\text{mT}$ corresponding to the tetrahedral envelope of Mn^{2+} ion in the ZnO NC. It is also found that g-factor of sample EPR spectra (1), (2), (3) is invariable and equals to $g_1 = g_2 = g_3 = 2.019$. For the EPR spectrum of supplemental peaks corresponding to the SII line group, g-factor equals to $g_{II} = 1.998$. Such value of g-factor can be indicative of that after the sample annealing at temperature $T_1 = 550^\circ\text{C}$, Mn^{2+} ions are located in the imperfect environment on the ZnO NC surface. These conclusions agree with the results in [6]. In this study, authors show that after the ZnO:Mn NCs annealing at tempera-

ture $T \sim 500^\circ\text{C}$, supplemental line group SII occurs in their EPR spectrum, which is caused by Mn^{2+} ions located in the thin layer of zinc hydroxide $\text{Zn}(\text{OH})_2$ covering the ZnO NC surface.

Thus, the study shows that the key feature of ZnO NC doping with manganese during the synthesis by the AP method is that under short-term nonequilibrium conditions of the NC forming, the Mn admixture is not disseminated over the whole ZnO NC volume, but is concentrated within its near-surface layer. Annealing in air at temperature $T = 850^\circ\text{C}$ for 1 hour only results in Mn admixture diffusion into the NC volume.

1. Погорілий, С.М. Рябченко, О.І. Товстоли́ткін. Спінтроніка основні явища тенденція розвитку.// Укр. фіз. журн. Огляди.т. 6. №1.(2010) с. 37-96.
2. T. Dietl, H. Ohno, F. Matsukura at al., Zener Model Description of Ferromagnetism in Zinc-Blende Magnetic Semiconductors. J. Science, **287**, (2000), 1019–1022.
3. P. Sharma, A. Gupta, K. Rao at al., Ferromagnetism above room temperature in bulk and transparent thin films of Mn-doped ZnO. J. Nature Materials, 2, 673 (2003).
4. V.Yu. Vorovsky, A.V. Kovalenko, A.I. Kushneryov, O.V. Khmelenko. Preparation of zincoxide nanopowders doped with manganese which have ferromagnetic properties at room temperature.// J. Functional Materials, 25, 1, 2018, p. 1-6.
5. Буланый М.Ф., Воровский В.Ю., Коваленко А.В., Хмеленко О.В. Синтез нанопорошков ZnO и ZnO:Mn методом ультразвукового пиролиза аэрозоля. Журнал нано-та електронної фізики, т.8. №2. (2016). с. 02043-02048.
6. H. Zhou, D M. Hofmann, A. Hofstaetter, B K Meyer. Magnetic resonance investigation of Mn^{2+} in ZnO nanocrystals, J. Appl. Phys, 94, 3, (2003) 1965.

INVESTIGATION OF EPR SPECTRA IN ZnS_xSe_{1-x} NANOCRYSTALS.

A. V. Kovalenko, E. G. Plakhtiy, O. V. Khmelenko

*Oles Honchar Dnipro National University
Ukraine, Dnipro, Gagarina av., 72, 49010*

ZnS_xSe_{1-x} nanocrystals (NC) of all compounds were obtained by self-propagating high-temperature synthesis. The NC synthesis of ZnS_xSe_{1-x} and ZnS_xSe_{1-x}:Mn solid solutions were produced in a quartz vessel placed in a sealed steel reactor. The vessel was loaded with mechanically blended powders of Zn, S and Se with appropriate ratios. It was found that the obtained samples had dimensions of 55 ± 5 nm and were characterized by a mixed crystalline framework. The minimum dimensions of the ZnS_xSe_{1-x} NC were specific to the value $x = 0.2$, and the maximum for the compound $x = 1$. The fraction of the hexagonal phase in the ZnS NC was $\sim (65 \pm 5)\%$, the cubic phase $\sim (35 \pm 5)\%$, in the ZnS_{0.8}Se_{0.2} NC – $(60 \pm 5)\%$ and $(40 \pm 5)\%$, in the ZnS_{0.8}Se_{0.2} NC – $(50 \pm 5)\%$ and $(50 \pm 5)\%$, and in the ZnSe NC – $(30 \pm 5)\%$ and $(70 \pm 5)\%$, respectively. Thus, when the x parameter decreases, the fraction of the cubic phase in the ZnS_xSe_{1-x} NC increased.

An investigation of the EPR spectrum of the ZnS_xSe_{1-x} NC of solid solutions showed that, even in the NC undoped by manganese, all compounds contain a hyperfine structure consisting of six equidistant lines specific to the Mn²⁺ paramagnetic centers (Fig. 1a). In the compound with $x = 1$, these lines turned out to be doubled that testify to overlapping of two EPR spectra. One of them, with the hyperfine structure constant $A = 7.15$ mT, belongs to the Mn²⁺ ions located in a hexagonal local environment. Another spectrum, with a hyperfine structure constant $A = 6.88$ mT, is associated with Mn²⁺ ions that are located in a cubic environment. The obtained result correlates with the X-ray diffraction analysis (XRD) data that established the presence of a mixed crystal framework of the ZnS_xSe_{1-x} NC. The weak lines are observed in the compounds with $x = 1$ and $x = 0.9$ (they are marked by dashed arrows in Fig. 1), that can be associated with forbidden transitions. For them, the change in the electron spin, as for the allowed transitions, is $\Delta M = \pm 1$, and the change of nuclear spin $\Delta m = \pm 1$, while for permissible transitions $\Delta m = 0$. The forbidden transitions were observed in the ZnS NC and by other authors [1]. Their occurring is stipulated by severe lattice strain, as well as numerous disrupted bindings on the surface specific to NC. A single EPR line with $g = 1.9998$ associated with Cr⁺ ions was recorded in the same NC. Such line is also observed in ZnS bulk crystals [2]. It should be highlighted that usually the EPR signal stipulated by Cr⁺ ions is detected in zinc sulphide crystals under UV excitation. The occurrence of such signal in unilluminated NC may indirectly indicate that the ZnS and ZnS_{0.9}Se_{0.1} NC have the n-type of conductivity.

It is the electron capture at local levels of chromium that isovalent substitute the zinc in the zinc sulphide lattice ($\text{Cr}^{2+} + e = \text{Cr}^+$), leads to the occurrence of a line associated with Cr⁺ ions in the EPR spectra. At the room temperature, the EPR

signal of Cr^{+} ions in zinc selenide crystals is not observed due to the decrease in the spin-lattice relaxation time. In compounds with $0.2 < x < 0.9$, the EPR line with

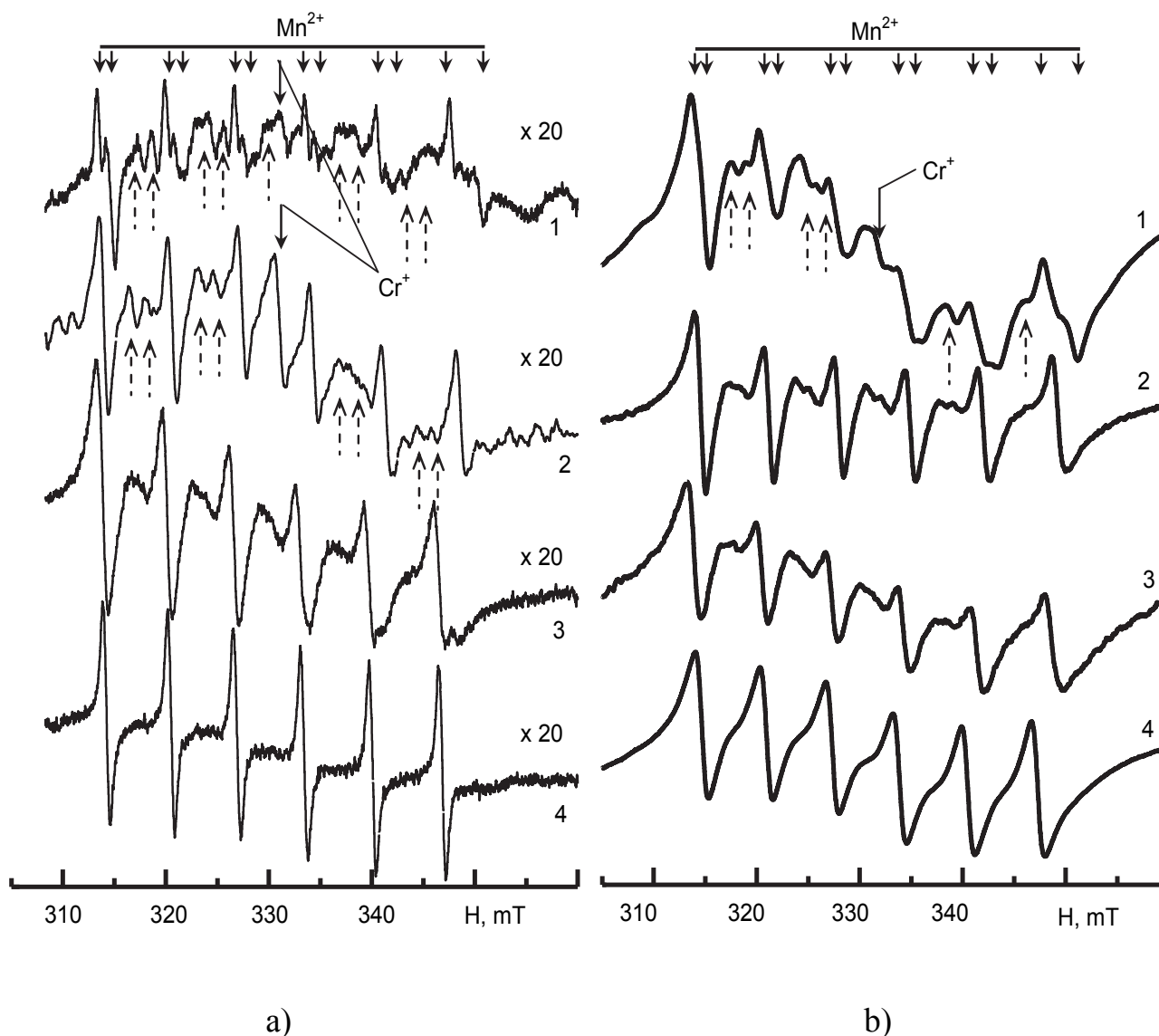


Fig. 1. EPR spectrum of self-activated (a) NC: ZnS (1), $\text{ZnS}_{0.9}\text{Se}_{0.1}$ (2), $\text{ZnS}_{0.2}\text{Se}_{0.8}$ (3), ZnSe (4); EPR spectrum of doped (b) NC: ZnS:Mn (1), $\text{ZnS}_{0.9}\text{Se}_{0.1}$:Mn (2), $\text{ZnS}_{0.2}\text{Se}_{0.8}$:Mn (3), ZnSe:Mn (4), dashed lines indicate forbidden transitions. ions changes abruptly, now they are surrounded by selenium ions. The ultrafine splitting constant decreases abruptly to a value $A = 6.55$ mT. A similar result was observed in $\text{ZnS}_x\text{Se}_{1-x}$ bulk crystals [3].

$g=1.9998$ was also not observed. The intensity of forbidden transitions was found to be at the noise level, and one group of six hyperfine structure lines specific to cubic local symmetry in ZnS crystals dominated the EPR spectrum of Mn^{2+} ions. For these compounds, the EPR ultrafine splitting constant of Mn^{2+} ions varies insignificantly and is within the range of $A=6.88 \div 6.91$ mT. Thus, it can be stated that in the NC of these compounds, the Mn^{2+} ions are not in a mixed environment but in the environment of sulfur ions, although the XRD data indicate the presence of triple compounds in this range of x . In compounds where $x < 0.2$, the crystal

framework of $\text{ZnS}_x\text{Se}_{1-x}$ NC, as noted by the XRD data, is characterized by the maximum degree of microdeformations and the density of dislocations. According to the EPR data, exactly in these compounds where the local environment of Mn^{2+}

The EPR spectrum of $\text{ZnS}_x\text{Se}_{1-x}$ NC doped by manganese are characterized by strong and wide lines of the hyperfine structure of Mn^{2+} ions. Only in the compound with $x = 1$ this line structure is doubled (Fig. 1b), that confirms the presence of mixed crystal framework of ZnS NC. A single EPR line is observed in these crystals stipulated by Cr^+ . In the compounds $0.9 \leq x \leq 1$, it is also possible to observe forbidden transitions with weak intensity. As in self-activated NC, despite the formation of mixed compounds according to XRD data, in $\text{ZnS}_x\text{Se}_{1-x}$ NC with $0.2 < x \leq 1$, the Mn^{2+} ions are not in a mixed environment but surrounded by sulfur ions. In compounds with $x \leq 0.2$, simultaneously with the jump of the hyperfine structure constant, that was mentioned above, the local environment of Mn^{2+} ions changes. In these NC, the Mn^{2+} ions are surrounded by selenium ions.

Thus, the obtained results testify that it is possible to obtain NC of $\text{ZnS}_x\text{Se}_{1-x}$ mixed compounds by SHS method, as well as to dope them during the synthesis with a manganese admixture. A mixed crystal framework characterizes NC in all compounds. In the compounds with $0.2 < x \leq 1$ according to the EPR data, the local environment of the Mn^{2+} ions is not mixed. The Mn^{2+} ions in these NC are surrounded by sulfur ions. In compounds with $x \leq 0.2$, the Mn^{2+} ions are surrounded by selenium ions. Simultaneously with the change in the local environment of Mn^{2+} ions, the hyperfine structure constant of the EPR of Mn^{2+} ions changes abruptly from a value $A = 6.88 \div 6.91$ mT to $A = 6.55$ mT. The presence of a single EPR line of Cr^+ ions in unilluminated $\text{ZnS}_x\text{Se}_{1-x}$ NC with $0.9 \leq x \leq 1$ can indirectly testify the n-type of the conductivity of the obtained samples.

References:

1. Gonzalez Beermann, P. A., McGarvey, B. R., Muralidharan, S., & Sung, R. C. (2004). EPR spectra of Mn^{2+} -doped ZnS quantum dots. *Chemistry of materials*, 16(5), 915-918. <https://doi.org/10.1021/cm030435w>
2. Reddy, D. A., Murali, G., Vijayalakshmi, R. P., & Reddy, B. K. (2011). Room-temperature ferromagnetism in EDTA capped Cr-doped ZnS nanoparticles. *Applied Physics A*, 105(1), 119. <https://doi.org/10.1007/s00339-011-6563-1>
3. Bulanyi, M. F., Geifman, I. N., Prokofev, T. A., & Khachapuridze, A. N. (1997). Hyperfine interaction constant of Mn^{2+} in $\text{ZnS}_{1-x}\text{Se}_x$ from EPR spectra. *Inorganic materials*, 33(12), 1234-1237.

THE OPTICAL PHONONS MANIFESTATIONS IN DYNAMICS OF THE OPTICAL ABSORPTION SPECTRA OF THE FLAT HETEROSTRUCTURES $\text{Al}_x\text{Ga}_{1-x}\text{N}/\text{GaN}/\text{Al}_x\text{Ga}_{1-x}\text{N}$ WITH QUANTUM WELLS OF DIFFERENT WIDTH

V.M. Kramar, D.V. Kondryuk, A.V. Derevyanchuk

*Yuriy Fed'kovych Chernivtsi National University,
2, Kotsiubynskogo Str., 58012 Chernivtsi, Ukraine*

Compounds AlN and GaN, as well as their alloys are strategic semiconductor materials for technologies of fabrication a various electronic, photo- and optoelectronic devices [1, 2]. Because of large direct bandgaps of these materials, which cover the range from ~ 3.4 (GaN) to ~ 6.2 (AlN) eV, such devices can be operates in the green, blue and UV spectral range. The essential cause of persistent attention to these materials is also their higher thermal and chemical stability.

Heterostructures (HS) GaN/AlN or GaN/AlGaIn with ultra-thin GaN quantum wells (QWs) are alternatives to AlGaIn alloys for deep-UV emission. This is due to the strong quantum confinement effect in such systems. For example, extreme quantum confinement in QWs thick only a few atomic monolayers of GaN in heterostructures GaN/AlGaIn increases the electronic gap of GaN by several electron volts what providing a light emission in the deep-UV [3].

Ability to change the spectral range of light absorption or emission by changing the width of a QW stimulated the construction a lot of devices, based on such HS. During the two last decades the higher efficient deep ultraviolet light emitting diodes (LEDs) and lasers [2], solar blind ultraviolet photodetectors [4] and other devices of great technological importance have been created on GaN/AlN-heterojunctions-based technologies. They can be uses for optical imaging, spectroscopy, higher density storage systems, early missile-plume detection, flame sensing, communication, solar-UV monitoring, as well as for optical sterilization and germicidal safety of medical procedures [5]. This HS also attracts attention for nitride high-electron-mobility transistor applications [6].

Such progress of optoelectronic devices fabrication is determined by the success in the processes of improvements of material quality. It is possible if there are instruments and methods of trusty control of the material quality. Among the methods of this kind of control is an exciton spectroscopy. The large binding energy of excitons in them makes it possible the exciton mechanism of light absorption even at room temperatures. Structure of exciton absorption spectra is a sensitive indicator of material quality.

Accordingly, the study of optical properties of GaN/AlGaIn-based HS as a function of the QW thickness and atomic composition of barrier material, are very important problem. There are number reports of experimental and theoretical studies of band gap variation of $\text{Al}_x\text{Ga}_{1-x}\text{N}$ alloys with different values of x . In particular, theoretical and experimental results for the electronic and optical properties of atomically thin GaN QW with AlN barriers are reported in [3], but authors of these

article have limited themselves to considering atomically thin (1 and 2 monolayers GaN) quantum wells with AlN barriers.

Here we present the results of theoretical investigation of electronic and optical properties of HS with single QW GaN/Al_xGa_{1-x}N. The energy of ground state of electron, hole and exciton in quasi-two-dimensional semiconductor nano-HS with single quantum well are calculated by using the dielectric continuum model, approximation of effective masses and Green's function method. Dependence of these energies on the well width and barrier material composition have been studied taken into account effects of quantum confinement, self-polarization of the heterojunction planes and interaction with various branches of optical phonons in such nano-HS. Specific calculation was made for GaN embedded in barrier material Al_xGa_{1-x}N, both of them has wurtzite-type structure. It has been studied on this base the influence of changes of well material thickness and barrier material composition on the spectral location the electron absorption edge and exciton peaks in such nano-HS. The results of this study may be of practical interest, since excitons provide a sensitive indicator of material quality.

We used the model of rectangular QW for which its width assumed equal to the thickness of well material a . Depth of QW is determined by the height of the bounded potential for the corresponding quasi particle (electron or hole) whose magnitude, in turn, is determined by the magnitudes of discrepancy of energy bands of the well and the barrier materials of HS, magnitude of the self-polarization potential of the plane of heterojunction and deformation potential characterizing differences of the parameters of crystalline lattices from both sides of this plane. All components of the bounded potential of quasi-particle at QW are determined by the parameters of the well and the barrier materials. Heterojunction GaN/Al_xGa_{1-x}N is considered to be unstrained, because the GaN and AlN compounds have close values of lattice parameters.

By use the techniques for determination of energy spectrum of carriers at rectangular QW accounting the effects of spatial confinement and interaction with all branches of longitudinal optics phonons in NF, as well as self-polarization of the heterojunction planes [7], we calculated the energies E_{e1} and E_{h1} of ground states of electrons and holes in own QWs. These do it possible to determine the absorption coefficient magnitude at the long-wavelength wing of interband absorption

$$\alpha_{\text{int}}(\omega) = \frac{\pi e^2 \varepsilon_P}{n c m_0 \omega l \hbar^2} \frac{m_e^* m_h^*}{m_e^* + m_h^*} |\langle \varphi_e | \varphi_h \rangle|^2 Y(\hbar\omega - E), \quad (1)$$

where m_0 – mass of free electron, m_e^* and m_h^* – effective masses of electron and hole at the well material with refraction index n and width of the forbidden zone E_g ; φ_e and φ_h – functions of the ground states of them at corresponding QWs; $Y(x)$ – the Heaviside function; ω – frequency; $E = E_g + E_{e1} + E_{h1}$ – energy of transition $h1 \rightarrow e1$; l – characteristic length determining extension of a wave function of a carrier into nano-HS, and $\varepsilon_P \approx 23$ eB – the Kane matrix element.

Interaction of electron with polar longitudinal optical phonons (LO-phonons) results in decreasing energy of its ground state. This circumstance can be taken

into account by substituting in Eq (1) the specified expression for the energy of transition

$$E = E_g + E_{e1} + E_{h1} - \Delta_e - \Delta_h, \quad (2)$$

where Δ_e (Δ_h) – values of displacement the bottom of ground mini-band of electron (hole) energy at the corresponding QW. Magnitude of displacement is determined by interaction with constrained, semi-constrained and interface phonons, the contribution of the each of them being determined by the thickness of well material (a), concentration of aluminum atoms at the barrier material (x) and temperature (T).

Vertical photo-transition from the ground state E_{h1} in QW of holes into the ground state E_{e1} in QW of electrons is accompanied by forming of exciton, as a consequence of Coulomb interaction. Assuming that interaction of an exciton with phonons is realized through individual interaction of electron and hole with them, one can represent the energy of transition into the ground exciton state as a sum

$$E_{ex} = E_g + E_{e1} + E_{h1} - E_b - \Delta_e - \Delta_h = E_{ex}^{(0)} - \Delta, \quad (3)$$

where E_b – bonding energy of quasi-2D exciton in QW, $\Delta = \Delta_e + \Delta_h$ – value of shift the bottom of exciton energy band caused by interaction with phonons, the technique of calculation of which is described in Ref [7].

In accordance with Eq (3), interaction of an exciton with optical phonons renormalizes the magnitude of energy of exciton transition, E_{ex} , determining position of the corresponding exciton peak at long-wavelength wing of the interband absorption at NF. As the energy of exciton transition, as well as the energies of the ground states of electron and hole, are depend on thickness of NF, temperature and concentration x , then the long-wave edge of fundamental absorption band as well as exciton absorption pick must be dependent on these values as parameters.

Calculations have been performed for HS $\text{Al}_x\text{Ga}_{1-x}\text{N}/\text{GaN}/\text{Al}_x\text{Ga}_{1-x}\text{N}$ whit concentration $x = 0.3, 0.5$, and 0.7 at low (near $T=0$) temperature as example. Used values of parameters are: $m_e = 0.2 m_0$, $m_h = 1.1 m_0$, $E_g = 3.47$ eV, LO-phonon energy 91.2 meV for GaN and $m_e = 0.4 m_0$, $m_h = 3.531 m_0$, $E_g = 6.128$ eV, LO-phonon energy 99 meV for GaN; band discontinuities at heterointerfaces $\Delta E_c = 2.0$ eV and $\Delta E_v = 0.7$ eV.

The results of calculations carried out by us for HS $\text{Al}_x\text{Ga}_{1-x}\text{N}/\text{GaN}/\text{Al}_x\text{Ga}_{1-x}\text{N}$ for $x = 0.3, 0.5, 0.7$ are the following. Interaction of electrons and holes with confined, semi-confined and interface branches of optical phonons spectra in QW results in shifting the bottom of the ground energy of electron and hole in own QW (Fig.1). Accordingly to (1) and (2), this will cause a shift of the edge of electron absorption band towards the long-wave range. Value of the shift depends on the NF thickness in a complex manner – it is rapidly increasing with its decrease from the value of ~ 110 meV for $a = 10$ nm to ~ 130 meV for $a = 2$ nm. For $a > 20$ nm the magnitude of such shift practically no depends on the film thickness and is about 100 meV.

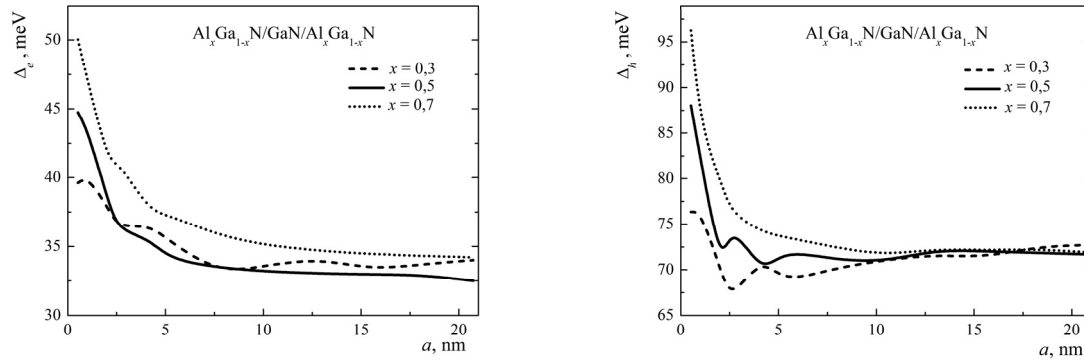


Fig. 1. Magnitudes of shifts of the electron (Δ_e) and hole (Δ_h) ground states

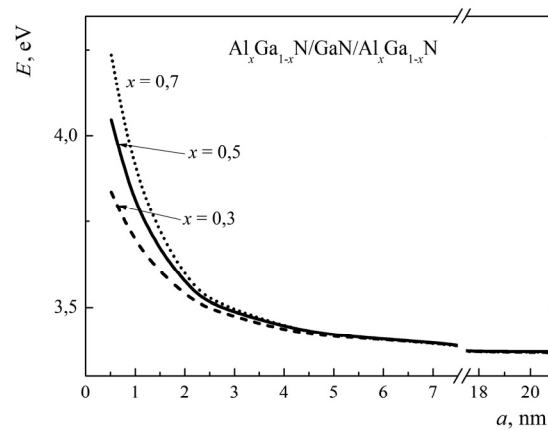


Fig. 2. Energy of transition to the underlying exciton state

The results of calculations of the changes position of the edge of fundamental absorption band in the studied QW with changes in their widths are depicted in Fig. 2. It can be seen, that with decreasing of QW widths from 20 nm, the energy of the interband transition increases. At $a < 4$ nm the quickness of this growth increases significantly. In ultrathin layers of GaN, the quickness of this growth is the greater, where concentration is higher.

1. H. Morkoç. Handbook of Nitride Semiconductors and Devices, GaN-based Optical and Electronic Devices. John Wiley & Sons, 2009.
2. K. Kamiya, Y. Ebihara, M. Kasu, and K. Shiraishi, Japan. J. Appl. Phys. **51**, 02BJ12 (2012).
3. D. Bayerl, S. M. Islam, Cr. M. Jones, *et al.*, Appl. Phys. Lett. **109**, 241102 (2016).
4. L. Sang, M. Liao, and M. Sumiya, Sensors (Basel) **13**, 10482 (2013).
5. X. Li, S. Sundaram, P. Dissix, *et al.*, Optical Materials Express **5**, 380 (2015).
6. S. Çörekçi, M. K. Öztürk, B. Akaoğlu, *et al.*, J. Appl. Phys. **101**, 123502 (2007).
7. D. V. Kondryuk, V. M. Kramar, Ukr. J. Phys. **60**, 458 (2015).

FEATURES OF OPTICAL PROPERTIES OF ZnSe <Al> SUBSTRATES WITH A MODIFIED SURFACE

**Makhniy V.P.¹, Berezovskiy M.M.¹, Vakhnyak N.D.², Litvin P.M.²,
Kinzerska O.V.¹, Senko I.M.¹**

¹*Yuriy Fedkovych Chernivtsi National University, Kotsyubynsky str. 2, 58012,
Chernivtsi, Ukraine*

²*Institute of Physics of the NAS of Ukraine, avenu Nauki 46, 03028, Kyiv, Ukraine
Email: illja.senko@yahoo.com, oksanakinszerska@gmail.com*

INTRODUCTION

At the present time, large crystals of ZnSe of good quality, which are non doped and doped with various elements, are obtained by the Bridgman-Stockbarger method [1]. Unfortunately, they usually contain a sufficiently large number of own and uncontrolled point defects, and therefore their physical and technical parameters do not always match the desired ones. This, in particular, concerns the combination of high electrical conductivity and the efficiency of edge radiation, one of the basic requirements for this compound when used in short-wave optoelectronics [2]. To fulfill these conditions, additional technological operations are used, which usually consist of high-temperature annealing in the melt or vapors of intrinsic components or other alloying elements [3-6]. An alternative to the above principles may be a concept based on methods for changing the physical properties of thin surface layers (surface modification) of a semiconductor substrate that do not substantially affect the key volume parameters of the latter.

On the other hand, it is the surface layers that are the active regions of many semiconductor devices and in fact determine their physical and technical parameters. The present work is devoted to the investigation of the effect of modification of the surface of ZnSe <Al> substrates on their certain optical properties.

SAMPLES AND INVESTIGATION TECHNIQUES

The bulk crystals of ZnSe <Al> were grown by the Bridgman-Stockbarger method and doped in the growth process, often used, by a donor Al impurity [3]. The objects of the research were cut from a crystal plate with the size 4x4x1mm³ and passed various methods of processing. In this case, after etching in the solution of the CrO₃:HCl = 2:3 composition, the surface of the samples was visually perceived as a mirror image (type 1), and in the solution H₂SO₄:H₂O₂ = 3:1- matte (type 2). Removal of the etching products was carried out for a long time (5-10 minutes) by washing in boiling distilled water and briefly rinsing the samples in concentrated acetic acid.

The optical transmission T_{ω} and luminescence N_{ω} spectra were measured in a universal installation that contained a diffractive monochromator of the MDR-23 type and a standard synchronous detection scheme. Luminescence was excited by an N₂-laser with a wavelength, and a halogen lamp with a "smooth" spectrum was used to study the transmission. The surface morphology of the samples was studied

by atomic force microscopy using the NanoScope IIIa Dimension 300™ microscope in the regime of periodic contact.

RESULTS AND DISCUSSIONS

As can be seen from Fig. 1, the photoluminescence spectrum (PL) of type 1 substrates at room temperature in the visible spectrum is represented by one wide yellow-green G-band. According to [3], it is due to associates ($V_{Zn}'' V_{Se}^\bullet$) and ($V_{Zn}'' Al_{Zn}^\bullet$), the contribution of each of which is determined by a number of factors - Al concentration, crystal growth and cooling regimes, excitation level, etc. Attention is drawn to the complete absence of a band of edge radiation in these samples, which is not observed at 300 K, even at the maximum excitation level ($L \approx 10^{18}$ kV / s).

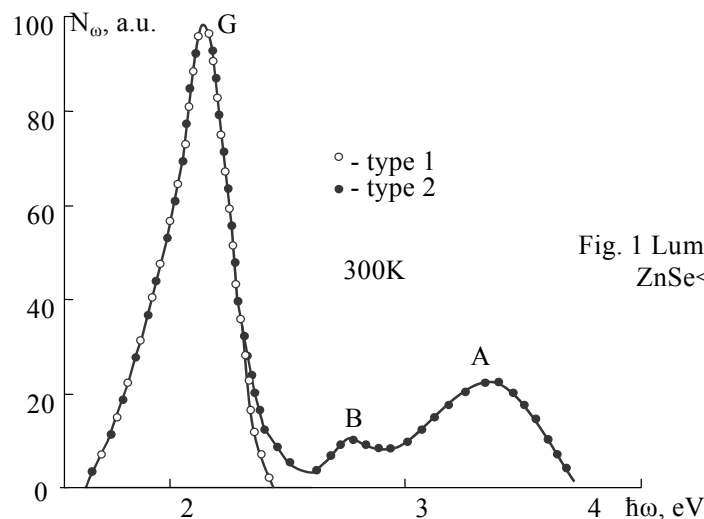


Fig. 1 Luminescence spectra of ZnSe<Al> substrates

At the same time, this radiation appears in samples of type 2 with a matte surface, and even at moderate values of L , the B band in Fig. 2. The position of its maximum correlates with the width of the band gap of zinc selenide ($E_g \approx 2.7$ eV at 300K) [3], and the large half-width indicates a complex B-band structure. This requires additional studies using modulation techniques or low temperatures, which goes beyond of this work.

The most interesting feature of the photoluminescence spectra of type 2 substrates is the presence of photons in it with an energy $\hbar\omega$ substantially exceeding the E_g of the material, the band A in Fig. 1. Note that it can not be caused by the formation of another chemical compound formed as a result of etching. This is confirmed by the similarity of differential spectra of optical reflection of samples of both types.

In this connection, we can assume that the most probable reason for the appearance in the PL spectra of the A-band is the surface nanostructure (PNS), which was formed as a result of chemical etching. This is confirmed experimentally by AFM-topograms, which for the samples under study are shown in Fig. 2. We draw attention to the fact that the picture of the surface of the substrates of type 2 agrees qualitatively with the AFM-topogram of the surface of CdTe substrates with a quantum-dimensional surface structure [7]. A detailed study of the latter shows that the surface consists of small (30-300nm) pyramids, which are combined into large pyramids with lateral dimensions (1-2 microns). In this case, the A-band is

formed by the vertices of small pyramids, and the absence of structural bands in it is due to the variance in the dimensions of these pyramids.

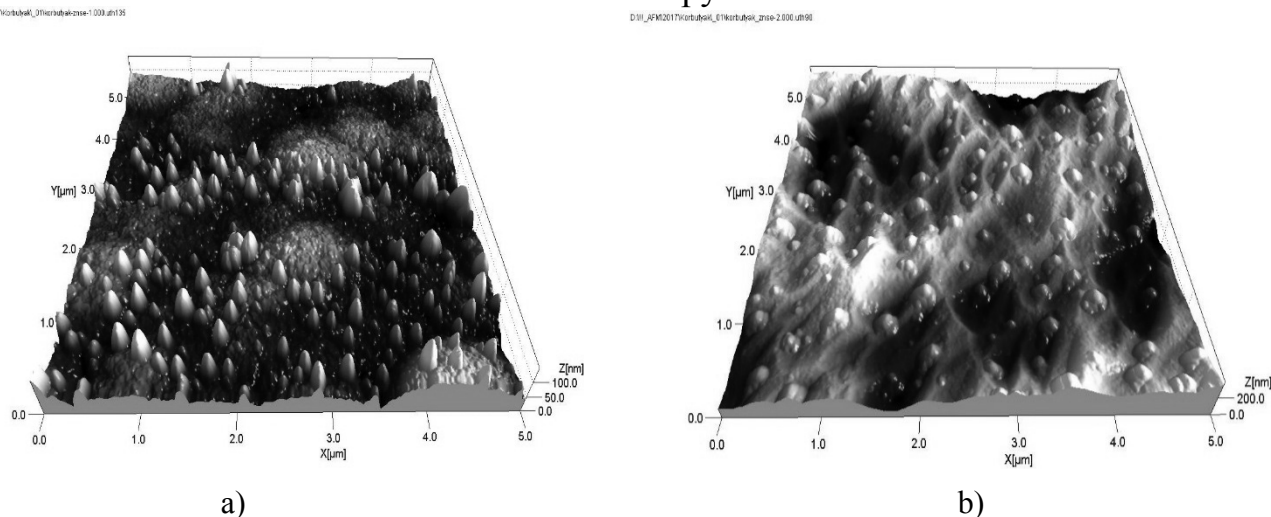


Fig 2. APM-topograms ZnSe<Al> substrates: type. 1(a), type.2(b)

Note that large pyramids, practically not taking part in the formation of the A-band, significantly change the transmission spectrum due to the increasing role of scattering processes and multiple reflection. This leads not only to a decrease in the absolute values, but also to a shift of the short-wavelength edge of the transmission spectrum to the low-energy side. Since these effects are associated with structural changes in the surface, they must also be accompanied by a deformation of the so-called Urbach's "tail" described by the known expression $\alpha_\omega = \alpha_0 \exp[\alpha^*(E^* - \hbar\omega)]$. Here α_ω is the absorption coefficient, which in the first approximation is equal to $\alpha_\omega = 1 - T_\omega$; α_0 and E^* are the coordinates of the focal point, and α^* is the parameter characterizing the degree of structural perfection.

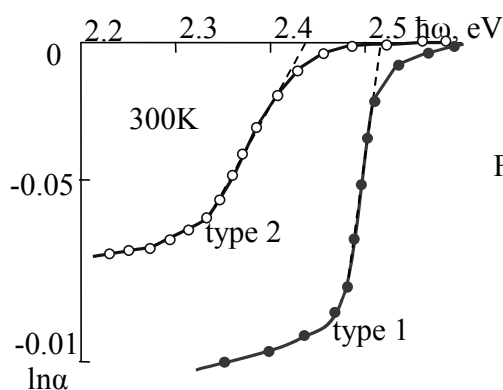


Fig. 3 Optical absorption spectra of ZnSe <Al> substrates

As can be seen from Fig. 3 sections of the spectra of the samples under study near the edge of the fundamental absorption are indeed repaired by the Urbach rule, and the violation of structural homogeneity (the transition from a mirror to a matte surface) causes a decrease in the slopes of the "tails" and their displacement into the low-energy region.

CONCLUSIONS

Thus, the observed features of the optical properties of ZnSe <Al> substrates are adequately explained by the formation of a surface nanostructure due to chemical etching in a $\text{H}_2\text{SO}_4:\text{H}_2\text{O}_2=3:1$ solution.

REFERENCES

- [1] N.K. Morozova, V.A. Kyznetsov, V.B. Rujukov, *Zinc Selenide: Preparation and Optical Properties*. Nauka, Moscow, 1992. 94 p.
- [2] Georgobian, A.N. and Kotlyarevsky, M.B., Problems of developing injection light-emitting diode on the base of wide-band A₂B₆ compositions, *Izvestiya Akademii Nauk USSR. Seriya fizicheskaya*, 1985, V.49, №10, P. 1916-1922.
- [3] D.D. Nedeoglo, A.V. Simashkevich, *Electrical and Luminescent Properties of Zinc Selenide*. Chisinau, Shtiintsa, 1984. 152 p.
- [4] M.M. Berezovskiy, V.P. Makhniy, V.V. Melnik, Influence of Li, Cd, In and As impurities on optoelectronic properties of ZnSe // *Neorganicheskie materialy*, 1997, V.33, №2, P. 181-183.
- [5] V.I. Gryvul, V.P. Makhniy, M.M. Slyotov, The origin of edge luminescence in diffusion ZnSe:Sn layers // *Semiconductors*, 2007, V.41, №7, P. 784-785.
- [6] V.P. Makhniy, O.V. Kinzerska, I.M. Senko, O.M. Slyotov High temperature luminescence of ZnSe:Yb crystals // *Tekhnologiya i Konstruirovanie v Elektronnoi Apparature*, 2016, №2-3 P. 37-40.
- [7] V.P. Makhniy Peculiarities of physical properties of a modified surface of cadmium telluride // *Semiconductors*, 2005, V.39, №7, P. 826-828.

THE EFFECT OF UV Nd:YAG LASER RADIATION ON THE OPTICAL AND ELECTRICAL PROPERTIES OF ZnO CRYSTAL: INITIATED PHASE TRANSITION

A. Medvid', P. Onufrijevs

Institute of Technical Physics, Riga Technical University, 3/7 Paula Valdena Str., Riga, LV-1048, Latvia

Abstract

The effect of UV Nd:YAG laser intensity on the conductivity and optical properties, such as: photoluminescence, Raman, transmittance spectra of hydrothermal ZnO crystal was studied. As a result, three laser intensities characterizing interactions with the crystal have been revealed. The improvement of ZnO crystal quality up to $3.2\text{MW}/\text{cm}^2$ was observed. There are the increase of free exciton band intensity and decrease of deep level emission band intensity in photoluminescence spectra. The intensity $I=290.0\text{MW}/\text{cm}^2$ leads to the formation of "black ZnO". It is caused by the emergence of Zn nanoparticles with size around 20 nm. XPS analysis and Raman spectra proved the presence of Zn in metallic form. At the same time conductivity of ZnO crystal continues to increase in the whole range of used laser intensities and exceeds the initial value by 300 times. The change of ZnO crystal optical and electrical properties by laser radiation is explained by generation, redistribution and agglomeration of Zn interstitials. Further irradiation of the structure leads to formation ZnO nanoparticles due to oxidation of Zn nanoparticles.

1 Introduction.

Zinc oxide (ZnO) has attracted quite much attention due to its unique optical and electrical properties for applications in optoelectronic devices [1], such as: LED, UV laser diodes, solar cells, etc. Moreover, ZnO crystal can be both highly transparent and highly conductive material. Therefore, it is a suitable candidate for the Transparent Conducting Oxide (TCO). ZnO crystals can be grown by various methods: vapor transport growth [2], pressurized melt growth – modified Bridgman process [3], pulsed laser deposition [4], hydrothermal growth [5], etc. Among them, the hydrothermal method is one of the most suitable for industrial use [6]. The advantage of this method is the possibility to grow much bigger crystals than with other methods [7]. The second advantage of this method is the possibility to achieve very high quality ZnO crystal, without block marks, twins and dislocations [8]. However, the main drawback of the hydrothermal method is a relatively slow growth rate and incorporation of Li and K impurities from the solvent, which causes low electron concentration and high resistivity [5]. It is known, that Li atoms substitute Zn forming a deep acceptor [9] that partially compensates n-type conductivity of ZnO, which is due to zinc interstitials (Zn_i) [10]. One of the ways to increase conductivity of ZnO is doping it by metal atoms, for example: Al, Ga, In, B [11] etc. However, doping leads to the deformation of the crystal lattice and at high concentration of doping formation of metallic inclusions takes place [12]. In this paper, we propose alternative approach to increase conductivity of hydrothermal ZnO crystal – generation and redistribution of Zn_i by strongly absorbed laser radiation ($h\nu > E_g$, where $h\nu$ - photons energy of laser radiation and E_g - the band gap of ZnO). Therefore, the aim of the present work is to study the possibility to control the conductivity and optical properties of hydrothermal ZnO crystal by pulsed Nd:YAG laser radiation.

2 Experimental.

In the experiments commercial ZnO single crystals (from Crystal Base Co.,Ltd.) grown by hydrothermal method with the size of $10.0 \times 10.0 \times 0.5 \text{ mm}^3$ were studied. The samples were irradiated by pulsed Nd:YAG (Ekspla NL301G) laser with following parameters: wavelength 266 nm, pulse duration 3 ns, intensities range from 1.0 to 290.0 MW/cm² (at lower laser intensity, than 1.0 MW/cm² no changes of electrical and optical properties were observed), repetition rate of 10 Hz, beam diameter 5 mm. Scanning of the laser beam was performed normally to the ZnO crystal surface with the speed of 10 mm/s. The irradiation of the samples was carried out at room temperature in ambient pressure. Measurements of photoluminescence (PL) spectra were performed using UV laser (DT-389QT) with excitation wavelength 265 nm. Morphological investigation of the samples was performed with a field emission scanning electron microscope (SEM) FEI Nova NanoSEM 650 using low vacuum mode and 15 kV electron beam. T

he crystal conductivity were performed by AFM in current measurement method. Optical transmittance spectra were obtained by Shimadzu - SolidSpec – 3700 spectrometers in the spectral range from 350 nm to 1500 nm. Raman spectra were studied at RT in back scattering geometry using “Renishaw inVia” spectrometer. As an excitation source the Ar⁺ laser ($\lambda=514 \text{ nm}$) was used.

3 Results and Discussion

It was found that the formation of Zn nanoparticles is initiated at two threshold intensities: the first threshold intensity at $I_{th1} = 3.5 \text{ MW/cm}^2$ causes a 10-fold increase in conductivity till the second laser exposure at an intensity of $I_{th2} = 290.0 \text{ MW/cm}^2$ that causes a 1000-fold increase in conductivity, Fig.1 [6]. The map of topography and spreading resistance at the outer edge of the laser irradiated spot do not overlap suggesting that the electrical current is not related to the topography. Parallel bands as shown in the topography and electrical conductivity (Fig 2) is explained by the laser induced periodic structure [16,17]. However, a band at 30 microns (white dashed lines) does not show any change in morphology, but a 4-fold increase in conductivity is detected, Fig 2b. It is proposed that an increase in conductivity at the outer perimeter arises from an increase in Zn_i concentration.

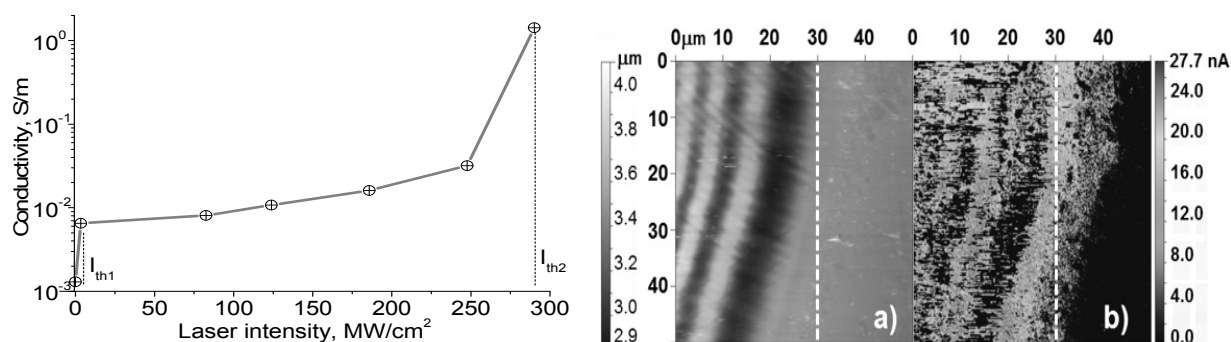


Figure 1. The dependence of the conductivity of the ZnO crystal on the laser intensity. Inset: point-to-point laser irradiated spots on a ZnO crystal after an increasing number of laser pulses: 1, 2, 5, 10 and 30.

Figure 2. AFM images: surface topography (a) and surface electrical current mapping (b). The non-irradiated area is on the right side of each image and the irradiated area is on the left side.

The process of Zn nanoparticles formation by Nd:YAG laser radiation is characterized by two stages. The first stage is an intensive generation and concentration of Zn_i at the irradiated surface of the ZnO crystal according to the thermogradient effect [18]. The second stage is an agglomeration of Zn_i into nanoparticles with the size depending on number of laser pulses, as shown in Fig.3 (b, c, d, e and f). As a result of Zn_i agglomeration, “black ZnO” is observed on the irradiated surface of ZnO crystal at intensity 315.0 MW/cm^2 , as shown in Fig.4.

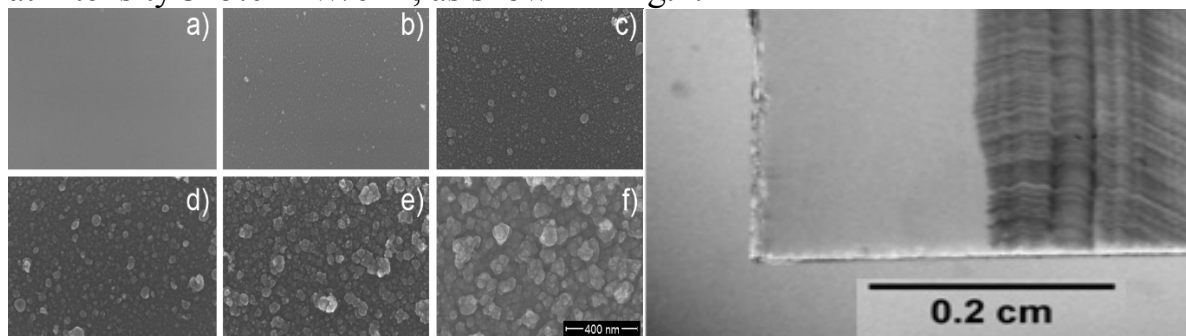


Figure 3. FESEM images of the irradiated surface of ZnO crystal at laser intensity 315.0 MW/cm^2 for increasing number of pulses: a. – 0; b. – 1; c. – 2; d. – 5; f. – 10; and g. – 30.

Figure 4. Optical microscope image of “black ZnO”.

The Raman spectra of the non-irradiated and irradiated surface of ZnO crystal at 300 K are presented in Fig.5. The non-irradiated sample has typical Raman spectra for ZnO crystal. It consists of E2(high) mode associated with oxygen atom vibration, which appears at 437 cm^{-1} with appreciable intensity, and E2(low) mode at 99 cm^{-1} associated with the heavy Zn sublattice [19, 20]. The peaks at 201 cm^{-1} and 332 cm^{-1} are attributed to the second-order Raman spectra, arising from the zone boundary phonons. After irradiation by the laser with intensity $I=315 \text{ MW/cm}^2$, the new band appeared at 70 cm^{-1} . According to G.A. Bolotin, et al [21], the frequency 70.5 cm^{-1} corresponds to E2g phonons of crystalline Zn. The appearance of 70 cm^{-1} band in Raman spectra after the irradiation by 1 and 2 laser pulses, shown in Fig.5, is an evidence of Zn phase formation in ZnO crystal. Dissipation of this band in Raman spectrum is observed after irradiation by 5, 10 and 30 pulses and is explained by the oxidation process of Zn nanoparticles. The evidence of this suggestion is appearance of a new broad band at 561 cm^{-1} in Raman spectra, the intensity of which increases with the number of laser pulses up to 5 pulses. The nature of this band relates to the surface optical phonon mode in ZnO nanocrystals with the size of 13 nm [22]. The Raman spectra has the highest intensity after 5 laser pulses due to Relay scattering on nanoparticles formed by laser radiation [23]. Investigation of both Raman and transmittance spectra allows us to find interesting peculiarities of the effect of nanoparticles formation. The intensities of both Raman bands, i.e., 70 cm^{-1} and 561 cm^{-1} , are non-monotonous functions of the number of laser pulses with maximums located at different number of the pulses – 2 and 5, correspondingly. Exactly, the maximum intensity band of 561 cm^{-1} corresponds to the minimal intensity band of 70 cm^{-1} . Therefore, we suppose that such peculiarity in Raman spectra is connected with oxidation of Zn nanoparticles in the air because some part of Zn nanoparticles are located on the irradiated surface.

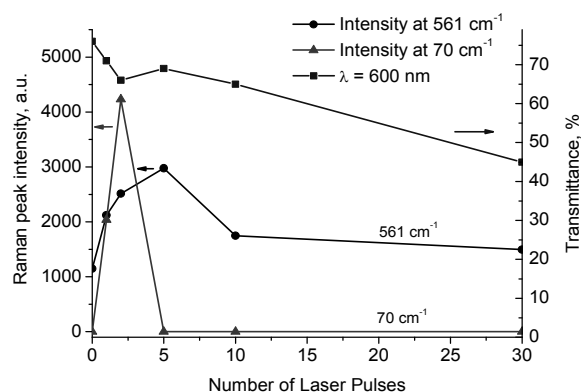
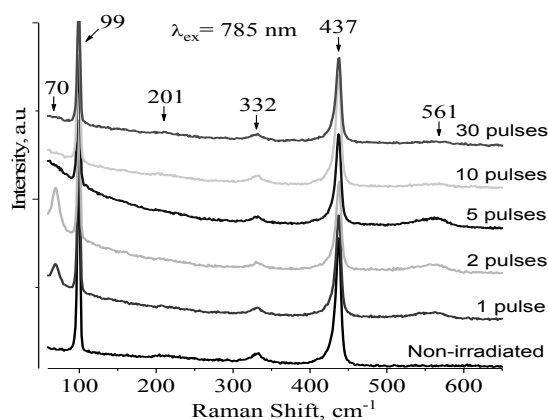


Figure 5. Raman spectra of ZnO crystal, irradiated by the laser with intensity $I = 315 \text{ MW/cm}^2$, for different numbers pulses.

Figure 6. The intensity of Raman bands of 70 cm^{-1} and 561 cm^{-1} and the sample transmittance at $\lambda = 600 \text{ nm}$ depending on the number of laser pulses at $I = 315.6 \text{ MW/cm}^2$.

Moreover, the transmittance of the ZnO crystal decreases non-monotonously after the irradiation depending on the number of laser pulses with minimum at 2 pulses. The further increase transmittance till 5 pulses it means, decrease absorption is explained by oxidation Zn nanoparticles, as shown in Fig.6.

References

- [1] A. Shimizu, M. Kanbara, M. Hada, and M. Kasuga, *Jpn. J. Appl. Phys.* 17, 1435 (1978).
- [2] C. Bundesmann, N. Ashkenov, M. Schubert, D. Spemann, *Appl. Phys. Lett.* 83, 1974 (2003).
- [3] M. Gabás, A. Landa-Cánovas, J. Luis Costa-Krämer, F. Agulló, *J. Appl. Phys.* 113, (2013).
- [4] S.-H. Jeong, H. Choi, J.Y. Kim, and T.-W. Lee, *Part. Part. Syst. Charact.* 32, 164 (2015).
- [5] L.-B. Luo, C. Xie, X.-H. Wang, Y.-Q. Yu, C.-Y. Wu, H. Hu, *Nano Energy* 9, 112 (2014).
- [6] P. Onufrijevs, A. Medvids, E. Dauksta, H. Mimura, *Opt. Laser Technol.* 86, 21 (2016).
- [7] S. Yoon, I. Huh, J.-H. Lim, and B. Yoo, *Curr. Appl. Phys.* 12, 784 (2012).
- [8] S. Takahashi, Y. Hasuiki, A. Noguchi, T. Tsuchi, *Jpn. J. Appl. Phys.* 49, 526021 (2010).
- [9] M. Nie, Y. Zhao, and Y. Zeng, *J. Laser Appl.* 26, (2014).
- [10] I. Markevich, V. Kushnirenko, *Semicond. Phys., Quantum Electron. Optoelectron.* 7, 350 (2004).
- [11] I. V Markevich, V.I. Kushnirenko, L. V Borkovska, *Phys. Status Solidi* 3, 942 (2006).
- [12] E.H. Khan, S.C. Langford, J.T. Dickinson, L.A. Boatner, *Langmuir* 25, 1930 (2009).
- [13] H. Kido, M. Takahashi, J. Tani, N. Abe, *IOP Conf. Ser. Mater. Sci. Eng.* 18, 72014 (2011).
- [14] Y. Sun and H. Wang, *Phys. B Condens. Matter* 325, 157 (2003).
- [15] See <http://crystalbase.co.jp/index/a/zno.html> for web page.
- [16] S.K. Das, H. Messaoudi, A. Debroy, E. McGlynn, *Opt. Mater. Express* 3, 1705 (2013).
- [17] X.D. Guo, R.X. Li, Y. Hang, Z.Z. Xu, B.K. Yu, H.L. Ma, Sun, *Mater. Lett.* 62, 1769 (2008).
- [18] A. Medvid, *Defect Diffus. Forum* 210–212, 89 (2002).
- [19] R. Jothilakshmi, in *Optoelectron. Mater. Tech.*, ed. P. Predeep (InTech, 2011), pp. 477–484.
- [20] R. Cuscó, E. Alarcón-Lladó, J. Ibáñez, L. Artús, J. Jiménez, *Phys. Rev. B* 75, 165202 (2007).
- [21] G.A. Bolotin, Y.I. Kuz'min, Y.V. Knyazev, Y.S. Ponomarev, *Phys. Sol. St.* 43, 1801 (2001).
- [22] J. Xu, G. Cheng, and Y. Du, *Chinese Phys. Lett.* 13, 765 (1996).
- [23] G. Gouadec and P. Colomban, *Prog. Cryst. Growth Charact. Mater.* 53, 1 (2007).

Electrical, structural and photoelectric features of thin ZnO:Al films on Si wafers

V.P. Melnik, B.M. Romanyuk, V.P. Kladko, V.G. Popov, O.Yo. Gudymenko,
O.I. Liubchenko, T.M. Sabov, O.S. Oberemok, O.V. Dubikovskiy,
Ju.V. Gomeniuk

*Lashkarev Institute of Semiconductor Physics NAS of Ukraine. 41Prospect Nauky,
Kyiv 03028, Ukraine. E-mail: romb@isp.kiev.ua*

ZnO is a wide bandgap semiconductor ($E_g = 3.37$ eV) with high transparency in the visible to near-infrared region and high exciton binding energy (60 meV) at room temperature [1]. In this connection ZnO based heterojunctions [2] are attracted considerable attention for solar cell, ultraviolet (UV) detector and light emitting diode creations. Naturally, ZnO is an *n*-type semiconductor because of a deviation from stoichiometry due to the presence of intrinsic defects such as oxygen vacancies and zinc interstitials that obviously form donor levels [3]. ZnO with silicon can form heterojunction. The presence of SiO_x native oxide and defects at the interface affects on the charge carrier generation and recombination and drastically change the electrical properties of the heterojunction.

As a rule, ZnO is doped by the IIIA group elements to obtain a layer with modified properties. Aluminum is the most suitable for this purpose because Al dopant atoms can replace a Zn atom in the structure and release a free electron that increases the free carrier concentration [4]. Besides, the optical band gap of ZnO films is changed as a function of aluminum content. ZnO:Al/Si heterojunctions have a higher switching speed and lower temperature budget in comparison with typical silicon *p-n* or *p-i-n* junctions. The heterojunction quality depends on the number and type of defects on the interface and in the thin film. Ion implantation with the next temperature treatments allow to change the point defect concentration in ZnO film and obtain the ZnO/Si structures with desired properties.

The purpose of this work was investigation of the structural, electrical and photoelectric properties of the ZnO:Al /Si heterojunctions.

Al-doped ZnO (ZnO:Al) thin films with thicknesses of 10-140 nm were deposited on Si substrate by DC reactive magnetron sputtering of the target with Al content of 2%. The film modification was carried out by Ar⁺ ion implantation (50 and 100 keV). The prepared films were annealed at temperature range from 450 to 750 °C by rapid thermal and furnace annealing.

The modified films were studied using X-ray diffraction (XRD), Secondary Ion Mass Spectrometry (SIMS) and Transmission electron microscopy (TEM). The diode structures were manufactured for investigation of initial and modified heterojunctions. I-V and C-V characteristics were measured in the fabricated structures.

From XRD studies, thickness, density and roughness of deposited films were determined (Table 1). It was found that the roughness of the Si/ZnO interface decreases with increasing thickness.

Table 1.

Sample No.	Film thickness nm	Film density g/cm ³	Root mean squared roughness of the Si/ZnO interface, nm	Root mean squared roughness of the ZnO surface, nm
1	10.2	5.9	0.4	0.54
2	20.8	5.62	0.34	0.52
3	41.6	5.59	0.02	0.51
4	65.8	5.60	0.05	0.6

In addition, in the films less than 50 nm, the films are textured, and at larger thicknesses, a polycrystalline structure of hexagonal modification is formed (Fig.1). This may be due to the large difference in the parameters of the silicon and zinc oxide lattices, which leads to an inhomogeneous growth of the ZnO film at small thicknesses. Mass spectrometric studies have shown that a tunnel-thin (2 nm) SiO₂ layer is formed on the boundary of the phase separation; the aluminum impurity is homogeneously distributed over the thickness of the film. It should be noted some features of the distribution of SiO₂⁻ ions, namely, the presence of two maxima near the boundary of phase separation, which are due to the peculiarities of the origin and growth of the ZnO film at the initial stages of magnetron sputtering. Studies were carried out on the processes of recrystallization of films after their amorphisation with argon ions and annealings. The sizes of crystallites and their change under the influence of ion irradiation are determined. It was established that ion implantation of structures leads to a change in their deformation state (compression in the direction of film growth - the crystallographic direction c). Moreover, with an increase in the implantation dose and ion energy, deformation increases. Also, the thickness of the films decreases somewhat and their porosity increases.

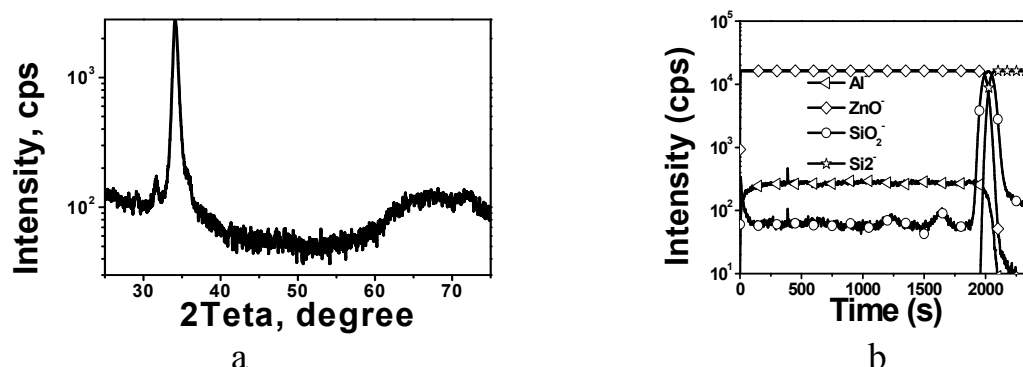


Fig.1. XRD spectra of a deposited ZnO film with a thickness of 65.8 nm (a), (b) is the distribution of impurities along the depth of the ZnO/Si structure

The study of I-V characteristics shows (Fig.2) that the diode structure is formed at film thickness greater than 60 nm. Reducing of the film thickness leads

to a significant increase in reverse currents and shortened diode. ZnO/Si heterostructures have photosensitivity in a wide spectral region, as shown in Fig.2. Voltage-capacitance characteristics were measured at frequencies of 1, 10, 100, and 1000 kHz. Fig.3a shows typical $C(V)$ characteristics of ZnO:Al/Si structures with a thickness of ZnO layer 65.8 nm. A barrier value of 0.66 eV was determined.

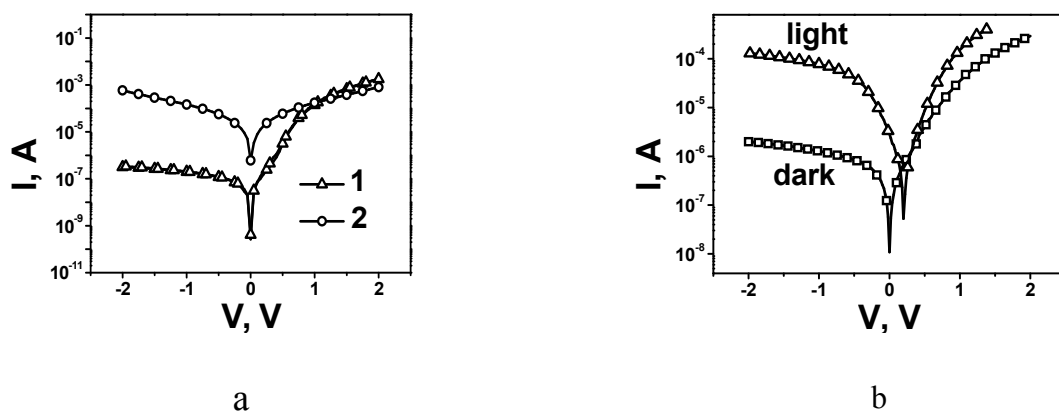


Fig.2. Current-voltage characteristics of ZnO:Al/Si structures for different thicknesses of ZnO film: 1 - 65.8 nm, 2 - 41.6 nm (a); b - characteristics of ITO/ZnO/Si structures before and after illumination with white light

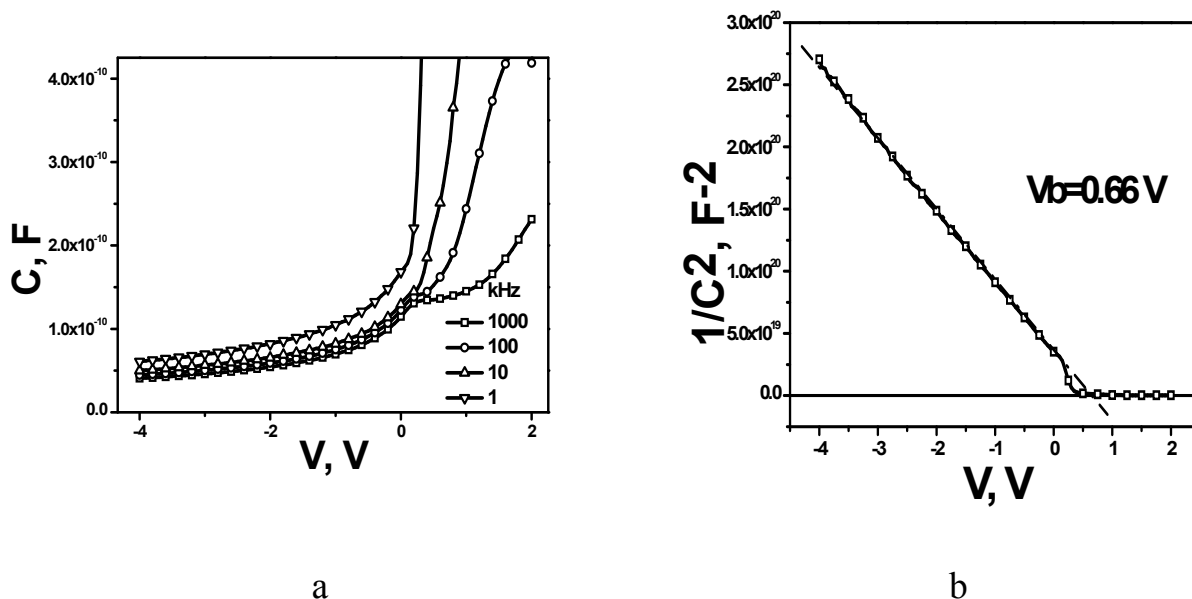


Fig.3. Voltage-capacitance characteristics of the ZnO:Al/Si structures (a) and determination of the potential barrier value (b)

Thus, the paper presents the results of investigations of structural and electro-physical characteristics of ZnO/Si heterostructures at magnetron film deposition from aluminum-doped ZnO target. The processes of film recrystallization are investigated and characteristic temperatures of microcrystal structure restoration and microcrystallite size are determined. It is shown that the ZnO/Si barrier is about 0.66 eV and depends on the annealing temperature of the implanted struc-

tures. Diode structures with a transparent electrode (ITO/ZnO/Si/Al) have a photosensitivity in the wide spectral region of 0.4-2.5 μm . The paper proposes model representations of photosensitivity in UV and IR regions of the spectrum. The mechanisms of photosensitivity in different spectral bands require detailed research.

References

- [1] S.J. Pearton, D.P. Norton, K. Ip, Y.W. Heo, T. Steiner, Recent progress in processing and properties of ZnO // Progress in materials science, v. 50 (3), p. 293-340 (2005).
- [2] Heterojunction with ZnO polycrystalline thin films for optoelectronic devices applications // Microelectronic Engineering, v. 51–52, p. 425-431 (2000).
- [3] A. Janotti, C.G. Van de Walle, Fundamentals of zinc oxide as a semiconductor // Reports on Progress in Physics, v. 72, 126501, 29p. (2009)
- [4] K. Ellmer, A. Bikowski, Intrinsic and extrinsic doping of ZnO and ZnO alloys // Journal of Physics D: Applied Physics, v. 49 (41), 413002, p. 1-33 (2016).

ELECTRICAL CONDUCTIVITY AND HALL MOBILITY OF Bi₂Se₃ THIN FILMS WITH DIFFERENT THICKNESSES

S.I. Menshikova, E.I. Rogacheva

*National Technical University “Kharkiv Polytechnic Institute”
2, Kyrpychova St., 61002, Kharkiv, Ukraine*

Bismuth selenide (Bi₂Se₃) belongs to the V₂VI₃ compounds, which are well known as materials for use in thermoelectricity (TE) [1]. At present the intensive development of nanotechnology stimulates studies of thin film properties. The experimental evidence of an enhancement in the TE figure of merit in low-dimensional V₂VI₃-based structures [2], predicted earlier theoretically [3], attracts attention to their properties in a thin film state. The growing interest in the V₂VI₃ compounds is also associated with the discovery of topological insulator properties in those semiconductors [4].

The properties of a material in thin film and bulk states can differ dramatically. When the thin film thickness d is comparable to the mean free path of charge carriers l or to the de Broglie wavelength λ_F , classical (CSE) or quantum (QSE) size effects, respectively, can be observed. The CSE is connected with the diffuse scattering of charge carriers at the film interfaces, and QSE occurs due to the quantization of energy spectrum of charge carriers. It is important to take into account the manifestation of size effects when predicting the properties of materials in a low-dimensional state.

Bi₂Se₃ thin films can be obtained by thermal evaporation [5,6], chemical deposition [7], molecular beam epitaxy [8], and other methods. Usually Bi₂Se₃ films prepared by thermal evaporation in vacuum have thicknesses $d > 50$ nm [6]. For the Bi₂Se₃ thin films ($d = 50 - 546$ nm) grown by this method onto glass substrates, a sharp increase in the region $d = 50 - 120$ nm and a weak growth in electrical conductivity σ at $d > 120$ nm were observed [6]. The observed rapid increasing of σ with growing d in the region $d < 120$ nm was attributed by the authors of [6] to the presence of a high concentration of structural defects at the initial stages of film growth. The behavior of the $\sigma(d)$ dependence in the region $d > 120$ nm was associated with the manifestation of CSE and described in the framework of the Fuchs-Sondheimer theory (FST). It should be noted that above-mentioned films had low values of the TE parameters, which indicated that the composition of the initial bulk crystal was not reproduced in the film state.

Recently [9], the effect of the film thickness on electrical conductivity of n -Bi₂Se₃ thin films ($d = 25 - 420$ nm) fabricated by thermal evaporation onto glass substrates has been investigated. It was experimentally shown that σ increased with increasing d , and the observed effect was explained as CSE and satisfactorily described using FST for the region $d > 60$ nm.

The goal of the present work is to study the effect of d on charge carrier Hall mobility in Bi₂Se₃ thin films, prepared by thermal evaporation of stoichiometric Bi₂Se₃.

Bi_2Se_3 thin films ($d = 55 - 420$ nm) were prepared by thermal evaporation of stoichiometric Bi_2Se_3 polycrystals in vacuum ($10^{-5} - 10^{-6}$ Pa) with subsequent deposition onto glass substrates at (500 ± 5) K. The condensation rate was $0.1 - 0.15$ nm/s. The condensation rate and d were controlled with the help of a quartz resonator. The resonator was calibrated using a MII-4 interferometer (for $d > 100$ nm) and using small angle X-ray diffraction techniques (for $d < 100$ nm). The latter method made it possible to determine d with an accuracy of ± 0.5 nm. The error of measuring d using a MII-4 interferometer was $\pm 10\%$. The Hall coefficient R_H and σ were measured using a conventional dc method in magnetic field $B = 1$ T. The error of measuring R_H and σ did not exceed 5 %. All measurements were carried out on freshly prepared double Hall cross-shaped samples at room temperature. The Hall mobility μ_H was calculated as $\mu_H = \sigma \cdot R_H$.

In accordance with the results of the measurements of R_H , the Bi_2Se_3 thin films exhibit n -type conductivity in the investigated thickness range. The d -dependence of μ_H in Bi_2Se_3 films is presented in Fig. 1.

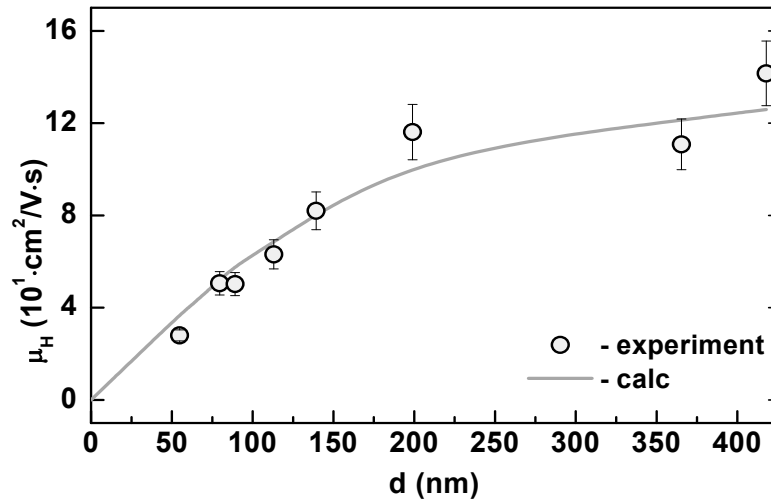


Figure 1 – Room-temperature dependence of charge carrier Hall mobility μ_H on Bi_2Se_3 film thickness d . The solid line denotes the dependence calculated theoretically in the framework of Fuchs-Sondheimer theory

As can be seen in Fig. 1, in the range $d = 55 - 420$ nm μ_H increases with increasing d . The experimentally observed d -dependence of μ_H of Bi_2Se_3 films can be explained as the manifestation of CSE. To confirm this assumption, we used the FST for metals to calculate the $\mu_H(d)$ dependence, taking into account the degeneration of the electron gas in the Bi_2Se_3 thin films. The dependence of charge carrier mobility on the metal plate thickness can be described in the framework of FST as: $\mu_H = \frac{\mu_\infty}{1 + \frac{3}{8}(1-p)\frac{l}{d}}$, where μ_∞ is the mobility in an infinitely thick film

(crystal), p is the specularity parameter (the proportion of carriers elastically scattered by film interfaces). Using the MatLAB 6.5 mathematical package, a program describing the experimental dependence $\mu(d)$ was written. In this program the val-

ues of p and l were varied parameters. The $\mu_H(d)$ dependence for the thickness range $d = 55 - 420$ nm (Fig. 1, solid line) was calculated, and the best agreement with experimental data was observed at $p = 0.44 \pm 0.02$ and $l = (800 \pm 50)$ nm. The calculated values of p and l are close to those obtained when doing an analogous computation of the $\sigma(d)$ dependences in [9].

Thus, the effect of d on the Hall mobility μ_H in Bi_2Se_3 thin films was studied. It was experimentally shown that μ_H increases with increasing d . The observed experimental dependence $\mu_H(d)$ was explained as the manifestation of CSE and satisfactorily described theoretically in the framework of the Fuchs-Sondheimer theory. The values of p and l , obtained at present work, are close to those obtained from the calculation for the $\sigma(d)$ dependence in [9].

References:

1. Rowe D.M. Thermoelectrics Handbook: Macro to nano, CRC Press, Taylor & Francis Group, Boca Raton, London, New York. – 2006.
2. Venkatasubramanian R., Siivola E., Colpitts T., et. al. Thin-film thermoelectric devices with high room-temperature figures of merit // *Nature*. – 2001. – 413. – P. 597-602.
3. Hicks L.D., Dresselhaus M.S. Effect of quantum-well structures on the thermoelectric figure of merit // *Phys. Rev. B Condens Matter*. – 1993. – 47(19). – P. 12727.
4. Hsieh D., Xia Y., Qian D., et al. A tunable topological insulator in the spin helical Dirac transport regime // *Nature*. – 460. – 2009. – P. 1101-1105.
5. Patil V.T., Toda Y.R., Gujarathi D.N. Structural, Transport and Optical Properties of Nanostructured Vacuum Evaporated Bi_2Se_3 Thin Films // *International Journal of Scientific & Engineering Research*. – 2014. – V.5, Issue 4. – P. 1220-1227.
6. Fouad S.S., Morsy A.Y., Talaat H.M., et al. Size and Temperature Dependence of Electrical Transport Properties of Vacuum Evaporated Bi_2Se_3 Films // *Phys. stat. sol. (b)*. – 1994. – V. 183. – P. 149-157.
7. Sun Z., Liufu S., Liu R., et al. A general strategy to bismuth chalcogenide films by chemical vapor transport // *J. Mater. Chem.* – 2011. – 21. – P. 2351-2355.
8. Bansal N., Kim Y.S., Brahlek M., et al. Thickness-Independent Transport Channels in Topological Insulator Bi_2Se_3 Thin Films // *PRL*. – 2012. – 109. – P. 116804.
9. Menshikova S.I., Rogacheva E.I., Sipatov A.Yu., et al. Dependence of electrical conductivity on Bi_2Se_3 thin film thickness // *Functional Materials*. – 2017. – 24. – N. 4. – P. 555-558.

THERMO-INDUCED CHANGES IN THE MECHANICAL CHARACTERISTICS OF MONOCRYSTALLINE SILICON

Yu.V. Pavlovskyy

Ivan Franko Drohobych State Pedagogical University, Drohobych, Ukraine

Semiconductor silicon (Si) today remains the main structural material of modern microelectronic technology. On the basis of silicon, super-large and ultra-fast integrated circuits and new elements of microelectronics are created and improved. Designed devices are widely used in various fields of science, technology and work in space, which necessitates their use in conditions of elevated temperatures. Therefore, today the task of studying thermal influences on mechanical properties of a material is extremely important.

The purpose of this work is to study the changes in the microhardness of industrial silicon, which are due to thermal effects in the range 700-1100°C and their comparison with the results obtained on the same material additionally doped with lead (Pb).

Heat treatment of samples was carried out in a tubular furnace in the air in the temperature range 700-1100°C at an interval of 50°C for 5 hours, followed by cooling in the air. We believe that the airborne annealing does not affect the formation of bulk thermal defects in Si, since the authors [1] have found that the oxidation of the surface of the samples can only lead to the additional generation of interstitial silicon atoms from the boundary between the separation of silicon and silicon matrix in volume crystal only with two-stage heat treatment with re-annealing at temperatures above 1100°C duration of more than 10 hours.

Microhardness was measured by the Vickers method on the DMM-3 device. Calculated by the formula

$$H_{\mu} = \frac{P}{F_{\text{вїд}}} = 2 \frac{P}{d^2} \sin \frac{\alpha}{2} = 1,854 \frac{P}{d^2}, [\text{GPa}],$$

where P – load on the indenter, H; $\alpha = 136^\circ$ – angle at the top of the diamond pyramid; d – the size of the diagonal of the print, averaged over the horizontal and vertical, mm. Used load $P = 1$ N. The load time of the diamond pyramid is like 15 s. At least 20 measurements were taken from each face and the average values of diagonal imprints were calculated.

The study of structural defects and their rearrangement during heat treatment was carried out using a metallographic instrumental microscope of type MIM-10. Before taking the photographs, the samples were mechanically treated (7 μm polishing and 2 μm diamond polishing) and chemically treated in two steps: first in a polishing herb $\text{HNO}_3 : \text{HF} = 4 : 1$ – 5-10 minutes, and then in a selective herb $\text{HF} : \text{CrO}_3 = 1 : 1$ – 20 minutes.

Results of measurement of microhardness (H_{μ}) are presented in Fig. 1: samples Si (curve 1) and Si [Pb] (curve 2). Each point in the graphs is an averaging of

40-50 individual measurements of the H_μ . It is seen that in all cases, with an increase in the temperature from 700 to 900°C, the microhardness increases, and at temperatures $T_{ht} > 900^\circ\text{C}$ – decreases and at $T_{ht} = 1100^\circ\text{C}$ approaches the initial value.

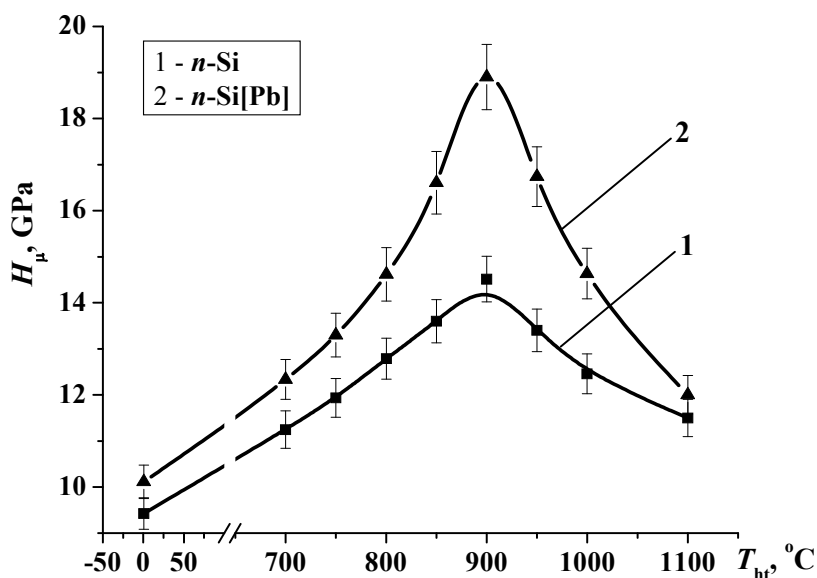


Fig. 1. Dependences of microhardness of samples Si (curve 1) and Si [Pb] (curve 2) on the temperature of their processing

Note that at room temperature, the microhardness of monocrystalline silicon is determined primarily by the mobility of non-equilibrium point defects [2]. Consequently, the growth of microhardness, in our case, can be associated with an increase in the concentration of impurity precipitates, the appearance of which leads to blocking the movement of point defects - the so-called cryodynamic mechanism.

In [3] it is shown that the strengthening of materials contributes to the impurity precipitate as a result of blocking the motion of dislocations. Moreover, the effect is enhanced by decreasing the distance between the precipitates. Therefore, the growth of microhardness at $T_{ht} \leq 900^\circ\text{C}$ can be associated with an increase in the concentration of impurity precipitates in the process of heat treatment. At annealing temperatures above 900°C , packaging defects and extended dislocation loops are formed [4]. As the temperature increases, their concentration increases, and the sizes decrease. The formation of such defects leads to a decrease in internal strain stresses in crystals, which, in turn, can lead to a decrease in microhardness.

The assumptions made are confirmed by the results of the study of structural defects in these crystals. The resulting photos of the etching surfaces are shown in Fig. 2

Since the doping of silicon with lead increases the intensity of the defect's precipitation, the observed features should be strengthened, as observed on both the changes in microhardness and in the patterns of selective etching.

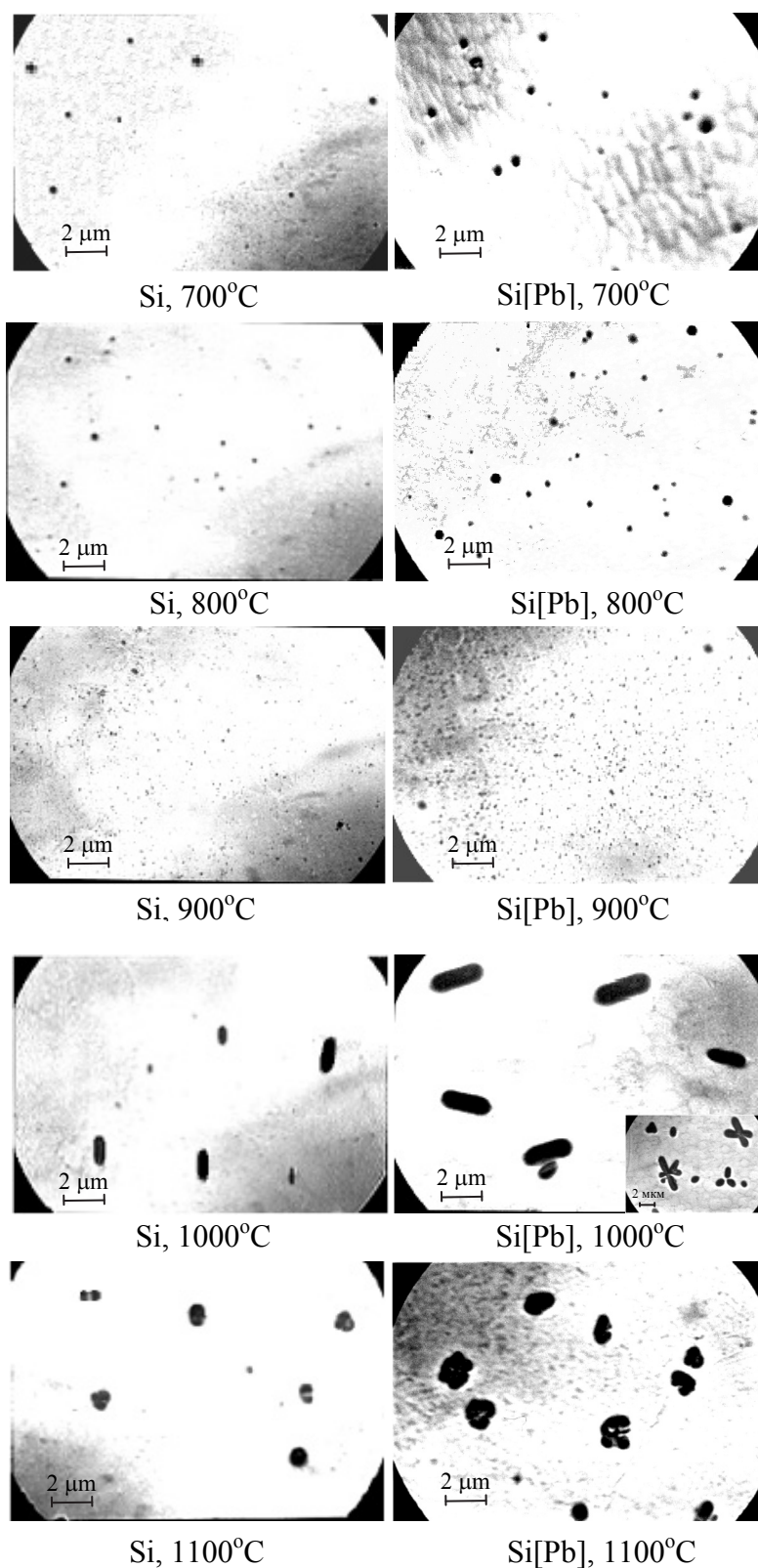


Fig. 2. Photographs of samples etching surfaces

- [1] *Deren Yang, Jia Chu, Jin Xu, Duanlin Que.* // J. Appl. Phys. – 2003. – V.93, №11. – P. 8926-8929.
- [2] *Yu.I. Golovin, A.I. Tyurin, B.Ya. Ferber.* Обратимое изменение микротвердости кристаллов *Si* вызванное малыми дозами облучения электронами // Phil. Mag. A.82, 10, 1857 (2002).

- [3] *Ф. Макклиток, А. Аргон.* Деформация и разрушение материалов. Мир. М. (1970). 443 с.
- [4] *Рейви К.* Дефекты и примеси в полупроводниковом кремнии // М.: Мир, 1984. – С. 475.

FEATURES OF MAGNETIC SUSCEPTIBILITY $\text{Si}_{0,97}\text{Ge}_{0,03}$ WHISKERS MODIFIED OF HIGH-ENERGY IRRADIATION

Yu.V. Pavlovskyy¹, P.G. Lytovchenko², A.V. Lytovchenko³

¹ *Ivan Franko Drohobych State Pedagogical University, Drohobych, Ukraine*

² *Institute of Nuclear Research NAS of Ukraine, Kyiv, Ukraine*

³ *College of Information Technology and Land Management of the National Aviation University, Kyiv, Ukraine*

The influence of irradiation by protons and fast neutrons on the magnetic susceptibility of $\text{Si}_{0,97}\text{Ge}_{0,03}$ whiskers has been investigated.

The irradiation of samples of 6.8 MeV by protons with dose of $1 \cdot 10^{17} \text{ p}^+/\text{cm}^2$ was carried out at 40°C on a cyclotron U-120, and by fast neutrons with dose of $8.6 \cdot 10^{17} \text{ sn}/\text{cm}^2$ at the reactor VVR-10M of the Institute of Nuclear Research of the National Academy of Sciences of Ukraine.

For the experiment, specimens with a diameter of 35-40 microns and a length of 2-3 mm, of the p -type conductivity with a specific electrical resistance $\rho = 0.018 \text{ Ohm}\cdot\text{cm}$ were selected.

Measurement of magnetic susceptibility (MS) was carried out on a modernized installation [1], the principle of which is based on the method of Faraday.

In fig. 1 shows the dependence of MS on the intensity of the magnetic field $\text{Si}_{0,97}\text{Ge}_{0,03}$ Whiskers irradiated by neutrons (curve 2), protons (curve 3) and not irradiated sample (curve 1). It should be noted that irradiation with doses up to $1 \cdot 10^{15} \text{ p}^+/\text{cm}^2$ did not lead to changes in MS.

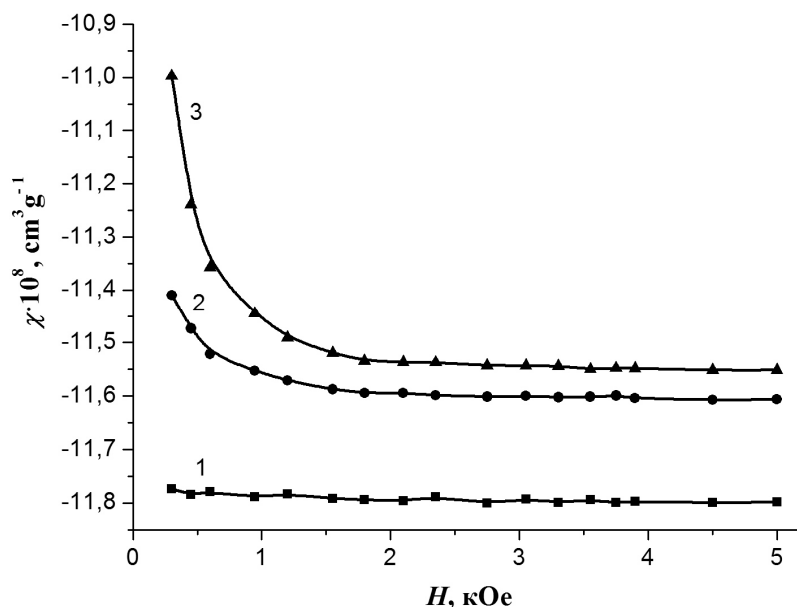


Fig. 1. The dependence of the magnetic susceptibility on the magnetic field intensity of the $\text{Si}_{0,97}\text{Ge}_{0,03}$ Whiskers: 1 – the original sample, 2 – irradiated by fast neutrons at a dose of $8.6 \cdot 10^{17} \text{ sn}/\text{cm}^2$, 3 – irradiated by protons at a dose of $1 \cdot 10^{17} \text{ p}^+/\text{cm}^2$

An increase in the dose of radiation results in the appearance of a paramagnetic component of magnetic susceptibility, which indicates the formation in crystals of dispersed paramagnetic centers between which there is no interaction.

The appearance of the nonlinearities of the dependence of the magnetic susceptibility on the intensity of the magnetic field indicates that, along with the dispersed paramagnetic centers in crystals, some of their clusters (complexes) are formed. They behave like a Langevin paramagnetism of atoms that have a magnetic moment of 10^3 - 10^5 times greater than the magnetic moment of individual atoms. As can be seen from Fig. 1 this feature is more pronounced in the case of proton irradiation.

To analyze the experimental dependences of magnetic susceptibility on the intensity of the magnetic field (Fig. 1, curves 2, 3) we use the theoretical model [2]:

$$\chi(H) = \chi_{ord}(H) + \chi_{par} + \chi_{latt} = N_C M_C L' \left(\frac{M_C H}{kT} \right) + \chi_{par} + \chi_{latt}, \quad (1)$$

where N_C is the concentration of magneto-ordered nanocomplexes, M_C is the magnetic moment of one complex, is derived from the Langevin function, k is Boltzmann's constant, T is temperature, χ_{par} is the paramagnetic component of magnetic susceptibility, χ_{latt} is the susceptibility of the crystalline lattice.

$$M_C = N_0 M_B g \sqrt{s(s+1)},$$

where N_0 is the number of paramagnetic centers in one magnetic complex, M_B is the Bohr magneton, g is the g -factor, s is the spin of the paramagnetic center, of which the complex is composed (we assume $s = 1/2$).

Thus, equation (1) will have a general view

$$\chi(H) = N_C N_0 M_B g \sqrt{s(s+1)} \cdot \left(\frac{N_0 M_B g \sqrt{s(s+1)}}{kT} \cdot \left(1 - \text{cth}^2 \left(\frac{N_0 M_B g \sqrt{s(s+1)}}{kT} \cdot H \right) \right) + \frac{kT}{N_0 M_B g \sqrt{s(s+1)} \cdot H^2} \right) + \chi_{par} + \chi_{latt} \quad (2)$$

The theoretical expression (2) evaluates the corresponding quantities. To do this, we use the Origin 6. To make things easier, we'll introduce the notation:

$$P1 = N_C N_0 M_B g \sqrt{s(s+1)}; \quad P2 = \frac{N_0 M_B g \sqrt{s(s+1)}}{kT};$$

$$P3 = \chi_{par}; \quad P4 = \chi_{latt} = -11,8 \cdot 10^{-8} \text{ cm}^3 \text{g}^{-1}.$$

Then

$$\chi(H) = P1 \cdot \left(P2 \cdot (1 - \text{cth}^2(P2 \cdot H)) + \frac{1}{P2 \cdot H^2} \right) + P3 + P4. \quad (3)$$

With computer computing, we obtained parameters P1, P2 and P3, in which the best agreement between the theoretical function (2) and the experimental points is observed (Fig. 1, curves 2, 3). The obtained parameters P1, P2 and P3 were used to determine the values of N_C , N_0 and, respectively, the formulas:

$$N_C = \frac{P1}{N_0 M_B g \sqrt{s(s+1)}} = \frac{P1}{kT P2};$$

$$N_0 = \frac{kT P2}{M_B g \sqrt{s(s+1)}};$$

$$P3 = \chi_{par},$$

taking into account that:

$$M_B = 9,27 \cdot 10^{-21} \frac{erg}{Gs}; \quad k = 1,387 \cdot 10^{-16} \frac{erg}{grad}.$$

In addition, the functions of distribution of complexes by their size were constructed and the most probable dimensions (D , nm) were determined. The results of calculations are given in Table 1.

Table 1. Calculated parameters

Sample Si _{0,97} Ge _{0,03}	$\chi_{par}, \text{cm}^3 \cdot \text{r}^{-1}$	$N_0, 1/\text{класстер}$	N_C, cm^{-3}	D, nm
source sample	—	—	—	—
$\Phi = 8,6 \cdot 10^{17} \text{ sn/cm}^2$	$0,21 \cdot 10^{-8}$	$9,7 \cdot 10^3$	$1,7 \cdot 10^9$	4
$\Phi = 1 \cdot 10^{17} \text{ p}^+/\text{cm}^2$	$0,3 \cdot 10^{-8}$	$1,6 \cdot 10^4$	$1,9 \cdot 10^9$	6

As is known, with approximately the same dose of irradiation by protons and neutrons in samples, roughly the same number of nanocomplexes is formed. However, at irradiation with protons in the material is formed 2-3 orders of magnitude more point defects interstitial and vacancy type. Since interstitial atoms are more mobile vacancies, the wines quickly go out to the surface, and vacancies, in turn, are combined into multi-station complexes, which, obviously, can exhibit magnetic activity. The given considerations are in good agreement with the experimental results (Fig. 1) and the computed parameters given in Table. 1

1. Пат. 77284 України, МПК(2006) G01R 33/16. Пристрій для вимірювання магнітної сприйнятливості матеріалів / Цмоць В.М. та ін. Заявник і власник Дрогобицький державний педагогічний університет імені І. Франка. – №20041008650; заявл. 25.10.2004; опубл. 15.11.2006, Бюл. № 11.
2. Study and simulation of magnetic susceptibility of Si and Si_{0,95}Ge_{0,05} whiskers / V.M. Tsmots, P.G. Litovchenko, N.T. Pavlovskaya, Yu.V. Pavlovskyy, I.P. Ostrovskyy // Semiconductors. – 2010. – Vol. 44, No. 5. – P. 623–627.

ELECTRICAL CONDUCTIVITY OF NON-STOICHIOMETRIC NiO THIN FILMS

H. P. Parkhomenko^{*}, P. D. Maryanchuk

*Department of Electronics and Energy Engineering
Yuriy Fedkovych Chernivtsi National University
Kotsyubynsky 2, 58012 Chernivtsi, Ukraine
^{*}e-mail: h.parkhomenko@chnu.edu.ua*

Thin metal oxide films are today of great scientific and practical interest. Extensive investigations of transparent conducting layers are stimulated by their application in electronics, optoelectronics, and solar energetics, as well as by the economic efficiency of using thin films instead of bulk crystals.

Most conducting transparent oxides possess n-type conductivity. However, it is known that nickel oxide (NiO) has p-type conductivity and good optical, electrical, and thermoelectric properties, as well as high chemical stability, and is widely used in various devices, especially in the photoelectric technique in the form of transparent layers (windows) for solar cells, antireflection coatings, and photodetectors. Thin NiO films are formed by various chemical and physical methods. The most widespread methods are reactive magnetron sputtering, which makes it possible to control various technological parameters in a wide range and to create high-quality films with desired properties, and spray pyrolysis, which is rather cheap and simple in use [1-4].

NiO thin films were deposited on preliminarily cleaned ceramic glass substrates in a Leybold-Heraeus L560 multipurpose vacuum system by dc reactive magnetron sputtering. Prior to sputtering, the vacuum chamber was evacuated to a residual pressure of 5×10^{-5} mbar.

The target and substrate surfaces were etched for a short time by bombarding argon ions to remove uncontrolled impurities. To deposit NiO films, a nickel target (99.99) (a disk 100 mm in diameter and about 1-mm thick) was placed on a water-cooled magnetron table at a distance of 7 cm from substrates.

The temperature of substrates was controlled by a system of thermocouples in the vacuum chamber so as to be ~ 373 K and ~ 523 K. A mixture of argon and oxygen gases in a required proportion was formed from two independent sources. The partial pressure in the vacuum chamber during the deposition was 4×10^{-3} mbar for argon and 4×10^{-3} mbar for oxygen. The installed magnetron power was 100 W. The deposition duration was 10 min.

The electrical conductivity were investigated in a temperature range of 77–330 K. The samples for the electrical conductivity measurements had four contacts and two current ohmic contacts, which were formed using a mask by reactive magnetron sputtering of nickel at a substrate temperature of ~ 373 K.

Electrical conductivity were measured at the dc current. The total error in the determination of the electrical conductivity was $\sim 2\%$.

Measured values of electrical conductivity are presented in Fig. 1. It is seen that thin films under study possess the semiconductor type of conduction. Carrier concentration at room temperature were $p \approx 4.1 \cdot 10^{19} \text{ cm}^{-3}$ ($T_s \approx 373 \text{ K}$) and $p \approx 4.3 \cdot 10^{18} \text{ cm}^{-3}$ ($T_s \approx 523 \text{ K}$). The origin of the temperature dependence of resistivity may be attributed to either the thermal excitation of holes from shallow acceptor levels or the thermal excitation of mobility. It may be suggested that the resistivity change of highly conductive NiO films obtained in this work results from the thermal excitation of holes from shallow acceptor levels because of high conductivity and high hole concentration [5].

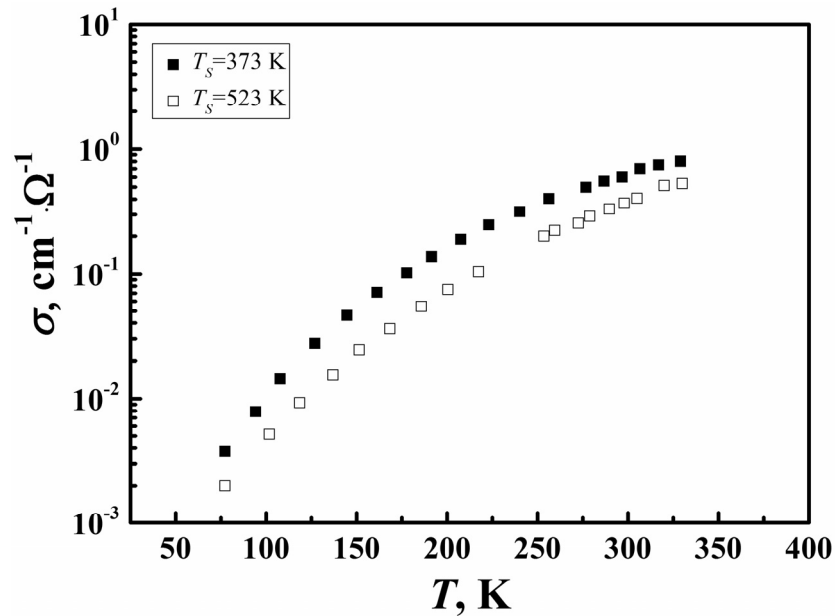


Fig. 1. Temperature dependence of the electrical conductivity of the NiO thin films deposited at different temperatures of the substrate T_s .

Figure 2 shows the dependence of electrical conductivity σ of the NiO thin films on the inverse temperature in a semilogarithmic scale. Two straightlinear segments can be distinguished in it, which indicates the exponential dependence of electrical conductivity.

The activation energy, which was determined from the straightlinear segment of dependence $\ln \sigma = f(10^3/T)$ for the NiO thin film, are 0.37 eV and 0.35 eV for films deposited at substrate temperatures of 373 K and 523 K respectively in the temperature range $77 \text{ K} < T < 150 \text{ K}$ and, possibly, corresponds to the depth of the burial of the working level, which is formed by the lack of nickel and correspondingly to the formation of nickel vacancies. As the temperature increases ($150 \text{ K} < T < 330 \text{ K}$), the activation energy increases and reaches 0.74 eV and 0.95 eV for films deposited at substrate temperatures of 373 K and 523 K respectively.

Since in films the large concentration of holes is due to vacancies of nickel, then the acceptor levels definitely form a subzone near the valence band, which causes two slopes on the logarithmic dependences of the electrical conductivity with different activation energies.

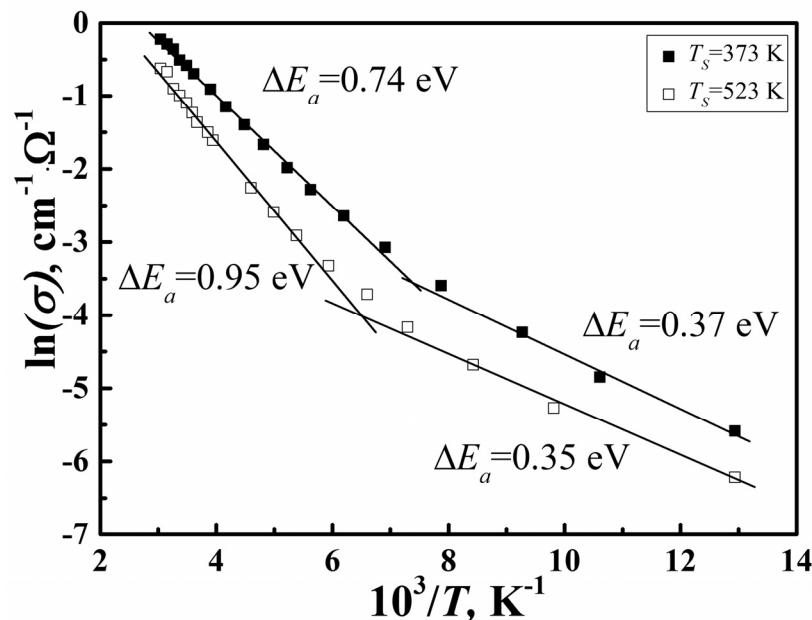


Fig. 2. Dependence of the electrical conductivity of the NiO thin films deposited at different temperatures of the substrate T_s on the inverse temperature in a semilogarithmic scale.

References

1. Guziewicz, M., Grochowski, J., Borysiewicz, M., Kaminska, E., Domagala, J. Z., Rzdokiewicz, W., Piotrowska, A. Electrical and optical properties of NiO films deposited by magnetron sputtering. *Optica Applicata*, (2011). 41(2).
2. Lee, C. Y., Chiang, C. M., Wang, Y. H., Ma, R. H. A self-heating gas sensor with integrated NiO thin-film for formaldehyde detection. *Sensors and Actuators B: Chemical*, (2007). 122(2), 503-510.
3. Chrissanthopoulos, A., Baskoutas, S., Bouropoulos, N., Dracopoulos, V., Pouloupoulos, P., Yannopoulos, S. N. Synthesis and characterization of ZnO/NiO p-n heterojunctions: ZnO nanorods grown on NiO thin film by thermal evaporation. *Photonics and Nanostructures-Fundamentals and Applications*, (2011). 9(2), 132-139.
4. Parkhomenko, H. P., Solovan, M. N., Mostovoi, A. I., Orletskii, I. G., Parfenyuk, O. A., Maryanchuk, P. D. Optical and electrical properties of thin NiO films deposited by reactive magnetron sputtering and spray pyrolysis. *Optics and Spectroscopy*, (2017). 122(6), 944-948.
5. Sato, H., Minami, T., Takata, S., Yamada, T. Transparent conducting p-type NiO thin films prepared by magnetron sputtering. *Thin solid films*, (1993). 236(1-2), 27-31.

INVESTIGATION OF CONDUCTIVITY AND OPTICAL TRANSMISSION PROCESSES IN CdTe:I SINGLE CRYSTALS GROWN FROM VAPOUR PHASE

V.D. Popovych¹, O.A.Parfenjuk², Z.F. Tsybrii (Ivasiv)³

¹*Ivan Franko Drogobych State Pedagogical University, 24 Ivan Franko str.,
82100 Drogobych, Ukraine*

²*Yurij Fed'kovych National University, 2 Kotsyubynsky str., 274012 Chernivtsi,
Ukraine*

³*V.Ye. Lashkaryov Institute of Semiconductor Physics of NAS of Ukraine,
45 pr. Nauki, 03028 Kyiv, Ukraine*

High-resistivity cadmium telluride is one of the main materials for fabrication of uncooled γ -ray detectors of spectrometric quality. Usually, doping of the crystals of this compound with a chlorine donor is used in order to achieve a semi-insulating state. Such doping leads to an exact compensation of the dominant CdTe native acceptor defects, mostly cadmium vacancies V_{Cd} and so-called A-centers (complexes of V_{Cd} and shallow donor). At the same time, the information about doping with other halogens, namely iodine, is very limited.

Investigated CdTe: I single crystals were grown by the modified physical vapour transport method at 950 – 970° C from pre-synthesized charge with initial iodine concentration $N_I = 10^{18}$ and 10^{19} cm^{-3} , obtained by alloying of the components (elemental Cd, Te of 6N-grade purity and dehydrated CdI_2 salt) in a vacuum [1]. Investigations of the electric properties were carried out by measuring the temperature dependences of the specific resistance ρ in the temperature interval of 295 – 430 K by four-probe technique. The type of conductivity was determined by the thermal probe. Optical characterization was done by measuring of infra-red (IR) transmission in the 2 – 25 μm range at room temperature (RT).

Unlike the case of CdTe: Cl [1] single crystals grown by the same method, the conductivity of the investigated CdTe: I samples is of electron type and their resistivities are much lower, being in the range $\rho = (2 - 3) \times 10^4 \Omega \cdot \text{cm}$ for a higher doped and $\rho = (1 - 5) \times 10^6 \Omega \cdot \text{cm}$ for a less doped material. Also, the conductivity of the material with $N_I = 10^{18} \text{ cm}^{-3}$ is controlled by deeper donor levels. It can be concluded that the range of exact compensation of the native acceptor defects with iodine in the CdTe matrix is narrower than that with chlorine, and its addition at a high concentration leads to overcompensation of the material. This conclusion is in coincidence with the results of the theoretical study [2], in which the compensation processes in CdTe: I have been simulated using the method of quasi-chemical reactions. The authors of this paper have found that, in addition to V_{Cd} and A-centers, the presence of significant concentrations of DX-centers is necessary to explain the decrease of CdTe: I resistivity. DX-centers are formed when doping atom shifts from the lattice to the interstitial site with subsequent capture of an electron, which causes significant distortion of the lattice in the vicinity of such a defect. The probability of DX-centers formation is growing with the decreasing of the ion radius of

the doping impurity, which is known to be lower for I than for Cl. The formation of DX centers leads to the self-compensation of shallow donors according to the reaction:



where d is a shallow donor dopant (iodine in our case).

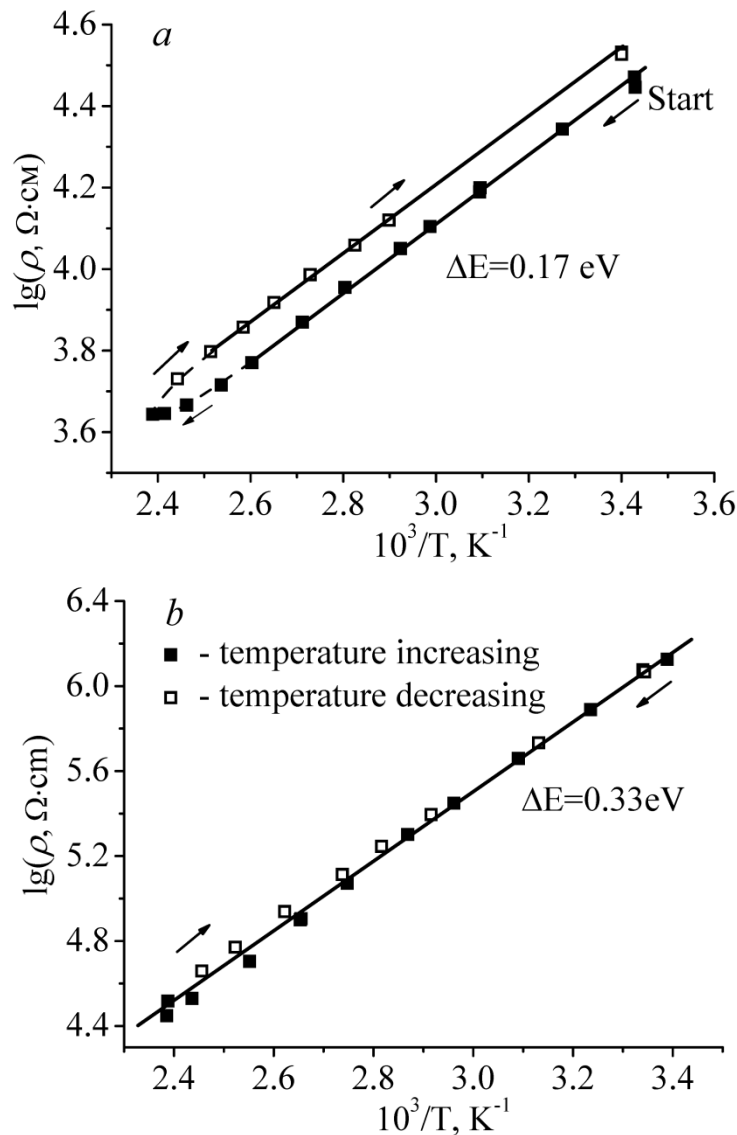


Fig. 1. Temperature dependences of electrical resistivity for the samples with $N_I = 10^{18} \text{ cm}^{-3}$ (a) and $N_I = 10^{19} \text{ cm}^{-3}$ (b). The arrows indicate the direction of the measurements (heating or cooling)

Similar to the case of Cl-doped crystals [3], the thermal instability of the investigated CdTe: I samples due to their low-temperature short-term annealing directly in the measurement process was detected. For the most samples an irreversible resistance increasing was observed as a result of the heating-cooling cycle (Fig. 1a). The activation energy of the process was increased in some samples, while it remained unchanged in the others. The observed annealing indicates that the defect system was at non-equilibrium thermodynamic state before the start of the measurements. The defects became more mobile with the temperature increasing and were incorporated into the host lattice, resulting in the decrease of its total energy.

However, some of the samples were stable in the temperature range under investigation (Fig. 1b).

An increase of IR-transmission in consequence of the annealing process, which have been detected for the highest doped CdTe:Cl crystals, as well as the dependence of the transmission curves on the doping level, were not observed for the investigated CdTe:I samples. For both iodine concentrations, IR-transmission level in the whole lengthwaves range was practically at a theoretical limit for CdTe compound.

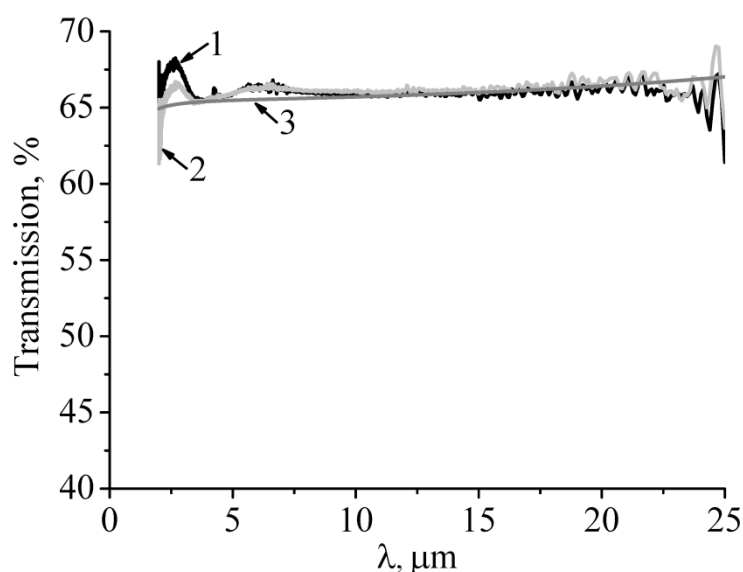


Fig. 2. The mid IR-transmission RT spectra of CdTe:I samples:
1 – $N_I = 10^{18} \text{ cm}^{-3}$; 2 – $N_I = 10^{19} \text{ cm}^{-3}$; 3 – theoretical limit for CdTe.

In summary, it can be concluded from the results of preliminary studies that more precise compensation and higher thermal stability during crystal growth should be reached for obtaining high-resistive CdTe: I, suitable for the production of high-energy radiation detectors.

References

- [1] V.D. Popovych, I.S. Virt, F.F. Sizov, V.V. Tetyorkin, Z.F. Tsybrii (Ivasiv), L.O. Darchuk, O.A. Parfenjuk, M.I. Ilashchuk, J. Cryst. Growth. 308 (2007) 63.
- [2] U.M. Pysklynets, V.V. Prokopiv, I.V. Gorichok, N.D. Freik, Phys. Chem. Solid State 11 (2010) 401.
- [3] V.D. Popovych, F.F. Sizov, O.A. Parfenjuk, Z.F. Tsybrii (Ivasiv), Semicond. Sci. Techn. 25 (2010) 0305001.

COMPOSITE THERMOELECTRIC MATERIALS BASED ON LEAD AND CADMIUM TELLURIDES

**V.V. Prokopiv¹, I.V. Horichok¹, Y.V. Ogorodnik², O.M. Matkivsky¹,
L.V. Turovska³**

¹*Vasyl Stefanyk Precarpathian National University, Ukraine*

²*Radiation Monitoring Devices, Inc., USA*

³*Ivano-Frankivsk National Medical University, Ukraine*

Lead Telluride is a semiconductor material, which is used to create on its basis thermocouples working in the temperature range 300-500 °C. The main disadvantage of using PbTe is the relatively low coefficient of efficiency of devices based on it (< 10 %). Therefore, finding ways to increase this value is an urgent task.

Obtaining thermoelectric samples by powder pressing method, which ensures the formation of a large area of grain boundaries, is promising. In addition to scattering of phonons, such boundaries can filter current carriers that pass electrons (holes) with "high" energies only, which should increase the coefficient of thermo-EMF of the material. It should be noted that for the pressed samples an important factor is the size of the powder fractions, which are used for compaction. The use of an additional nanodispersed component of another material can provide the creation of an additional scattering surface for phonons, and in the case of the use of metallic nanoparticles, create high quality conductive contacts for the electrons between the grains.

In present paper, mechanical mixtures of microdispersed PbTe and CdTe have been investigated. The main factor in the choice of cadmium telluride is its rather low thermal conductivity.

Synthesis of PbTe was carried out in vacuumed quartz ampoules [1]. The resulting ingots were crushed, pressed under pressure (1.0-2.0) GPa and annealed at temperatures (200-500) °C. In the case of mechanical mixtures, the base material powder was mixed with the microdispersed powder of CdTe, particle size of which was (32-50) μm. The phase composition and structure of the synthesized ingots and samples were investigated by X-ray diffraction methods on the automatic diffractometer STOE STADI P. Surface morphology was studied using an optical microscope NEXUS 400A. Hall measurements were carried out in constant magnetic and electric fields using a four-zone method. The value of the coefficient of thermo-EMF was calculated by measuring the voltage at the ends of the sample when the temperature gradient was ≈5 °C. The specific electrical conductivity σ was determined by measuring the voltage drop on the sample at the passage of alternating current. The coefficient of thermal conductivity k was determined by the method of radial heat flux [1].

Synthesis of cadmium telluride for obtaining the mechanical mixtures was carried out in the sealed quartz ampoules. Additionally, in contradistinction to the conditions of the synthesis of IV-VI compounds, the ampoules were graphitized by

acetone pyrolysis. The temperature mode of synthesis consisted of several stages of heating and exposing, and the direct synthesis was carried out at a temperature of 1120 °C. The resulting ingots were granulated in a ball mill.

The chemical analysis of CdTe ingots has shown a low content of uncontrolled impurities. Composition and technological parameters of preparation of PbTe-CdTe samples are given in Table. Optimum compression pressure for these compositions is 1.5 GPa, exposure time under pressure is 15 minutes, the size of the fraction of the base material is (0.05-0.5) mm. All samples were annealed at 500 °C for 15 minutes. Unlike the mechanical powder mixtures studied in [2], for these samples the used additional component was not nanometer but micrometer size in order to increase the volume of the additional phase, and not the number of additional boundaries, as in the previous cases.

Table. Composition of PbTe-CdTe composite materials (ingot XXXIX)

Number of sample	Composition
1a	PbTe
1b	PbTe
2a	PbTe + 1 mass % CdTe (32-50) μm
2b	PbTe + 1 mass % CdTe (32-50) μm
2c	PbTe + 1 mass % CdTe (32-50) μm

The lattice parameter of homogeneous PbTe is 6.4583(2) Å, but for the pressed and annealed composite sample – 6.4566(2) Å. Such an effect may be due to the influence of technological factors (pressing, annealing) [1] and the chemical interaction between the base and additional materials.

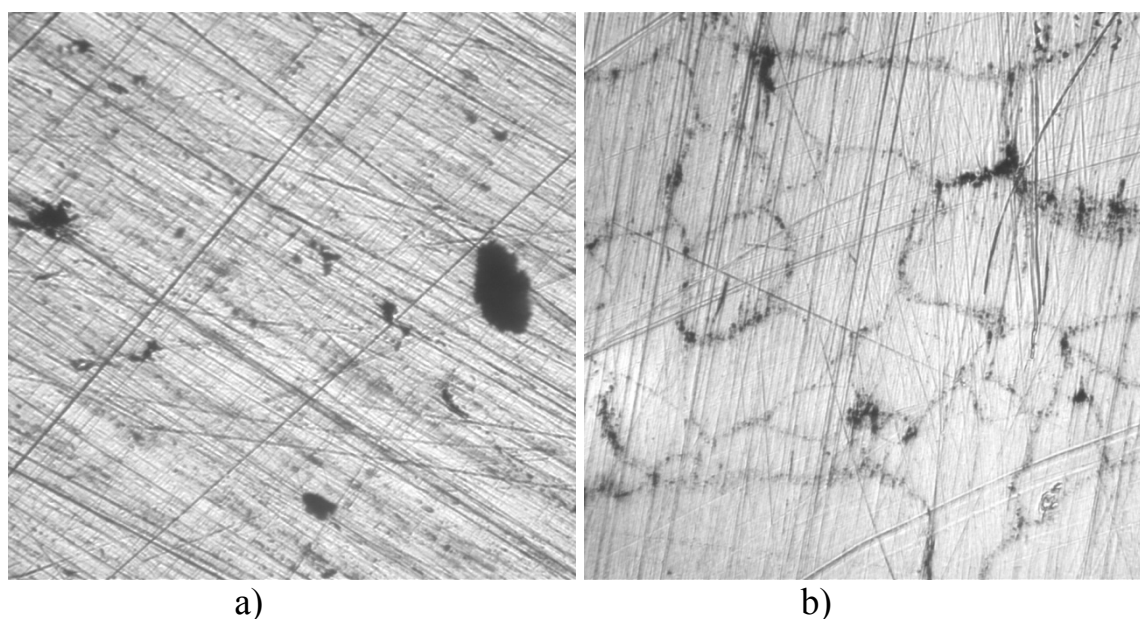


Fig. 1. Surface structure of pressed at 1.5 GPa and annealed at 500 °C sample of pure PbTe (a) and composite sample PbTe-CdTe (b) (1 mass % CdTe) (the size of the photo is 460x460 μm^2).

Surface structure of pressed and annealed at 500 °C PbTe-CdTe samples was more porous than in the case of pure PbTe, but less porous than in the case of composites investigated in [2]. The hardness is $H_V = 312$ MPa, which does not differ significantly from the pure PbTe – $H_V = 297$ MPa (pressing pressure was 1.5 GPa, annealing temperature was 500 °C) unlike composites studied in [2].

Based on the Hall effect study, it has been found that when adding CdTe (1 mass % CdTe) the temperature dependence of the carrier concentration is decreasing (Fig. 2), however, the change in the value of n_H in the measured temperature range is not significant and does not exceed the measurement error.

Decrease in electrical conductivity of the samples and the invariability of the thermo-EMF coefficient when adding CdTe seems to be logical: the additional component reduces the total area of the conducting channels, in turn it practically does not conduct the current, and CdTe has no effect on the kinetic parameters of the carriers passing between the grains of the base material. In logarithmic scale, the dependence $\sigma(T)$ is satisfactorily approximated by a straight line according to the equation $\lg(\sigma) = A - 2.5 \lg(T)$. The coefficient 2.5 clearly indicates the dominance of the mechanism of scattering of carriers on acoustic phonons. The deviation from the linear dependence for the points obtained at the maximum temperature, most likely, indicates the beginning of the region of its own conductivity. It is important to note that the presence of impurity does not change the dominant scattering mechanism. In particular, there is no appreciable effect of grain boundaries in the investigated materials.

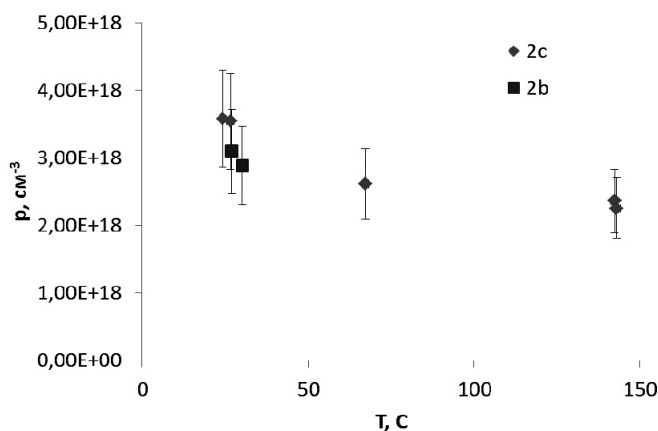


Fig. 2. Temperature dependences of carrier concentration in composite materials PbTe-CdTe

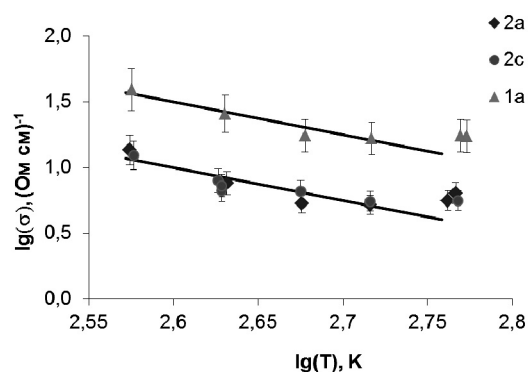


Fig. 3. Dependence of specific electrical conductivity on temperature for PbTe and PbTe (1 mass % CdTe)

In contrast to PbTe-ZnO (TiO₂) nanocomposites studied in [2], for PbTe-CdTe samples, a certain decrease of the coefficient of thermal conductivity is recorded (Fig. 4). That is, on the one hand, the electrical conductivity of the samples and their thermal conductivity decrease as a result of the addition of the microdispersed CdTe, and on the other hand, scattering in the composite materials is determined only by the interaction of current carriers with acoustic phonons. Given the above, we can assume that responsibility for reducing σ is not due to additional

grain boundaries, but decrease in the effective cross section of the sample, by which the current transfer is carried out, since the slope of the curve $\sigma(T)$ in logarithmic scale for pure and composite samples is not changed. In the case of phonons, it is most likely that the additional boundaries are the main factor in reducing the intensity of their scattering. Comparing the obtained data with the results in [2], it can be said that no less important factor is thermal conductivity of the additional component. Precisely due to the fact that the thermal conductivity of ZnO or TiO₂ is much higher than the thermal conductivity of the base material, in [2], reducing the value of k was not achieved.

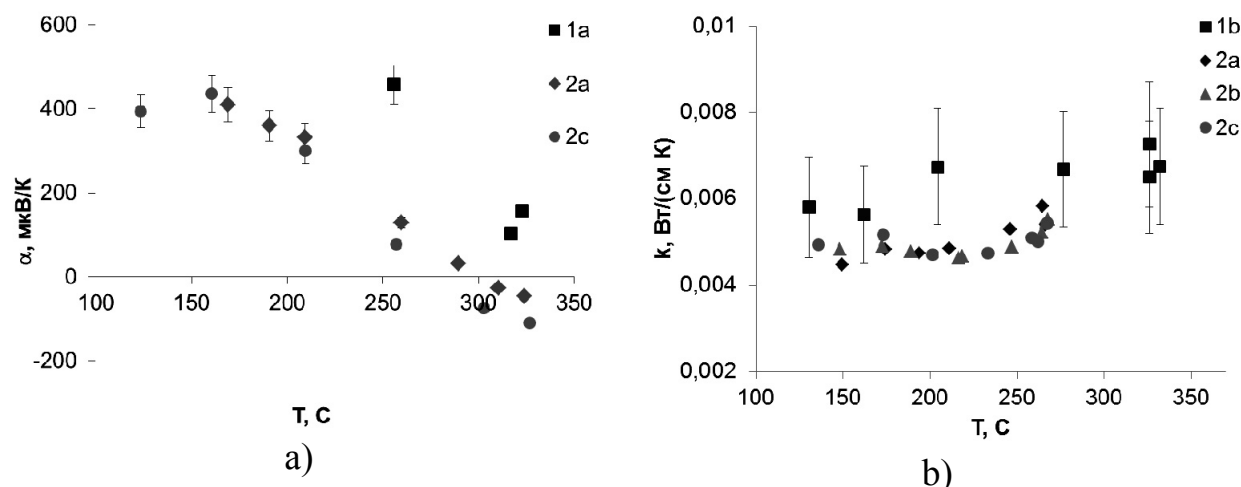


Fig. 4. Temperature dependences of coefficients of thermo-EMF (a) and thermal conductivity (b) for PbTe-CdTe composite samples with 1 mass % content of the microdispersed component of CdTe.

- [1] I.B. Горічок, І.М. Ліщинський, С.І. Мудрий, О.С. Оберемок, Т.О. Семко, І.М. Хацевич, О.М. Матківський, Г.Д. Матеїк, Р.О. Дзумедзей. Технологічні аспекти отримання термоелектричного PbTe // SEMST. – 2017. – Т.14, № 3. – сс. 53-64.
- [2] I.V. Horichok, M.O. Galushchak, O.M. Matkivskyj, I.P. Yaremij, R.Ya. Yavorskyj, V.S. Blahodyr, O.I. Varunkiv, T.O. Parashchuk. Thermoelectric Properties of Nanostructured Materials Based on Lead Telluride // JNEP. – 2017. – V.9, N.5. – pp. 05022-1 - 05022-7.

As₂S₃ doped with Mn or Ag: Raman and XRD study
Revutska L.O.^{a,1}, Shportko K.V.^b, A.V. Stronski^b, Popovych M.V.^a,
A.Yo. Gudymenko^b, O.P. Paiuk^b, Ts.A. Kryskov^c.

^a*National Technical University of Ukraine “Ihor Sikorski KPI”, Kyiv, Ukraine.*

^b*V. Lashkaryov Institute of Semiconductor Physics NAS of Ukraine, Kyiv, Ukraine.*

^c*Kamianets-Podilsky National University, Kamianets-Podilsky, Ukraine.*

¹*e-mail: liubov.revutska@gmail.com*

Abstract

This work is devoted to the study of structural characteristics of the amorphous bulk As₂S₃ glasses doped with Ag (concentration 10 and 15 wt.%) or Mn (1 and 2 wt.%). Structural studies were carried out using X-ray diffraction technique and Raman spectroscopy. The radial distribution functions of doped and undoped bulk glasses were obtained and analyzed. Our Raman data shows that studied chalcogenides are nanostructurized materials.

Introduction

Amorphous chalcogenides attract much attention due to their properties. Chalcogenide glasses (CG) are widely used in versatile technological applications such as infrared optical elements, acoustical and optical and all-optical switching devices, holography recording media etc. Chalcogenide glasses and films serve as a base of their numerous applications due to their unique properties such as, transparency in the IR region, quasi-stability, photoinduced change of properties, ion-conductivity of doped chalcogenide glasses and films, etc. Information on the short-range order structure of chalcogenide glasses is particularly valuable for establishing useful correlations between their structural and macroscopic properties.

Experimental

The As₂S₃ glasses with manganese concentration from 0 up to 2 wt. % and As₂S₃ glasses with silver concentration from 0 up to 15 wt. % were prepared by standard melt-quenching technique using constituent elements of 6N purity in vacuum-sealed silica ampoules. X-ray diffraction measurements (XRD) were carried out using ARL X'tra (Thermo scientific) setup. Cu K λ radiation ($\lambda=0.154$ nm) was used. Room temperature Raman spectra were recorded using Fourier spectrophotometer Bruker IFS-55 Equinox with FRA-106 attachment (with resolution of 1 cm⁻¹). Nd:YAG laser light with 1.06 μ m wavelength was used for excitation.

Results and discussion

XRD

The structure of arsenic chalcogenide glasses has been studied previously by [1,2]. The experimental XRD profiles (Fig.1, 2) from glasses of different compositions were similar but showed a systematic variation with composition. Diffraction profiles confirm the amorphous nature of the chalcogenide glass, which is a disor-

dered system without long-range order and three-dimensional periodicity. However, there is short-range order in which the atoms around any system of atoms can be described by radial distribution function of the atoms (RDF) [3].

In Fig.1 and Fig. 2 the calculated RDF profiles for As_2S_3 samples doped with Mn concentration 0%, 1% and 2 wt.% and Ag concentration 0%, 10% and 15 wt.% are shown. The location of the peaks indicates prominent interatomic distances and the area under peaks, after correction for differences in scattering factors, gives a measure of the average coordination number. As one can see, the addition of silver does not significantly affect the structure. The position of the first peak corresponds to the value of 2.29 Å, position of the second peak – 3.44 Å for glasses doped on Mn and 3.48 Å for glasses doped on Ag. The results are in agreement with the results of previous researchers on the structure of the As_2S_3 glasses using X-ray analysis [1].

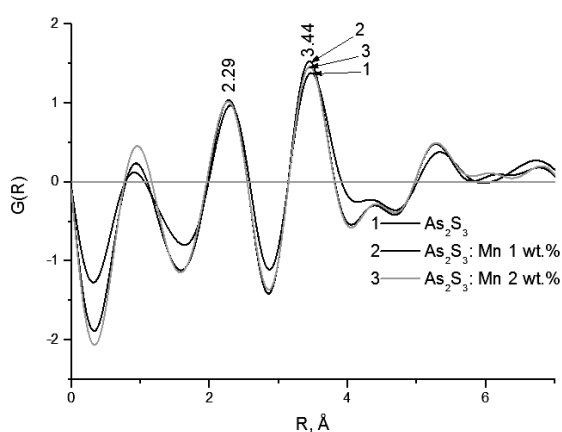


Fig.1. The RDF profiles for Mn doped As_2S_3 with Mn concentration (0, 1 and 2 wt.%).

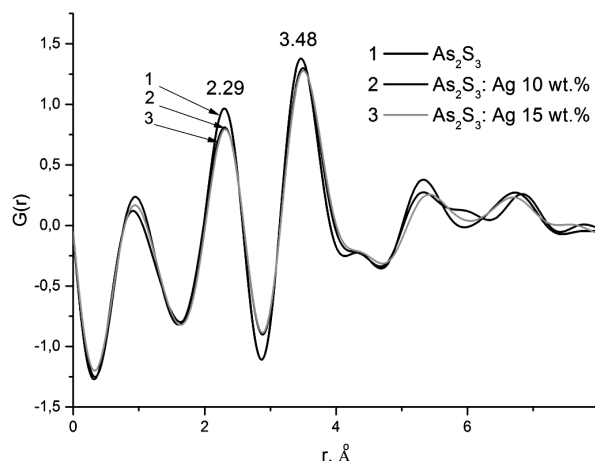


Fig.2. The RDF profiles for Ag doped As_2S_3 with Ag concentration (0, 10 and 15 wt.%).

Raman spectra

The structural changes in As–S glasses doped with transitional metals were obtained from Fourier Raman spectra (Fig. 3, 4). Introduction of such dopants leads to the increase of concentration of non-stoichiometric molecular fragments. Introduction of manganese leads to the increase of intensity of bands at 192, 227, 236, 365 cm^{-1} that correspond to the vibrations of non-stoichiometric molecular fragments As_4S_4 . Intensity of band near 496 cm^{-1} ,

which is characteristic for vibrations of S–S bonds is decreasing. Bands, that can be connected with the creation of new sulphur containing structural units, similar to MnS molecular fragments appear in 130–190 cm^{-1} range. The main feature of Raman spectra under the introduction of manganese into As_2S_3 glass matrix is in the change of relative concentration of the main and non-stoichiometric structural elements typical for As_2S_3 glasses [2].

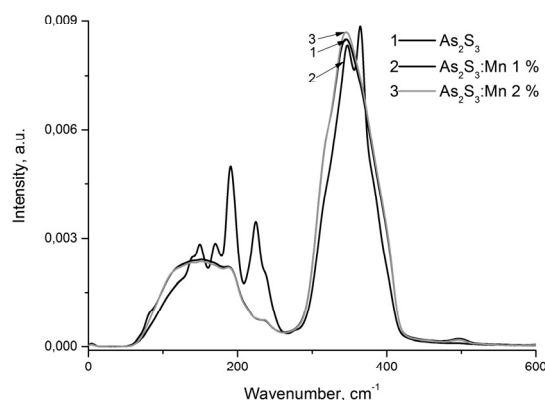


Fig.3. Raman spectra of As_2S_3 glasses with Mn concentration (0, 1 and 2 wt.%).

From obtained HH and HV-polarized Raman spectra (Fig. 4) of doped $\text{As}_2\text{S}_3\text{:Ag}$ it can be seen that structure changes. The Raman spectra of these ChGs are dominated by a strong band at 340 cm^{-1} attributed to the symmetric As-(S)-As stretching vibrations in $\text{AsS}_{3/2}$ pyramids [4]. Besides this there is a strong band at 340 cm^{-1} , there are additional features (shoulders) at 314 cm^{-1} that can be assigned to the asymmetric stretching modes of $\text{AsS}_{3/2}$ pyramids. Weak bands located at 187, 221, 231 cm^{-1} correspond to the presence of the non-stoichiometric molecular fragments of As_4S_4 nanophase. Doping of As_2S_3 glass with Ag causes a slight increase of the bands' intensity located at 187, 221, 231 cm^{-1} . The presence of excess sulfur is indicated by the weak band at 475 cm^{-1} , which is characteristic for the vibrations of S-S bonds, and it is increased with the Ag introduction. Obtained Raman spectra were analyzed in software CoRa [5]. Deconvolution of Raman spectra was performed for analysis of their compositional dependencies.

The main effect that is observed at introduction of silver into nanostructured As_2S_3 glass is the change of the relative concentration of the main and non-stoichiometric molecular structural units that are characteristic for As_2S_3 glasses.

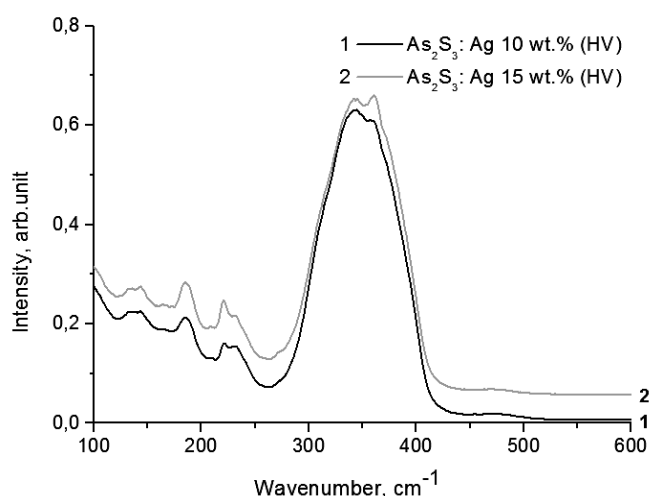


Fig.4. Raman spectra of As_2S_3 glasses with Ag concentration (0, 10 and 15 wt.%) (HV polarization).

Conclusions

In this paper the results of X-ray diffraction studies for characterization of As_2S_3 glasses are presented. It was shown that Ag doping influences the structural properties of studied chalcogenide glasses, the addition of manganese does not significantly affect the structure. This can be used for the creation of nanocomposites on the base of chalcogenide glasses with new properties, optimization of sensitivity, stability improving of registering media on their base, etc.

References

- [1] I. Kaban, P. Jóvári, T. Wágner, M. Barto, M. Frumar, B. Beuneu, W. Hoyer, N. Mattern, J. Eckert, Structural study of AsS_2 – Ag glasses over a wide concentration range, 357 (2011) 3430–3434.
doi:10.1016/j.jnoncrsol.2011.06.015.
- [2] A. Stronski, O. Paiuk, A. Gudymenko, V. Klad, P. Oleksenko, N. Vuichyk, M. Vlcek, Effect of doping by transitional elements on properties of chalcogenide glasses, *Ceram. Int.* 41 (2015) 7543–7548.
- [3] T. Petkova, P. Petkov, S. Vassilev, Y. Nedeva, Structural investigations of ternary chalcogenide glasses, *Surf. Interface Anal.* 36 (2004) 880–883.
doi:10.1002/sia.1791.
- [4] K. Ogusu, S. Maeda, M. Kitao, H. Li, M. Minakata, Optical and structural properties of Ag(Cu)- As_2Se_3 chalcogenide films prepared by a photodoping, *J. Non. Cryst. Solids.* 347 (2004) 159–165.
- [5] H. Shportko, K. Ruekamp, R. Klym, CoRa: An Innovative Software for Raman Spectroscopy, *J. NANO- Electron. Phys.* 7 (2015) 1–4.

ELECTRON SPECTRUM ON THE DYNAMICALLY DEFORMED ADSORBED SURFACE OF A SEMICONDUCTOR WITH A ZINC BLENDE STRUCTURE

M.Ya. Seneta, R.M. Peleshchak, Yu.M. Hal', Ya.M. Voronyak, M.G. Stan'ko

*Drohobych Ivan Franko State Pedagogical University, 24 I.Franko Str., 82100
Drohobych, Ukraine*

The dispersion relations for the electron spectrum on a dynamically deformed adsorbed surface of the semiconductor with the Zinc blende structure are received. It was shown that the dependence of the electrons concentration change on the concentration of adsorbed atoms on the surface has a nonmonotonous character, determined by the height of the inequality of the surface of semiconductor.

Keywords: surface electron states, electron spectrum, adsorbed atoms, acoustic quasi-Rayleigh wave.

1. Introduction

The creation of a new class of micro and nanoelectronic devices with controlled parameters needs the research of electron spectrum on the dynamically deformed adsorbed surface of semiconductors. Such dynamic deformation on the adsorbed surface of semiconductor can be formed by the quasi-Rayleigh acoustic wave [1]. Interaction between the quasi-Rayleigh acoustic wave and adatoms renormalizes the electron spectrum due to deformation potential [2]. Changing technologically the concentration of adsorbed atoms, it is possible to change the frequency of surface acoustic wave (SAW) and the electronic structure of subsurface layer. Such correlation between the adsorbed atoms concentration, the frequency of surface acoustic wave and the electron structure of subsurface layer can be used in practice for the change of coefficients of electromagnetic waves reflection from the interface of media and for the change of dispersion law of plasma oscillations [3].

The purpose of this work is the investigation of the influence of the adsorbed atoms concentration on the spectrum of surface electron states and the distribution of electron density on a dynamically deformed adsorbed surface of a semiconductor with the Zinc blende structure.

2. Formulation of the problem and the main results

We consider the subsurface layer of a semiconductor in the molecular beam epitaxy or implantation process [4]. At the action of atoms flow, the atoms are adsorbed with an average concentration N_{0d} . Due to the deformation potential and the local renormalization of the surface energy, the adatoms and the deformation field of the surface acoustic quasi-Rayleigh wave deform inhomogeneously the subsurface layer. In turn, this self-consistent deformation through the deformation potential redistributes adsorbed atoms along the surface. The influence of adsorbed atoms is reduced to a change of boundary conditions for a stress

tensor σ_{ij} on $z = 0$ surface. The layer, defect-enriched by adatoms, can be considered as a film of a thickness, ρ density and Young's modulus E . It is connected rigidly with substrate – the other semiconductor part with elastic parameters ρ_s and E_s . The connecting plane of film and substrate $z = a$ is parallel to the surface (100). The axis z is directed into the single crystal depth, the axes x and y are directed along two orthogonal crystallographic directions of type [100].

A surface acoustic quasi-Rayleigh wave, extending in x axis direction with $\omega'(\vec{q}, N_{0d})$ frequency, forms the dynamic deformation and interacts with adatoms. The deformed surface form along the x axis depending on time can be described by the following function [10]:

$$z_0(x, t) = \tilde{\zeta}(N_{0d}) \cos(qx - \omega'(q, N_{0d}) \cdot t), \quad (1)$$

where $q = 2\pi / L_x$; L_x is period of roughness (length of acoustic wave) along the x axis; N_{0d} is a the spatially homogeneous component of adatoms concentratoin.

The dispersion law $\omega'(q, N_{0d}) = Re(\omega)$ of quasi-Rayleigh wave and the width $\omega''(q, N_{0d}) = Im(\omega)$ of acoustic phonon mode are determined in the work [5].

The height of the roughness $\tilde{\zeta}(N_{0d}) = |u_z^l(0)| + |u_z^t(0)|$, where $\vec{u}^l(\vec{r}, t)$, $\vec{u}^t(\vec{r}, t)$ are the normal components of the displacement vector of longitudinal and transversal waves, respectively, on the plane $z = 0$ [2]. (4)

The components $u_z^l(0)$, $u_z^t(0)$ of the displacement vector of the medium points are founded from the equation solution [5]:

$$\frac{\partial^2 \vec{u}}{\partial t^2} = c_t^2 \Delta_{\vec{r}} \vec{u} + (c_l^2 - c_t^2) \overrightarrow{\text{grad}}(\text{div} \vec{u}). \quad (2)$$

The electron spectrum on the rough boundary of the semiconductor with the Zinc blende structure are founded from the non-stationary Schrodinger equation [6]

$$i\hbar \frac{\partial \psi(x, z, t)}{\partial t} = -\frac{\hbar^2}{2m^*} \left(\frac{\partial^2 \psi}{\partial x^2} + \frac{\partial^2 \psi}{\partial z^2} \right) + V_0 e^{-k_l z} e^{ikx - i\omega t} \psi(x, z, t) \quad (3)$$

with deformation potential formed by the surface acoustic quasi-Rayleigh wave

and adsorbed atoms; where $V_0 = -\frac{|\lambda| \tilde{\zeta}(N_{0d}) q^2 (2 - \xi_0) c_l^2}{k_l c_l^2}$; m^* is the effective electron mass; λ is the constant of deformation potential; $1/k_l$ is the depth of sound penetration in semiconductor, ξ_0 is a quantity depended on the ratio between the longitudinal c_l and transversal c_t sound velocity.

We assume that the motion of conduction electrons is bounded by an uneven wall which is an infinitely high potential barrier. We use the method of successive approximations for a small parameter $q\tilde{\zeta}(N_{0d}) \ll 1$ regarding amplitudes with $n=1; 0; -1$, where $\tilde{\zeta}(N_{0d}) = \tilde{\zeta}(0) + \delta\tilde{\zeta}(N_{0d})$, $\tilde{\zeta}(0)$ is the height of the roughnesses of the surface, created only by a surface acoustic wave.

The roughness of the two media division is the cause of the surface electronic states appearance. The wave function of the surface electronic states is determined by the following expression [7]

$$\psi_k = A_0 e^{-|\delta k_0|z + i|k_x x - \omega_k t|}, \quad (4)$$

where k_x is the component of the electron wave vector;

$k_0(\tilde{\zeta}(N_{0d})) = k_0(\tilde{\zeta}(0)) + \delta k_0(\tilde{\zeta}(N_{0d}))$ determines the spectrum of electron states on a surface with roughness; $A_0 = \sqrt{2|\delta k_0|/L_x L_y}$, where L_x, L_y are the model sizes in x and y directions, respectively.

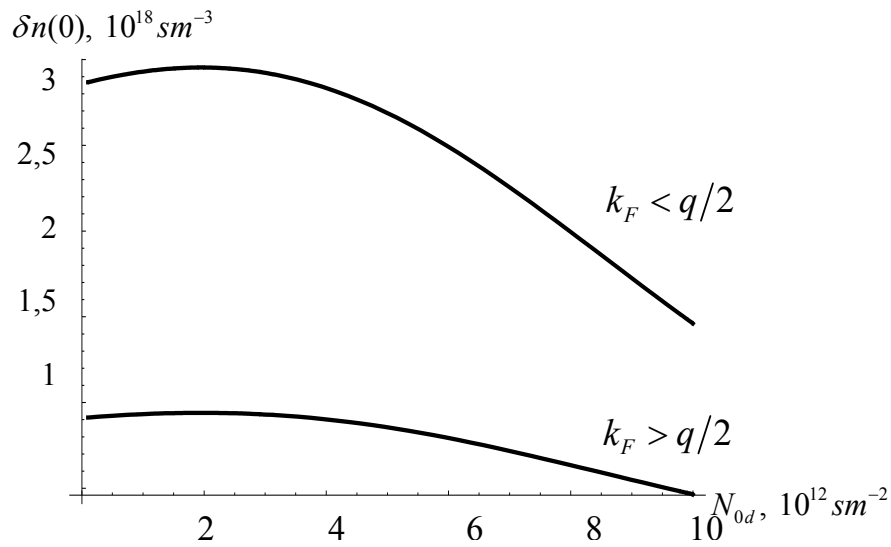


Fig. 1. The change of the electrons concentration on the $z = 0$ surface of the semiconductor GaAs (100), depending on the concentration of adsorbed atoms

The dependence of the wave function of surface electron states on the z coordinate leads to the appearance of an inhomogeneous electron plasma in the $z > z_0$ region. The basic parameters of this plasma can be expressed due to the characteristics of the surface roughness. We will determine the change of electrons concentration $\delta n_0(z)$:

$$\delta n_0(z) = \sum_{k_x} \psi_k \psi_k^* n_{k_x} = \frac{2}{S} \sum_{k_x} n_{k_x} |\delta k_0| e^{-2|\delta k_0|z}, \quad (5)$$

where n_{k_x} is the number of electrons with the wave vector k_x ; the sum is carried out at all values of k_x . In this case, the minimum k_x value is determined by the model sizes in the x direction, that is, the value L_x , and the maximum - by the Fermi impulse $\hbar k_F$. The total number of particles in the $z > 0$ region is equal to

$$\sum_{k_x} n_{k_x}.$$

$$\text{The surface density } n_s = \int_0^\infty \delta n_0(z) dz = \sum_{k_x} n_{k_x} / L_x L_y.$$

A graphic representation of the dependence of the electrons concentration change $\delta n(0)$ on the adsorbed atoms concentration on the $z = 0$ surface is given in Figure 1. The nonmonotonous character of the curves is determined by the nonmonotonous functional dependence of the height of the semiconductor surfaces roughnesses on the adsorbed atoms concentration.

3. Conclusions

The dispersion relations for the spectra of surface electron states on a dynamically deformed adsorbed surface of a GaAs (CdTe) semiconductor were derived.

It was established that the dependences of the band gap width and of the electrons concentration on the adatoms concentration have the nonmonotonous character.

It was shown that the dependence of the electrons concentration change on the concentration of adsorbed atoms on the surface has a nonmonotonous character, determined by the height of the inequality of the surface of the solid. In particular, the maximum change of electron density on the surface of a GaAs (100) semiconductor is achieved at the concentration of adsorbed atoms $N_{0d} = 1,9 \cdot 10^{12} \text{ sm}^{-2}$.

References

1. Liu B., Chen X., Cai H., Mohammad A.M., Tian X., Tao L., Yang Y., Ren T. J. Semicond., 2016, 37 (2), 021001; doi:10.1088/1674-4926/37/2/021001.
2. Bir G.L., Pikus G.E., Symmetry and strain-induced effects in semiconductors, Wiley, NY, 1974.
3. Khankina S.I., Yakovenko V.M., Yakovenko I.V., Radiophys. Quantum El., 2002, 45 (10), 813; doi:10.1023/A:1022488518808.
4. Peleshchak R.M., Kuzyk O.V., Dan'kiv O.O., Cond. Mat. Phys., 2014, 17, 23601; doi:10.5488/CMP.17.23601.
5. Peleshchak R.M., Seneta M.Ya., Condens. Matter Phys., 2016, 19 (4), 43801; doi:10.5488/CMP.19.43801.
6. Seneta M.Ya., Peleshchak R.M., Brytan V.B., J. Nano- Electron. Phys., 2017, 9 (5), 05023; doi:10.21272/jnep.9(5).05023.
7. Khankina S.I., Yakovenko V.M., Yakovenko I.V., Low Temp. Phys., 2011, 37, 913; doi:abs/10.1063/1.3672158.

PECULIARITIES OF SHORT-WAVE RADIATION OF HEXAGONAL α -ZnSe AND α -ZnSe_xS_{1-x}

M.M. Slyotov, O.M. Slyotov

*Yuriy Fedkovych Chernivtsi National University,
Kotsubinsky Str., 2, 58012, Chernivtsi, Ukraine*

An important question of modern information technology is the expansion of spectral range of the optical information display systems. For them it is still important to obtain materials with high-efficiency radiation. Such can be II-VI compounds, the direct band-gap E_g of which is an important factor for the high efficiency of the generation-recombination processes. Among them zinc selenide with cubic structure (β) of crystalline lattice and $E_g = 2.7$ eV deserves on a special attention. However, the existing processes of materials obtaining are characterized by high complexity, cost and does not allow to obtain a stable hexagonal modification (α). Therefore, the question of finding a method for obtaining of zinc selenides with hexagonal modification and studying the possibilities of obtaining short-wave radiation of high efficiency is relevant.

Heterolayers (HL) of α -ZnSe hexagonal modifications and α -ZnSe_xS_{1-x} solid solution of substitution were obtained by the method of isovalent replacement. For this purpose, the isothermal annealing of the α -CdS substrates in a vacuum consistently in saturated pairs of Zn and Cd was used. It allowed one to obtain heterolayers with stable properties in time. The universal measuring complex used for research of optical processes allowed to determine the properties of the obtained heterolayers. The energy structure of α -ZnSe is characterized by the next parameters, that is $E_g = 2.89$ eV, $\Delta_{cr} = 0.07$ eV and $\Delta_{so} = 0.37$ eV. The last one are the values of the valence band splitting into the subzone due to the action of the crystalline field Δ_{cr} and the spin-orbital interaction Δ_{so} that were defined for the first time. The obtained heterolayers of α -ZnSe have an intensive photoluminescence (PL) in a short-wave region with high quantum efficiency $\eta \sim 8-10\%$ at 300 K (versus 0.1-0.3% for the widely used β -ZnSe single crystals). The radiation is formed by bands, the dominant of which is determined by the annihilation of bound excitons. There is also an intense radiation in the range of photon energies $\hbar\omega \geq E_g$. It is formed by the interband recombination of free charge carriers at their transitions from the main zone and subzone splited by the crystalline field Δ_{cr} . The change in the annealing temperature of α -CdS makes it possible to obtain ZnSe_xS_{1-x} solid solutions of substitution. At $x = 0.47$, the parameters of the band structure are $E_g = 3.20$ eV, $\Delta_{cr} = 0.066$ eV and $\Delta_{so} = 0.311$ eV. The obtained layers also have an intense PL in the violet and near ultraviolet ranges. The mechanism of the recombination processes repeats α -ZnSe, namely, the annihilation of bound excitons and interband transitions of free charge carriers. The estimation of quantum efficiency of PL gives a value $\eta \sim 5.8\%$. Experimentally is established the weak temperature dependence of radiation up to $T = 540$ K and repeatability with time and stability of characteristics and parameters at high temperatures that is important for practical use.

Effect of symmetry of small stoichiometric zirconia particles on their spectral characteristics

O.V. Smirnova, A.G. Grebenyuk, V.V. Lobanov

*Chuiko Institute of Surface Chemistry, NAS of Ukraine,
17 General Naumov Str., Kyiv 03164, Ukraine, olsmirnova2001@ukr.net*

Zirconia is an important functional material which has excellent physical and chemical properties. In order to elucidate the peculiarities of the spatial and electronic structures of relative materials, they can be examined by means of both experiment (in particular, spectroscopy) and theoretical simulation [1].

In this work, the absorption spectra (XPS, IR and UV) of pure zirconia have been calculated by density functional theory method (B3LYP/3-21G**). Calculations were performed by means of the software package PC GAMESS (version FireFly 8.1.0 (<http://classic.chem.msu.su/gran/firefly/index.html>) [2] by A.Granovsky). In the calculations, a cluster approximation was used using molecular models of the composition $\text{Zr}_{19}\text{O}_{38}$, Zr_6O_{12} and Zr_4O_8 (Fig. 1).

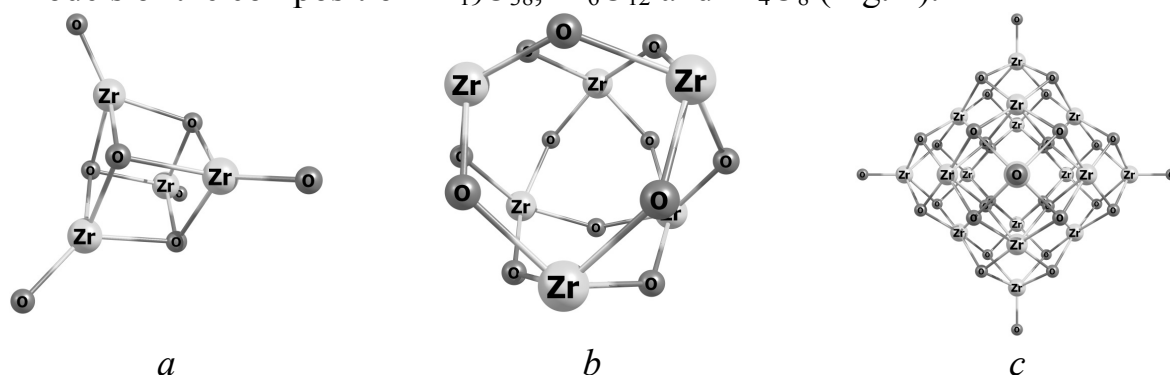


Fig. 1. Optimized structures of zirconium dioxide clusters with composition Zr_4O_8 (a), Zr_6O_{12} (b), and $\text{Zr}_{19}\text{O}_{38}$ (c).

The Zr_4O_8 molecule was treated with and without imposing symmetry conditions of T_d point group. The results of calculations are presented in Table 1.

The spectral consequences of symmetry breaking of small stoichiometric zirconium dioxide particles (the Zr_4O_8 cluster model being taken as an example) are shown in Fig. 2.

It follows from the results of calculations that the imposition of symmetry leads to some distortion of the calculated values. In particular, the first six calculated frequencies corresponding to the rotational and translational motions of the molecule as a whole in calculation without symmetry restrictions are exactly zero with zero intensity, while in calculation under symmetry conditions these quantities are nonzero, although they are relatively small (11 and 2 cm^{-1}). Besides, in the calculation without symmetry restrictions, it is possible to evaluate some groups of calculated frequencies close in magnitude. The corresponding quantities, taking into account the symmetry, are completely identical, which is assumed initially to be a symmetry condition. Obviously, for large clusters, these differences in calcu-

lations are insignificant, and it is possible to calculate the spectral characteristics for a cluster with geometry restrictions within various types of symmetry point groups.

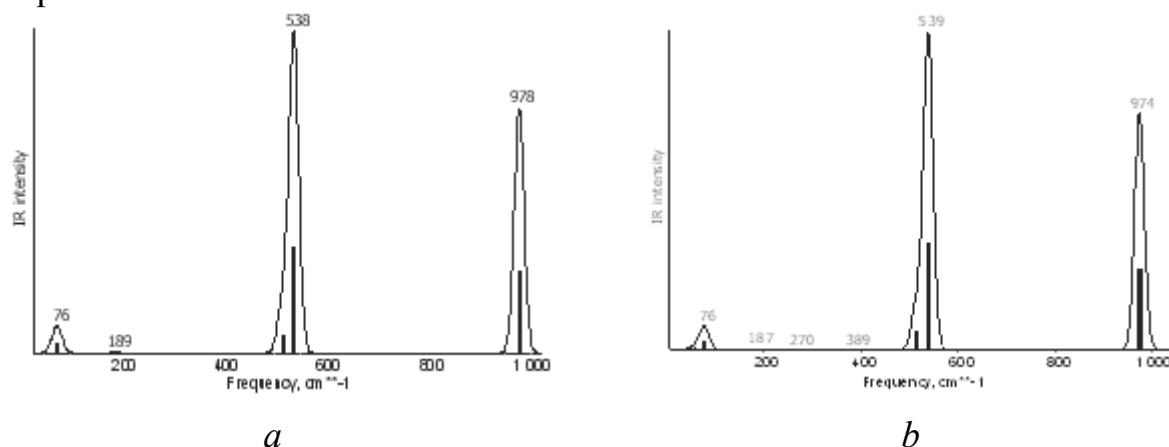


Fig. 2. IR spectra of the Zr_4O_8 cluster with imposing symmetry conditions (point group T_d , *a*) and without spatial restrictions (*b*).

Thus, we have calculated the IR spectrum for clusters of the composition Zr_6O_{12} and $\text{Zr}_{19}\text{O}_{38}$ within O_h symmetry point group (Fig. 3).

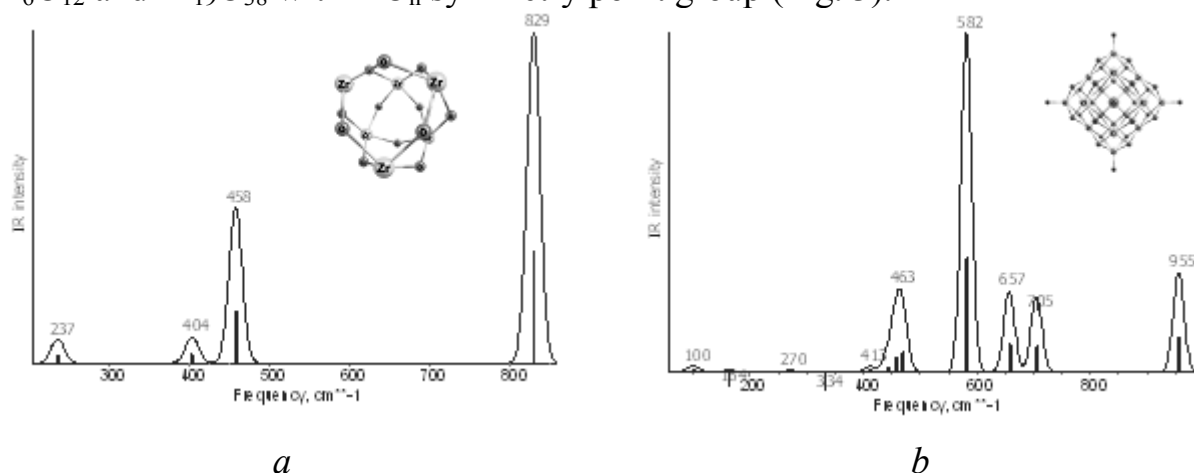


Fig. 3. IR spectra of the clusters of composition Zr_6O_{12} (*a*), and $\text{Zr}_{19}\text{O}_{38}$ (*b*) within symmetry point group O_h .

The real symmetry of the cluster slightly differs from the supposed ideal one, which makes it purposeful to search for an approximate solution by imposing a point group symmetry restrictions on the real object.

As a result of calculations, it has been found that the calculated vibration frequency of the Zr_4O_8 cluster in the 583.6 cm^{-1} region corresponds to the "breathing" vibrations of Zr-O bonds. In the IR spectrum of the Zr_6O_{12} cluster, there is no absorption band 581 cm^{-1} .

In the IR spectrum of the Zr_4O_8 cluster, the absorption band in the range of 978 cm^{-1} corresponds to the stretching vibrations of Zr=O groups. For the $\text{Zr}_{19}\text{O}_{38}$ cluster, this value corresponds to 955 cm^{-1} .

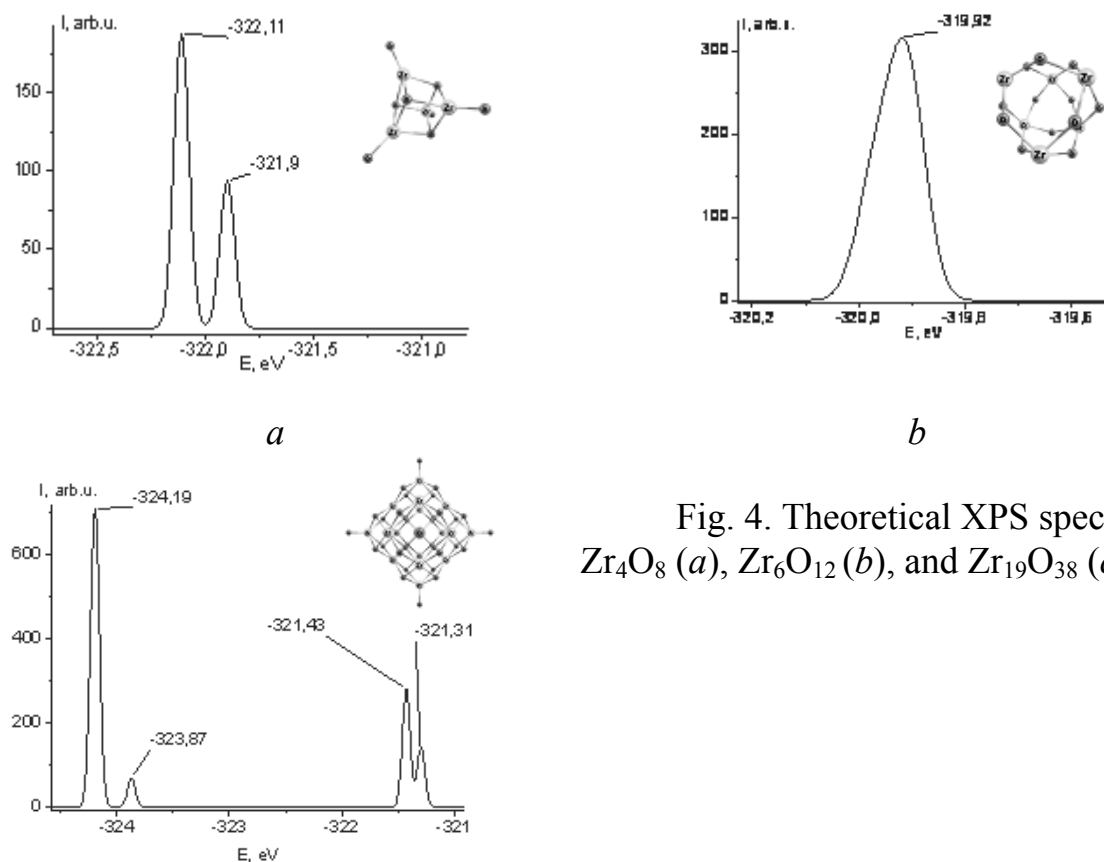


Fig. 4. Theoretical XPS spectra of Zr_4O_8 (a), Zr_6O_{12} (b), and $Zr_{19}O_{38}$ (c).

Table 1. Energy levels of $Zr3p$ in Zr_6O_{12} and $Zr_{19}O_{38}$ clusters.

No of orbital	-E, a.u.	-E, eV	No of atom	No of group
Zr_4O_8 (T_d)				
33-40	11.8371	322.11	1-4	I
41-44	11.8296	321.90	1-4	
Zr_6O_{12} (O_h)				
49-54	11.7586	-319.97	4, 5	I
55-66	11.7565	-319.91	1-3, 6	
$Zr_{19}O_{38}$ (O_h)				
165-188	11.9147	324.19	8-19	III
153-164	11.9135	324.23		
189-191	11.9019	323.87	1	I
192-203	11.8121	321.43	2-7	II
204-209	11.8074	321.30		

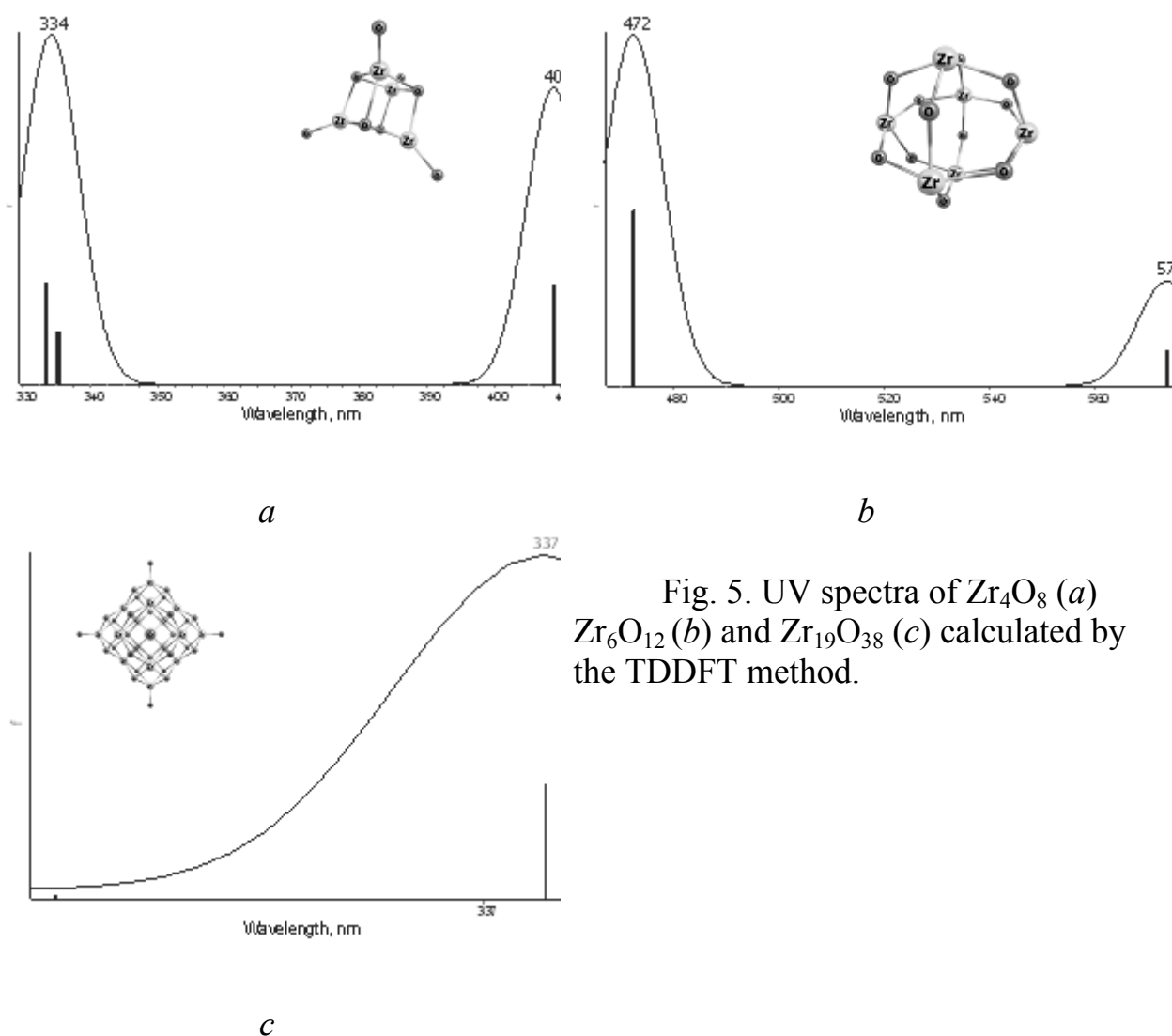


Fig. 5. UV spectra of Zr_4O_8 (a) Zr_6O_{12} (b) and $Zr_{19}O_{38}$ (c) calculated by the TDDFT method.

It follows from the results of calculations of the UV spectra that all the clusters have absorption bands with maxima at 337 nm. The appearance of another absorption band of cluster Zr_4O_8 in the range of 410 nm is due to the presence of chromophores $Zr=O$. However, in the UV spectrum of cluster $Zr_{19}O_{38}$ this band (410 nm) is absent, but there is a band 342 nm with zero intensity. Cluster Zr_6O_{12} has a distorted structure, so a bathochromic shift occurs of relative absorption bands.

Thus, one can jump to conclusion that the spectra of zirconia small particles are highly characteristic concerning the energies of spectral transitions and uniquely correspond to their spatial structures.

1. Structures, growth modes and spectroscopic properties of small zirconia clusters. Shougang Chen, Yansheng Yin, Daoping Wang, Yingcai Liu, Xin Wang // Journal of Crystal Growth. - 2005. - V. 282. - P. 498.
2. Schmidt M., Baldridge K., Boatz J., Elbert S., Gordon M., Jensen J., Koseki S., Matsunaga N., Nguyen K., Su S., Windus T., Dupuis M., Montgomery J. General Atomic and Molecular Electronic Structure System // J. Comput. Chem. - 1993. - V. 14. - P.1347.

Temperature dependences of voltage-to-current characteristics of Tl_4HgI_6 and Tl_4CdI_6 crystals

Solovyov M.V., Kashuba A.I., Franiv V.A.

Ivan Franko National University of Lviv, Faculty of Physics, Cyryl and Methody str. 8a, 79005 Lviv, Ukraine

Introduction: The problem of finding new materials for the sensors of temperature [1, 2] remains urgent in microelectronics. The main requirements for such materials are following: optimal sizes, maximum possible temperature-to-signal transformation ratio, available temperature range, multiple use of material during operation. Reports on the promising use of compounds of the group A_4BI_6 (Tl_4HgI_6 and Tl_4CdI_6), as materials for the active elements of functional electronics, appear episodically in literature [1-7].

There are periodic reports on the electric properties of crystals of the group A_4BI_6 [1, 8]. In Ref. [1], the authors have studied the conductivity for Tl_4HgI_6 sample and have found the activation energy of 0.8 eV. The temperature behavior of the spectra of electrical conductivity is presented in Ref. [8]. However, in contrast to the previous papers [2, 9], in Ref. [8], the structural transformations have not been found in the samples. Also, in none of the above papers [1, 8], the temperature dependences of the voltage-to-current characteristics (VCC) and the dynamics of resistance changes were not investigated.

The main goal of the present investigation is the study of temperature influence on the VCCs of the samples (Tl_4HgI_6 and Tl_4CdI_6) and the determination of main mechanisms forming those VCCs. On this basis, the determination of the temperature range for application the investigated compounds as materials for the temperature sensors would be possible.

Method of calculations: Synthesis of Tl_4HgI_6 and Tl_4CdI_6 compounds have been performed from the crystalline binary compounds TlI , HgI_2 and CdI_2 taken in equimolar ratios. The synthesis process and growth of crystals were realized in the quartz ampoules of the diameter 12 mm. The corresponding rate of the temperature decrease used was 2°C/h . The crystals Tl_4HgI_6 and Tl_4CdI_6 were grown by the Bridgman method with ampules in a vertical oven (with the growth rate of 2 mm/h). Both crystals are described by the spatial group of symmetry D_{4h}^{16} [2, 6, 9]. More details related to the crystals synthesis and growths are presented in Refs. [2] and [9].

For the measurement of VCC, the corresponding crystal samples with two symmetrical electrodes were prepared by imposing a silver paste onto the sample's surfaces. A block diagram for the study of temperature dependencies of VCC is presented in Fig. 1. In the process of VCC measurement, the sample under study was placed in an electric furnace at the isothermal conditions. The temperature of the samples in a furnace was installed and controlled using the PID-regulator of temperature PE-202 using a thermocouple of the type "K". The relative error of temperature did not exceed 0.2 %.

The constant voltage was applied to the sample studied using the stabilized programmable sources M8872 Maynuo. The value of the current flowing through the sample was determined by the Ohm law on a homogeneous section of the circle on the basis of a voltage drop on a series-switched measuring shunt (resistance store P4831 of the accuracy class $0.02/2 \times 10^{-6}$). A voltage on the investigated sample and the measuring shunt were performed using a digital two-channel recorder Disco2Pro.

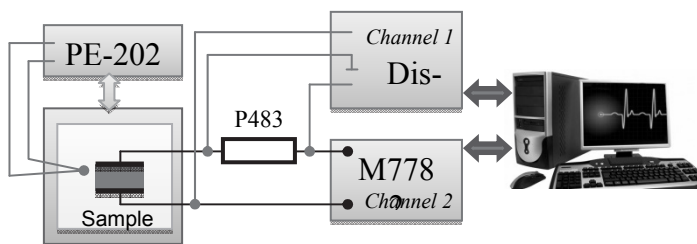


Fig. 1. Scheme of the experimental setup

Results and discussion: In the figures 2 and 3, the VCC of Ti_4HgI_6 and Ti_4CdI_6 crystals are presented. They are of a straightening character because the temperatures increase of the VCC slope.

The behavior of a VCC can be approximated by different functional dependences [10]. In the case of semiconductors, VCCs are fitted most often by using the power (1), exponential (2) or logistic (3) functions. In the relations (1) – (3), x is a voltage V and y is a corresponding electric current I . Other symbols in the relations (1) – (3) are the sample dependent parameters.

$$y = a \cdot x^n \quad (1)$$

$$y = y_0 + A_1 e^{x/t_1} \quad (2)$$

$$y = \frac{A_1 - A_2}{1 + (x/x_0)^p} + A_2 \quad (3)$$

An analysis of the mechanisms of injection and recombination of the charge carriers in a semiconductor is based on the diversity of behavior the injected charge carriers and their influence on VCC.

Approximation by the function (1) of the experimental VCC for Ti_4HgI_6 crystal at the temperature $T = 293$ K is characterized by the coefficient of determination $R^2 = 0.986$ with the parameters $a = 8.99 \times 10^{-7}$ and $n = 1.48$. Here, the convergence of the calculated results to the experimental ones is not sufficient enough, therefore one can't assert about the possible mechanism of double injection [10] in the semiconductor. However, with increasing temperature, the convergence to the experimental dependence with the function (1) becomes better, $R^2 = 0.998$ ($a = 0.0013$, $n = 1.37$, $T = 458$ K). This means that with increase of temperature the double injection mechanism in Ti_4HgI_6 may appear.

Having analyzed the VCC by the function (2) and (3), a much higher convergence have been obtained, $R^2 = 0.9955$ ($y_0 = -3.89 \times 10^{-5}$, $A_1 = 3.63 \times 10^{-5}$, $t_1 = -16.84$) and $R^2 = 0.9958$ ($A_1 = -2.12 \times 10^{-6}$, $A_2 = 0.0243$, $x_0 = 2379.09$, $p = 1.23$), respectively. It should be noted that with increasing temperature, the convergence of

the calculated results obtained using the functions (2) and (3) to the experimental data also increases ($R^2 = 0.998$, $T = 458$ K). Therefore, one may adopt the weak injection [10, 11] and the constant field between contacts [10, 12] as the prevailing modes in these cases.

Thus, we have found that at room temperature the weak injection and the constant field between the contacts are the predominant modes in Tl_4HgI_6 crystal and the mechanism of double injection is rather weak. At higher temperatures, all these three modes might be active in equal extents. However, taking into account the temperature stimulated increase of the first derivative of VCC ($\alpha = dI/dU$) from the magnitude $\alpha_{293\text{K}} = 0.01$ to the value of $\alpha_{458\text{K}} = 0.25$, it was found that the double injection mode does not appear in Tl_4HgI_6 samples [10]. Thus, the behavior of VCC in Tl_4HgI_6 remains to be of the weak injection and the constant field between contacts.

For a sample of Tl_4CdI_6 , in the temperature range of 293 K - 473 K, we did not detect significant changes in the behavior of the VCC. Having analyzed the VAC by the function (1), we have obtained a slight convergence of $R^2 = 0.977$ ($a = 3.41 \times 10^{-7}$, $n = 1.3$, $T = 293$ K). Having carried out the fitting of the experimental data by the functions (2) and (3), the high convergences $R^2 = 0.993$ ($y_0 = 0.0621$, $A_1 = -0.0621$, $t_1 = 64941.72$) and $R^2 = 0.993$ ($A_1 = -2.43 \times 10^{-6}$, $A_2 = 1340.29$, $x_0 = 1.41$, $p = 0.99$), respectively, have been obtained. Similar temperature dependences of VCC have been found for Tl_4HgI_6 samples. Magnitudes of the coefficient α mentioned above varied from $\alpha_{293\text{K}} = 0.001$ to $\alpha_{462\text{K}} = 0.01$. These results permit to suggest that similar physical phenomena lie in the ground of VCC in Tl_4CdI_6 and Tl_4HgI_6 samples.

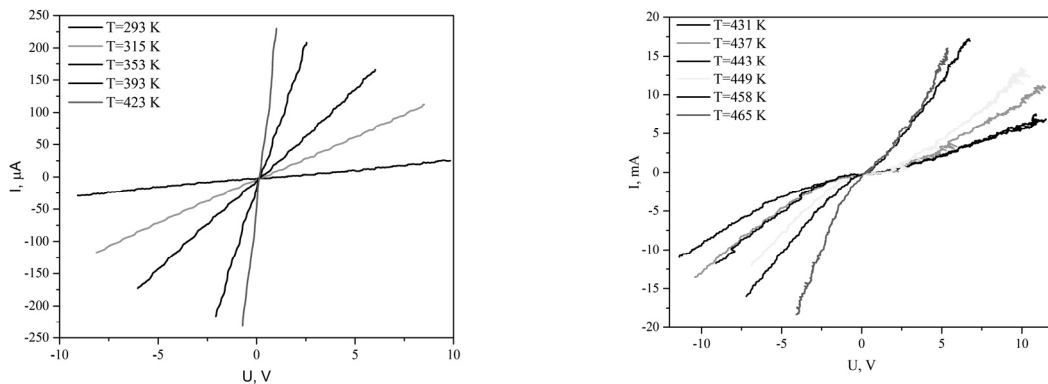


Fig. 2. VCC of Tl_4HgI_6 crystal presented for different temperatures

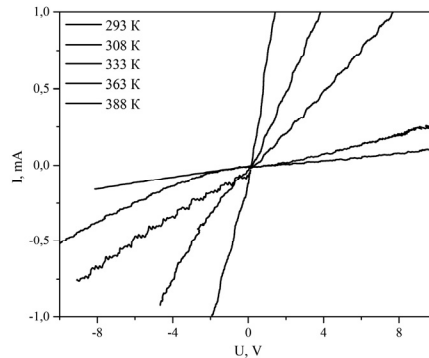


Fig. 3. VCC of Tl_4CdI_6 crystal presented for different temperatures

Conclusions: Experimental study and analysis of the voltage-to-current characteristics of Tl_4HgI_6 and Tl_4CdI_6 crystals at the room temperature reveal the corresponding predominant modes of weak injection and constant field between the electrical contacts. It was found out that the mechanism of double injection doesn't takes place in the samples under study.

References:

1. Kalyagin D.S., Ermolenko Y.E., Vlasov Y.G. Diffusion of Tl-204 Isotope and Ionic Conductivity in Tl_4HgI_6 Membrane Material for Chemical Sensors // Russian Journal of Applied Chemistry. – 2008. – 81(12). – P. 2172.
2. Franiv A.V., Kushnir O.S., Girnyk I.S., Franiv V.A., Kityk I.V., Piasecki M., Plucinski K.J. Growth, crystal structure, thermal properties and optical anisotropy of Tl_4CdI_6 single crystals // Ukr. J. Phys. Opt. – 2013. – 14(1). – P. 6.
3. Patent US 8,519,347 B2, 2013.
4. Kahler D., Singh N.B., Knuteson, Wagner B., Berghmans A., McLaughlin S., King M., Schwartz K., Suhre D., Gotlieb M. Performance of novel materials for radiation detection: Tl_3AsSe_3 , TlGaSe_2 , and Tl_4HgI_6 // Nuclear Instruments and Methods in Physics Research Section A. – 2011. – 652(1). – P. 183–185.
5. Badikov D.V., Badikov V.V., Kuz'micheva G.M., Panyutin V.L., Rybakov V.B., Chizhikov V.I., Shevyrdyaeva G.S., Shcherbakova E.S. Growth and X-ray diffraction study of Tl_4HgI_6 crystals // Inorganic Materials. – 2004. – 40(3). – P. 314.
6. Solovyov M., Kashuba A., Franiv V., Franiv A., Futey O. X-ray luminescence of Tl_4CdI_6 crystals // YSF-2017, Conference paper. – 2017. – P. 195.
7. Wang S., Liu Z., Peters J.A., Sebastian M., Nguyen S.L., Malliakas C.D., Stoumpos C.C., Im J., Freeman A.J., Wessels B.W., Kanatzidis M.G. Crystal Growth of Tl_4CdI_6 : A Wide Band Gap Semiconductor for Hard Radiation Detection // Crystal Growth & Design. – 2014. 14(5). – P. 2401.
8. Franiv V.A., Czaplá Z., Dacko S., Franiv A.V., Kushnir O.S. Structural transformations in Tl_4HgI_6 and Tl_4CdI_6 crystals as evidenced by dielectric properties and conductivity // Ukr. J. Phys. – 2014. – 59(11). – P. 1078-1082.
9. Piasecki M., Lakshminarayana G., Fedorchuk A.O., Kushnir O.S., Franiv V.A., Franiv A.V., Myronchuk G., Plucinski K.J. Temperature operated infrared nonlinear optical materials based on Tl_4HgI_6 // Journal of Materials Science: Materials in Electronics. – 2013. – 24(4). – P. 1187.
10. Ciach R., Dotsenko Yu.P., Naumov V.V., Shmyryeva A.N., Smertenko P.S. Injection technique for the study of solar cell test structures // Solar Energy Materials & Solar Cells. – 2003. – 76. – P.613–624.
11. Zyuganov A.N., Svechnikov S.V. Contact-injection phenomena in semiconductors. – Naukova dumka, Kyiv, 1981.
12. Bagratishvili G.D., Dzhanlidze R.B., Jishiashvili D.A., Zyuganov A.N., Mikhe-lashvili V.M., Piskanovskii I.V., Smertenko P.S. Mechanism of charge flow through the $\text{M-Ge}_3\text{N}_4\text{-GaAs}$ structure // Phys. Status Solidi A. – 1981. – 65. – P. 701.

CDS - BASED SEMIMAGNETIC SEMICONDUCTOR NANOPARTICLES AND THEIR BIOCOMPLEX WITH PROTEIN FOR BIOIMAGING AP- PLICATIONS

**I. D. Stolyarchuk¹, R. Wojnarowska - Nowak², J. Polit², S. Nowak³,
M. Romerowicz - Misielak³, H. M. Klepach^{4,5}, E. M. Sheregii²**

¹*Department of Physics, Ivan Franko Drohobych Pedagogical University, 24 I. Franko str., 82100 Drohobych, Ukraine*

²*Centre for Microelectronics and Nanotechnology, University of Rzeszow, 1 Pigo-
nia Str., 35959 Rzeszow, Poland*

³*Department of Animal Physiology and Reproduction, Institute of Applied Biotech-
nology and Basic Sciences, University of Rzeszow, Werynia 502, 36100
Kolbuszowa, Poland*

⁴*Department of Analytical Biotechnology, Institute of Cell Biology, National Acad-
emy of Sciences of Ukraine, Drahomanov Street 14/16, 79005 Lviv, Ukraine*

⁵*Department of Biology and Chemistry, Ivan Franko Drohobych Pedagogical Uni-
versity, 24 I. Franko str., 82100 Drohobych, Ukraine*

Nanotechnology plays a central role in the recent advances in the areas of disease diagnosis, drug design and drug delivery. The nanotechnological applications to disease treatment, diagnosis, monitoring, as well as to the control of biological systems are one of the most interesting and developed issues. One of the promising materials that can be used for this purpose are semiconductor nanocrystals (NCs), also known as quantum dots (QDs). Research on their application in nanomedicine, has intensified rapidly in the past few decades. From a point of view of biomedical applications, the II-VI based QDs have particular interest due to broad absorption spectra, narrow photoluminescence spectra, size-tunable spectra and high sensitivity [1]. Due to unique size dependent optical properties, QDs can be successfully used as a novel probes in biosensors as well as bioimaging and biolabeling. QDs were conjugated to proteins, antibodies, enzymes, DNA and peptides to could be successfully used in wide range of biological application [2].

The human serum albumin (HSA) is the most abundant and one of the most important proteins in blood plasma. His is produced by liver and it provides more than 50% of the total proteins in plasma. Albumin has many different and very important physiological functions: connecting and handling to the cells a variety of endogenous and exogenous ligands (including hormones, metabolites, ions or fatty acids), drug transportation, toxins binding, and maintaining of the oncotic pressure (through the water-binding capacity) [3,4]. It can be also a diagnostic marker for determining some diseases like inflammatory states [5].

Besides the optical and functional properties of the QDs, the interactions between QDs and HSA and their mechanisms, have been investigated in many

works. Several reports have been devoted to the study of such kinds of interactions of the II–VI based nanoparticles with HSA as well as with bovine serum albumin (BSA) [6,7]. However, the processes of the interactions of these molecules between each other and with other molecules in human body are highly complex and complicated and still are not well known. Therefore, it is very significant for nanomedicine purpose to investigate the processes occurring between the nanoparticles and the major carrier protein like HSA. Furthermore, covering of QDs by the natural protein seems to be a promising solution for reducing their toxicity. Therefore, forming the QD-HSA complexes is important in order to remove toxicity from the QDs.

In the present work, the results of research dedicated to the CdS and CdS:Mn (Co) quantum dots interaction with human serum albumin (HSA) and human cell culture are reported. The UV-VIS optical absorption, photoluminescence, micro-Raman and Fourier Transform Infrared (FTIR) spectra of compounds are supplemented by results obtained after combined QDs with a HSA.

Transmission electron microscopy (TEM), scanning electron microscopy (SEM) and atomic force microscopy (AFM) are often used in order to confirm the structure of nanoparticles and bionanocomplexes. The estimate shape and average size of nanocrystals, as well as the composition and crystal structure are analyzed by the above mentioned methods. A drop of colloidal suspension is placed on a carbon-coated copper grid and dried for the TEM analysis. Samples are usually placed on the highest grade mica or graphite surface before an AFM measurement. The composition SEM microscope with an energy dispersive X-ray spectroscopy (EDS) can be used for the chemical analysis of QDs. Obtained results suggest that the shape of the NPs is close to spherical and crystalline structure of QDs is perfect (described as uniform in all directions without any significant defects). The particle size is distributed in range from 4 to 7 nm with the average size of ~5 nm. The average size of bionanocomplexes was confirmed by AFM measurement, and it was about 10-15 nm.

The absorption spectra are recorded and analyzed for the evaluation of optical properties of pure QDs, pure HSA and QD-HSA complex. The region of the fundamental absorption edge of the all QDs are studied. An addition of HSA to colloidal nanoparticles leads to a gradual decrease of optical density and broadening of exciton structure. However, energy position of the exciton bands is not shifted. The obtained results indicate that the binding process between the QDs and the protein molecules do not change the electron states in the QDs.

Photoluminescence spectroscopy provides qualitative and quantitative information about the interaction between QDs and HSA. Our results showed that the intrinsic fluorescence of HSA was quenched through static quenching mechanism. The quenching constants and the number of binding sites increase with increasing of average size of QDs. At same times, the quenching constants decrease with increasing temperature, which also indicates that the quenching mechanism mainly arises from static quenching type. The presence of HSA protein leads to strong quenching of FL emission, which could be explained by covalent interaction

between the QDs and the quencher, demonstrating the formation of QD–HSA bio-complex.

Obtained data enable us to find optimal QDs concentration useful for 134b carcinoma cells bioimaging. The human osteosarcoma is the primary malignant bone tumor in children and adult. Early detection is particularly important, because the tumor is prone to metastasize (especially in the lung) and further mutation and genetic changes often occur. The low toxicity as well as high stability of the QDs - HSA biocomplexes in the case of their using as bio-imaging probes for the 143b osteosarcoma cells has been demonstrated. However, in case of CdS:Mn (Co) QDs - HSA biocomplex using for labeling this molecule, the concentration of QDs should be higher. The results suggest that CdS and CdS:Mn (Co) QDs-HSA bioconjugate can be potentially employed for bioimaging osteosarcoma cells with minimal adverse effect.

1. Handbook of Nanophysics: Nanomedicine and Nanorobotics, in: J. Sattler, D.Klaus (Eds.), CRC Press, 2011, ISBN 978-1-4200-7546-5.
2. J. Simeunovic, J. Pekarkova, J. Zak, I. Chamradova, J. Hubalek, Monatshefte fuer Chemie/Chemical Monthly 148(11) (2017); DOI 10.1007/s00706-017-2038-1
3. K.D. Wegner, N. Hildebrandt, Chem. Soc. Rev. 44 (2015)4792–4834.
4. S.J. Rosenthal, J.C. Chang, O. Kovtun, J.R. McBride, I.D. Tomlinson, Chem. Biol. 18 (2011)10–24.
5. G.J. Quinlan, G.S. Martin, T.W. Evans, Albumin: biochemical properties and-therapeutic potential, Hepatology 41 (6) (2005) 1211–1219.
6. B. Nithyaja, K. Vishnu, S. Mathew, P. Radhakrishnan, V.P.N. Nampoori, J. Appl. Phys. 112 (2012) 064704-1–064704-6.
7. J. Hemmateenejad, S. Yousefinejad, J. Mol.Struct. 1037 (2013) 317–322.

Magneto-optical studies of CdTe / CdMnTe double quantum wells

O.V.Terletsii¹⁾, V.Yu. Ivanov²⁾, L.Owczarczyk²⁾, S.M.Ryabchenko¹⁾,
V.I.Sugakov³⁾, G.V. Vertsimakha³⁾, G. Karczewski²⁾.

1) Institute of Physics NASU, Prospect Nauki 46, 03680 Kyiv, Ukraine;

2) Institute of Physics PAS, Al. Lotnikow 32/46, PL-02-668 Warsaw, Poland;

3) Institute for Nuclear Research NASU, Prospect Nauki 47, 03680 Kyiv, Ukraine

Excitons photoluminescence (PL) from the lowest spatial-quantized states in asymmetric double quantum wells was studied in magnetic fields up to 6T. The semimagnetic, and nonmagnetic quantum wells in the CdMgTe/ Cd_{0.95}Mn_{0.05}Te/ CdMgTe/ CdTe/ CdMgTe structure were separated by a tunnel-transparent 6 ml width CdMgTe barrier (1ml \approx 0.324 nm). In such structures, tunnel transparency of the barrier between the wells causes formation besides of usual direct excitons of the excitons with spatially separated of electron and hole (so-called indirect excitons, IX, – see the arrows marked as IX in Fig.1). The PL excitation was provided by over-barrier green (2.373eV) or under-barrier red (1.8785eV) light in the wide range of excitation power (0.1-10 W/cm²). The studied structures had the CdTe quantum wells of different width (18, 21, 24, 27 and 30 ml) whereas the width of the semimagnetic well was the same (46 ml).

For the past few decades, properties of coupled double quantum wells (DQW) and dots have been widely investigated,, including BEC in DQW [1,2], magnetic polaron states [3], and spectra of double quantum dots [4]. Despite that probability of indirect optical transitions is about two or more orders of magnitude less than for direct transitions, a long lifetime of the indirect excitons ($\sim 10^{-8}$ sec) makes possible their accumulation in the structures. Last allows observe their PL spectra if indirect excitons energy turn out lower than of energy of direct ones.

It should be noted that prevalent part of the experimental studies were carried

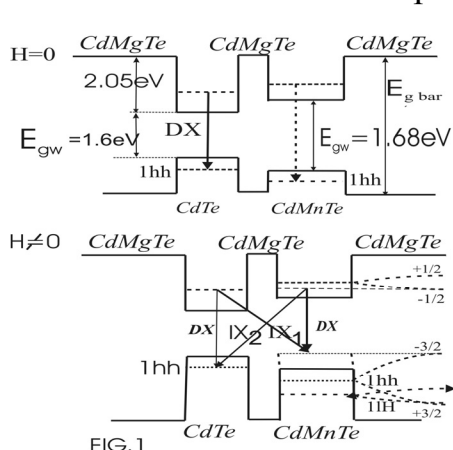


FIG.1

in the presence of electric field providing required shifts of the positions of the carriers' states in the QWs. As the result, in the electric field, one of the possible indirect excitons becomes the lowest exciton state in the system. For DQW structures, where one of the wells is semimagnetic, tuning of the IX energy can be provided by application of magnetic field due to the effect of giant spin splitting [5, 6]. In this case, the charge current, caused by a pres-

ence of the electric field under sample irradiation, doesn't arise. In such way the influence of this current on the results is removed.

In our case, the structures are asymmetric (wells have different widths and are prepared from different materials). In the absence of magnetic field, the first quantized state of heavy holes (1hh) in the non-magnetic well is significantly

higher than the similar state in semimagnetic one for all the samples. Therefore, in the equilibrium state, the hole state in the semimagnetic well is almost empty.

Fig. 1 shows the scheme of both DX and IX transitions between the first spatially quantized electron levels (1e) of the QWs, which enter in DQW, and 1hh levels of these QWs for the lowest optically allowed exciton transition in the σ^+ polarization taking into account the giant spin splitting of mentioned states [5, 6].

Figs 2a, b show the maps of the dependencies of the energy and intensity of the σ^+ PL spectra on the magnetic field for the cases of under-barrier and over-barrier excitations correspondingly and their field dependence (insert in Fig. 2b).

Parameters of the DQW structures, for which the observation of such transitions in PL is the most probable, were chosen on the base of previous magneto-optical studies of the σ^+ exciton luminescence and calculations of spatially quantized states (Fig. 3). Energies of both possible 1eCdTe - 1hhCdMnTe and 1eCdMnTe - 1hh CdTe indirect excitons were calculated [7,8] taking into account a mixing the four lowest states of electron and hole in double QWs.

For zero magnetic field and weak red excitation (Fig. 2a), the trion line from the CdTe wells dominates. The energy position of DX line from CdTe QW are in agreement with the results of the calculations. The DX and IX transitions from the CdMnTe QW were almost not observed.

As the pumping power ($h\nu = 1.8785$ eV: the density of power ≈ 6.4 W/cm²) and magnetic field

increase (up to 0.5 -1.0 T), two new lines arise. The energy position of one of them corresponds to the result of the calculations of spatially quantized energy states for direct exciton in CdMnTe QW (see Fig. 3), and it doesn't depend on CdTe QW width. The intensity of this PL line from DX in CdMnTe QW increases as the magnetic field rises. Also, another line appears on its red wing at the energy distance from the first one that depends on the CdTe QW width. The magnetic field dependence of the energy of this line indicates that its giant spin splitting (GSS) [5,6] in the fields up to 4.5 T is reduced by 1/5 in comparison with the GSS for the DX exciton in CdMnTe QW. It is equal to the contribution in the GSS from of the electron in the semimagnetic quantum well. We believe that this line corresponds to the spatially separated indirect exciton 1eCdTe - 1hhCdMnTe.

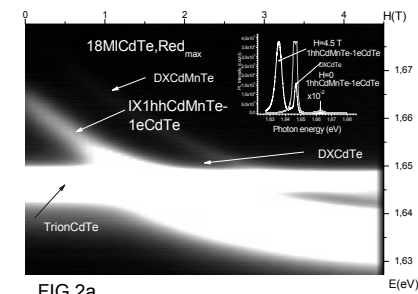


FIG.2a

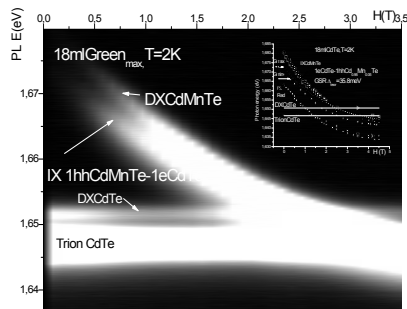


FIG.2b

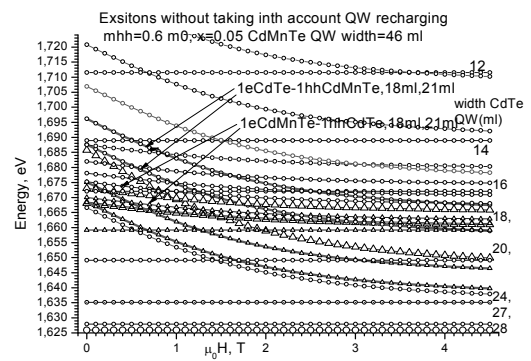
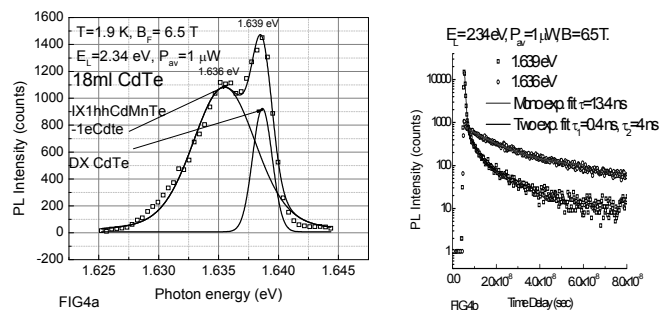


FIG.3

This is evidenced by the experiments on time-dependent spectroscopy PL from IX line. In Fig. 4a, b, one can see the results of the field and time dependent experiments, which show

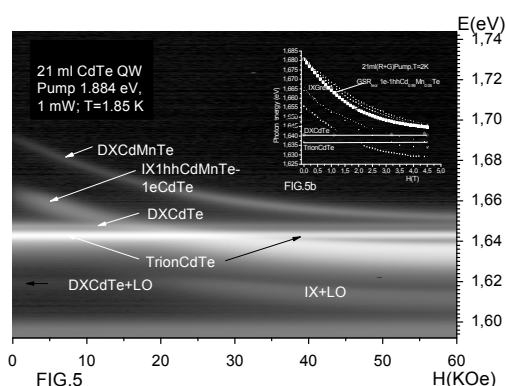


that the lifetime of the IX exceed by two orders of magnitude the lifetime of the trion states in the CdTe well.

The PL spectrum in is shown in Fig. 5 for the sample with 21 ml width

of the CdTe QW in and the case of the relatively low density of red excitation.

Though the spectral positions of DX in both the CdTe and CdMnTe wells are consistent with the calculation, the spectral position of the IX exciton and first of all its dependence on the excitation energy do not correspond to the calculations. We assumed that excited photo-carriers and background 2D gas of the carriers are unevenly distributed between two wells that leads to different volumetric charges in the wells. This charge difference depends on the conditions of the excitation and recombination of photo-carriers and excitons in different wells. The resulting electrical potential leads to the different shifts of the IX transitions depending on the conditions of the excitation.



The calculation of the position of the observed excitons in the assumption that one of the wells has an excess charge relative to the other showed that this assumption can qualitatively reconcile the calculation with the experiment. The charge almost doesn't change the energy positions of the direct excitons. It was found also that the PL position of the 1eCdTe - 1hhCdMnT IX exciton in over-barrier (green) excitation can be agreed with the calculation without taking into account

a charge difference in the wells if one does not take into account observed dependence of the energy of this line from the intensity of over-barrier excitation. At the same time, in order to agree the observed and calculated positions of the PL line of this IX exciton for under-barrier red excitation, it was necessary assumed that the semimagnetic well has an excessive negative charge compared to the CdTe well with the 2D electron density of order of 10^{10} cm^{-2} . The calculation of the amount of the excess charge in one of the wells remains a task for the future. One can only note that the over-barrier excitation is absorbed mainly in the coating layer of the structures, and the photo-carriers (excitons) must diffuse into the wells, while in the under-barrier case the light is absorbed directly in the quantum wells.

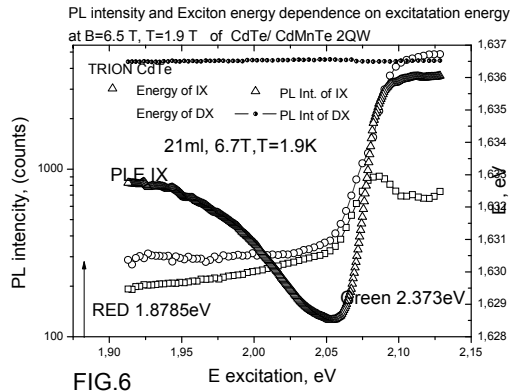


FIG.6

The measurements of the PL excitation (PLE) spectra of individual PL lines are also a confirmation that the difference in excitation quanta affects the energy of the indirect exciton. An example of such results is shown in Fig. 6 for the sample with the 21ml width CdTe QW. In this Fig. it can be seen that the difference in the IX spectral position for the green and red PL excitation is about 3meV for $H = 6.5T$.

The difference of the energy of the IX for green and red excitations increases as the widths of CdTe wells rises (from 18 till 30ml) up to almost 15meV (Fig. 7a, 7b).

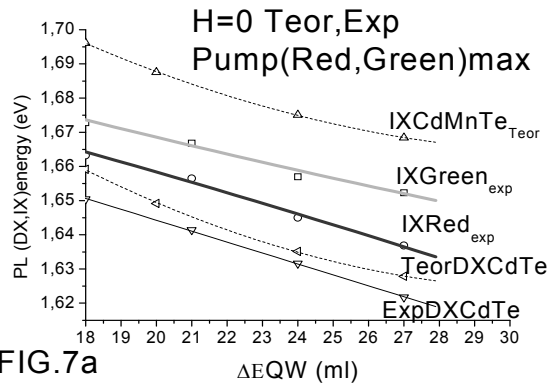


FIG.7a

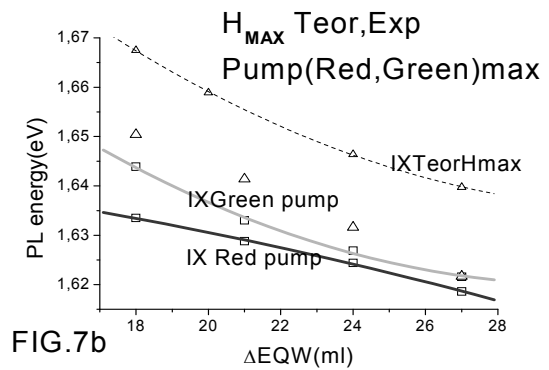


FIG.7b

Reference

1. L. V. Butov and A. I. Filin, Phys. Rev. B 58, 1980 (1998).;
2. V. B. Timofeev, A. V. Larionov, J. Zeman, G. Martinez, J.Hvam, D. Birkedal, and K. Soerensen, Physics-Uspekhi 41,109 (1998).
3. I. I. Reshina, S. V. Ivanov, D. N. Mirlin, I. V. Sedova, and S. V. Sorokin, Phys. Rev. B 74, 235324 (2006); A. Akimov, I. T. Godde, K. V. Kavokin, D. R. Yakovlev, I. I. Reshina, I. V. Sedova, S. V. Sorokin, S. V. Ivanov, Yu. G. Kus-rayev and M. Bayer, Condens. Matter 7, Jan (2017).
4. Ł. Kłopotowski, P. Wojnar, Ł. Cywinski, T. Jakubczyk, M. Goryca, K. Fronc, T. Wojtowicz, and G. Karczewski Condens. Matter 12 Feb.2015.
5. A.V. Komarov, S. M. Ryabchenko, I. I. Zheru, R. D.Ivanchuk, O. V. Terletskii, Sov. Phys. JETP 46, 318 (1977).
6. J. K. Furdyna, J. Appl. Phys. 64, R29 (1988).
7. A.Vertsimakha, S.Lev, and V.Sugakov, Physics of the Solid State 46, 948(2004).
8. S.Lev, V.Sugakov, and G.Vertsimakha, J.Phys.: Condens.Matter 16, 4033 (2004).
9. O.Terletskii, S.Ryabchenko, V.Sugakov, A.Vertsimakha, O.Tereshchenko, and G.Karczewski.Phys. Status Solidi C 14, No. 5, 1700124 (2017).

Structure and properties of Ge adsorption complexes on the Si(001) face

O.I. Tkachuk, M.I. Terebinska, Ya.S. Krivoruchko, V.V. Lobanov

*Chuiko Institute of Surface Chemistry of National Academy of Sciences of Ukraine,
17 General Naumov Str., Kyiv, 03164, Ukraine,*

E-mail: tkachuk_olya@bigmir.net

The state-of-art of natural science is characterized by a rapidly growing interest in the structures of the nanometer range, the technology of their obtaining, the physical and chemical properties of such systems, due to the prospects for their further practical use. Nanosystems are also called quantum-sized and include films, threads and dots. The latter are formed as a result of the spatial constraints of three-dimensional systems along three directions and have characteristic sizes of ~ 10 nm. They are also called 0D structures, among which the dominant position is occupied by heterostructures formed due to deposition of atomic Ge on the Si(001) face by the method of molecular beam epitaxy [1].

Surface Si(001) is obtained using cycles of silicon surface treatment with Ar^+ ions followed by annealing at $T=1173$ K in an ultrahigh vacuum. The data of slow electrons diffraction indicate that after this processing, the face Si(001)(1×1) is reconstructed with the appearance of sections of types (2×1) and (4×2) on it.

An analysis of literature data on the suitability of quantum chemistry methods for describing the structure and properties of the surface Si(001) as pure and containing adsorbed Ge atoms has shown that the experimentally found buccal structure of surface dimers $>\text{Si}=\text{Si}<$ and $>\text{Ge}=\text{Si}<$ is fairly reproduced only with use of the methods that take into account the electronic correlation, including the functional density theory method with the exchange-correlation functional B3LYP and the 6-31 G** basis set.

Nowadays there is no complete understanding of the physical chemistry of the formation of germanium nanodots Ge/Si, especially with regard to the initial stages of Ge atoms and Ge_2 dimers adsorption on the of Si(001) face, due to the lack of reliable data found and mismatch between them. In experimental studies, the usual structure and properties of Ge islands are determined, and the initial stages of their formation remain unaddressed. In this case, methods of quantum chemistry are useful, which allow us to study nanostructures at atomic level.

The unreconstructed surface Si(001) was simulates by the $\text{Si}_{96}\text{H}_{84}$ cluster, its optimization led to a structure of type (2×1) (Fig. 1a), which corresponds to the local minimum on the surface of potential energy. The transition to the global minimum, i.e, to the structure of type (4×2), was carried out by the additional displacement of the atoms of surface dimers according to their antisymmetric arrangement in each row and with respect to the neighbors in adjacent strings (Fig. 1b).

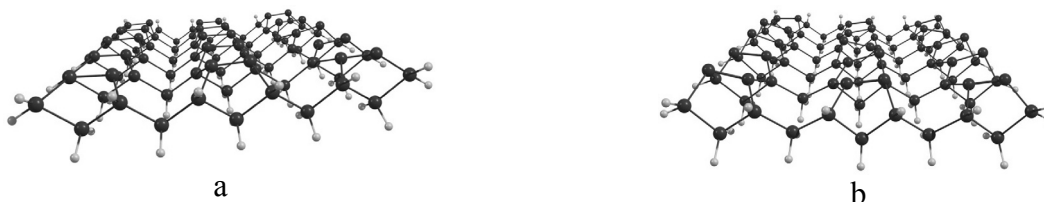


Fig. 1. Clusters that simulate the Si(001)(2×1) (a) and Si(001)(4×2) surfaces (b)

The results of the calculations performed have shown that the energy of the cluster, which simulated for the reconstructed surface Si(001)(4×2), is 24 eV below that of the cluster respective to the face Si(001)(2×1).

The calculated band gap width E_g for cluster 1 b was 1.32 eV, and that for the surface with symmetric dimers was 0.57 eV, while its experimental value is 1.21 eV at $T = 0$ K. A slight difference between the theoretically calculated value E_g and the experimentally obtained one is a proof of the adequacy of the use of cluster 1 b for further calculations [2].

The formation of a quantum dot on the face Si(001) starts with the adsorption of isolated Ge atoms on the active surface sites. These include the silicon atoms of surface dimers (in *up* and down positions).

Direct calculations of the equilibrium structure of the Si(001)•Ge adsorption complexes with different initial positions of the Ge atom relative to the atoms of the Si(001) face led to a structure with adatom localization in the silicon down-atom neighborhood of the surface dimer with the binding energy of 7.8 eV (Fig. 2).

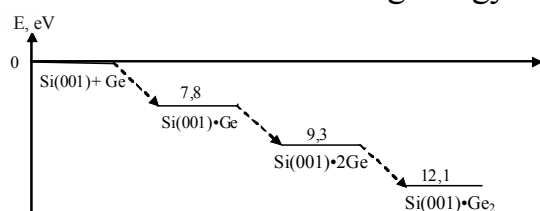


Fig. 2. Formation energy of the adsorption complexes Si(001)•Ge, Si(001)•2Ge and Si(001)•Ge₂

The adsorption complex was represented by the cluster Si₉₆H₈₄•Ge, its ground electronic state appeared to be singlet, despite the fact that the ground state of its constituents is triplet. In this complex, the Si–Ge bond length is 2.44 Å, while in the two-atomic Si–Ge molecule in the triplet (ground) state it is 2.11 Å. Such an elongation of the Si–Ge bond in the adsorption complex indicates the mobility of the Ge atom and its possible displacement over the surface, i.e. the possibility of surface diffusion.

The energy of the cluster Si₉₆H₈₄•Ge₂ formation from the cluster Si₉₆H₈₄•Ge and a Ge atom is 1.5 eV (see Fig. 2). A significant deviation of this value from the binding energy of the cluster Si₉₆H₈₄ of the first Ge atom indicates a significant interaction of Ge atoms in the adsorption layer of the surface Si(001).

After adsorption of two Ge atoms on the Si(001) surface, their surface diffusion takes place, with the formation of an adsorption complex Si₉₆H₈₄•Ge₂, its energy being for 2.8 eV below that of the complex with separated Ge atoms at the surface (see Fig. 2).

An analysis of experimental data and the results of quantum-chemical calculations allow us to propose four different configurations of Ge₂ dimers relative to surface silicon dimers (see Fig. 3). The Ge₂ dimer may be located above the surface >Si=Si< dimers in parallel with them (configuration A). The configuration B differs from the previous rotation of the Ge₂ dimer by 90° and is characterized by the perpendicularity of the surface dimers >Si=Si< and dimer Ge₂.

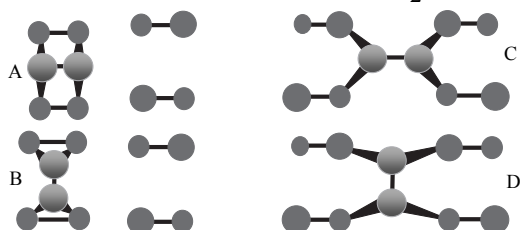


Fig. 3. Schematic representation of the structure of possible Ge₂ sorption complexes on the reconstructed face Si(001)(4×2)

According to our calculations, the most advantageous in energy is the configuration A, followed by the configuration B (210 meV), then the configuration C (820 meV), and the configuration D (1.8 eV) is the least stable [3].

After the formation of the Ge₂ dimer in configuration A, one or two Ge atoms can be diffused into the bulk phase of the substrate with the simultaneous release of one or two silicon atoms, respectively.

Configuration A1 (Fig. 4), its energy is 80 meV more, is the closest to energy of configuration A. In the configuration A2, two Ge atoms in the bulk phase of the substrate are located on one side of the newly formed surface dimer >Si=Si<. The energy of this configuration is 120 meV above that of the configuration A. Transition to the configurations A3 and A4 is due to the income of 220 meV of energy relative to the energy of configuration A.

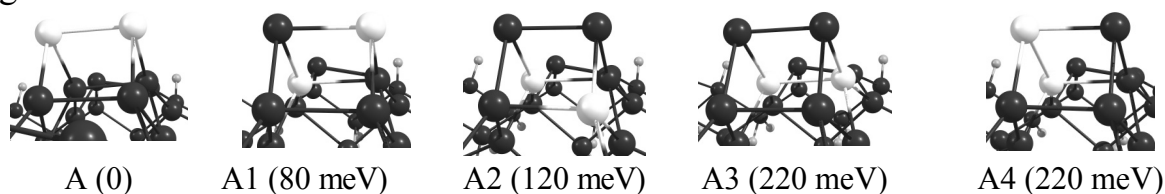


Fig. 4. The configuration of Ge–Ge dimer (A0) and configurations derived from it by the interchange of Ge atoms and Si atoms on substrate Si(001)(4×2)

The most accurate and exhaustive information on the structure of adsorption complexes and on the local environment of atoms in molecular systems, which can also be related to adsorption complexes on the solid surface, can be obtained from the analysis of photoelectron spectra [4].

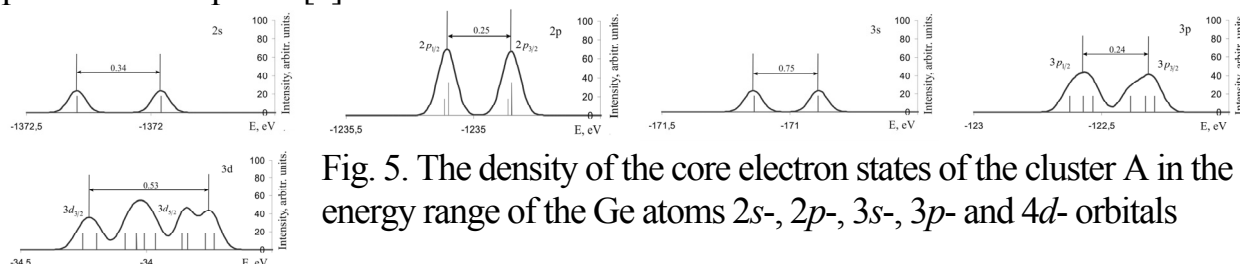


Fig. 5. The density of the core electron states of the cluster A in the energy range of the Ge atoms 2s-, 2p-, 3s-, 3p- and 4d- orbitals

The spectrum of the density of single-electron states of the cluster Si₉₆H₈₄•Ge₂ (Fig. 5) shows that the peaks 2s - and 3s- have a bimodal form that reflects the nonequivalence of Ge atoms in the surface dimer >Ge=Ge< of the reconstructed surface Si(001)(4x2). In addition, the intensities of the 2p(3/2) and 2p(1/2), as well as the 3p(3/2) and 3p(1/2) components are practically the same, which does not meet the theoretical statements on the population of the respective levels, what is true for the Ge₂ molecule. The shape of the line of the segment of the spectrum, which corresponds to the energy of the Ge atom 3d- electron, differs from the bimodal and to some extent retains the motives of the form of the corresponding line of the Ge₂ molecule. It should be noted that in this case, its complicated form is due not only to the formation of internal molecular orbitals (IMO), but also to the already mentioned equivalence of Ge atoms in the surface dimmer >Ge=Ge<. An analysis of the density of single-electron core levels in the range of the Ge atom energies 2s-, 2p-, 3s-, 2p- and 3d-electrons in clusters A, A1–A4 shows that the position of 3d- is the most sensitive to the mutual positions of Ge and Si atoms.

The table shows the shifts of the levels of the spin-orbital component 3d(5/2) of the clusters A1-A4 relative to their positions in cluster A, where it can be concluded that the

penetration of the Ge atoms of surface dimer $>\text{Ge}=\text{Ge}<$ into the bulk phase of the substrate leads to increase in the absolute values of $3d$ - electrons binding energy for clusters A1 and A4, i.e. for clusters that simulate configurations where there is a mixed $>\text{Si}=\text{Ge}<$ dimer on the surface.

Table

Chemical shifts (eV) of the component $3d(5/2)$ of the $\text{Ge}(3d)$ line in clusters A1, A2, A3, and A4 relative to its position in cluster A.

+0.12	-0.08	-0.07	+0.10
-------	-------	-------	-------

Thus, the results of the calculations performed using the expanded cluster model of the $\text{Si}(001)(4\times 2)$ face allow the following conclusions to be made:

- the adsorption of one Ge atom takes place on a triple-coordinated silicon down-atom of the surface dimer, the energy effect of the corresponding process is 7.8 eV;
- the energy effect of adsorption of the second Ge atom by the $\text{Si}_{96}\text{H}_{84}\bullet\text{Ge}$ cluster is only 1.6 eV, indicating a significant interaction between the adsorbed Ge atoms;
- formation of dimer Ge_2 on the surface of the cluster $\text{Si}_{96}\text{H}_{84}\bullet\text{Ge}_2$ is also an exothermic process, which results in the formation of a pure surface dimer $>\text{Ge}=\text{Ge}<$ which is placed over a row of surface dimers $>\text{Si}=\text{Si}<$ parallel to them (configuration A);
- the energies of the configurations formed upon the mutual exchange of Ge atoms of the surface dimer $>\text{Ge}=\text{Ge}<$ with the silicon atoms of the surface dimers $>\text{Si}=\text{Si}<$ slightly differ from the energy of the initial configuration A.
- atomic orbitals of a completely occupied d - subshell of the Ge atom take part of the formation of IMO, which determine the high binding energy of the surface dimer $>\text{Ge}=\text{Ge}<$;
- for the cluster $\text{Si}_{96}\text{H}_{84}\bullet\text{Ge}_2$ with one Ge atom embedded in to the crystalline substrate, the chemical displacement of the components $3d(5/2)$ of the $\text{Ge}(3d)$ line is positive, what corresponds to an increase in the binding energy of the relative electrons in comparison with the cluster containing the surface dimer $>\text{Ge}=\text{Ge}<$. For the cluster $\text{Si}_{96}\text{H}_{84}\bullet\text{Ge}_2$ with two Ge atoms in the substrate, the chemical shift is negative.

References

- [1] O.I. Tkachuk, M.I. Terebinska, V.V. Lobanov. Chemistry, Physics and Surface Technology 5(3) (2014).
- [2] O.I. Tkachuk, M.I. Terebinska, V.V. Lobanov Physics and Chemistry of Solid State 16(2) (2015).
- [3] O.I. Tkachuk, M.I. Terebinska, V.V. Lobanov, Surface. 5(20), 26 (2013).
- [4] O.I. Tkachuk, M.I. Terebinska, V.V. Lobanov, A.V. Arbuznikov, Computation 4(14) (2016).

Photovoltaic properties of nanocomposite ionatron structures InSe <RbNO₃>

**I.G. Tkachuk, V.M. Vodopianov, V.I. Ivanov, Z.D. Kovalyuk ,
V.V. Netyaga**

Selenium indium is one of the most promising 2D materials. Structurally perfect 2D crystals InSe are characterized by higher electron mobility values ($> 10^3 \text{ cm}^2 \cdot \text{B}^{-1} \cdot \text{s}^{-1}$ at $T = 300 \text{ K}$) as compared to other 2D materials. It is also more stable in relation to the environmental impact (O_2 , H_2O molecules). On the basis of this material, various van der Waals heterostructures with high quality heterogeneous structures were created.

Solid-state ion-neutron structures based on laminated InSe crystals and RbNO₃ ionic salt can be made by introducing ion saline in the van der Waals cleavers. Studies on the chemical composition, structure and morphology of these materials have shown that they can be considered as vertical ionatron structures such as "2D semiconductor - in - ion salt oxide". The formation of oxide on the heterogeneous boundary between the ionic salt and the layers of the semiconductor with this technology takes place when the ion salts are decomposed into nitrides and nitrates. In this change the morphology and chemical composition of the heterogeneous structures of these structures

Mechanisms of photoconductivity of ionatron structures are practically not investigated. An effective method for investigating the photoconductivity of heterophasic materials is the method of impedance spectroscopy, which is also used to study the ion conductivity of ionic nanocomposites.

The ionatron nanostructures formed on the basis of InSe and RbNO₃ consisted of sequentially placed InSe layers along the C-axis, ultra-thin layers of In₂O₃ oxide and ion salt islands. The latter had a height lower than the width of the Van der Waals slit InSe ($\sim 0.35 \text{ nm}$) and formed in planes (0001) nanoscale rings with a diameter $< 50 \text{ nm}$. The superficial density of the arrays of the rings was $\sim (109 \div 1010) \text{ cm}^{-2}$.

The photosensitivity spectra of the structures were studied using modulated light flux using the MDR-3 monochromator. The spectral distribution of relative quantum efficiency was determined by the ratio of the value of the photocurrent to the number of incident photons.

The spectral characteristics of photoconductivity for the ionatron structure InSe <RbNO₃> and the pure InSe crystals investigated at $T = 300 \text{ K}$ are shown in Fig. The effect of the existence of significant photosensitivity in ion-neutron materials at energies $h\nu < E_g$ is associated with the formation of a nanotexturized boundary between ionic salt and a layered crystal under plastic deformation of InSe and the characteristics of photoconductivity in structures formed on the basis of anisotropic layered crystals.

The photosensitivity of ionatron structures significantly exceeds the photosensitivity of InSe single crystals. It is observed only when applying a constant voltage $V \sim (5 \div 10) \text{ B}$. At $V > 10 \text{ V}$ (outside the "electrochemical window of a

solid electrolyte"), the effects of increasing photosensitivity and photosensitivity are not observed. However, they are restored at a voltage drop of $\sim 5 \div 10$ V. Unlike traditional MES structures, for ion-structure structures, electric breakdown and oxide destruction at high voltages are not observed.

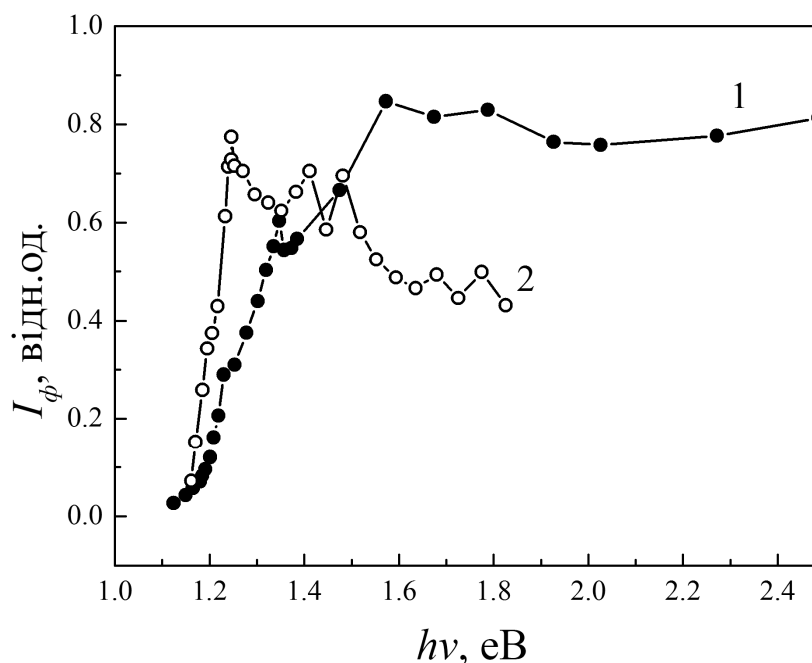


Fig. Spectral distribution of photosensitivity InSe (curve 1) and InSe <RbNO₃> (curve 2)

The photosensitivity of bulk pure n-InSe crystals along the crystallographic axis C is limited by the high concentration of packaging defects, which cause small values of the diffusion length for non-equilibrium photoconductors (\sim several microns). In our case, the ring ion nanostructures are at a short distance (\sim dozen nm) one relative to another. It is much smaller than the diffusion length of nonequilibrium carriers for InSe crystals. The photosensitivity of vertical 2D structures is proportional to the lifetime of minority carriers τ_l to the transit time τ_t (electron transfer between the contacts). The value τ_t depends on the distance between the contacts t , the applied constant voltage V and the electron mobility μ : $\tau_t = t^2 / \mu V$. Consequently, photosensitivity in 2D materials increases with decreasing t and increasing V . These conditions are fulfilled for the investigated bulk ionatronic structures. In these, carrier transport takes place between 2D InSe layers (thickness of which is $t \sim$ dozen nm) in conditions of high electric field strength created by double-layer electric nanocomponents.

Thus, it was established that the creation of an ion nanocomposite with high ionic conductivity on the heterogeneous boundary between the ionic salt and the n-In₂O₃ oxide is a prerequisite for achieving high photosensitivity in ion-structured structures formed on the basis of an InSe layered semiconductor and an ion salt of RbNO₃. High photoconductivity in these structures is associated with the formation of nanocomposers with an electric double layer when applied to structures of constant voltage and with the transfer of non-equilibrium current carriers in a strong electric field created by these nanocompulsors.

Characterization of PbTe and PbSe thin films prepared using pulsed laser deposition method

Tur Yu, Virt I.S.

Drohobych State University, I. Franko, 24, 82-100, Ukraine

Topological insulators represent a novel state of matter with surface charge carriers. The topological insulator phase has been predicted and confirmed to exist in a number of binary compounds. Thin films of PbTe and PbSe is an materials are attractive to fundamental physics studies and technological applications. This chalcogenides have attracted considerable attention because of their potential applications especially for small-scale devices and for power generators in remote systems. In this paper the pulsed laser deposition method was used for films preparation.

The deposition of thin films with adequate morphology and a crystalline structure is a key point in the development of many research fields. During the last two decades, the pulsed laser deposition (PLD) technique has been applied increasingly to the synthesis of thin films because of its versatility for the deposition of practically any kind of material with a relatively simple experimental set-up [1, 2]. The versatility of PLD also lies in the possibility of obtaining films very adherent to the substrates, even at room temperature and with a high predictable growth rate, which can be precisely controlled through a priori studies of the experimental parameters. Adequate selection of the irradiation conditions, as well as the chemical and physical properties of the target materials, is crucial for the production of very adherent thin films [3]. Moreover, the choice of substrate temperature may also affect the quality of thin films from the morphological and structural features point of view [4].

This paper discusses laser methods for fabricating vaporizes. Quality PbTe and PbSe topological insulators films were epitaxially grown on Si (100) substrate using pulsed laser deposition (PLD). Laser is a powerful tool in many applications. Often the light beam is intense enough to vaporize the hardest and most heat resistant materials. A proposed method is to use a defocused laser to apply energy at a single nucleation site, and then propagate materials growth by scanning the laser along the substrate. The explanation of epitaxy mechanisms in PLD is a most important and difficult problem. The deposition process of Pb thin films by PLD technique was also studied by using the fundamental wavelength of Nd:YAG at 1064 nm. However, the deposited films were non-homogeneous with a high droplet density on the film surface. It is well known that the quality of the deposited films is strongly related to the laser parameters, such as laser wavelength and laser fluence. In the same paper was also showed that the droplet density lowered by the laser fluence. Therefore, in this work the laser fluence was fixed as closely as possible to the ablation threshold in order to reduce the thermal effects on the target during the ablation process decreasing, in this way, the formation of the melted material which is responsible of the presence of droplets on the film surface. The substrate temperature was changed as effort to improve the homogeneity of the Pb

thin films which is very important for the application of such device as photocathode.

The study is of great interest for the R&D of photocathodes and in particular for Nb superconducting radio-frequency guns (SRF), which combine the advantages of photo-assisted production of high brightness and short electron pulses with reduced electrical losses and continuous wave operation [2]. SRF cavities present a main drawback in the low quantum efficiency (QE) of the material used for their fabrication with respect to other metallic photocathodes, reducing the possibility of obtaining electron beams of high current [4]. The most promising alternative seems to be the insertion of a small photo-emitting spot made of an alternative material, which improves the photoemission performance of the SRF cavity but preserves its quality factor [3]. The use of Pb has been proposed as an excellent solution because its superconducting critical temperature of 7.2 K is quite similar to that of Nb (9.3 K) and the QE of Pb is an order of magnitude higher than that of Nb [1].

With the idea of a hybrid Nb/Pb cathode, after a dedicated study to find the most suitable experimental conditions to get Pb thin films with morphological and structural characteristics adequate for a photocathode, we deposited a Pb thin film on a Nb substrate to test the photoemission performances of such device comparing the results with a Pb bulk cathode.

Thin films of different thickness, 100-1000 nm, have been prepared PLD on Si substrates by at temperature 200 °C. It has been shown that the structural features of the films. The films deposited on Si have a polycrystalline textured structure. The films were polycrystalline, but the deposition time, the substrate temperature, and the kind of a substrate used affected significantly the film crystallographic order. The evolution of the film structure and morphology as a function of the film thickness was investigated. One concludes that the increase of a particular orientation is due to an increase of the number of crystallites along the plane. Low texture coefficients indicate that the films have a low degree of crystalline order which can be improved by the increase of the crystallite size. The results demonstrate the potential of PLD for the growth of PbTe and PbSe and related materials for topological insulator studies.

- [1] Freik D. M., Galushchak M. O., Krynytskyi O. S., Matkivskyi A. M. New nanocomposite thermoelectric materials // *Physics and Chemistry of Solid* - 2013 - T.14, №2 - P.317.
- [2] Virt I. S., Kurylo I. V., Rudyi I. O., Lopatynskyi I. E., Fruzhynskyi M. S. Structure and electrical properties of thin films Bi_2Te_3 , Sb_2Te_3 i Bi_2S_3 and uper-structures Bi_2Te_3 - Sb_2Te_3 , received by pulsed laser deposition // *Visn. Nat. Univ. "Lviv Polytechnic"*. - 2007. - № 592: Electronics. - P. 115-121.
- [3] Pei Y.-L. Electrical and thermal transport properties of Pb-based chalcogenides: PbTe, PbSe, and PbS / Y.- L. Pei, Y. Liu // *Journal of Alloys and Compounds*. - 2012. - number 514 - P. 40 - 44.
- [4] Zhu P.-W .. High thermoelectric properties of PbTe doped with Bi_2Te_3 and Sb_2Te_3 / P.-W. Zhu, Y. Imai, Y. Isoda, Y. Shinohara, X.-P. Jia, G.-T. Zou. // *Chin.Phys.Lett* .. - 2005. - V.22, N 8. - P. 2103-2105.

Nanocomposite elements for HIC and sensors with a fusible glass matrix

Lepikh Ya.I., Lavrenova T.I.

*Interdepartmental scientific-educational physicotchnical centre of MES and NAS of Ukraine at the Odessa I.I.Mechnikov national university
e-mail: ndl_lepikh@onu.edu.ua*

Functional basis of materials (pastes) for thick-film elements of hybrid integrated circuits and sensors are, as a rule, metal-oxide compounds of ruthenium, silver, palladium and gold and also oxides, carbides, boruicides, nitrides, silicides of the other metals. Nanocomposite elements based on the "glass-metal compounds" are formed by the annealing of the pastes which are composed of a mix of superfine powders of a glass and a functional material which disperse in special organic binding agent. During the pastes annealing glass powders fuse and cake in a glass matrix in which particles of a functional phase are fixed, forming current-carrying circuits. Therefore the complex of physical properties of composite elements is appreciably caused by properties and structure of glass binding agent (the temperature of softenings beginning, CLETR, specific surface resistance, chemical stability etc.). The basic lacks of known glass binding agents: the high temperature of softenings beginning of a glass binding agent $580 - 750^{\circ}\text{C}$, which raises expenses of energy for nanocomposite manufacturing during their annealing (annealing temperature $800-900^{\circ}\text{C}$); presence of toxic lead connections.

In the work the processes of glass forming and crystallization and physical properties of glasses on the basis of system $\text{Bi}_2\text{O}_3\text{-SiO}_2\text{-B}_2\text{O}_3\text{-ZnO-MgO-CdO}$, CuO at different concentrations of initial components ratio are investigated. As the basic glass-forming component of a glass the bismuth oxide which enables receiving of more fusible glasses is selected instead of plumbum.

Optimum concentration of initial components and alloying impurities for reception of fusible glassy materials [1] are established.

Advantages of a fusible glass are: reduction of the temperature of a glass softening beginning ($400 - 450^{\circ}\text{C}$); withdrawals from the glass compound of toxic lead; reduction CLETR; increasing of specific surface resistance $1 \cdot 10^{14} - 5 \cdot 10^{14}$ Ohm /cm. The glass does not crystallize in the interval of temperatures $300-1000^{\circ}\text{C}$. The glasses have II hydrolytic class.

References:

- [1] Patent Ukrainy na vynahid №113565. Legkoplavke sklo dlya nanokompozitiv // Ya. I. Lepikh, T.I. Lavrenova. MPK C03C 3/062. publ. 10.02.2017, Byul. №3.

A METHOD OF MINORITY CHARGE CARRIERS BASIC PARAMETERS DETERMINATION IN SOLID MATTER

Y. Uhryn, V. Brytan, I. Kosivchak, M. Govda

*Drohobych Ivan Franko State Pedagogical University, 24 I. Franko Street., 82100
Drohobych, Ukraine*

Up to now the researchers found the magnetoresistance measurements to be not informative concerning charge carriers basic parameters in solid matter [1].

The aim of this paper is to develop the magnetoresistance method to determine basic parameters of the minority charge carriers in solid matter [2] and apply it to a different solids.

To achieve this aim we must consider the phenomenological model of galvanomagnetic phenomena for isotropic material with two types of charge carriers (having opposite or the same sign). It is known [5] that the transverse resistivity ρ for this case depends upon the magnetic field induction in the following way:

$$\rho = \frac{1}{\sigma} = \frac{1}{e} \frac{n\mu_n + p\mu_p + \mu_n\mu_p(n\mu_p + p\mu_n)B^2}{(n\mu_n + p\mu_p)^2 + \mu_n^2\mu_p^2(n-p)^2B^2}, \quad (1)$$

If we state now the condition $d^2\rho/dB^2 = 0$ we obtain the magnetic field position of ρ flex point B_f

$$B_f = (1 + ab)/(\sqrt{3}(1 - a)\mu_n), \quad (2)$$

where $a = n/p$, $b = \mu_n/\mu_p$.

Let us write the condition for electrons as minority charge carriers. It is $a \ll 1$. Since, the minority charge carriers mobility is, as the rule, higher or compared with the majority ones, that is $b \geq 1$, then $a \ll b$ and the magnetic field dependence of ρ gets the form:

$$\rho = \rho_0 \left(1 + \frac{\mu_n}{\sqrt{3}B_f} B^2 \right) / \left(1 + \frac{1}{3B_f^2} B^2 \right), \quad (4)$$

For $B = B_f$ writing for convenience $\rho(B_f) = \rho_f$ we obtain:

$$\mu_n = \frac{\sqrt{3}}{B_f} \left(\frac{4}{3} \frac{\rho_f}{\rho_0} - 1 \right), \quad (5)$$

Thus, as can be seen from the last formula if the condition $n \ll p$ is fulfilled, the measuring of the transverse magnetoresistance provides the information about the minority charge carriers mobility. Is enough to find the magnetoresistance flex point B_f and to measure resistivity in this point ρ_f and in zero field ρ_0 .

From equation (2) for $a \ll 1$, taking into account that $ab = \sigma_n/\sigma_p$, we get another useful formula

$$\sigma_n/\sigma_p = 4(\rho_f/\rho_0 - 1), \quad (6)$$

In the strong field limit, taking into account that $a \ll 1$ and $a \ll b$, equation (1) results after the simple treatment in the formula for saturation resistivity:

$$\rho_{\infty} = \frac{1}{\sigma_p}. \quad (7)$$

From this equation, eq. (5) and (6) and taking into account that $\sigma_n = en\mu_n$ we obtain formula for determining the concentration of minority charge carriers on the base of experimentally measured values

$$n = \frac{4B_f}{\sqrt{3}e\rho_{\infty}} \left(\frac{\rho_f}{\rho_0} - 1 \right) / \left(\frac{4}{3} \frac{\rho_f}{\rho_0} - 1 \right). \quad (8)$$

Return to the equation (4). In the strong field limit we can neglect 1 in comparison with the summand containing B in the numerator and denominator of (4), getting another formula for determining μ_n

$$\mu_n = \rho_{\infty} / \sqrt{3} \rho_0 B_f. \quad (10)$$

Combining the latter formula with (5) we get the relation between the experimentally measured values ρ_0, ρ_f and ρ_{∞} :

$$\rho_{\infty} = 4\rho_f - 3\rho_0. \quad (11)$$

which is the test relation for the semi classic behaviour (1) of a real experimental curve.

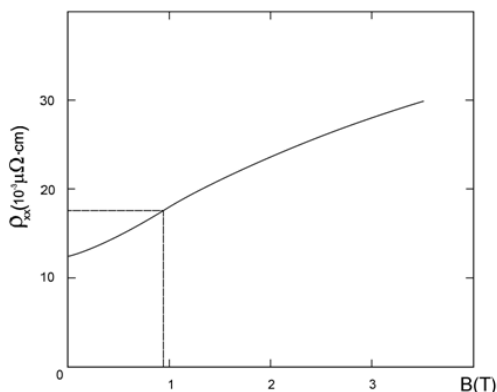


Fig. 1 – Magnetic field dependence of transverse resistivity for refined Al. Dashed lines indicate flex point B_f and resistivity in this point $\rho(B_f)$. The curve is obtained from experimental data of [4].

Now we give some examples illustrating how the introduced method works.

Fig. 1 shows the magnetic field dependence of resistivity for refined sample of this metal [4]. In fact, the presence of transverse magneto-resistivity is the evident of two types charge carriers existence. Calculations using formula (5), (6), (7) and (8) for different refined Al are introduced in the Table. 1.

As another example of conductor take an organic one $(BEDT-TTF)_2KHg(SCH)_4$.

Table. 1 – Purification dependence of electron mobility μ_n , electron concentration n , electron conductivity σ_n and hole conductivity σ_p for Al

purification	$\mu_n \left(\frac{m^2}{V \cdot s} \right)$	$n (10^{28} m^{-3})$	$\sigma_n (10^9 \Omega \cdot m)$	$\sigma_p (10^9 \Omega \cdot m)$	σ_n / σ_p
refined	1.75	1.9	5.4	2.9	1.87
zone refining	14.3	2.0	45.9	23.3	1.97
superrefined	19.6	1.9	61.1	32.5	1.88
99.999+%	20.1	2.1	66.9	33.3	1.87

For semiconductor we get the result what is in good agreement with the Hall-

effect measurement results [5].

The most interesting example of is calculating the minority charge carriers mobility of superconductor in the critical temperature range.

Fig. 2 shows the experimental dependences of transverse resistivity on the magnetic field inductance for several temperatures for high temperature multilayer superconductor $\left[YBa_2Cu_3O_7 \left(72 \text{ \AA} \right) / PrBa_2Cu_3O_7 \left(12 \text{ \AA} \right) \right]_{25}$ near critical point $T_c = 89.5 \text{ K}$, namely for $T > T_c$. The fact of appearance of magnetoresistance at $T < 91 \text{ K}$ testifies the rise of a new sort of charge carriers.

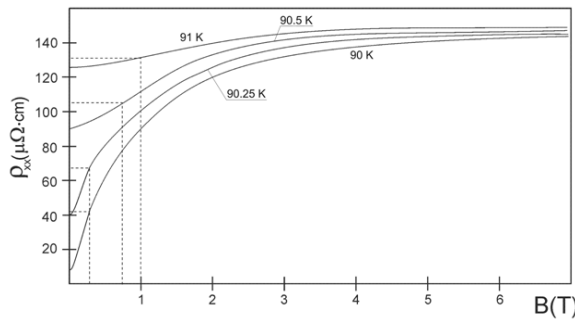


Fig. 2 – Magnetic field dependences of transverse resistivities for multilayer superconductor $\left[YBa_2Cu_3O_7 \left(72 \text{ \AA} \right) / PrBa_2Cu_3O_7 \left(12 \text{ \AA} \right) \right]_{25}$ at different temperatures near critical one ($T = 89.5 \text{ K}$). Magnetic field is perpendicular to the layers. Dashed lines indicate flex points B_f and resistivities in these points. Experimental data are obtained from temperature dependences of transverse resistivity at different magnetic fields from [6]

The results of the calculations are shown in Table. 2 demonstrating the sharp increase of the negative sign charge carriers mobility, when the temperature approaches to superconductivity transition, which causes the same rate of their conductivity increasing. At the same time, majority charge carriers conductivity remains constant, what certainly shows their basic parameters to be constant. This abrupt conductivity change from hole to electron-like induces us to suppose that electrons being minority charge carriers in the normal state play majority role in the superconductive state.

Table. 2 – Temperature dependence of charge carriers basic parameters in layered superconductor $\left[YBa_2Cu_3O_7 \left(72 \text{ \AA} \right) / PrBa_2Cu_3O_7 \left(12 \text{ \AA} \right) \right]_{25}$. The meanings of the symbols are the same as in Table. 1.

T_n (K)	$\mu_n \left(\frac{m^2}{V \cdot s} \right)$	$\mu_p \left(\frac{m^2}{V \cdot s} \right)$	p (10^{27} m^{-3})	σ_n / σ_p	σ_p ($10^5 \Omega \cdot m$)	σ_n ($10^5 \Omega \cdot m$)	n ($10^{24} \Omega \cdot m$)	a	b
91	0.7	0.0018	2.2	0.23	6.5	1.5	1.3	0.0059	390
90.5	1.3	0.0018	2.2	0.67	6.5	4.4	2.1	0.0095	720
90.25	7.1	0.0018	2.2	2.7	6.5	17.6	1.5	0.0068	3900
90	40.9	0.0018	2.2	16.5	6.5	107	1.7	0.0077	22000

Since one can find out the similar magnetoresistivity behavior near T_c in other cuprate high temperature superconductors, doped by *Nd*, *Tm*, *Bi*, *Ca*, *Sr*, as well as in conventional ones [6], we can suppose that this temperature dependence of mi-

nority to majority charge carriers conductivity ratio is general, including the case when the minority charge carriers are positive, as it is for *Nd-Ce-Cu-O* [7].

Note also, that applying of our equations, which origin from semiclassical analysis of galvanomagnetic phenomena is reasonable for this case, since experimental curves showed in the Fig. 2 are in good agreement with the test equation (11).

The introduced interpretation of magnetoresistance behavior in superconductors also solves the problem of Hall-effect anomaly near critical temperature [6].

We explain this sign reversal by the great electron mobility obtained above. As we can see from the expression for the Hall constant in the weak magnetic field [3]

$$R_H = (p - nb^2) / e(p + nb)^2. \quad (12)$$

the sign of R_H will reverse negative when $b^2 > p/n$ that in its turn is provided by the great value of electron mobility μ_n .

We can conclude that the introduced new method of determination the minority charge carriers mobility can be applied for all solid materials (probably not only for solid ones) giving new opportunities for their studying. The most interesting result after using this method is found for a superconductor showing rapid increase of minority charge carriers mobility when the temperature approaches the critical one from the normal state temperature region. This rapid increase makes minority charge carriers responsible for appearance of superconductive state.

REFERENCES

1. E.V. Kuchis, Galvanomagnitnye Effecty i Methody of ikh issledovania, Radio i Sviaz, Moscow, (1990).
2. Y. Uhryn, Invention Patent N 87695, Bulletin N 15, 10.08.2009.
3. Smith R., Semiconductors, Cambridge University Press, (1978).
4. Luck R., Phys. Stat. Sol, 18, 49, (1966).
5. Y.O. Uhryn, R.M. Peleshchak, V.B. Brytan, A.A. Velchenko Magnetoresistance based determination of basic parameters of minority charge carriers in solid matter Condens. Matter Phys., 2017, vol. 20, No. 4, 43702.
6. C.P. Poole, H.A. Faserach, R.J. Creswick, Superconductivity, Elsevier, (2014).
7. Qiu X.G., Jakob G., Moshchalkov V.V., Bruynseraede Y. and Adrian H., Phys. Rev. B, 52, 12994, (1995).

Low Frequency Noise in Polycrystalline ZnO Thin Films

Virt I.^{1,2}, Didovska O.¹, Bester M.²

¹*Ivan Franko Drohobych State Pedagogical University, Drohobych, Ukraine*

²*Centre for Innovation and Transfer of Natural Sciences and Engineering Knowledge, University of Rzeszow, Rzeszow, Poland*

As a broadband semiconductor ($E_g = 3.3\text{eV}$), the easily produced semiconductor, zinc oxide (ZnO) has a lot of interest due to the potential for a wide range of optoelectronic applications and is a functional material. One of the important applications is based on ZnO UV light sensor [1]. Doping can also significantly improve both the optical and electrical properties of 2D ZnO thin films. In this work we present the results of low frequency noise measurements from polycrystalline Zn-based polycrystalline layers in the dark as well as under UV radiation under normal conditions.

In this study, polycrystalline layers were used in ZnO-cobalt-doped layer synthesized on Al_2O_3 substrate by pulsed laser deposition. The samples were made by the laser spraying the target at 30°C for 30 minutes. A rectangular sample measuring $7.0 \times 3.0\text{ mm}$ was made to test the electrical conductivity of the material. Metallic Ag contacts were then made. Photoelectronic and noise properties will also be discussed. ZnO photoconductance is often dominated by surface-mediated phenomena, and oxygen chemisorptions always play a key role in photosensitivity regulation. A high-quality ceramic ZnO disk was used as the target source. The pressure in the chamber was maintained at 10^{-6} Pa during the sputtering process. The thickness of the films ZnO was about 300 nm. The sample was placed in a shielded kilt. Amplifier was 100 by UNIPAN amp. The noise current was fed to the low level amplifier and the output signals were analyzed using a DSO oscilloscope. The frequency range of $10\text{ Hz} \div 1\text{ MHz}$ was selected for noise measurements. To determine the frequency content of the sampled signal, the discrete Fourier transform – DFT was used. The resolution that is obtained in the frequency domain depends on the time at which N samples of the input signal were collected. This time was related to the sampling frequency f_s and the length of the recorded record N as $t = N/f_s$. Then the number of collected samples required to obtain the appropriate resolution Δf is $N = f_s/\Delta f$.

The figure that shows the noise spectrum measured at approximately 30°C . The spectral power density of the measured S_V voltage fluctuations is presented. The spectral shape has also been corrected due to the amplifier transition function for the used amplifier. The power density DFT PD in Fig. 1. The sample shows the typical fluctuation characteristics of the time constraints and the frequency of ZnO photoconductive detectors. It is noted that the noise curve ZnO w is linear. While the ZnO layer is UV-exposed, the electric current increases significantly. The characteristic frequency dependence has the form $1/f$ [2]. In this case, the spectral density of the fluctuations, for example the voltage, can be shown in the $S_V(f)$ form, and for the relative S_N fluctuations (f) we have $S_N(f) = G_V(f)/V^2 = G_R(f)/R^2$,

where V , R are the average voltage and resistance of the test sample, and $G_V(f)$, $G_R(f)$ are the voltage and noise resistance spectra respectively [3].

Low-frequency noise, measured by UV radiation, is an order of magnitude higher in the dark. In the samples, the dependence of the spectral noise characteristic as $1/f$ was observed as well as the square dependence of its intensity on the average voltage. $1/f$ low frequency noise behaviour is observed on ZnO layers both in the dark and under UV illumination. After lighting with the energy of the photon around the energy reserve, photogeneration is partly electron-hole. The low frequency noise of the ZnO layers shows the proportionality f^{-1} similar behavior in both darkness and under lighting, where there is the frequency indicator. As you can see, the spectrum of measured fluctuations differs significantly from the $1/f$ ratio. The $f \cdot S$ from f plot has a maximum for the frequency $f_{\max} = 3$ kHz. The time

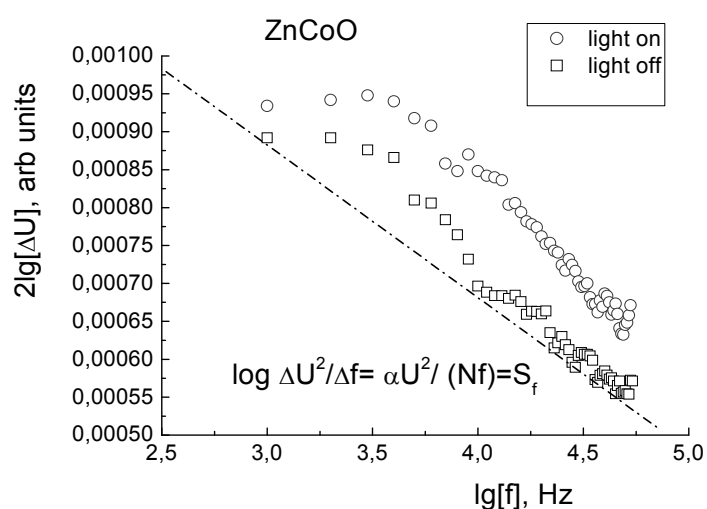


Fig. 1. The log–log plot of the voltage dependence of the noise power spectral density both in the dark and under UV illumination. The solid lines are linear fits $1/f$ to the data.

scale of changes is shown in Figure 1. As to other semiconductors, point defects also play an important role in the electrical and noise properties of the ZnO layers. To determine if the noise of the ZnO layer is derived from point defects, a measurement of noise in UV light was performed, which gives a higher conductivity. In the presence of UV light, the measured noise is usually one level of magnitude higher than the dark noise. A series of stochastic processes (trapping electrons) occurs, causing fluctuations in the dark current. After lighting with

photon energy above E_g , there are photogenerated electron-hole pairs. Anihilation of holes with negatively charged oxygen ions at the grain boundaries reduces the height of the inter-spherical barrier, which leads to increased conductivity with the participation of photogenerated electrons [4].

The indexed noise component contributes to an increase in the noise level in UV illumination by one order of magnitude. The superposition of kinetics of cargo trapping and migration has a continuous distribution of relaxation times. Distribution of activation energy would be almost constant in a sufficiently wide range to show $1/f$ noise. Some holes migrate to the grain boundaries and discharge negatively charged oxygen ions, which has a non-uniform distribution of oxygen-bound trap states or uneven distribution of intergranular barriers in the ZnO layer.

The current level of noise in ZnCoO nanostructural layers was investigated. Based on experimental research, it has been shown that the normalized spectral power density characteristic of disordered systems has an excessive $1/f$ -type noise. Excessive low frequency noise is usually a decisive factor in the spatial heterogeneity of semiconductor materials. It has been found that in comparison with other spatially unordered materials, these samples show a low degree of resistance changes which changes with ultraviolet (UV) lighting.

- [1] S.J. Chang, B.G. Duan, C.H. Hsiao, S.J. Young, B.C. Wang, T.-H. Kao, K.S. Tsai, and S.L. Wu IEEE Photonics Technology Letters, **V. 25**, 2043, (2013).
- [2] W.C. Lai, J.T. Chen, Y.Y. Yang *Optics Express*, **V. 21**(8), 9643-9651(2013).
- [3] O.V. Gerashchenko Technical Physics Letters, **V. 34**, pp 124–125, (2008).
- [4] D. Li, Y. Meng, P. Zhang, Z. Liu, and H. Zhao Japanese Journal of Applied Physics, **V. 52**, 084101, (2013)

ELECTRONIC STRUCTURES OF $\text{Si}_{1-x}\text{Sn}_x$ SEMICONDUCTORS: FIRST PRINCIPLES AND MODEL PSEUDOPOTENTIAL CALCULATIONS

P.M. Yakibchuk, O.V. Bovhyra, I.V. Kutsa

*Ivan Franko National University of Lviv, 8a, Kyrylo and Mefodiy Str.,
79005 Lviv, Ukraine, e-mail: oleh.bovhyra@lnu.edu.ua*

In semiconductor alloys, the band gap value and the lattice parameter are among the most important physical parameters, since these parameters control the band off-set and the mismatching in the different devices. A full range of technological advances are expected if it becomes possible to achieve semiconductors with any desired bandgap that can be adapted to specific applications. The bandgaps range that can be achieved in bulk crystalline alloys is practically limited by the strict requirement of the lattice matching in planar epitaxial growth. The larger tolerance to lattice mismatch at the nanoscale allows semiconductor alloy nanomaterials provide new opportunities for bandgap engineering.

The progress in epitaxial growth of GeSn and SiGeSn alloys paved the way toward direct bandgap optoelectronic devices as well as GeSn-based nanoelectronics with an enormous potential specifically regarding monolithic integration. Alloys and ordered compounds of Si-Ge-Sn group have particularly unique optoelectronic properties for applications in quantum-well intersubband technology, MOS-FET and n-FET devices. The demonstration of lasing in Si-Ge-Sn alloys can be seen as a breakthrough in group IV photonics [1].

Direct and indirect energy gaps, electron and hole effective masses as well as their composition dependences are the most critical parameters for band-structure calculations of tin based group IV semiconductor alloys. Therefore, an accurate knowledge of these parameters for binary $\text{Ge}_{1-x}\text{Sn}_x$ and $\text{Si}_{1-x}\text{Sn}_x$, ternary $\text{Ge}_{1-x-y}\text{Si}_x\text{Sn}_y$ is very important. Moreover, calculation of band offsets for $\text{Ge}_{1-x-y}\text{Si}_x\text{Sn}_y$ is useful for calculating the energy bands in quantum heterostructures.

There are many theoretical studies devoted to simulation of the band structures of binary GeSn and SiSn and ternary SiGeSn compounds using various approaches like the empirical pseudopotential method, the kp method, tight binding and density functional theory (DFT) based methods, which cover pseudopotential, full potential and coherent potential approximations (CPA).

Most of the reports cover only a limited composition range and the full range composition dependence of the band structure and band offsets is absent. The significant inconsistency in the reports data is observed for some properties, like the composition dependences of the band gaps, the threshold of Sn content causing indirect – direct crossover, the dependence of the energy gaps on the atomic distribution and the band offsets in the alloys.

Several theoretical reports have predicted that the indirect – direct crossover in $\text{Si}_{1-x}\text{Sn}_x$ alloys will occur at values from $x = 0.25$ to 0.67 , depending on the calculation method [2-5]. This dissimilarity in the results is mainly due to the difficulty of handling the randomness in alloy systems.

To help understand behaviour of bowing and related properties of the materials, we performed a calculation of the electronic band parameters for series $\text{Si}_{1-x}\text{Sn}_x$ semiconductor alloys. For this purpose, we have used model and ab initio pseudopotential plane wave methods within the mixed-atom supercell model of alloys. First principles calculations generally underestimate the band gap energies and require substantial computational time. The issue of band gap underestimation also becomes worse for narrow band gap materials, such as SiSn alloy.

In this study, for band structure calculation of $\text{Si}_{1-x}\text{Sn}_x$ alloys, we used the model pseudopotential (MP) plane wave method, which can predict the band structure of semiconductors with good accuracy [6].

Also, the DFT calculation was performed using the sX-LDA formalism in conjunction with a 4x4x4 Monkhorst-Pack grid in the first Brillouin zone and a 500 eV energy cutoff. The cell dimensions and atomic positions were optimized to yield the ground state crystalline structures.

In this study, we model a series of 8-atom unit cells of the $\text{Si}_{1-x}\text{Sn}_x$ alloys (where discrete Sn compositions of 12.5%, 25%, 37.5%, 50%, 62.5%, 75%, and 87.5% or $x = 0.125, 0.25, 0.375, 0.5, 0.625, 0.75, \text{ and } 0.875$), in which Si and Sn

are distributed on the various substitutional sites to form alloy structures as homogeneous alloys.

Our calculated equilibrium lattice constants are 5.461 Å for Si and 6.657 Å for $\alpha\text{-Sn}$, which are consistent with previously reported experimental data and theoretical results. Fig. 1 shows lattice parameters related to the pure silicium, isotropic $\text{Si}_{1-x}\text{Sn}_x$ arrangements of the intermediate compositions, and $\alpha\text{-Sn}$. The strong linear relation between lattice

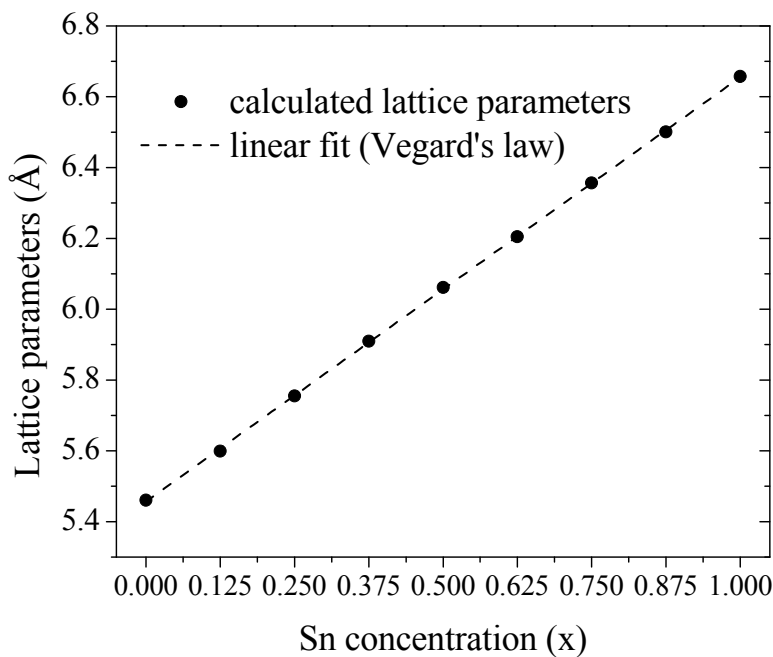


Fig. 1. Compositional dependence of lattice parameters in $\text{Si}_{1-x}\text{Sn}_x$ alloys.

parameters and composition of $\text{Si}_{1-x}\text{Sn}_x$ alloys exhibits Vegard behavior and can be written as $a_{\text{SiSn}} = a_{\text{Sn}}x + a_{\text{Si}}(1-x) + bx(1-x)$, yielding a bowing coefficient $b = 0.084$ Å. The Si and Sn atoms are displaced from the initial position in a diamond lattice structure by strain relaxation due to the difference in atomic radius between them.

Calculated band structures for Sn with Sn% as 37.5%, 50%, and 62.5% are shown in Figs. 2(a)–2(c), respectively.

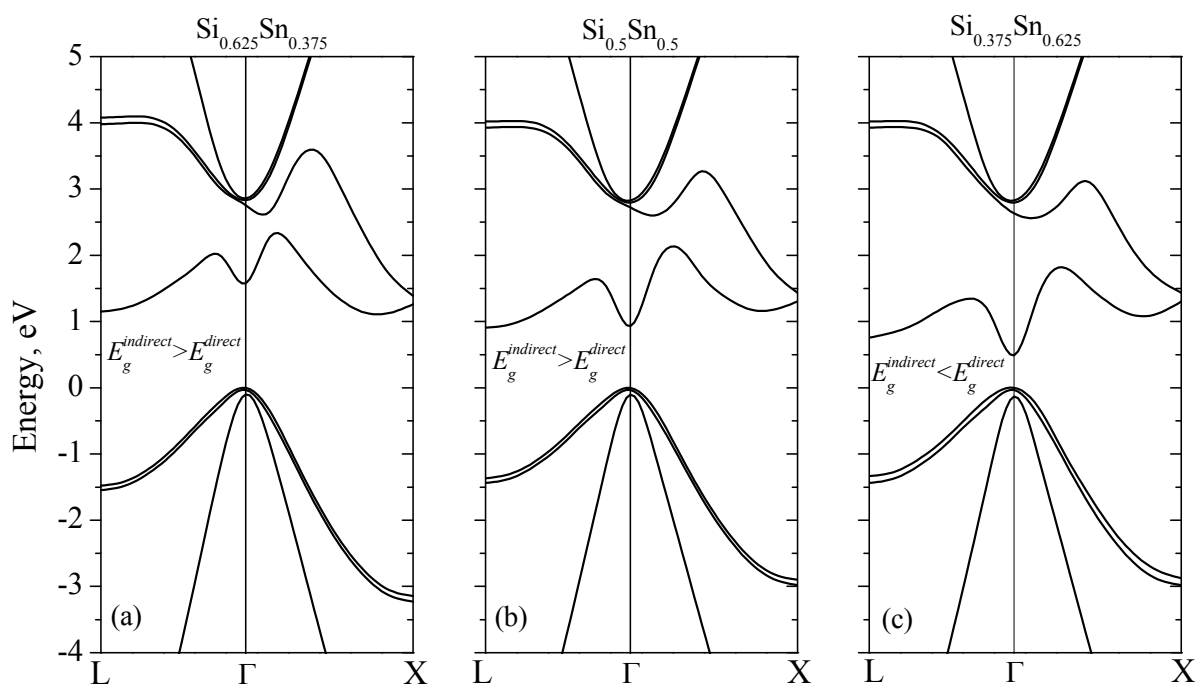


Fig. 2. Electronic band structures of $\text{Si}_{1-x}\text{Sn}_x$ along L- Γ -X path for (a) $x = 0.375$, (b) $x = 0.50$, and (c) $x = 0.625$, showing the transition from indirect to direct band gap.

Supercell approaches used to calculate the electronic properties of $\text{Si}_{1-x}\text{Sn}_x$ produce accurate, but folded, band structures. Using an optimized algorithm, we unfold the band structure to an approximate $E(k)$ relation associated with an effective Brillouin zone. We must indicate that the effect of the atom displacement in $\text{Si}_{1-x}\text{Sn}_x$ on its electronic properties, to consider the structural relaxation is very important for the band calculation. The band diagrams of $\text{Si}_{8-n}\text{Sn}_n$ structural models were calculated for all atomic configurations with the geometrical relaxation. Then, the calculated E_g results were averaged by considering the formation probability of each point. Fig. 3 shows the indirect to direct band gap transition for $\text{Si}_{1-x}\text{Sn}_x$.

A closer inspection of changes in the band structure upon increased Sn incorporation reveals that as the direct band gap shrinks, the electron and hole valleys at Γ point become narrower. Thus, as Sn content in $\text{Si}_{1-x}\text{Sn}_x$ increases, effective masses at Γ point decreases for both electrons and holes.

The band gap energy of $\text{Si}_{1-x}\text{Sn}_x$ at X, L, and Γ points obtained from the band structures calculated by MP is plotted against Sn compositions in Fig. 3. On Fig. 3 we also plot experimental value of indirect gap around $x = 0.18$ [7]. We can see that the band gaps values at Γ and L points decrease with increasing Sn content. The dependence of the X-point band gap on Sn compositions exhibits a simplest linear function relation with a correlation coefficient of 0.79754. In contrast, the L-point band gaps are highly sensitive to Sn compositions.

The calculated indirect-direct band gap crossover in $\text{Si}_{1-x}\text{Sn}_x$ alloys is found close to approximately tin content $x = 0.6$, which is extracted from appropriate curve-fitting of Γ and L valley band gaps. The corresponding energy gap is $E_g = 0.75$ eV, which is suitable for the on-chip optoelectronic devices.

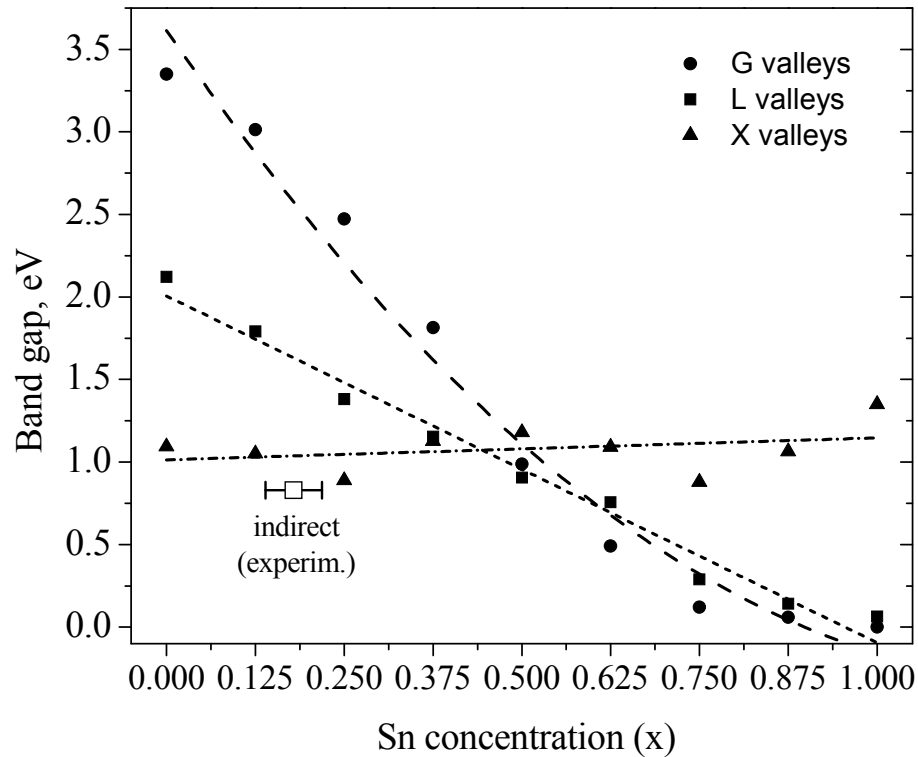


Fig. 3. The calculated band gap energies of L, Γ and X-point at various Sn compositions.

In summary, we present a model pseudopotential method to calculate the electronic band structure properties of SiSn alloys. Obtained results reveal that by increasing the Sn content, the $\text{Si}_{1-x}\text{Sn}_x$ alloys could become a direct band-gap material, which would be quite beneficial in the field of Si photonics.

- [1] Wirths, S., Buca, D. & Mantl, S. Si–Ge–Sn alloys: From growth to applications. *Prog. Cryst. Growth Charact. Mater.* **62**, 1–39 (2016).
- [2] Tolle, J. *et al.* Low temperature chemical vapor deposition of Si-based compounds via $\text{SiH}_3\text{SiH}_2\text{SiH}_3$: Metastable SiSn/GeSn/Si(100) heteroepitaxial structures. *Appl. Phys. Lett.* **89**, 231924 (2006).
- [3] Moontragoon, P., Ikonić, Z. & Harrison, P. Band structure calculations of Si–Ge–Sn alloys: achieving direct band gap materials. *Semicond. Sci. Technol.* **22**, 742–748 (2007).
- [4] Nagae, Y. *et al.* Density functional study for crystalline structures and electronic properties of $\text{Si}_{1-x}\text{Sn}_x$ alloys. *Jpn. J. Appl. Phys.* **55**, 08PE04 (2016).
- [5] Oda, M., Kuroda, Y., Kishi, A. & Shinozuka, Y. Electronic structure calculation of $\text{Si}_{1-x}\text{Sn}_x$ compound alloy using interacting quasi-band theory. *Phys. status solidi* **254**, 1600519 (2017).
- [6] Yakibchuk, P. M., Bovgyra, O. V. & Kutsa, I. V. Model pseudopotential calculations for the electronic structure of Si, Ge, and GaAs. *J. Phys. Stud.* **19**, (2015).
- [7] Kurosawa, M. *et al.* Near-infrared light absorption by polycrystalline SiSn alloys grown on insulating layers. *Appl. Phys. Lett.* **106**, 171908 (2015).

SYNERGISTIC EFFECTS IN IRRADIATED SEMICONDUCTOR CRYSTALS. RADIATION STABILITY CONSTANTS

M. Zavada¹, O. Konoreva¹, P. Lytovchenko¹, I. Petrenko¹, M. Pinkovska¹,
O. Radkevych², V. Tartachnyk¹, V. Shlapatska³

¹*Institute for Nuclear Research, NAS of Ukraine, 47, prospect Nauky, 03028 Kyiv*

²*SE 'SRI of Microdevices' STC 'Institute for Single Crystals', NAS of Ukraine, 3, Pivnichno-Syretska str., 04136, Kyiv*

³*L.V. Pisarzhevski Physical Chemistry Institute NAS of Ukraine, 31, pr. Nauky, 03028 Kyiv*

Introduction

Condensed medium under external energy flows appears to be an open system. In order to describe the regularity behavior of such systems and the processes of its structural changes the methods and principles of synergetic are used.

Synergism might be especially inherent in samples with high concentration of radiation defects (RD). Stochastic origin of initial defects and fluctuation character of structure defects' forming are the reason of the variety of all observed phenomena in irradiated crystals. The effect of synergism the most obviously occurs after reaching a definitely critical dose and might manifest itself in the atypical behavior of dose dependence of conductivity, oscillation nature of anneal curves and its additional stages, and also in superlattices' arising [1, 2]

Experiment

Complex semiconductors GaP, GaAsP and CdP₂, irradiated at room temperature by high fluences of electrons within 1-30 MeV energy interval and 80 MeV α -particles, were studied. Samples were annealing after irradiation within the interval of 140 to 700 K during 20 min. Electrical parameters (conductivity σ , carrier concentration n and mobility μ) and also positron life-time τ were analyzed. Measurements of electroluminescence were carried out.

Results and discussion

It was discovered that recovery processes of the electrical parameters (σ , μ , n) during annealing of GaP samples irradiated by 4 MeV electrons with $\Phi = 10^{17} \text{ cm}^{-2}$ and 12 MeV electrons with $\Phi = 5 \cdot 10^{16} \text{ cm}^{-2}$, were substantially different from the annealing of identical samples, irradiated by 1 MeV electrons with $\Phi = 10^{17} \text{ cm}^{-2}$. Typical anneal picture for moderate defect concentration consists of three stages 140-160 °C, 280 °C and 470 °C, where phosphorous vacancy V_P anneals at the first stage, gallium vacancy V_{Ga} anneals at the second stage and point defects' cluster anneals within the third stage borders [3].

When point defect concentration grows, annealing behavior changes: recovery stage with 500 °C maximum appears, followed by the negative annealing stage, where the electrical parameters worsened sharply and the mobility annealing curve has become multi-stage.

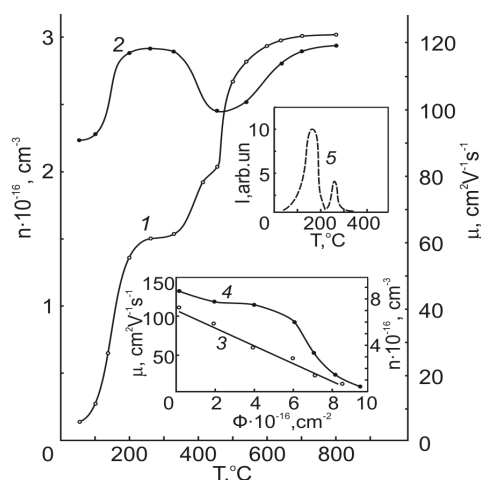


Fig. 1. Recovery of the electrical parameters of GaP crystal, irradiated with $E = 12$ MeV electrons, $\Phi = 5 \cdot 10^{16} \text{ cm}^{-2}$, in the process of isochronous annealing; 1 – concentration, 2 – mobility. Electron concentration (3) and mobility (4) dependences on the fluence are given in the insert. The curve (5) shows the conductivity relaxation amplitude as the annealing temperature function.

The increase of the electron irradiation energy as well as the increase of the defect concentration causes the new qualitative changes of the annealing process character.

One can see in the Figure 1 that the electron mobility annealing curve in the 150-350 °C intervals reaches wide maximum. Then μ drops and it might testify about transformation of the previously formed defects into qualitatively new kind. One can strictly observe such transformation in the concentration recovery curve – specific contribution of the second annealing stage grows nearly to 50 percents (curve 1). The changes of the defect kind are supposed by the increase of the relaxation intensity (see curve 5).

It is possible to observe the transit of quantity changes into qualitative ones on the radiation defects' accumulation kinetics when electron fluence grows. Figure 2 shows resistivity dependence on the electron fluence for two cadmium diphosphate samples. The increase of defect concentrations causes the resistivity increase, but when $\Phi > 10^{17} \text{ cm}^{-2}$ another tendency is evident – resistivity drops monotonously and might be less than initial one.

Measure of the positron lifetime during annealing in GaP irradiated by 80 MeV alpha-particles with fluence 10^{17} cm^{-2} demonstrates the same process of quantity changes' transit into new qualitative (Figure 3). Life-time increase during irradiation is caused by the vacancy defect accumulation with low electron density.

The decrease of positron life-time testifies about vacancy annealing ($T < 400$ °C), but at $T > 700$ °C life-time grows due to the forming of vacancy emptiness most possible bivacancies or complex vacancy type defects. We observe this phenomenon while analyzing the conductivity annealing curves of irradiated GaP.

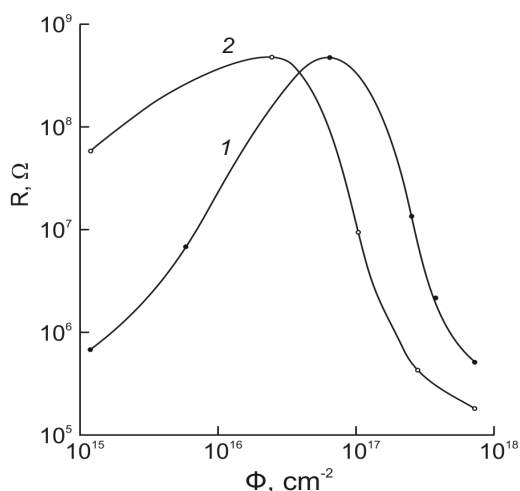


Fig. 2. Cadmium diphosphate resistivity dependence on 14 MeV electrons' fluence.

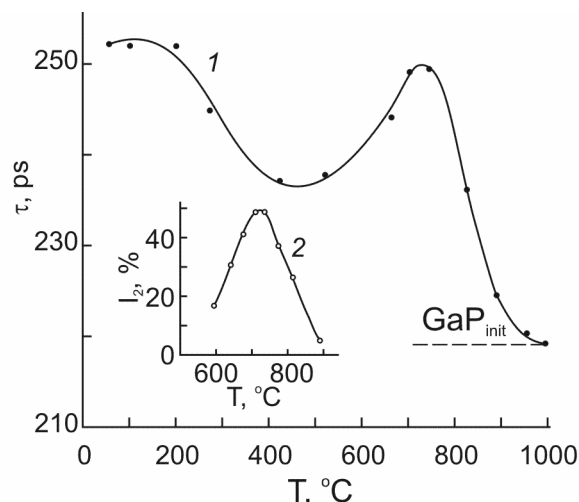


Fig. 3. The average positron life-time dependence on isochronous annealing temperature. Long-living component curve is given in the inset.

The degradation radiation constant k_τ is determined based on the dose dependences of the emitting intensity $I(\Phi)$, which occurs primarily due to the decrease in the life-time of minority charge carriers as a result of the introduction of deep irradiation centers. The electroluminescence intensity degradation of diodes, by analogy with the relative speed of charge carrier removing, might be estimated by the value of the relative change in the intensity of radiation, which corresponds to the unit flow of particles

$$\frac{d\left(\frac{L_0 - L}{L}\right)}{d\Phi} = k, \quad (1)$$

where L_0 – the intensity of the initial diode, L is the intensity of the irradiated diode, k is the coefficient of degradation.

The degradation lifetime constant k_τ is determined from the dependence [4]

$$\frac{1}{\tau_\Phi} = \frac{1}{\tau_0} + \frac{\Phi}{k_\tau}, \quad (2)$$

where values τ_0 and τ_Φ correspond to the life-time of the initial and irradiated sample.

According to the inclination of experimental dependence $\left(\frac{L_0}{L} - 1\right) = f(\Phi)$ one can obtain both the constants of k and k_τ , which characterize the radiation resistance of the electroluminescent structures. Comparing the radiation resistance of the red GaP(Zn-O) with green GaP(N) diode, it turned out that the stability of the first one is noticeably higher ($k_\tau^{\text{Zn-O}} = 4,3 \cdot 10^8 \text{ cm}^{-2}\text{s}$ versus $k_\tau^{\text{N}} = 1,6 \cdot 10^7 \text{ cm}^{-2}\text{s}$). The reason for this difference may obviously be due to the lower depth of the isoelectron trap N compared with Zn-O.

GaAsP-based emitters exhibit significantly higher radiation tolerance than GaP, although light emitting diodes based on GaP are considered to be relatively radiation-resistant. Depending on their composition, their radiation constants range from $4,28 \cdot 10^9 \text{ cm}^{-2}\text{s}$ (yellow diode) to $2,31 \cdot 10^{10} \text{ cm}^{-2}\text{s}$ (orange diode), which may

be due to a greater depth of the levels of the pairs of NN_1 and NN_2 – the main centers of the excitons' localization.

Conclusion

Irradiated crystal which as a nonequilibrium open system is able to demonstrate quality transit in the moment when monotonously changing separate inner factor (which influence on system properties) reaches the critical value. It is clear from above studied annealing process that concentration of radiation defects is such factor. When the defect concentration exceeds some critical value defects of new kind are formed: oscillation picks in the isochronous annealing curve appear and defects with high cross-section of defect scattering and capture are created. Accumulation of defects during irradiation might provoke an opposite effect to initial one – the conductivity of the sample with high defect concentration has become greater than in non irradiated sample.

High temperature annealing of the irradiated sample with increased vacancy concentration causes the appearing of the vacancy emptiness's with the lower electron density.

An increase in the dose of radiation leads to the decrease in the rate of removing current carriers.

1. P.A. Selishchev. *Selforganization in Radiation Physics*. Kiev, Aspect-poligraf. 2004 (in Russian).
2. V.J. Sugakov. *The basis of synergetics*. Kyiv. Oberehy, 2001 (in Ukraine).
3. O.F. Nemets, V.V. Voyakov, V.G. Litovchenko, V.G. Makarenko, V.Ya. Opilat, V.P. Tartachnyk, I.I. Tychyna. Radiation defects in gallium phosphide / *Doklady Akademii Nauk USSR. Ser. A*, **5**, p. 47-50 (1988) (in Ukrainian).
4. F.P. Korshunov, G.V. Gatal'sky, G.M. Ivanov. *Radiation effects in semiconductor devices* Minsk, Nauka i Technika. 1978 (in Russian).

IMPURITY AND IMPURITY- STRUCTURAL COMPLEXES OF TECHNOLOGICAL AND RA- DIATION ORIGIN

THERMODONORS IN SILICON CRYSTALS: PRACTICAL ASPECTS OF p - n JUNCTION CREATION IN Cz-Si MATERIAL USING BURIED n -TYPE LAYERS OF THE CONDUCTIVITY DEFINED BY SHALLOW THERMODONORS

V. Babich, O. Dubikovskiy, V. Popov, B. Romanyuk, S. Sapon, T. Sabov, O. Lyubchenko

V. Lashkarev Institute of Semiconductor Physics NAS of Ukraine

The first studies devoted to the role of oxygen in the formation of the properties of silicon were published by Fuller et al [1, 2]. However the problems associated with oxygen in Si single crystals remain relevant, in particular, for the use of experimental and theoretical data for semiconductor device fabrication.

At the initial stage of the research, the main characteristics of oxygen in Si single crystals were determined: its solubility and location in Si lattice, diffusion coefficients at different temperatures, and, most importantly, the appearance of thermodonor centers (TD) during various thermal treatments (TT) [1, 2] as well as acceptor (A-centers) [3] of the oxygen nature during irradiation of crystals by γ - and electron irradiation.

The TT of oxygen-containing Si crystals in the temperature range of 400 ... 1200 °C leads to the decomposition of a supersaturated oxygen solid solution in such crystals and to the formation of a number of microdefects of oxygen nature: both electrically active thermodonor (TD) and thermoacceptor (TA) complexes and more complex defect agglomerations - oxygen precipitates and interstitial silicon atoms (Si_i), which lead to corresponding changes in the electrophysical and structural properties of Si crystals [4].

In our work, the basic properties of a large set of TD centers were analyzed. And these, first of all, are the TD-I (twice-charged, shallow single-charged and deep TD-centers), as well as a wide range of the TD-II centers (in the range of ionization energies of 10-200 meV). The analysis was to select such TD centers, which are characterized by a high concentration after the corresponding thermal treatment and exhibit thermal stability after thermal treatment at temperatures above 650 °C. This allows the practical use of crystal doping at the expense of TD for semiconductor device fabrication. In view of this, our attention was given to shallow centers in silicon crystals enriched with carbon impurity, which are formed at annealing in the range of 550-650 °C [5,6].

Shallow thermodonors (STDs) with the lowest ionization energy and the largest g -factors proved to be resistant to TT at 650 °C and at higher temperatures (1000 and 1100 °C). By comparing the STD parameters (ionization energy, g -factor, heat resistance) with the TD-II parameters ("new" TD according to [7]), which are formed in the same crystals in the initial stages of the TT in the temperature range of 600-750 °C, we came to the conclusion that this type of STD has the same nature as the TD-II. It is for this reason that the TT at 650°C does not destroy them, and the subsequent increase in the TT duration at these temperatures leads to a further increase in their concentration.

The practical use of the STD centers was limited by their low concentration ($2 \cdot 10^{15} \text{ cm}^{-3}$), which is due to the low solubility of carbon in silicon single crystals ($4 \text{ to } 5 \cdot 10^{17} \text{ cm}^{-3}$). Carbon in the state C_s acts as a nucleus for the formation of STD centers, and therefore their concentration depends on the concentration of carbon in the lattice nodes. In [8, 9] we removed this limitation by using the method of implantation of carbon ions into silicon wafers.

Using different characterization methods (electrophysical, X-ray diffraction, electron microscopy, etc.), it was found [8, 9] that carbon implantation into p -Si-Cz oxygen-containing silicon crystals followed by the corresponding TT in the temperature range of $550\text{--}750^\circ\text{C}$, a buried layer of n -type conductivity have been created. The same effect has been observed in the p -Si-FZ material under double implantation of carbon and oxygen ions O_2^+ . It is shown that the n -type conductivity of the buried layer is determined by the STD with the maximum concentration in the n -type of $\approx 7 \cdot 10^{16} \text{ cm}^{-3}$ at implantation dose of $D = 20 \text{ } \mu\text{C}/\text{cm}^2$ and TT at a temperature of 600°C for 30 min. Such concentrations of MTD in a buried layer is 1.5 order of magnitude higher than the concentration of MTD obtained in the original samples of Cz-Si after long (up to 100 h) TOs without carbon implantation. The activation energy of the n -type MTD created in the layer was found to be 0.012 eV .

P -type Cz-Si with oxygen concentration of 10^{18} cm^{-3} were implanted by carbon ions with energies of 90 kV and doses of 10 (group 1) and 20 (group 2) $\mu\text{C}/\text{cm}^2$ through 100 nm thick oxide layer. The samples were subsequently annealed at 600°C for 30 minutes. Some samples were etched to remove a surface layer of 50 nm and 100 nm . The thickness of the removed layer was determined by the "Dektak" profilometer. Ohmic contact were formed to acquire the current-voltage characteristics (CVC) using L2-56 equipment. The photosensitivity of the structures was studied using laser irradiation at wavelengths of 405 and 532 nm .

The results of CVC measurements of structures after etching the surface layer are shown in Fig. 1.

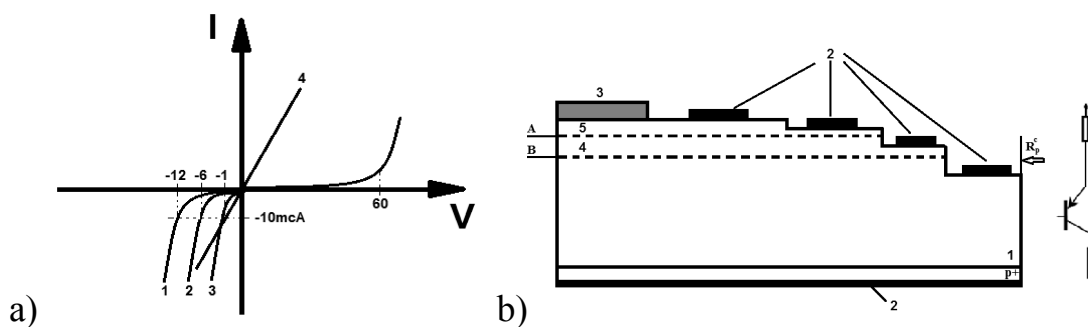


Fig.1. (a) - CVC of the structures after annealing and etching of the surface layer (1- not etched, 2, 3, 4 - after etching layer 50 , 100 , 300 nm , respectively); (b) - chemical section of the structure: 1 - substrate, 2 - Ohmic contacts, 3 - SiO_2 surface layer, 4 - area of C^+ distribution, 5 - p -type surface layer. To the right is the equivalent sketch of the structure.

From the Figure 1a it is evident that the threshold voltage changes when the deeper p - n junction (B) is displaced in the forward direction as the surface layer is removed, whereas the reverse current remains unchanged for all the samples. This effect is associated with the fall of the applied voltage in the reverse biased p - n junction (A), located near the surface. After the breakdown of this junction there is an exponential growth of the current through the p - n junction (B). After removing the p -type surface layer, we have a typical CVC for the diode. In our paper, the possible role of a positive charge embedded in SiO_2 precipitate, formed in the implanted area, is also discussed. The presence of charge leads to an additional displacement of the current-voltage characteristics of p - n junctions.

In illumination of the structures with a laser with wavelength $\lambda = 405$ nm, we obtained the CVCs, which are shown in Fig.2.

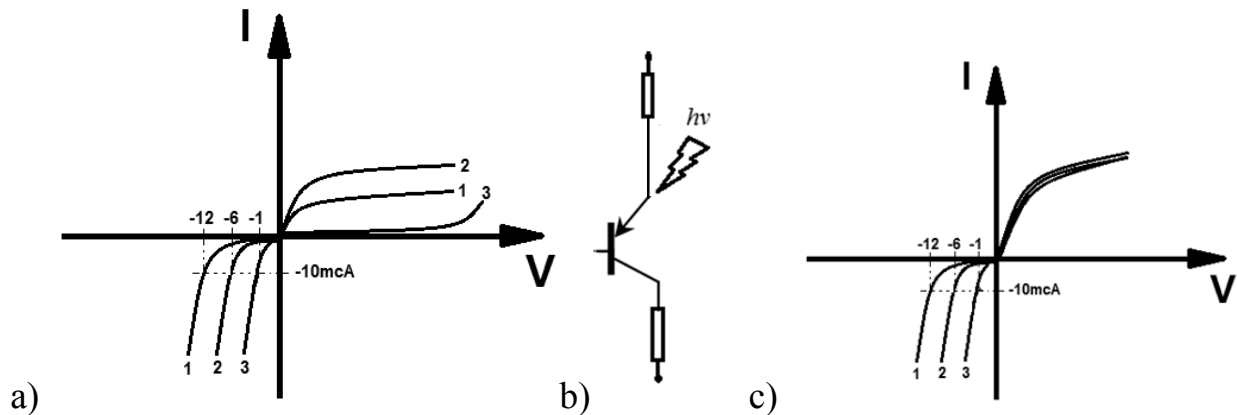


Fig.2. CVC of the samples, illuminated by a laser with wavelength of 405 nm (a): 1 - not etched, 2 - 50 nm etched, 3 - 100 nm etched; Equivalent sketch of the structure (b); c - CVC of the samples illuminated by a laser with a wavelength of 532 nm: 1-not etched, 2 - 50 nm etched, 3 - 100 nm etched

The photosensitivity of the structures depends on the thickness of the removed surface layer. The maximum photosensitivity has structures in which the surface layer was removed with a thickness of 50 nm. The observed effect could be explained by the fact that the light in the short-wave spectrum region is absorbed in a thin surface layer (100 nm). Due to the high surface recombination, only a small portion of the generated charge carriers contributes to the photo EMF. If the generation region approaches the p - n junction, the photosensitivity increases. The structure works like a phototransistor. After the p - n junction A removal, the photosensitivity disappears, since the generated carriers are recombined in the surface region and do not reach the B p - n junction.

Another situation is observed at illumination of the structures with a laser with a wavelength $\lambda = 532$ nm. The CVC for this case is shown in Figure 2c. The photosensitivity of all structures is almost the same, since light is absorbed behind the region of the space charge region of the p - n junction B (at a depth of 1000 nm) and surface recombination of generated current carriers gives a small contribution to the decrease of the magnitude of the photo-EMF.

References

1. Fuller C. S., Ditsenbergen J.A., Hannay N.V., Buehler E., Phys.Rev. -1954. -V 96, n. 3. -P. 833
2. Kaiser W., Frisch H.L., Reise H., Phys. Rev. -1958. - V.112, n.5. - P.1546-1554.
3. Watkins G. D. Corbett J. W., Walker R. M., J. Appl. Phys. -1959. -V.30, n.8 - P.1198-1203.
4. Babich VM, Bletskan NI, Wenger E.F. Oxygen in single crystals of silicon. Kyiv Interpress LTD. 1997. - 240 p.
6. Babich VM, Baran N.P., Dotsenko Yu.P., Zotov K.I., Kovalchuk VB, Skorokhod M.Ya., Inorganic materials. -1988 - T.24, No. 2. - p.133-137.
7. Babich V.M., Baran N.P., Dotsenko Yu.P., Zotov K.I., Koval'chuk V.B. and Maksimenko V.M., Sov.Phys. Semicond - 1992 - V.26, n.3. - P.253-256
8. Kanamori A., Kanamori M., J. Appl. Phys. - 1979. - V.50, n.12. - P. 8095-8101.
9. Romanyuk B., Melnik V., Popov V., Litovchenko V., Babich V., Ilchenko V., Kladko V., Vanchellemont J., ECS Transactions. - 2014. - V.64 (11). -P.187-198.
10. Romanyuk B., Melnik V., Popov V., Babich V., Kladko V., Gudymenko O., Ilchenko V., Vasyliiev I., Gorlachko A., Nanoscale Research Lethers. - 2014 - V.9. - P.693-698.

RADIATION-INDUCED CHANGES IN ELECTROMECHANICAL AND OPTICAL CHARACTERISTICS OF SILICON STRUCTURES

**B.V. Pavlyk, D.P. Slobodzyan, R.M. Lys, M.O. Kushlyk, R.I. Didyk,
J.A. Shykorjak**

*Department of Sensor and Semiconductor Electronics,
Ivan Franko National University of Lviv,
79017, 107 Hen. Tarnavskoho Str., Lviv, Ukraine
pavlyk@electronics.lnu.edu.ua*

The presence of spot and line defects can significantly affect the surface activity. This can be reflected in the efficiency and durability of these elements due to weak electromagnetic fields, in particular.

Monocrystalline silicon of p -type conductivity, intended for solar energy was used in the research. The plastic deformation occurred at a temperature of 1000 K and a pressure of 10^7 Pa. On the surface (111) of p -Si crystals, the distribution of dislocation concentrations from 10^2 to 10^7 cm⁻² was obtained. Plots with a concentration of 10^2 , 10^4 , 10^5 , 10^7 cm⁻² formed surface-barrier structure (SBS) of Schottky type. The changes in the surface resistance of silicon mono-crystals, capacitance-volt characteristics (CVCH), surface state (SS) density and electroluminescence LES were analyzed.

The aim of the work was to form a surface-barrier structure and light-emitting structure (LES) on the basis of p -Si with different dislocation concentration on the surface of the semiconductor substrate and to investigate the change in their electro physical and optical characteristics under the influence of X-radiation.

With the increase in the dose of X-irradiation, the resistance of p -Si additionally increases. Moreover, the value of the resistance R is directly proportional to the square root of the radiation dose. The resistance of irradiated and non-irradiated samples of "solar" silicon with elastic compression decreases. The decrease in the resistance of silicon crystals with increasing load is related to a decrease in the longitudinal effective mass of heavy holes and a corresponding increase in their mobility under compression.

It was found that the nature of resistance change of "solar" silicon of p -Si type on the size of the mechanical stress is independent of the speed of compression. A similar feature was observed in both non-irradiated and irradiated samples. The value of the longitudinal resistance, unlike similar dependencies of longitudinal resistance on mechanical stress for "electronic" silicon changes by a relatively small value, (< 0.5 %) and it slightly decreases under the increase in load (Fig. 1a).

Irradiation of experimental samples with X-rays (480 Gy) does not virtually affect the general nature of the change in longitudinal resistance of "solar" silicon during the elastic deformation (Fig. 1b). During the mechanical stress, the resistivity decreases by a very small value (± 0.1 %).

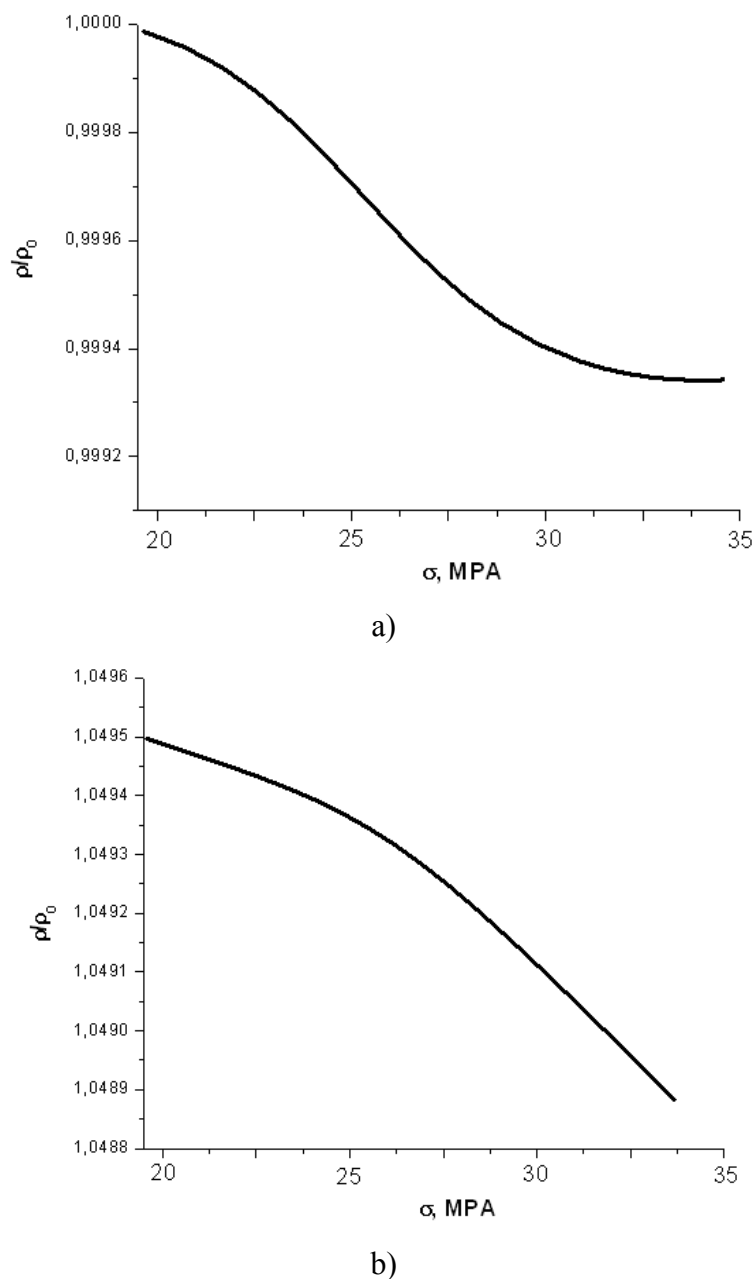


Fig. 1. Dependence of longitudinal resistance of "solar" silicon during elastic deformation with a growing strength of compression: a) $D = 0$ Gy, compression speed $32 \mu\text{m}/\text{min}$.; b) $D = 130$ Gy compression speed $8 \mu\text{m}/\text{min}$

As the concentration of dislocations increases, an increase in the surface resistance of silicon is observed. The reason is the process of heating of main charge carriers with linear defects.

It is shown that high dislocation concentrations on the silicon surface (111) are generated by methods of plastic deformation and high-temperature annealing in an oxygen atmosphere. This allows the creation of highly effective Al-Si(p) emitting structures.

The analysis of CVCH and SS (fig. 2) irradiated SBS on the basis of non-dislocation samples of "solar" silicon (10^2 cm^{-2}) confirmed the existence of two competing radiation processes: the radiation-stimulated ordering of the defect

structure of the near-surface layer ($D < 390$ Gy) and the generation of defects ($D > 390$ Gy).

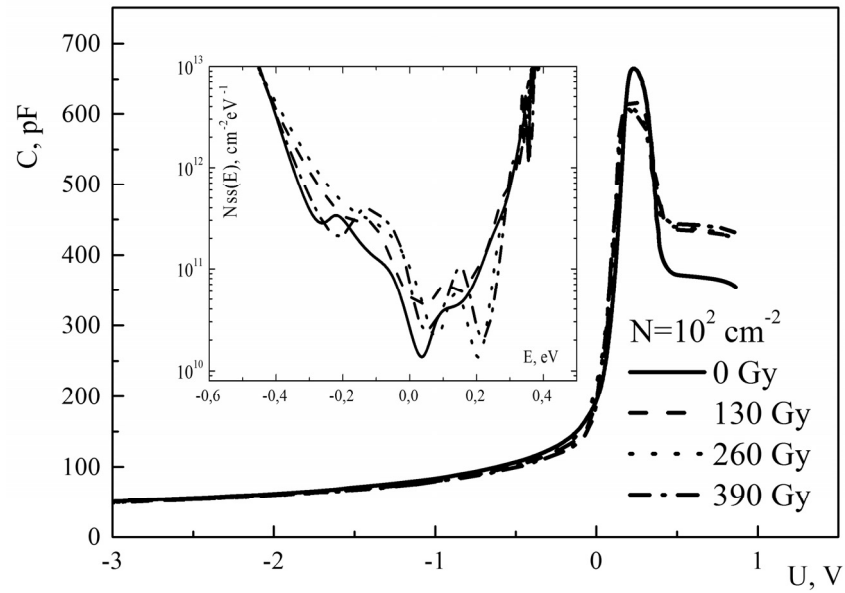


Fig. 2. Capacitance-volt characteristics and surface state irradiated surface-barrier structure

As the concentration of dislocations exceeds 10^4 cm^{-2} , certain non-monotonies of charge accumulation at the Si-SiO₂ (fig. 3) separation boundary is observed, due to the additional influence of the mechanical field of dislocations and the electric field of the Cottrell cloud on the X-stimulated changes in the parameters of these structures.

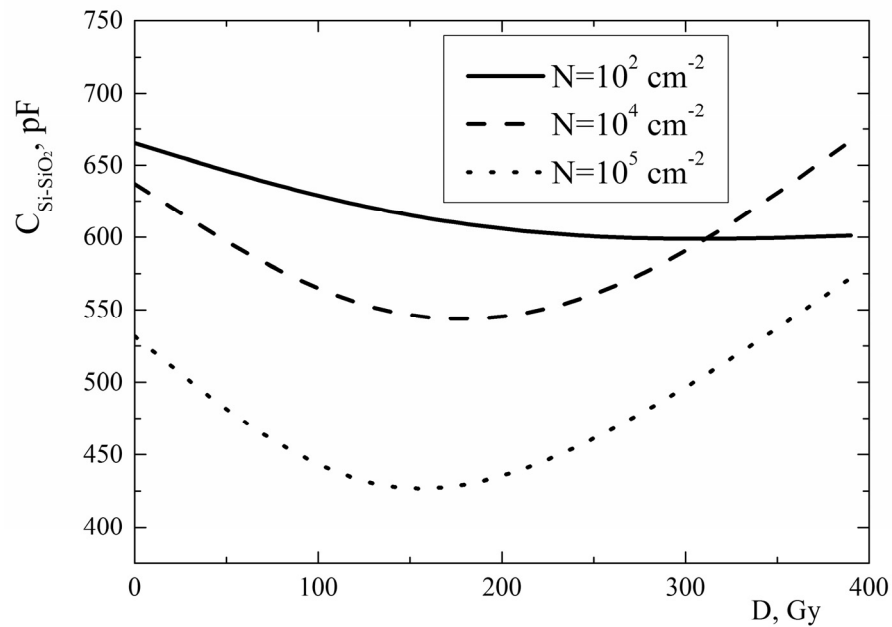


Fig. 3. X-stimulated changes charge accumulation at the Si-SiO₂

TOPOLOGICAL INSULATORS BASED ON THE SEMIMETAL HgCdTe ALLOYS

P. Śliż, M. Marchewka, D. Żak, J. Polit, E.M. Sheregii*

*Centre for Microelectronics and Nanotechnology, University of Rzeszow,
Pigonia str. 1, 35-959 Rzeszow, Poland*

**Email: sheregii@ur.edu.pl, web site: <http://www.nanocentrum.univ.rzeszow.pl/>*

ABSTRACT. HgCdTe (MCT) alloy is a typical material with strong spin-orbital interaction which lifts the Γ_8 band above the Γ_6 one. That is why a Dirac point (the Γ_6 and Γ_8 crossing that causes massless fermions) is realized when the composition of MCT is varied from HgTe to CdTe what makes the 3D topological Dirac semi-metal HgCdTe as a natural analogue of graphene in 3D. That is confirmed by experimental results presented in this report.

RESULTS AND DISCUSSION. The experimental results of the magneto-transport measurements over a wide interval of temperatures for nineteen samples of MCT ($x \approx 0.13 - 0.15$) grown by MBE [1] are presented.

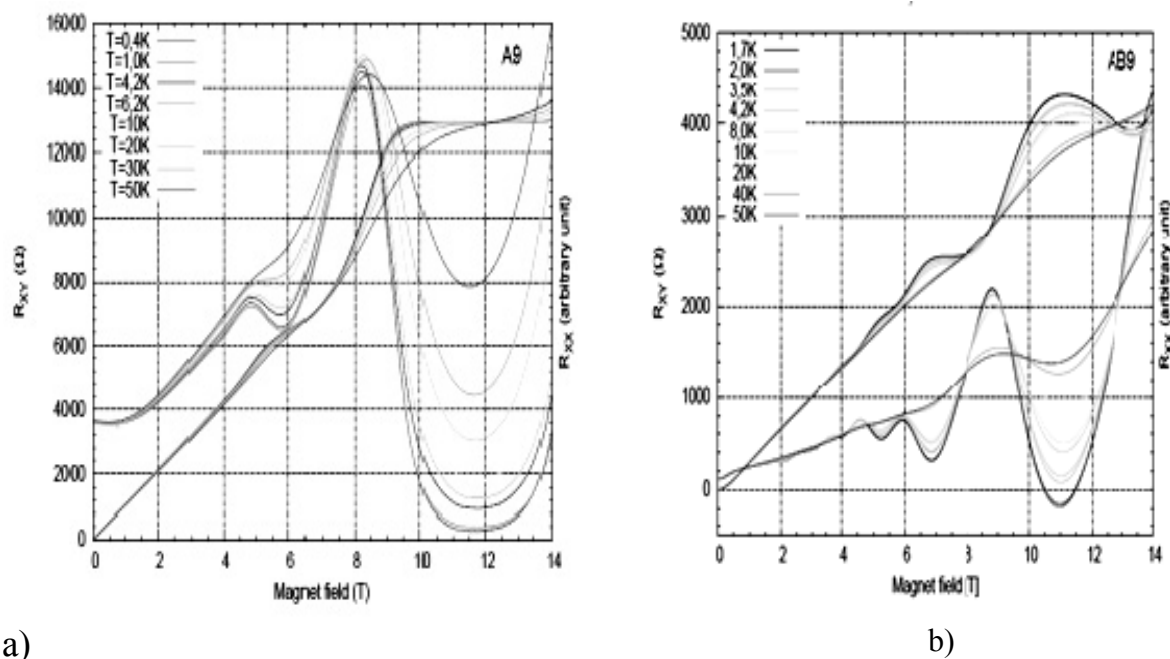


Fig1. Magneto-resistances, R_{xx} and R_{xy} vs magnetic field at the temperatures of 0.4 - 50 K for a) sample of series A; b) sample of series AB.

The results obtained for sample A9 – strained thin layer on the GaAs/CdTe substrate – are presented in Fig. 1a. The $R_{xx}(B)$ and $R_{xy}(B)$ curves are shown for different temperatures over wide range from 0.4 K to 50 K. The well-defined quantized plateaus in R_{xy} with values $h/(2e^2) = 12.9 \text{ k}\Omega$, accompanied by vanishing R_{xx} is observed at 0.4 K what explicitly indicate on the Integer Quantum Hall Effect (IQHE) and Shubnikov-de Haas (SdH) oscillations characteristic for 2D electron gas. The $R_{xx}(B)$ and $R_{xy}(B)$ curves are reproducible up to 20 K and above this tem-

perature the IQHE is observed up to 50 K. That can be explained by conductivity on Topologically Protected Surface States (TPSS). An amazing temperature stability of the SdH-oscillation period and amplitude is observed in the entire temperature interval of measurements up to 50 K for samples of series AB (Fig.1b) and B also. Moreover, the IQHE behavior of the Hall resistance is registered in the same temperature interval. In the case of not strained layers (series AB and B) it is assumed that the QHE conductivity on the TPSS contributes also to the conductance of the bulk samples [2].

CONCLUSION. As are shown by the calculations in the framework of **kp**-model the Topological Insulator (TI) HgCdTe have important advantages: high value of the Fermi velocity $v_F = 10^6$ m/s – approximately the same as for graphene, what leads to an increase in the attractiveness of this TI for future applications: as massless Weyl fermions [3]. In comparison with pure HgTe: the energy dispersion in semimetal HgCdTe is closer to linearity in the wider range of the momentum) lead to an increase in the attractiveness of the TI based on semimetal HgCdTe alloy for future applications: as massless Weyl fermions for example with addition of non-compensated spins of Mn [3].

REFERENCES

1. J. Grendysa, G. Tomaka, P. Śliż, C. R. Becker, M. Trzyna, R. Wojnarowski-Nowaka, E. Bobko and E.M. Sheregii, *Journal of Crystall Growth*, **480**, 1–5 (2017)
2. G. Tomaka, J. Grendysa, P. Śliż, C. R. Becker, J. Polit, R. Wojnarowska, A. Stadler, and E. M. Sheregii, *Phys. Rev. B*, **93**, 205419 (2016).
3. M. Marchewka, J. Grendysa, D. Żak, G. Tomaka, P. Śliż and E.M. Sheregii, *Solid State Communication*, **250**, 104 (2016)

ACKNOWLEDGMENTS

We acknowledge support from the grant - contract WND-PPK.01.03.00-18-053/12.

CLUSTER PHASE: FORMATION, PROPERTIES AND MODELING

ION-INDUCED PROCESSES IN POLYMERS AND COMPOSITE MATERIALS: POSITRON ANNIHILATION SPECTROSCOPY STUDY

**T. Kavetskyy^{1,2}, K. Iida³, Y. Nagashima³, M.O. Liedke⁴, M. Butterling⁴,
A. Wagner⁴, R. Krause-Rehberg⁵, O. Šauša⁶, T. Petkova⁷, V. Boev⁷,
A.L. Stepanov^{8,9}, L. Meshi¹⁰, D. Fuks¹⁰, A. Kiv^{10,11}**

¹*Drohobych Ivan Franko State Pedagogical University, 82100 Drohobych, Ukraine*

²*The John Paul II Catholic University of Lublin, 20-950 Lublin, Poland*

³*Department of Physics, Tokyo University of Science, Shinjuku, 162-8601 Tokyo, Japan*

⁴*Institute of Radiation Physics, Helmholtz-Zentrum Dresden-Rossendorf, 01328 Dresden, Germany*

⁵*Department of Physics, University Halle, 06099 Halle, Germany*

⁶*Institute of Physics, Slovak Academy of Sciences, 84511 Bratislava, Slovakia*

⁷*Institute of Electrochemistry and Energy Systems, Bulgarian Academy of Sciences, 1113 Sofia, Bulgaria*

⁸*Kazan Physical-Technical Institute, Russian Academy of Sciences, 420029 Kazan, Russia*

⁹*Kazan Federal University, 420008 Kazan, Russia*

¹⁰*Department of Materials Engineering, Ben-Gurion University of the Negev, 84105 Beer-Sheva, Israel*

¹¹*South-Ukrainian National Pedagogical University, 65000 Odessa, Ukraine
E-mail: kavetskyy@yahoo.com*

The present work will review recent results on application of positron annihilation spectroscopy (PAS) using a variable-energy slow positron beam (VESPB) [1-5] as a key technique that shows a completely new way to understand ion irradiation-induced processes and defect structures in a variety of polymer and composite materials important for practical use. In this respect, PAS-VESPB is demonstrated as a powerful experimental tool applied, in particular, to polymer nanocomposites with carbon nanostructures and metal nanoparticles (MNPs). Recent investigations of nanoparticle loaded polymer brushes by means of PAS-VESPB have been reported in [6, 7].

The results concerning 30 keV Ag⁺ implanted PMMA, ureasil, ureasil/As₂S₃, and ureasil/Ag-As₂S₃ composites will be discussed (see, as an example, Figure 1 [5]). PAS-VESPB techniques confirm previously suggested self-organized carbonization of ion-irradiated polymer and a step by step formation of carbon-shell Ag-core NPs.

Also, PAS-VESPB was applied with aim of structural study of the U₄Al₇Si₅ compound subjected to 30 keV Ar⁺ irradiation [8]. In [9] it has been established that in materials, whose composition includes atoms with very different masses, under ion bombardment in certain energy intervals the so-called heavy clusters are formed. At the same time, the ion-induced disordering of the block structure of the

mentioned compound occurs [10]. Here the PAS-VESPB is utilized to clarify the mechanism of ion-induced structure kinetics.

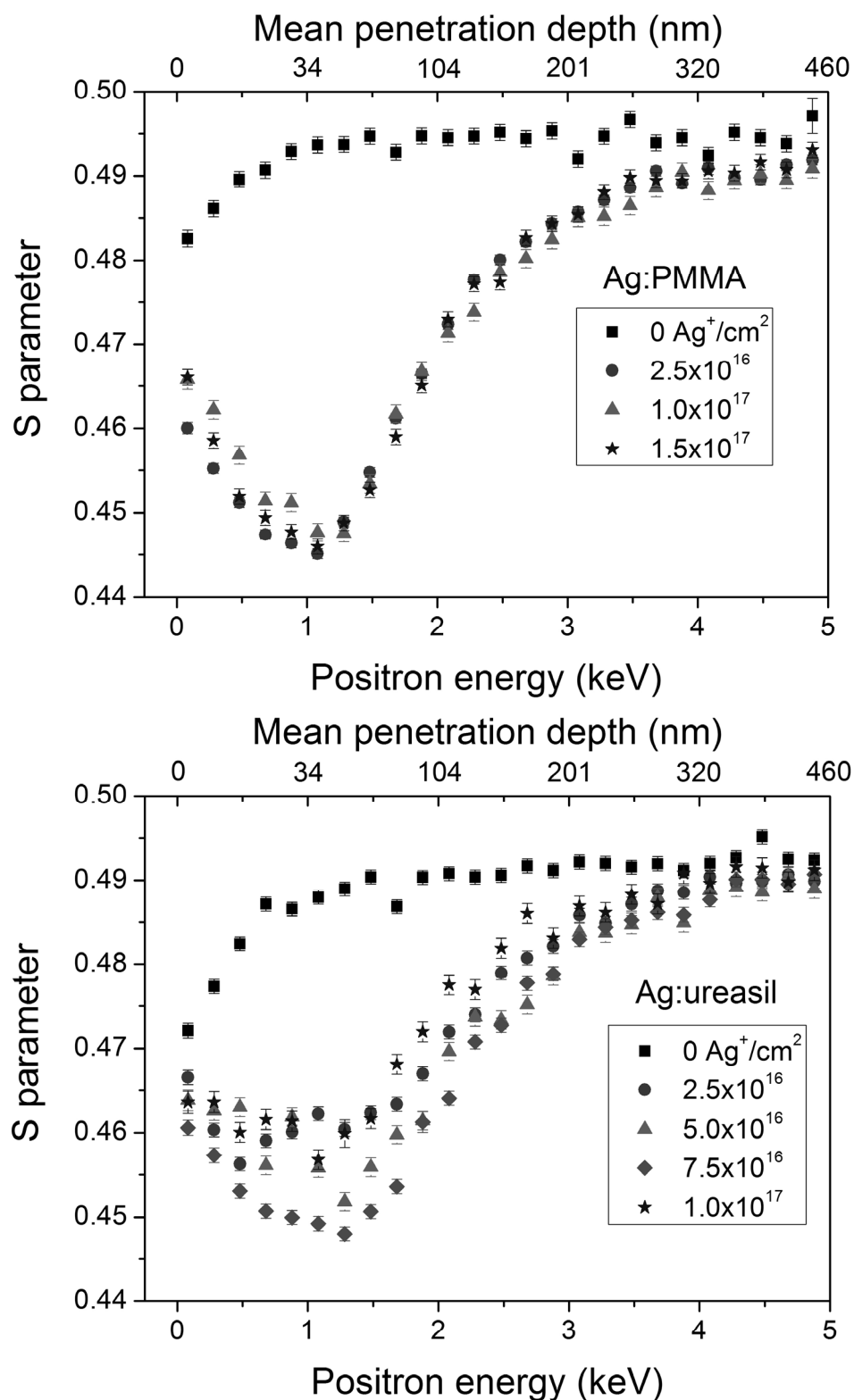


Figure 1. Doppler broadening S -parameter for the pristine (non-irradiated) and irradiated Ag:PMMA (top) and Ag:ureasil (bottom) samples with various fluences as a function of incident positron energy in the range of 0-5 keV. The error bars are within the size of the symbol [5].

Acknowledgments

This work was financially supported in part by the Ministry of Education and Science of Ukraine (projects #0116U004737, #0117U007143 and #0118U000297 to TK), by the Slovak Grant Agency VEGA (project #2/0157/17 to OŠ), and Slovak Research and Development Agency (project #APVV-16-0369 to OŠ), by the National Science Fund of the Bulgarian Ministry of Education (project #FNI-DN09/12-2016 to TK, TP and VB) and by the Russian Foundation for Basic Research (project #17-08-00850 to ALS). TK also acknowledges the SAIA (Slovak Academic Information Agency) for scholarship in the IPSAS within the National Scholarship Programme of the Slovak Republic.

References

- [1] T. Kavetsky, V. Tsmots, A. Kinomura, Y. Kobayashi, R. Suzuki, H.F.M. Mohamed, O. Šauša, V. Nuzhdin, V. Valeev, A.L. Stepanov, *J. Phys. Chem. B* **118** (2014) 4194.
- [2] T.S. Kavetsky, V.M. Tsmots, S.Ya. Voloshanska, O. Šauša, V.I. Nuzhdin, V.F. Valeev, Y.N. Osin, A.L. Stepanov, *Low Temp. Phys.* **40** (2014) 747.
- [3] T.S. Kavetsky, A.L. Stepanov, In: “Radiation Effects in Materials” (W.A. Monteiro, ed.), Rijeka: InTech, 2016, Chapter 11, P. 287-308.
- [4] T. Kavetsky, K. Iida, Y. Nagashima, A. Kuczumow, O. Šauša, V. Nuzhdin, V. Valeev, A.L. Stepanov, *J. Phys.: Conf. Ser.* **791** (2017) 012028.
- [5] T.S. Kavetsky, M.O. Liedke, N. Srinivasan, A. Wagner, R. Krause-Rehberg, O. Šauša, T. Petkova, V. Boev, A.L. Stepanov, In: NATO Science for Peace and Security Series A: Chemistry and Biology “Nanostructured Materials for the Detection of CBRN” (J. Bonca, S. Kruchinin, eds.), Dordrecht: Springer, 2018, Chapter 21, DOI: 10.1007/978-94-024-1304-5_21.
- [6] G. Panzarasa, S. Aghion, G. Soliveri, G. Consolati, R. Ferragut, *Nanotechnology* **27** (2016) 02LT03.
- [7] G. Panzarasa, S. Aghion, G. Marra, A. Wagner, M.O. Liedke, M. Elsayed, R. Krause-Rehberg, R. Ferragut, G. Consolati, *Macromolecules* **50** (2017) 5574.
- [8] T. Kavetsky, K. Iida, Y. Nagashima, M.O. Liedke, N. Srinivasan, A. Wagner, R. Krause-Rehberg, O. Šauša, A.L. Stepanov, L. Meshi, A. Kiv, D. Fuks, I. Dahan, *Abstracts of the 18th Israel Materials Engineering Conference (IMEC-18)* (Leonardo Club Hotel Dead Sea, Israel, 6-8 February, 2018), <https://events.eventact.com/ProgramView2/Agenda/Lecture?id=167644&code=3250098>.
- [9] A. Kiv, N. Mykytenko, D. Fuks, I. Dahan, L. Meshi, *Intern. J. Adv. Comp. Technol.* **4** (2016) 81.
- [10] L. Meshi, G. Yaniv, P. Horak, J. Vacik, N. Mykytenko, G. Rafailov, I. Dahan, D. Fuks, A. Kiv, *Materials* **11** (2018) 228.

AMPEROMETRIC ENZYME BIOSENSORS BASED ON NOVEL ORGANIC-INORGANIC AND PHOTOCROSS-LINKED POLYMERS

**T. Kavetskyy^{1,2}, O. Smutok³, M. Gonchar³, Y. Kukhazh¹,
O. Šauša⁴, H. Švajdlénková⁵, T. Petkova⁶, V. Boev⁶, V. Ilcheva⁶,
S. Kasetaitė⁷, J. Ostrauskaite⁷**

¹*Drohobych Ivan Franko State Pedagogical University, 82100 Drohobych, Ukraine*

²*The John Paul II Catholic University of Lublin, 20-950 Lublin, Poland*

³*Institute of Cell Biology, National Academy of Sciences of Ukraine, 79005 Lviv, Ukraine*

⁴*Institute of Physics, Slovak Academy of Sciences, 84511 Bratislava, Slovakia*

⁵*Polymer Institute, Slovak Academy of Sciences, 84541 Bratislava, Slovakia*

⁶*Institute of Electrochemistry and Energy Systems, Bulgarian Academy of Sciences, 1113 Sofia, Bulgaria*

⁷*Kaunas University of Technology, 50254 Kaunas, Lithuania*

E-mail: kavetskyy@yahoo.com

Technogenic pressure on the environment significantly affects the pollution of water resources. Especially dangerous are xenobiotics – products of the chemical and pharmaceutical industry, which negatively impact on the physiological state of living organisms and have carcinogenic properties even at very low concentrations. Conservation and restoration of water resources is a huge problem for modern society. Some xenobiotics, apart from wastewater treatment plants, are also in the surface and underground waters, because they were only partially removed in the process of the existing technological schemes for cleaning of wastewater.

One of such innovations is creation of highly sensitive biosensors for analysis of the level of wastewater pollution. The one of the most dangerous pollutants of wastewater are xenoestrogens. For example, xenoestrogen bisphenol A is a monomer that is used for the manufacture of polycarbonate plastic and epoxy resins, which are raw materials for the production of packaging materials for food and drinks. Xenoestrogens, classified as carcinogens, are toxic to healthy compounds that cause disruption of the endocrine system of human and animals.

The commercial laccase was used in the role of catalytic bioselective element of amperometric enzyme biosensor sensitive to different aromatic phenols and amines. Laccase (EC 1.10.3.2 p-diphenol: benzenediol oxygen oxidoreductase from *Trametes versicolor*) is a copper containing enzyme which is able to catalyze the oxidation of several phenolic compounds and aromatic amines [1].

Laccase is one of the first enzymes, which was proved to have the ability to direct transfer of electrons on the surface of amperometric transducer. This ability of laccase was used for creation of mediatorless biosensor of the “third generation”. A direct electron transfer is possible only with molecules of monolayer of enzyme that is directly in contact with the surface of the electrode in case of the

proper orientation of the active center of enzyme in sufficient distance to the electrode for electron transfer.

For the first time, novel polymer matrixes based on the urea-silicate or ureasil composites [2-6] were tested for immobilization of laccase and construction of amperometric enzyme biosensors [7]. The biosensor characteristic such as sensitivity of the bioelectrode was determined and analyzed for the ureasil/As₂S₃ composite, ureasil, and ureasil/As₂S₃ composite with incorporated silver nanoparticles (NPs) synthesized by high-fluence 30 keV Ag⁺ irradiation. A very high sensitivity of amperometric biosensor with ureasil-chalcogenide glass composite was established and a well expressed influence on the sensor's characteristics by polymer matrix and Ag NPs was detected [7].

In this study, a correlation between the network properties as revealed by low-temperature positron annihilation lifetime spectroscopy (PALS), and swelling experiments and biosensor characteristics of pure ureasil and ureasil/As₂S₃ composite of different history (fresh and aged during one year) is reported (see, as an example, Table 1) [8-10]. The observed findings could be further used for improvement of operational parameters of laccase-based amperometric enzyme biosensors, which may have potential for monitoring the level of pollution of wastewater containing xenoestrogens.

With aim to search a new polymer matrix as the sensing layer of an amperometric enzyme biosensor, for the first time, the novel photocross-linked polymer matrixes [11] based on epoxydized linseed oil (ELO), bisphenol A diglycidyl ether (RT) and photoinitiator – 50% mixture of triarylsulfonium hexafluoroantimonates in propylene carbonate (FI) marked as C1 (ELO + 10 mol.% RT + 3 mol.% FI) and C2 (ELO + 30 mol.% RT + 3 mol.% FI) with different density of cross-links were also tested for immobilization of laccase and construction of amperometric enzyme biosensors. Low-temperature PALS and swelling experiments were carried out to find a correlation between the network properties of polymers and parameters of constructed amperometric biosensors.

Table 1. Free-volume V_h at T_g obtained from the positron annihilation lifetime measurements in the range of 15-350 K in the cooling cycle, molecular weight between two crosslink points M_c , comparative analysis of swellability, biosensor response I_{\max} , Michaelis-Menten constant K_M to ABTS as the substrate, and the sensitivity of bioelectrodes constructed based on laccase immobilized by the developed ureasil-based polymer matrixes [8-10].

Sample*	V_h (nm ³)	M_c	Swell	I_{\max} (μA)	K_M (mM)	Sensitivity (A·M ⁻¹ ·m ⁻²)
K0-fresh	0.123 ± 0.002	92.47	+	7.62 ± 1.7	0.64 ± 0.17	794
K0-aged	0.123 ± 0.003	44.0	– –	10.96 ± 3.38	0.35 ± 0.14	1762
K4-fresh	0.104 ± 0.001	99.22	++	43.77 ± 2.71	0.045 ± 0.005	39,817
K4-aged	0.134 ± 0.001	76.52	–	86.8 ± 0.9	0.030 ± 0.008	60,413

* K0-fresh: ureasil polymer freshly synthesized (2 months after preparation); K0-aged: ureasil polymer aged (1 year after preparation); K4-fresh: ureasil/As₂S₃ composite freshly synthesized (2 months after preparation); K4-aged: ureasil/As₂S₃ composite aged (1 year after preparation).

Acknowledgments

This work was financially supported in part by the Ministry of Education and Science of Ukraine (projects #0116U004737, #0118U000297 to TK, OS, YK, MG, and #0117U007142 for Young Scientists to YK), by the Slovak Grant Agency VEGA (project #2/0157/17 to OŠ), Slovak Research and Development Agency (project #APVV-16-0369 to OŠ, HŠ), and by the National Science Fund of the Bulgarian Ministry of Education (project #FNI-DN09/12-2016 to TK, TP, VB, VI). TK also thanks the SAIA (Slovak Academic Information Agency) for scholarship in the IPSAS within the National Scholarship Programme of the Slovak Republic.

References

- [1] P. Giardina, V. Faraco, C. Pezzella, A. Piscitelli, S. Vanhulle, G. Sannia, *Cell. Mol. Life Sci.* **67** (2010) 369.
- [2] V. Boev, J. Pérez-Juste, I. Pastoriza-Santos, C.J.R. Silva, M.J. Gomes, L.M. Liz-Marzán, *Langmuir* **20** (2004) 10268.
- [3] V.I. Boev, C.J.R. Silva, G. Hungerford, M.J.M. Gomes, J. Sol-Gel Sci. Technol. **31** (2004) 131.
- [4] V.I. Boev, A. Soloviev, C.J.R. Silva, M.J.M. Gomes, D.J. Barber, J. Sol-Gel Sci. Technol. **41** (2007) 223.
- [5] T. Kavetsky, N. Lyadov, V. Valeev, V. Tsmots, T. Petkova, V. Boev, P. Petkov, A.L. Stepanov, *Phys. Status Solidi C* **9** (2012) 2444.
- [6] T. Kavetsky, O. Šauša, J. Krištiak, T. Petkova, P. Petkov, V. Boev, N. Lyadov, A. Stepanov, *Mater. Sci. Forum* **733** (2013) 171.
- [7] T. Kavetsky, O. Smutok, M. Gonchar, O. Demkiv, H. Klepach, Y. Kukhazh, O. Šauša, T. Petkova, V. Boev, V. Ilcheva, P. Petkov, A.L. Stepanov, *J. Appl. Polym. Sci.* **134** (2017) 45278.
- [8] T. Kavetsky, O. Šauša, K. Čechová, H. Švajdlenková, I. Mat'ko, T. Petkova, V. Boev, V. Ilcheva, O. Smutok, Y. Kukhazh, M. Gonchar, *Acta Phys. Pol., A* **132** (2017) 1515.
- [9] T.S. Kavetsky, O. Smutok, M. Gonchar, O. Šauša, Y. Kukhazh, H. Švajdlenková, T. Petkova, V. Boev, V. Ilcheva, In: NATO Science for Peace and Security Series B: Physics and Biophysics "Advanced Nanotechnologies for Detection and Defence Against CBRN Agents" (P. Petkov, D. Tsiulyanu, C. Popov, W. Kulisch, eds.), Dordrecht: Springer, 2018, Chapter 30, DOI: 10.1007/978-94-024-1298-7_30.
- [10] T.S. Kavetsky, H. Švajdlenková, Y. Kukhazh, O. Šauša, K. Čechová, I. Mat'ko, N. Hoivanovych, O. Dytso, T. Petkova, V. Boev, V. Ilcheva, In: NATO Science for Peace and Security Series B: Physics and Biophysics "Advanced Nanotechnologies for Detection and Defence Against CBRN Agents" (P. Petkov, D. Tsiulyanu, C. Popov, W. Kulisch, eds.), Dordrecht: Springer, 2018, Chapter 32, DOI: 10.1007/978-94-024-1298-7_32.
- [11] A. Remeikyte, J. Ostrauskaite, V. Grazuleviciene, *J. Appl. Polym. Sci.* **129** (2013) 1290.

FORMATION OF NANOCLOUDS ON THE ADSORBED SURFACE UNDER THE ACTION OF COMPREHENSIVE PRESSURE AND ELECTRIC FIELD

R.M. Peleshchak, O.V. Kuzyk, O.O. Dan'kiv, M.V. Bui

*Drohobych Ivan Franko State Pedagogical University,
24, Ivan Franko Str., Drohobych, Ukraine 82100
e-mail: rpeleshchak@ukr.net*

Recently the subject of intensive researches is to obtain the semiconductor structures with self-assembled nanoclusters by methods of molecular beam epitaxy, ion implantation and under the influence of laser irradiation, and also possibility of controlling their physical properties [1, 2].

The non-linear diffusion-deformation theory of self-organization of nanoclusters of the implanted impurity in semiconductor which considers the elastic interaction of the implanted impurities among themselves and with atoms of a matrix is developed in [3, 4]. The impurity which gets to a matrix, leads to changes in its volume and energy, and the initial fluctuation of deformation under certain conditions causes emergence of deformation-induced flows of the implanted impurities. In a result, in the non-uniform deformation-concentration field there are forces proportional to gradients of concentration and deformation which further deform the matrix. These forces are cause an increase of initial fluctuation and lead to self-organization of clusters of impurities.

The information on nucleation (incipient state of formation) of periodic nanostructures of adatoms and the implanted impurity is important for optimization of technological process and the predicted controlling of physical parameters of the semiconductor structures with nanoclusters. In particular, to calculate the symmetry, the period and formation time of the surface structures, it is sufficient to analyze only the initial (linear) stage of the development of the defect-deformation instability [5].

The theory of spontaneous nucleation of the surface nanometer lattice which is caused by instability in system of the adatoms interacting with the self-consistent surface acoustic wave (SAW) is developed in [5, 6]. Within this theory the conditions of formation of nanoclusters on the surface of solid states are established and the periods of a nanometer lattice as functions of concentration of adatoms and temperature are defined.

Due to the high mobility of charge carriers, gallium arsenide is widely used in the production of quantum-dimensional structures and high-frequency lasers on their basis. The considerable attention of researchers has recently been paid to laser modification of morphology of near-surface GaAs layers at which the conditions of formation of nanoclusters are controlled [7].

In the paper, the influence of the electric field on the conditions of formation and the period of the surface superlattice of the adatoms in the n-GaAs semiconductor is investigated. Periodic deformation appearing on a semiconductor surface leads to modulation of the bottom of the conduction band, hence, to electron-density modulation. As a result, a nonuniform electric field arises, which cause nonuniform displacements of lattice sites, hence, a change in the SAW amplitude. The electric field, interacting with nonuniformly distributed electrons on the surface, leads to the creation of additional pressure (Fig. 1):

$$\sigma_{zz}^{el} = en(x)E,$$

where $n(x)$ is the concentration of conduction electrons, E is the electric field strength.

It is established that in the GaAs semiconductor, an increase in the electric field strength, depending on the direction, leads to an increase or decrease of the critical temperature (the critical concentration of the adatoms), at which the formation of a self-organized nanostructure is possible.

It is shown that in the strongly alloyed n-GaAs semiconductor, the increase of the electric field strength leads to a monotonous change (decrease or increase depending on the direction of the electric field) of the period of self-organized surface nanostructures of the adatoms. It is established that the influence of the electric field on the conditions of formation and the period of surface superlattice does not depend on the sign of the deformation potential of adatoms.

The role of acoustoelectric effects in the formation of nanoscale adatom structures, resulting from the self-consistent interaction of adatoms with the surface acoustic wave and the electronic subsystem in the case of charged and uncharged adsorbed atoms was studied.

It was shown that, in the case of charged adatoms in semiconductor GaAs, an increase in the donor dopant concentration results in a decrease in the critical adatom concentration at which the formation of self-assembled nanostructures is possible or an increase in the semiconductor doping level with donor impurities (an

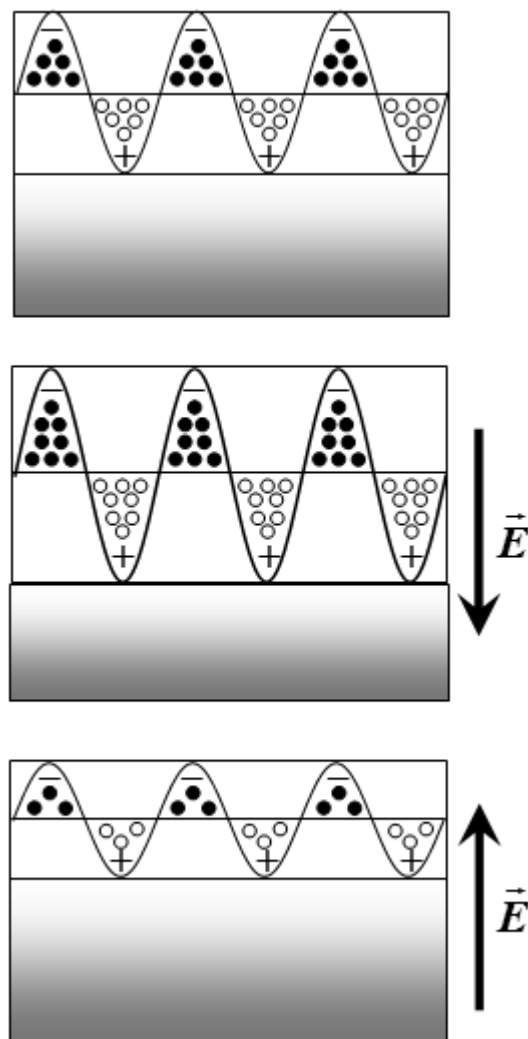


Fig. 1. Geometric model of formation of the surface superlattice of the adatoms under the action of electric field:

- – the defects that are stretching centers;
- – the defects that are squeezing centers

increase in the free electron density) at a fixed average adatom concentration results in an increase in the critical temperature below which self-assembly processes occur.

It was found that an increase in the donor dopant concentration in the case of charged adatoms in semiconductor GaAs leads to a decrease in the period of self-assembled surface nanostructures of adatoms.

It was shown that acoustoelectric interaction causes a change in the inhomogeneous deformation resulting from the spatial redistribution of adatoms. It was found that, depending on the semiconductor doping level with donor impurities, the strain can vary up to 17% in the case of ionized adatoms and only up to 2% in the case of uncharged adatoms.

The theory of nucleation of nanometer structure of the adatoms under the action of comprehensive pressure taking into account acousto-electronic interaction is developed. Self-organization occurs as a result of defect-deformation instability caused by self-consistent interaction between the adsorbed atoms and the surface acoustic wave. Within this theory the influence of comprehensive pressure and doping degree of semiconductor on the conditions of formation and the period of nanometer structure of the adatoms is investigated. The period of nanometer structure of the adatoms depending on the value of comprehensive pressure, temperature, average concentration of the adatoms and conduction electrons is defined [8]. It is established that the increase in pressure leads to expansion of temperature intervals within which nanometer structures of the adatoms are formed, and the decrease of their period.

References

1. Yamada I., Matsuo J., Tojoda N., Phys. Research B, 2003, **206**, 820.
2. Ipatova I.P., Malyskin V.G., Maradudin A.A., Phys. Rev. B, 1998, **57**, 12968.
3. Peleshchak R.M., Kuzyk O.V., Ukr. J. Phys., 2009, **54**, 702.
4. Peleshchak R.M., Kuzyk O.V., Dan'kiv O.O., Journal of nano- and electronic physics, 2016, **8**, 02014.
5. Emel'yanov V.I., Laser Phys., 2008, **18**, 1435.
6. Peleshchak R.M., Kuzyk O.V., Dan'kiv O.O., Condensed Matter Physics, 2015, **18**, 43801.
7. Vlasenko A.I., Baidullaeva A., Veleschuk V.P., Mozol P.E., Boiko N.I., Litvin O.S., Semiconductors, 2015, **49**, 229.
8. Peleshchak R.M., Kuzyk O.V., Dan'kiv O.O., Journal of nano- and electronic physics, 2018, **10**, 01014.

INVESTIGATION OF THE RELAXATION CHARACTERISTICS OF EPOXY POLYMERS BY CALORIMETRIC METHOD

M.I. Shut, T.G. Sichkar, L.K. Yanchevsky, O.S. Tulzhenkova, M.O. Rokyt-skyi

*National Pedagogical Dragomanov University,
9 Pirogova St., 01601 Kiev, Ukraine*

Traditionally, relaxation characteristics of polymers are determined by method of relaxation spectrometry proposed by G.M. Bartenev [1-3]. In our work it is justified the use of calorimetric method as a more informative express method for determining the complex of relaxation characteristics exactly for glass transition [4-6].

Investigation of the glass transition relaxation characteristics (activation energy U_α and pre-exponential factor B_α) of epoxy polymers with temperature – frequency measurements [1, 2] demonstrates the sufficiently high dependence of activation energy upon temperature and accordingly the low value of pre-exponential factor.

Such state witnesses a complex character of the epoxy polymers glass transition and needs the separate study of its peculiarities. Firstly, difficulties can arise because of stoichiometrical misbalance of the oligomer and curing agent when unresolved (excess) reactionable component groups exist. In this case the resulting glass transition process consists of different parts depending of cross-linking level and hence glass transition temperature. Opposite situation appears when the glass transition overlaps with different nature processes, particularly, such as curing process [7]. Realization of these processes with repeatedly heating provokes an after-curing peak appearance, which overlaps with a jump of heat capacity in the glass transition process on the curve of heat capacity dependence upon temperature.

Studying of the epoxy polymer glass transition process and using the calorimetric method of experimental relaxation characteristics complex determination for the glass transition process is the aim of this work.

In the first case the processes overlapping makes temperature range of the glass transition wider, but in the second case, it makes that range shorter. So, it should be considered the experimental sensitives to such difficulties. Thus it is expedient to use for the glass transition characteristics complex determination the method based on experimentally obtained temperature range [4-7].

This complex comprises: activation energy U_α , kinetic unit self oscillation frequency B_α , glass transition temperature T_α , glass transition cooperative level w , segment cooperative activation energy $U_{\alpha \text{ coop}}$ for edge components of glass transition and the most probable glass transition temperature.

The object of the study was epoxy dianous resin ED-16. Maleic anhydride was used as a curing agent. Diaminylanilin was used as a modifier in ratio of 0.5 mass parts of the modifier to 100 mass parts of ED-16.

Investigation on dependence of compositions properties upon curing agent amount was performed to develop a method for determining the curing agent optimal amount. The optimal amount of the curing agent provides the reaching of maximum conversion level [8] during curing mode at 473K for 12 hours. Different temperature and time modes allows the obtaining of samples with excess or shortage of appropriate reactive groups, e. a. the samples of systems with different content of segments for future studying.

The second group of samples, in which the object of research was the system of UP-643+IMTHPA (isomethyltetrahydrophthalic anhydride), was obtained with the optimal ratio of resin and curing agent, but with the different curing modes. This allows the obtaining of the samples with different solidification level and different intensity of after-curing process under repeated heating.

It was obtained two groups of the samples. One of them is related to system with slow-change of amount of uninvolved reactive groups with no involving opportunity under repeated heating, e. a. exfoliation of the system depending on segment contents is modeled. The second group of the samples is related to system with optimized quantity of reactive groups, but with change of after-curing process, different intensity of the after-curing processes and overlapping with the glass transition process is modeled. We can consider that such point of view allow us to detach the glass transition process and its components, neglecting the overlapping of other processes.

Received data allow the obtaining of the optimal ratio of resin to curing agent using T_α behavior or changes of $U_{\alpha \text{ coop } 1,2}$. Traditional methods allow one to do this when T_α reaches the maximum. In suggested method the optimality responds to the maximum approaching $U_{\alpha \text{ coop } 1}$ to $U_{\alpha \text{ coop } 2}$ and reaching them to the maximum. Equality of heat capacity C_x in the both methods justifies applicability of suggested method. It is necessary to note that difference between C_{opt} and C_{stoich} is considerably big (38 and 40 mass parts respectively). This tells about experimental correction of value C_x for obtaining high quality products made of epoxy resins. Suggested method provides more information and allows observing of dynamics of system segment contents heterogeneity change. And even more, it is shows unattainability of the full system homogeneity even with C_{opt} .

About second group of the samples UP-643+IMTHPA we can mention that analysis of the obtained results allow us to suggest the calorimetric method for epoxy compositions conversion level estimation.

The conversion level α was obtained with traditional method using the following equation:

$$\alpha = (\Delta H_0 - \Delta H) / \Delta H_0 \cdot 100\%,$$

where ΔH – enthalpy of after-curing process of sample; ΔH_0 – enthalpy of resin and curing agent mixture, taken at once after mixing. K factor can be derived using equation:

$$K = \Delta T_{\text{exp}} / T_{\text{calc}} \cdot 100\%.$$

This equation is based on fact that ΔT_{exp} is deformed by overlapping of the after-curing peak and ΔT_{calc} is not. Thus more intensive after-curing peak produces the smaller value of ΔT_{exp} . That is why the value of K factor corresponds to changes of the conversion level. It is evident that α and K factors have different destinations. In the beginning α can quite efficiently describe the conversion level, but K factor can efficiently describe the ending of this process. It is practically important, as estimation of conversion level in the ending phase allow evaluating the completion level of the reaction, quality of the compiled products made of epoxy resins. Introduction and using of calculated K factor is more important because of any method among the methods of epoxy polymers curing process kinetics investigation, which are widely used in techniques (ultrasonic, infrared spectrometry, titration of detached samples) can't allow to evaluate the conversion level in the ending phases of reaction.

Thus, the new method has been suggested for determination of the complex of epoxy polymers glass transition relaxation characteristics. This method can free the glass transition from overlapping with processes of other nature. Also it can help to obtain the components of the complex glass transition process in heterogeneous system with segment contents.

Suggested calorimetric method is based on experimental investigation of epoxy polymer heat capacity. This is universal method, as it allows to:

- determine the relaxation characteristics (activation energy U_{α} and pre-exponential factor B_{α});
- investigate the samples of completed production and control the curing process from the beginning to the end;
- determine the optimal ratio of resin to curing agent in epoxy composition;
- obtain the conversion level of epoxy composition in the ending phases of reaction and in completed products.

References

1. N.I. Shut, G.M. Bartenev, M.V. Lazorenko, T.G. Sichkar, *Acta Polimerica*, **42**, 384 (1991).
2. G.M. Bartenev, N.I. Shut, V.P. Dushchenko, T.G. Sichkar, *Vysokomolek. Soyedin., Ser. A*, **28**, 627 (1986) [in Russian].
3. A.I. Slutsker, Yu.I. Polikarpov, K.V. Vasileva, *Fizika tverdogo tela*, **44**, 1529 (2002) [in Russian].
4. L.K. Yanchevski, V.V. Levandovski, *Acta Polimerica*, **44**, 29 (1993).
5. T.G. Sichkar, L.K. Yanchevsky, O.V. Gorshunov, M.I. Shut, *Issues of Chemistry and Chemical Technology*, **1**, 228 (2004) [in Russian].
6. M.I. Shut, M.A. Rokitskiy, A.M. Shut, G.V. Rokitskaya, *Funct. Mater.*, **20**, 221 (2013). <http://dx.doi.org/10.15407/fm20.02.221>
7. N.I. Shut, T.G. Sichkar, A.P. Dyn, V.P. Dushchenko, *Acta Polimerica*, **38**, 446 (1987).
8. M. Urbaniak, *Polimery*, **56**, 240 (2011).

STRONG CORRELATION EFFECTS IN THERMODYNAMICS OF THE LATTICE BOSE-FERMI GAS

I.V. Stasyuk, V.O. Krasnov

Institute for Condensed Matter Physics of NAS of Ukraine, Lviv, Ukraine

The new stage in investigation of strongly correlated lattice systems of quantum particles started in a 2000s in connection with a creation of optical lattices with ultracold atoms. The main role in physics of these systems is played, together with the particle transfer in a lattice, by their on-site interaction. The quantum lattice gas models, similar to the Hubbard model, were formulated for optical lattices: the Bose-Hubbard model [1] for a lattice with Bose-atoms and the Bose-Fermi-Hubbard model [2] for lattices with their mixtures. The number of properties of these systems, e.g. their thermodynamics and phase transitions between normal (MI, Mott insulator) and superfluid (SF) phases were described.

Transition to the SF phase in the Bose-Hubbard (BH) model, which is of the 2nd order and related to the appearance of Bose-Einstein condensate, is well-studied (see [3]). Analogous transition in the Bose-Fermi-Hubbard (BFH) model is more complicated due to the fermion presence. In the literature, the considerable attention is devoted to this effect. First experiments in this direction were performed in [2] with the ^{87}Rb - ^{40}K mixture, where the loss of coherence of the Bose-atoms ^{87}Rb and decay of condensate with the raise of the Fermi-atoms ^{40}K concentration, was noticed. To describe it, the renormalization of the boson hopping parameter, the excited boson bonds influence, the effects of correlated hopping, etc., were considered. In general, the difference at the local boson-fermion repulsion or attraction in behavior of the boson-fermion mixtures and in the shape of corresponding phase diagrams was noticed [4].

The effect of fermions on the BE-condensate appearance was considered recently based on the application of the grand canonical ensemble within a simplified version of the BFH model (a heavy-fermion limit and the hard-core boson approach). Such a model was proposed in [5]. Phase diagrams for boson-fermion mixture and changes in their shape as well as the phase transition order, depending on the fermion chemical potential level, were investigated in the case of BF repulsion ($U' > 0$). The complete analysis of the role of this interaction needs the performing of the similar investigation for $U' < 0$. This is the problem that is set up at the present study. At the same time, we show that the BFH model possesses an internal symmetry based on fermion-hole transformation that enables to match each other the thermodynamical functions and phase diagrams for the $U' > 0$ and the $U' < 0$ cases.

In our investigation we use the Hamiltonian of BFH model written as [2]

$$\hat{H} = \frac{U}{2} \sum_i n_i^b (n_i^b - 1) + U' \sum_i n_i^b n_i^f - \mu \sum_i n_i^b - \mu' \sum_i n_i^f + \sum_{i,j} t_{ij} b_i^\dagger b_j + \sum_{i,j} t'_{ij} a_i^\dagger a_j, \quad (1)$$

passing through to hard-core bosons (at $U \rightarrow \infty$ the bosonic operators became the Pauli ones) and restricting by heavy-fermion limit ($t'_{ij} \rightarrow 0$) in thermodynamics of the model in the random-phase approximation. Chemical potentials of bosons and fermions are considered as independent variables. Thermodynamical equilibrium is determined by absolute minima of the grand canonical potential at the given values of μ and μ' .

There exists some internal symmetry in the Bose-Fermi-Hubbard model. It can be seen when we will perform the operator transformation.

$$\begin{aligned} a_i &= c_i^\dagger; \quad a_i^\dagger = c_i \\ n_i^f &= a_i^\dagger a_i = c_i c_i^\dagger = 1 - c_i^\dagger c_i = 1 - n_i^b \\ a_i^\dagger a_j &= -c_i^\dagger c_j \quad (i \neq j), \end{aligned} \quad (2)$$

and introduce the notations $U' - \mu = -\bar{\mu}$; $\mu' = -\bar{\mu}'$; $t'_{ij} = -\bar{t}_{ij}$. Then, transformed Hamiltonian differs from the initial one only by the substitution $U' \rightarrow -U'$. In other words, the formal replacement

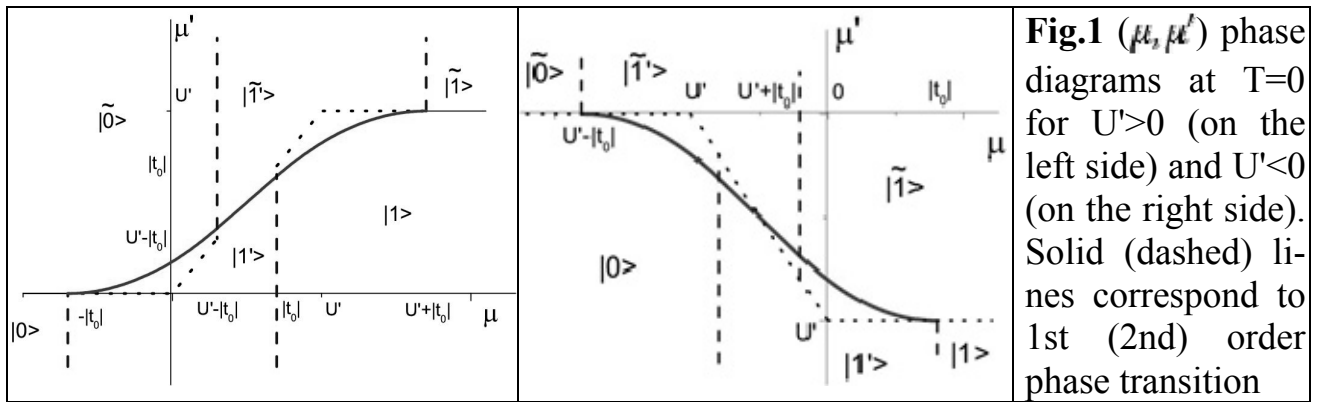
$$U' - \mu \rightarrow -\mu; \quad \mu' \rightarrow -\mu'; \quad t'_{ij} \rightarrow -t'_{ij}; \quad U' \rightarrow -U', \quad (3)$$

in the Hamiltonian of the BFH model establishes a correspondence between the cases with positive and negative values of interaction parameter U' . In this situation the results, obtained at the investigations of thermodynamics and energy spectrum of BFH model with boson-fermion repulsion, can be transferred to the case of the model with the attraction using the transformation (3).

Below, we illustrate this possibility on the example of simplified version of the BFH model (in the hard-core boson and heavy fermion limit) considered earlier at $T=0$ in [5] for $U'>0$. The model which appears in this case is the four-state one consisting of the states $|0\rangle = |0,0\rangle, |1\rangle = |1,0\rangle, |\tilde{0}\rangle = |0,1\rangle, |\tilde{1}\rangle = |1,1\rangle$, where the reduced basis $|n_i^b, n_i^f\rangle$ is formed by the occupation numbers $n_i^b = 0,1; n_i^f = 0,1$.

We consider, at first, the phase diagrams (μ, μ') at $T=0$ which illustrate the regions of existence of different phases (MI and SF). In the case of zero temperature they are the regions of different ground states of the system.

Construction of diagrams for $U'<0$ (case II), using the diagrams for $U'>0$ (case I) obtained in [5], reduces to two transformations on the plane (μ, μ') : 1) the mirror reflection with respect to the horizontal axis μ ; 2) the shift to the left along the μ axis by $|U'|$. Obtained in such a way new diagram in the case $\frac{|U'|}{2} < |t_0| < |U'|$ is presented (as well as initial one) in the fig.1.



The phases, marked on diagrams, correspond to the ground states of the system and are described by the initial basis in the case of MI phase (the states $|0\rangle$, $|1\rangle$, $|\tilde{0}\rangle$ and $|\tilde{1}\rangle$ with different numbers of bosons and fermions). In the case of SF phase these ones are the states $|1'\rangle$ and $|\tilde{1}'\rangle$ (the eigenstates of diagonalized Hamiltonian in the presence of the BE-condensate). They describe the SF phases of two types - with small ($SF|1'\rangle$) and large ($SF|\tilde{1}'\rangle$) concentrations of fermions.

As one can see from these diagrams, a gradual suppression of SF phase takes place due to appearing of fermions and growth of their concentration (this occurs when the chemical potential μ' increases).

For $|t_0| < |U'|/2$, the SF phase disappears with the further increase of μ' ; this effect takes place at $\mu' \geq |t_0|$ for $U'>0$ and at $\mu' \geq U'+|t_0|$ for $U'<0$. The difference between cases I and II consists, however, in the fact that with appearing of fermions in the first case the condensate with the small boson concentration disappears the first, while in the second one - vice versa, with the large concentration of bosons. Besides, phase transition occurs by itself at the increase of μ' in the case I from SF phase $|1'\rangle$ to MI phase $|\tilde{0}\rangle$ (where $n_F=1$, $n_B=0$), while in the case II - from SF phase $|\tilde{1}'\rangle$ to MI phase $|\tilde{1}\rangle$ (for the last we have $n_F=1$, $n_B=1$). This is manifestation of effect of B-F repulsion, or, respectively, attraction.

If $|U'|/2 < |t_0| < |U'|$, the situation, in general, remains similar. However, the gap which divides the regions of two type of condensates in (μ, μ') diagram, does not exist. Besides of that, in the intermediate region of μ' values they co-exist. Transition between them takes place on the line of the 1st order transitions, which has the opposite inclination opposite inclination with respect to μ and μ' axis in the cases I and II. The different effect of the boson-fermion interaction effect on the phase transition to the state with BE-condensate in the cases of $U'>0$ and $U'<0$ one can see from $(|t_0|, U')$ diagrams presented at fig.2.

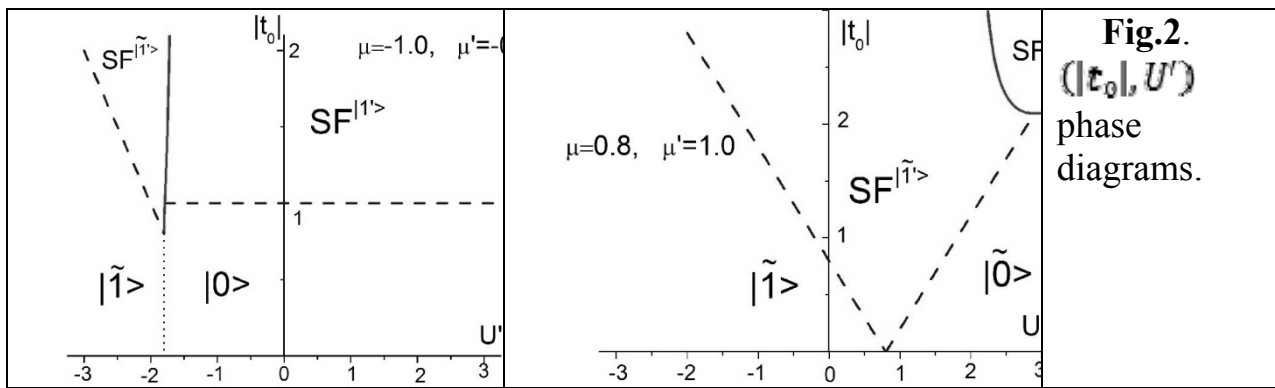


Fig.2.
($|t_0|, U'$)
phase
diagrams.

The shape of diagrams strongly depends on values of chemical potentials of fermions μ' and bosons μ which are considered to be fixed

The presented figures show that in the region of strong repulsion ($U' > 0$) the superfluid phase $SF|1'>$ is always present, transforming at the decrease of parameter of the boson hopping into the phase $|0>, |1>$ or $|0\tilde>$.

The different behavior is observed in the case of boson-fermion attraction ($U' < 0$). Here, at the increase of attraction only two phases $SF|1'>$ and $|1>$ remain. The phase transition between them takes place on the line $|t_0| = \mu - U'$ and is of the 2nd order. The MI phase here is formed by the on-site boson-fermion pairs and in the SF phase the BE-condensate exists at concentrations \bar{n}_B close to the full filling on the background of filled fermion states. Such phases can exist at any large attraction when the condition $|t_0| > \mu - U'$ is fulfilled.

The general shape of the obtained ($|t_0|, U'$) diagrams reproduces the measured in [4] features of the BE condensate appearance at the tuning (with the help of Feshbach resonance) of the BF interaction constant in a wide range of negative as well positive values.

References:

- [1] Jaksch D., Bruder C., Cirac J. I. et al. // Phys. Rev. Lett., 1998., Vol. 81, P. 3108.
- [2] Albus A., Illuminati F., Eisert J. // Phys. Rev. A, 2003, Vol. 68, P. 023606.
- [3] Bloch I., Dalibard J., Zwierger W. // Rev. Mod. Phys., 2008, Vol. 80, P. 885.
- [4] Best T., Will S., Schneider U. et al. // Phys. Rev. Lett., 2009, Vol. 102, P. 030408.
- [5] Stasyuk I. V., Krasnov V. O. // Condens. Matter Phys., 2015, Vol. 18, N. 4, P. 43702.

ВНЕСОК УКРАЇНСЬКИХ ВЧЕНИХ У СТАНОВЛЕННЯ КАТОДНО-ПРОМЕНЕВОЇ ФІЗИКИ

Шендеровський Василь Андрійович

*доктор фізико-математичних наук, професор, провідний науковий
співробітник Інституту фізики НАН України, Київ,
(schender@iop.kiev.ua, 525-07-77)*

The article, based on the research of scientific sources, reveals the little-known page of the historical development of X-ray in Ukraine after the discovery of X-rays. The scientific, practical and organizational activities of our compatriots, in particular, Ivan Puluj, Joseph Kosonogov, and Mykola Pilchikiv, are described in detail.

Серед чи не найвизначніших відкриттів XIX століття є відкриття невидимих Х-променів. Сьогодні ці промені здобули найширше визнання і повсюдно застосовуються для комп'ютерної томографії і Х-променеграфії, Х-мікроскопії, Х-спектроскопії тощо. У будь-якому фізичному словнику чи енциклопедії можна прочитати, що Х-промені – це електромагнітне йонізувальне променювання, яке міститься у спектральній смузі між гама- і ультрафіолетовим променюванням у межах довжин хвиль від 10^{-4} до 10^3 А (від 10^{-12} до 10^{-5} см). Його джерелом є спеціальна рурка, в якій пришвидшені електричним полем електрони бомбардують металевий анод, у результаті чого утворюються промені, здатні протинати непрозоре тіло так, що ними можна просвітлювати, наприклад, людський організм тощо.

За допомогою Х-променевого обстеження досліджують кістки черепа (краніографія) і хребта (вертебрографія). У випадку пухлин мозку вторинні зміни спостерігаються і на плоских кістках черепа. І хоча нервова тканина є невидимою для Х-променів, цей метод залишається незамінним у випадку підозри на травматичні ушкодження мозку або деякі інші захворювання, зокрема пухлини мозку та гіпофізу. Останніми роками широко застосовують Х-контрастні препарати, які вводять внутрішньовенно безпосередньо перед обстеженням для більш рельєфного зображення органа.

Найвагоміший внесок у відкриття катодно-променевої фізики зробив наш співвітчизник Іван Пулюй, славетний вчений: математик, електротехнік, математик, астроном, теолог, енергобудівник, а також педагог, громадський діяч, професор Віденського університету, засновник першої кафедри електротехніки в Європі, ректор Німецької Вищої школи у Празі.

Багато науковців досліджували праці Рентгена, Ленарда, Тесли, Пулюя, які працювали над проблемою з'ясування природи катодних променів та Х-променів. І можна однозначно стверджувати про пріоритет Івана Пулюя у багатьох аспектах. Зокрема, він:

- а) вперше сконструював власноручно рурку (за 14 років до відкриття);
- б) пояснив природу виникнення Х-променів;

в) встановив здатність Х-променів йонізувати газ;
 г) виявив їх просторовий розподіл, тобто де і як вони виникають (фактично природа Х-променів);

д) вперше (!) наголосив на важливості застосування Х-променів у медицині, зокрема вперше зробив 18 січня 1896 року світлину руки 11-річної дівчинки, а 2 лютого 1896 року вперше продемонстрував світлину кістяка мертвонародженої дитини.

Незважаючи на такі визначні результати Івана Пулюя, Нобелівська премія за це відкриття була присуджена 10 грудня 1901 року Конраду Рентгену з формулюванням: «Вільгельму Конраду Рентгену на знак визнання його видатних заслуг, доведених його відкриттям променів, які сьогодні носять його ім'я».

Шлях променології, започаткований відкриттям Х-проміння, в Україні продовжив Микола Дмитрович Пильчиків, про якого ми знаємо дуже мало. Хронологія його досліджень свідчить, що він був попередником поширення Х-променології в Москві та Петербурзі. Виявляється, вдалі експерименти з Х-променями, що відкрили низку ще не знаних їхніх властивостей, Пильчиків виконав уже 19 січня 1896 року, коли в Одесі ще не було точних відомостей про попередні повідомлення Рентгена. У ті дні він скористався руркою конструкції Пулюя, що переконливо засвідчує обізнаність Пильчиківа з попередніми дослідженнями над Х-променями свого далекого українського колеги. Рурка Пулюя дала змогу М. Пильчиківу істотно скоротити тривалість експозиції. «Одна невелика машина Фосса, – писав Пильчиків, – з однією такою руркою (Пулюя) замінює котушку зі звичайною руркою Крукса. Використовуючи котушку, опісля пристрій Тесли, ми досягаємо зменшення тривалості експозиції до кількох хвилин, а згодом – до 30 секунд».

За кілька днів, замінивши електромашину Фосса на машину Вінсхерта, Пильчиків звів тривалість експозиції до двох секунд. У ті січневі дні то була найкоротша експозиція у світі. Дослідники ж, які користувалися рурками Крукса у Петербурзі, одержували світлини з експозицією близько тридцяти хвилин.

Наприкінці січня Пильчиків удосконалив рурку Пулюя, застосувавши увігнутий антикатод. Цей прилад і здобув назву «фокус-рурка Пильчиківа». Публічні лекції вченого на початку 1896 року для професорів, викладачів гімназій, інженерів, морських офіцерів, студентів і гімназистів про казкові властивості невидимих Х-променів здобули Пильчиківу широку популярність в Україні. Адже його власні експерименти в Одесі були результативніші, ніж у Петербурзі та Москві. Вони показали можливість застосування Х-проміння для діагностики захворювань.

1883 року Пильчиків почав досліджувати Курську магнітну аномалію і одним з перших заклав основи теорії аномалій геомагнетизму, обґрунтував наявність покладів залізної руди, відкрив нові ділянки аномалії біля Прохоровки та Мар'їної. Саме за це дослідження його нагороджено медаллю Російського географічного товариства. 1893 року вчений переїхав до Новоросійського університету на посаду екстраординарного професора. Тут він

уперше відкрив можливість електронної фотографії, винайшов протектор, який захищав прилади – телефони, маяки, семафори, гармати, міни – від дії на них електричних хвиль стороннього походження. 1902 року очолив кафедру фізики в Харківському технологічному інституті.

Микола Пильчиків – винахідник понад 25 оригінальних приладів та установок, конструктор диференційного ареометра, термостата, сейсмографа, рефрактометра, моделі радіокерованого протимінного захисту кораблів.

12 лютого 1908 року вченого обрали дійсним членом Російського фізико-хімічного товариства.

19 травня 1908 року Миколу Пильчиківа знайдено мертвим, обставини його смерті так і не було з'ясовано.

Яскрава, хоч і маловідома сторінка історії розвитку Х-променевої фізики – це науковий, технічний, організаційний та практичний доробок ще одного нашого співвітчизника з Києва – Йосипа Йосиповича Косоногова, професора Київського університету.

Народився український фізик-експериментатор Йосип Косоногов 12 квітня 1866 року. Саме Йосип Косоногов стояв біля джерел створення Української Академії наук, був організатором низки наукових товариств у Києві. Косоногов – учень і співробітник Михайла Авенаріуса, одного з творців першої фізичної школи в Україні. Понад 20 років Йосип Косоногов очолював кафедру географії університету, а від 1885 року – Київську метеорологічну обсерваторію. Написав посібник «Конспект лекцій з атмосферної електрики і земного магнетизму», який тривалий час був єдиним підручником з цих галузей знань. Саме Косоногов обґрунтував на засіданні підкомісії для організації фізико-математичного відділу Академії наук потребу створення фізичного інституту, його головні напрями.

Проте внесок Косоногова у становлення Х-променевої фізики є вагомим. Зазначимо, що до початку війни 1914 року у царській Росії налічувалося 146 рентгенових апаратів закордонного виробництва, 1900 року в Київському військовому шпиталі з'явився перший рентгенів апарат.

Вже 5 вересня 1914 року київська інтелігенція переважно з викладачів хімії та фізики високих та середніх навчальних закладів утворює комісію допомоги пораненим. Очолив комісію професор Й. Косоногов. Комісія швидко здобула популярність і через кілька місяців налічувала понад 80 осіб. До складу комісії увійшли всі члени Фізико-математичного товариства Київського університету, що працювали в галузі фізики.

З дозволу попечителя Київського навчального округу комісії надали у тимчасове користування для обладнання рентгенових кабінетів придатне для цього обладнання з фізичних кабінетів середніх і високих навчальних закладів Києва. Завдяки цьому комісія отримала змогу обладнати 7 рентгенових кабінетів і підготувати обладнання у трьох шпиталях.

За два перших роки комісія обладнала у Києві 17 рентгенових стаціонарних кабінетів, що обслуговували шпитальну мережу з 12000 ліжок, і провела близько 3000 обстежень. У під відомстві комісії перебувала рентгенова мережа Чернігова і Жмеринки. Було створено лабораторію й майстерні

ремонту рурок. Адже вони вироблялися за кордоном, коштували дорого, а лихоліття війни створювало перешкоди до їх придбання. Була сконструйована оригінальна модель рурки, що одержала назву «колегія». З 1915 року почало виходити періодичне видання «Відомості київської рентгенової комісії». За два з половиною роки вийшло 15 номерів.

У кінці 1916 року з ініціативи професора Й. Й. Косоногова було поставлено питання про організацію та відкриття курсів і шкіл для підготовки спеціалістів з рентгенології на базі медичного факультету Київського університету.

Професор Й. Косоногов розробив програму курсів рентгенотехніки, що мала фізико-технічне спрямування. Пізніше, уже після ліквідації діяльності комісії, її членами у 1919-1920 роках створюється київська міська рентгенова допомога. Київ перетворюється на своєрідний технічний центр, де було налагоджено ремонт рентгенових рурок та інструментарію і виробництво нових виробів: підсилюючих екранів, дозиметрів та ін.

Список використаних джерел:

1. Влох О.Г., Гайда Р.П., Пляцко Р.М. Іван Пулюй та становлення рентгенології// Нариси з історії природознавства і техніки. – 1994. - № 41. – С. 69.
2. Шендеровський В. Він належав до тих, хто... формував світ// Вісник НАН України. – 1995. - № 1-2. – С. 56-60.
3. Розенберг Ф. Історія фізики. – Москва-Ленінград. ОНТБ. – С. 401.
4. Попов М.Ф. Еволюція принципів конструкції рентгенових рурок// Рейнберг С.О. Нариси розвитку медичної рентгенології. – Москва: «Медвид». – 1948. – С. 247.
5. Косоногов Й.Й. Матеріали про діяльність в Київському фізико-математичному Товаристві. Ф. 202. о.п.І. – Центральний науковий архів інституту архівознавства ЦНБ ім. В.І. Вернадського.
6. Романчук О.К. Фокус-трубка Пильчиківа// Аксіоми для нащадків. – Львів. – 1992. – С. 213.
7. Про організацію і відкриття курсів і шкіл для підготовки спеціалістів з рентгенології 1917 року. Медичний факультет Київського університету. – Ф. 16. – Держархів м. Києва.
8. Троїцький Е.Є. Мартинкевич О.О. Нариси діяльності Київської рентгенової комісії у 1914-1917 роках. // Заг. ред. Рейнберг С.О. Матеріали з історії рентгенології в СРСР. – Москва: «Медвид». – 1948. – С. 146 – 153.

Table of CONTENTS

QUANTUM-SIZE CONFINEMENT PHENOMENA	5
EFFECT OF SWITCHING IN THE CONDUCTIVITY OF InGaAs/GaAs HETEROSTRUCTURES WITH TUNNEL-COUPLED QUANTUM WELLS P.A. Belevskii, <u>M.M. Vinoslavskii</u> , V.M. Poroshin	6
OPTICAL PROPERTIES OF THE ARRAYS DIFFERENT FORM QUANTUM DOTS <u>V.I. Boichuk</u> , <u>I.V. Bilynskiy</u> , R.I. Pazyuk	10
TWO ELECTRONIC MOLECULA CONTAINING THREE SPHERICAL QUANTUM DOTS <u>Boichuk V.I.</u> , <u>Holskyj V.B.</u> , Leshko R.Ya.	12
EFFECT OF POLARIZATION TRAPS, DONOR AND ACCEPTOR IMPURITIES ON THE INTRABAND AND INTERBAND LIGHT ABSORPTION OF QUANTUM DOTS <u>Boichuk V.I.</u> , <u>Leshko R.Ya.</u> , Karpyn D.S., Ivanchyshyn I.B., Toma I.P.	14
THE JOINED EFFECT OF ELECTRIC AND MAGNETIC FIELD ON THE OPTICAL PROPERTIES OF NANOSTRUCTURE CdS/HgS/CdS/HgS/CdS V.A. Holovatsky, <u>M.Ya. Yakhnevych</u> , <u>N. Ya. Yakhnevych</u>	17
BACGROUND IMPURITIES AND DELTA-DOPED QWs <u>O.Fomina</u> , V.Tulupenko, R. Demediuk, V. Akimov, C. A. Duque, A.L.Morales and D. Sushchenko	21
SYNTHESIS OF DOPED NCs CdTe <u>O.A. Kapush</u> , D.V. Korbutyak, S.I. Budzulyak, N.D. Vakhniak	25
ELECTRONIC PROPERTIES OF SURFACE VACANCIES IN CDS NANOCRYSTALS <u>I.M. Kupchak</u> , N.F. Serpak, O.A. Kapush, D.V. Korbutyak	27
ЕФЕКТ НЕГАТИВНОЇ ДИФЕРЕНЦІАЛЬНОЇ ПРОВІДНОСТІ У 2D НАПІВПРОВІДНИКОВИХ МОНОШАРАХ: ТЕОРЕТИЧНА МОДЕЛЬ В.Г.Литовченко, А.І.Курчак, М.В.Стріха	31
EFFECT OF ELECTRIC FIELD ON OPTICAL PROPERTIES OF SEMICONDUCTOR QUANTUM RINGS IN INRR-RED REGION OF THE SPECTRUM O.M. Makhanets, <u>V.I. Gutsul</u>	33
PROPERTIES OF ELECTRON QUASI-STATIONARY STATES IN DOUBLE-BARRIER NANOSTRUCTURE WITHIN THE MODEL OF POSITION DEPENDENT EFFECTIVE MASS <u>J.O. Seti</u> , M.V. Tkach, O.M. Voitsekhivska	36
EFFECT OF POLARIZATION PHONONS ON ELECTRON, HOLE AND EXCITON STATES IN SPHERICAL QUANTUM DOTS OF CUBIC LATTICE STRUCTURE I. S. Shevchuk	39

SYNTHESIS OF NANOCOMPOSITE POLYMER FILMS WITH THE EMBEDDED CIS NANOCRYSTALS AND THEIR OPTICAL PROPERTIES <u>V. Tokarev</u> , O. Shevchuk, H. Ilchuk, N. Bukartyk, R. Petrus, S. Tokarev, D. Korbutyak, S. Budzulyak, O. Kapush, V. Ermarov, S. Kalytchuk, N. Vakhnyak	42
ON REARRANGMENT OF THE ENERGY SPECTRUM OF DELTA-DOPED QUANTUM WELLS IN THE THZ RANGE <u>V. Tulupenko</u> , R. Demediuk, V. Akimov, C. A. Duque, A. L. Morales, D. Sushchenko, and O. Fomina	45
OBTAINING AND OPTICAL PROPERTIES OF ZnS, ZnS:Fe NANOCRYSTALS <u>Yu. F. Vaksman</u> , Yu. A. Nitsuk	49
ELECTRONIC TRANSPORT, OPTIC, PHOTOELECTRIC AND MAGNETIC PROPERTIES OF SEMICONDUCTOR CRYSTALS	53
SPATIO-TEMPORAL TRANSFORMATION OF INFRA-RED FEMTOSECOND LASER PULSES IN CRYSTAL SILICON Ivan Blonskyi, <u>Viktor Kadan</u> , Svitlana Pavlova, Ihor Pavlov, Andriy Rybak, Laurent Calvez, Oleh Shpotyuk	54
BIMETALLIC NANOCATALYSTS PtCu AND PtNi FOR FUEL CELLS <u>Chernikova O. M.</u> , Ogorodnik Y. V.	57
LOW FREQUENCY RAMAN SPECTRA OF As_xS_{100-x} GLASSES AND LOW FREQUENCY QUASI-LOCALIZED VIBRATIONS OF SOFT AND RIGID As_NS_M NANOCCLUSERS DEPENDING ON NUMBER OF FIXED POINTS R. Holomb, V. Mitsa, L. Himics, M. Veres	61
GENERATION OF ELECTRONIC EXCITATIONS IN SEMICONDUCTORS UNDER THE ACTION OF CHEMICAL REACTION ON THE SURFACE <u>V. P. Grankin</u> , D. V. Grankin	65
OPTICAL PROPERTIES OF PMMA NANOCOMPOSITES IMPLANTED BY LIGHT AND HEAVY IONS <u>T. S. Kavetsky</u> , M. Trzeciński, M. M. Kravtsiv, K. V. Zubrytska, O. R. Mushynska, A. L. Stepanov	68
FABRICATION OF PHOTONIC CRYSTAL BY ION IMPLANTATION: POSSIBILITY TO USE A CHALCOGENIDE FILM SUBSTRATE <u>T. S. Kavetsky</u> , K. V. Zubrytska, A. V. Stronski, L. I. Pan'kiv, P. Petkov, V. I. Nuzhdin, V. F. Valeev, A. M. Rogov, Y. N. Osin, A. S. Morozova, A. L. Stepanov, J. Ruan, H. Tao, X. Zhao	71
STRUCTURE AND PHYSICO-CHEMICAL PROPERTIES OF GRAPHENE-LIKE NANODOTS <u>Karpenko O. S.</u> , Demianenko E. M., Lobanov V. V., Kartel M. T.	74
FIRST-PRINCIPLES STUDY OF THE CONDUCTIVITY OF $In_xTl_{1-x}I$ SOLID SOLUTIONS OF SUBSTITUTION Kashuba A. I., Franiv A. V., Solovyov V. V.	78

RADIATION-INDUCED CREATION OF ATOMIC CLUSTERS IN POLYATOMIC CRYSTALS <u>A. E. Kiv</u> , N. A. Mykytenko, Yu. V. Bondaruk, I. I. Donchev	82
PARTICULARITIES OF ZnO:Mn NANOCRYSTALS DOPING AT THEIR SYNTHESIS BY AEROSOL SPRAY PYROLYSIS METHOD <u>A.V. Kovalenko</u> , V.Yu. Vorovsky, M.F. Bulaniy, O.V. Khmelenko	85
INVESTIGATION OF EPR SPECTRA IN $\text{ZnS}_x\text{Se}_{1-x}$ NANOCRYSTALS. <u>A. V. Kovalenko</u> , E. G. Plakhtiy, O. V. Khmelenko	89
THE OPTICAL PHONONS MANIFESTATIONS IN DYNAMICS OF THE OPTICAL ABSORPTION SPECTRA OF THE FLAT HETEROSTRUCTURES $\text{Al}_x\text{Ga}_{1-x}\text{N}/\text{GaN}/\text{Al}_x\text{Ga}_{1-x}\text{N}$ WITH QUANTUM WELLS OF DIFFERENT WIDTH <u>V.M. Kramar</u> , D.V. Kondryuk, A.V. Derevyanchuk	92
FEATURES OF OPTICAL PROPERTIES OF ZnSe <Al> SUBSTRATES WITH A MODIFIED SURFACE Makhniy V.P., Berezovskiy M.M., Vakhnyak N.D., Litvin P.M., Kinzerska O.V., <u>Senko I.M.</u>	96
THE EFFECT OF UV Nd:YAG LASER RADIATION ON THE OPTICAL AND ELECTRICAL PROPERTIES OF ZnO CRYSTAL: INITIATED PHASE TRANSITION A. Medvid', P. Onufrijevs	100
ELECTRICAL, STRUCTURAL AND PHOTOELECTRIC FEATURES OF THIN ZnO:Al FILMS ON Si WAFERS V.P. Melnik, B.M. Romanyuk, V.P. Kladko, V.G. Popov, O.Yo. Gudymenko, O.I. Liubchenko, <u>T.M. Sabov</u> , O.S. Oberemok, O.V. Dubikovskiy, Ju.V. Gomeniuk	104
ELECTRICAL CONDUCTIVITY AND HALL MOBILITY OF Bi_2Se_3 THIN FILMS WITH DIFFERENT THICKNESSES <u>S.I. Menshikova</u> , E.I. Rogacheva	108
THERMO-INDUCED CHANGES IN THE MECHANICAL CHARACTERISTICS OF MONOCRYSTALLINE SILICON Yu.V. Pavlovskyy	111
FEATURES OF MAGNETIC SUSCEPTIBILITY $\text{Si}_{0.97}\text{Ge}_{0.03}$ WHISKERS MODIFIED OF HIGH-ENERGY IRRADIATION Yu.V. Pavlovskyy, P.G. Lytovchenko, A.V. Lytovchenko	115
ELECTRICAL CONDUCTIVITY OF NON-STOICHIOMETRIC NiO THIN FILMS <u>H. P. Parkhomenko</u> , P. D. Maryanchuk	118
INVESTIGATION OF CONDUCTIVITY AND OPTICAL TRANSMISSION PROCESSES IN CdTe:I SINGLE CRYSTALS GROWN FROM VAPOUR PHASE <u>V.D. Popovych</u> , O.A.Parfenjuk, Z.F. Tsybrii (Ivasiv)	121
COMPOSITE THERMOELECTRIC MATERIALS BASED ON LEAD AND CADMIUM TELLURIDES <u>V.V. Prokopiv</u> , I.V. Horichok, Y.V. Ogorodnik, O.M. Matkivsky, L.V. Turovska	124

As ₂ S ₃ DOPED WITH Mn OR Ag: RAMAN AND XRD STUDY <u>Revutska L.O.</u> , Shportko K.V., A.V. Stronski, Popovych M.V., A.Yo. Gudymenko, O.P. Paiuk, Ts.A. Kryskov	128
ELECTRON SPECTRUM ON THE DYNAMICALLY DEFORMED ADSORBED SURFACE OF A SEMICONDUCTOR WITH A ZINC BLENDE STRUCTURE <u>M.Ya. Seneta</u> , R.M. Peleshchak, Yu.M. Hal', Ya.M. Voronyak, M.G. Stan'ko	132
PECULIARITIES OF SHORT-WAVE RADIATION OF HEXAGONAL α -ZnSe AND α -ZnSe _x S _{1-x} <u>M.M. Slyotov</u> , O.M. Slyotov	136
EFFECT OF SYMMETRY OF SMALL STOICHIOMETRIC ZIRCONIA PARTICLES ON THEIR SPECTRAL CHARACTERISTICS <u>O.V. Smirnova</u> , A.G. Grebenyuk, V.V. Lobanov	137
TEMPERATURE DEPENDENCES OF VOLTAGE-TO-CURRENT CHARACTERISTICS OF Tl ₄ HgI ₆ AND Tl ₄ CdI ₆ CRYSTALS Solovyov M.V., Kashuba A.I., Franiv V.A.	141
CDS - BASED SEMIMAGNETIC SEMICONDUCTOR NANOPARTICLES AND THEIR BIOCOMPLEX WITH PROTEIN FOR BIOIMAGING APPLICATIONS <u>I. D. Stolyarchuk</u> , R. Wojnarowska - Nowak, J. Polit, S. Nowak, M. Romerowicz - Misielak, H. M. Klepach, E. M. Sheregii	145
MAGNETO-OPTICAL STUDIES OF CdTe / CdMnTe DOUBLE QUANTUM WELLS O.V.Terletsii, V.Yu. Ivanov, L.Owczarczyk, S.M.Ryabchenko, V.I.Sugakov, G.V. Vertsimakha, G. Karczewski.	148
STRUCTURE AND PROPERTIES OF Ge ADSORPTION COMPLEXES ON THE Si(001) FACE <u>O.I. Tkachuk</u> , M.I. Terebinska, Ya.S. Krivoruchko, V.V. Lobanov	152
PHOTOVOLTAIC PROPERTIES OF NANOCOMPOSITE IONATRON STRUCTURES InSe <RbNO ₃ > I.G Tkachuk V.M. Vodopianov, V.I. Ivanov, Z.D. Kovalyuk , V.V. Netyaga	156
CHARACTERIZATION OF PbTe AND PbSe THIN FILMS PREPARED USING PULSED LASER DEPOSITION METHOD <u>Tur Yu</u> , Virt I.S.	158
NANOCOMPOSITE ELEMENTS FOR HIC AND SENSORS WITH A FUSIBLE GLASS MATRIX <u>Lepikh Ya.I.</u> , Lavrenova T.I.	160
A METHOD OF MINORITY CHARGE CARRIERS BASIC PARAMETERS DETERMINA- TION IN SOLID MATTER Y. Uhryn, <u>V. Brytan</u> , I. Kosivchak, M. Govda	161
LOW FREQUENCY NOISE IN POLYCRYSTALLINE ZnO THIN FILMS <u>Virt I.</u> , Didovska O., Bester M.	165
ELECTRONIC STRUCTURES OF Si _{1-x} Sn _x SEMICONDUCTORS: FIRST PRINCIPLES AND MODEL PSEUDOPOTENTIAL CALCULATIONS P.M. Yakibchuk, <u>O.V. Bovgyra</u> , I.V. Kutsa	168

SYNERGISTIC EFFECTS IN IRRADIATED SEMICONDUCTOR CRYSTALS. RADIATION STABILITY CONSTANTS M. Zavada, O. Konoreva, P. Lytovchenko, I. Petrenko, M. Pinkovska, O. Radkevych, V. Tartachnyk, V. Shlapatska	172
IMPURITY AND IMPURITY-STRUCTURAL COMPLEXES OF TECHNOLOGICAL AND RADIATION ORIGIN	176
THERMODONORS IN SILICON CRYSTALS: PRACTICAL ASPECTS OF p-n JUNCTION CREATION IN Cz-Si MATERIAL USING BURIED n-TYPE LAYERS OF THE CONDUCTIVITY DEFINED BY SHALLOW THERMODONORS V. Babich, O. Dubikovskiy, V. Popov, B. Romanyuk, S. Sapon, T. Sabov, O. Lyubchenko	177
RADIATION-INDUCED CHANGES IN ELECTROMECHANICAL AND OPTICAL CHARACTERISTICS OF SILICON STRUCTURES B.V. Pavlyk, D.P. Slobodzyan, R.M. Lys, M.O. Kushlyk, R.I. Didyk, J.A. Shykorjak	181
TOPOLOGICAL INSULATORS BASED ON THE SEMIMETAL HgCdTE ALLOYS P. Šliž, M. Marchewka, D. Žak, J. Polit, E.M. Sheregii	184
CLUSTER PHASE: FORMATION, PROPERTIES AND MODELING	186
ION-INDUCED PROCESSES IN POLYMERS AND COMPOSITE MATERIALS: POSITRON ANNIHILATION SPECTROSCOPY STUDY T. Kavetsky, K. Iida, Y. Nagashima, M.O. Liedke, M. Butterling, A. Wagner, R. Krause-Rehberg, O. Šauša, T. Petkova, V. Boev, A.L. Stepanov, L. Meshi, D. Fuks, A. Kiv	187
AMPEROMETRIC ENZYME BIOSENSORS BASED ON NOVEL ORGANIC-INORGANIC AND PHOTOCROSS-LINKED POLYMERS T. Kavetsky, O. Smutok, M. Gonchar, Y. Kukhazh, O. Šauša, H. Švajdlenková, T. Petkova, V. Boev, V. Ilcheva, S. Kasetaitė, J. Ostrauskaite	190
FORMATION OF NANOCLOUDS ON THE ADSORBED SURFACE UNDER THE ACTION OF COMPREHENSIVE PRESSURE AND ELECTRIC FIELD R.M. Peleshchak, O.V. Kuzyk, O.O. Dan'kiv, M.V. Bui	193
INVESTIGATION OF THE RELAXATION CHARACTERISTICS OF EPOXY POLYMERS BY CALORIMETRIC METHOD M.I. Shut, T.G. Sichkar, L.K. Yanchevsky, O.S. Tulzhenskova, M.O. Rokytskyi	196
STRONG CORRELATION EFFECTS IN THERMODYNAMICS OF THE LATTICE BOSE-FERMI GAS I.V. Stasyuk, V.O. Krasnov	199
ВНЕСОК УКРАЇНСЬКИХ ВЧЕНИХ У СТАНОВЛЕННЯ КАТОДНО-ПРОМЕНЕВОЇ ФІЗИКИ Шендеровський В.А.	203
Table of CONTENTS	207
AUTHOR's INDEX	212

AUTHOR'S INDEX

- Akimov V. 21, 45
 Babich V. 177
 Belevskii P.A. 6
 Berezovskiy M.M. 96
 Bester M. 165
 Bilynskiy I.V. 10
 Blonskyi I. 54
 Boev V. 187, 190
 Boichuk V.I. 10, 12, 14
 Bondaruk Yu. V. 82
 Bovgyra O.V. 168
 Brytan V. 161
 Budzulyak S. 25, 42
 Bui M.V. 193
 Bukartyk N. 42
 Bulaniy M.F. 85
 Butterling M. 187
 Calvez L. 54
 Chernikova O.M. 57
 Dan'kiv O.O. 193
 Demediuk R. 21, 45
 Demianenko E.M. 74
 Derevyanchuk A.V. 92
 Didovska O. 165
 Didyk R.I. 181
 Donchev I. I. 82
 Dubikovskiy O. 104, 177
 Duque C.A. 21, 45
 Ermarov V. 42
 Fomina O. 21, 45
 Franiv A.V. 78
 Franiv V.A. 141
 Fuks D. 187
 Gomeniuk Ju.V. 104
 Gonchar M. 190
 Govda M. 161
 Grankin D.V. 65
 Grankin V.P. 65
 Grebenyuk A.G. 137
 Gudymenko A.Yo. 128
 Gudymenko O.Yo. 104
 Gutsul V.I. 33
 Hal' Yu.M. 132
 Himics L. 61
 Holomb R. 61
 Holovatsky V.A. 17
 Holskyj V.B. 12
 Horichok I.V. 124
 Iida K. 187
 Ilcheva V. 190
 Ilchuk H. 42
 Ivanchyshyn I.B. 14
 Ivanov V.I. 156
 Ivanov V.Yu. 148
 Kadan V. 54
 Kalytchuk S. 42
 Kapush O.A. 25, 27, 42
 Karzewski G. 148
 Karpenko O.S. 74
 Karpyn D.S. 14
 Kartel M.T. 74
 Kasetaitė S. 190
 Kashuba A.I. 78, 141
 Kavetskyy T. S. 68, 71, 187, 190
 Khmelenko O.V. 85, 89
 Kinzerska O.V. 96
 Kiv A.E. 82, 187
 Kladko V.P. 104
 Klepach H. M. 145
 Kondryuk D.V. 92
 Konoreva O. 172
 Korbutyak D.V. 25, 27, 42
 Kosivchak I. 161
 Kovalenko A.V. 85, 89
 Kovalyuk Z.D. 156
 Kramar V.M. 92
 Krasnov V.O. 199
 Krause-Rehberg R. 187
 Kravtsiv M.M. 68
 Krivoruchko Ya.S. 152
 Kryskov Ts.A. 128
 Kukhazh Y. 190
 Kupchak I.M. 27
 Kushlyk M.O. 181
 Kutsa I.V. 168
 Kuzyk O.V. 193
 Lavrenova T.I., 160
 Lepikh Ya.I., 160
 Leshko R. Ya. 12, 14
 Liedke M.O. 187
 Litvin P.M. 96
 Liubchenko O.I. 104
 Lobanov V.V. 74, 137, 152
 Lys R.M. 181
 Lytovchenko A.V. 115
 Lytovchenko P.G. 115, 172
 Lyubchenko O. 177
 Makhanets O.M. 33
 Makhniy V.P. 96
 Marchewka M. 184
 Maryanchuk P. D. 118
 Matkivsky O.M. 124
 Medvid' A. 100
 Melnik V.P. 104
 Menshikova S.I. 108
 Meshi L. 187
 Mitsa V. 61
 Morales A.L. 21, 45
 Morozova A.S. 71
 Mushynska O.R. 68
 Mykytenko N. A. 82
 Nagashima Y. 187
 Netyaga V.V. 156
 Nitsuk Yu.A. 49
 Nowak S. 145
 Nuzhdin V.I. 71
 Oberemok O.S. 104
 Ogorodnik Y.V. 57, 124
 Onufrijevs P. 100
 Osin Y.N. 71
 Ostrauskaite J. 190
 Owczarczyk L. 148
 Paiuk O.P. 128
 Pan'kiv L.I. 71
 Parfenjuk O.A. 121
 Parkhomenko H. P. 118
 Pavlov I. 54
 Pavlova S. 54
 Pavlovskyy Yu.V. 111, 115
 Pavlyk B.V. 181
 Pazyuk R.I. 10
 Peleshchak R.M. 132, 193
 Petkov P. 71
 Petkova T. 187, 190
 Petrenko I. 172
 Petrus R. 42
 Pinkovska M. 172
 Plakhtiy E.G. 89
 Polit J. 145, 184
 Popov V.G. 104, 177
 Popovych M.V. 128
 Popovych V.D. 121
 Poroshin V.M. 6
 Prokopiv V.V. 124
 Radkevych O. 172
 Revutska L.O. 128
 Rogacheva E.I. 108
 Rogov A.M. 71
 Rokytskyi M.O. 196
 Romanyuk B. 104, 177
 Romerowicz-Misielak M. 145
 Ruan J. 71
 Ryabchenko S.M. 148
 Rybak A. 54
 Sabov T.M. 104, 177
 Sapon S. 177
 Šauša O. 187, 190
 Seneta M.Ya. 132
 Senko I.M. 96
 Serpak N.F. 27
 Seti J.O. 36
 Sheregii E. M. 145, 184
 Shevchuk I. S. 39
 Shevchuk O. 42
 Shlapatska V. 172
 Shportko K.V. 128
 Shpotyuk O. 54
 Shut M.I. 196
 Shykorjak J.A. 181
 Sichkar T.G. 196
 Šliž P. 184
 Slobodzyan D.P. 181
 Slyotov M.M. 136
 Slyotov O.M. 136
 Smirnova O.V. 137
 Smutok O. 190
 Solovyov M.V. 141
 Solovyov V.V. 78
 Stan'ko M.G. 132
 Stasyuk I.V. 199
 Stepanov A.L. 68, 71, 187
 Stolyarchuk I. D. 145
 Stronski A.V. 71, 128
 Sugakov V.I. 148
 Sushchenko D. 21, 45
 Švajdlenková H. 190
 Tao H. 71
 Tartachnyk V. 172
 Terebinska M.I. 152
 Terletskii O.V. 148
 Tkach M.V. 36
 Tkachuk I.G. 156
 Tkachuk O.I. 152
 Tokarev S. 42
 Tokarev V. 42
 Toma I.P. 14
 Trzciński M. 68
 Tsybrii (Ivasiv) Z.F. 121
 Tulupenko V. 21, 45
 Tulzhenkova O.S. 196
 Tur Yu. 158
 Turovska L.V. 124
 Uhryn Y. 161
 Vakhniak N.D. 25
 Vakhnyak N.D. 42, 96
 Vaksman Yu.F. 49
 Valeev V.F. 71
 Veres M. 61
 Vertsimakha G.V. 148
 Vinoslavskii M.M. 6
 Virt I.S. 158, 165
 Vodopianov V.M. 156
 Voitsekhivska O.M. 36
 Voronyak Ya.M. 132
 Vorovsky V.Yu. 85
 Wagner A. 187
 Wojnarowska - Nowak R. 145
 Yakhnevych M.Ya. 17
 Yakhnevych N. Ya. 17
 Yakibchuk P.M. 168
 Yanchevsky L.K. 196
 Žak D. 184
 Zavada M. ,172
 Zhao X. 71
 Zubrytska K.V. 68, 71
 Курчак A.I. 31
 Литовченко B.Г. 31
 Стріха M.B. 31
 Шендеровський B.A. 203

Traditional **PROGRAM** *of conference*



Prykarpattya

We are looking forward to your coming at Drohobych and Truskavets.

Drohobych is the second largest town in Lviv region, one of the biggest industrial and cultural centre in Prykarpattya historical region. It's a city with over 900 years of old and glorious history, as well as friendly and courteous atmosphere.

Truskavets is a small but amazingly beautiful green city. Its location is wonderful – a picturesque valley in the foothills of the Eastern Carpathians, gentle wooded slopes and streams. Truskavets consistently leads the ranking of Ukraine "Best Cities for Life".



Participants of Conference are working and living in the Dnipro-Beskyd health resort.



The traditional recreation program includes tours of the attractive Carpathian, pleasant communication in an informal setting.



ЖИТТЄВИЙ ТА ТВОРЧИЙ ШЛЯХ
доктора фізико-математичних наук, професора
Бойчука Василя Івановича
(03.06.1953 – 04.06.2018)

Василь Бойчук народився 3 червня 1953 року у с. Іллінці Снятинського району на Івано-Франківщині в селянській родині. У 1970 році закінчив із золотою медаллю середню школу. З 1970 по 1975 роки навчався в Чернівецькому державному університеті ім. Ю. Федьковича, який також закінчив із відзнакою. З 1975 по 1978 рік навчався в аспірантурі на кафедрі теоретичної фізики цього ж університету; з 1978 року по лютий 1980 року працював молодшим науковим співробітником наукової частини університету. З лютого 1980 року розпочав свою науково-педагогічну діяльність в Дрогоби-



цькому державному педагогічному університеті ім. І. Франка на посадах: викладач, старший викладач, доцент, професор, завідувач кафедри теоретичної фізики, директор навчально-наукового інституту фізики, математики, економіки та інноваційних технологій, голова конференції трудового колективу університету. У 1980 році захистив кандидатську дисертацію «Екситонні стани в тонких напівпровідникових плівках». У 1995 році – докторську дисертацію «Теорія взаємодії квазічастинок в обмежених кристалічних системах». У 2000 році Бойчук В.І. нагороджений відзнакою «Відмінник освіти України». Вченою радою ДДПУ у 2010 році Василю Бойчуку присвоєно почесне звання «Заслужений професор Дрогобицького педагогічного університету». У 2011 році нагороджений Почесною Грамотою обласної держадміністрації. Бойчук В.І. був Делегатом III Всеукраїнського з'їзду працівників освіти України, академіком Академії Вищої школи України.

Наукові інтереси професора Бойчука В.І. завжди були пов'язані з фізичними дослідженнями електронних, діркових, фононних, поляронних та екситонних станів у напівпровідникових наногетероструктурах різної вимірності – наноплівках, квантових дротах, нанокристалах та надґратках на їхній основі. Професор Бойчук В.І. створив та очолив наукову школу «Теорія електронних, поляронних та екситонних станів у наногетероструктурах напівпровідників та діелектриків». За час роботи у Дрогобицькому державному педагогічному університеті під керівництвом Бойчука В.І. виконано біля двох десятків госпдоговірних досліджень, наукових робіт і замовлень Державного фонду фундаментальних досліджень та Міністерства освіти і науки України з фундаментальних та прикладних тем. Лише з 2001 року по 2017 рік він керував дев'ятьма науково-дослідницькими роботами на загальну суму 1.140.000 грн. З 2018 р.

по 2020 р. під керівництвом В.І. Бойчука заплановано виконання науково-дослідної роботи «Оптимізація умов іммобілізації сегментів на наночастинках у полімерних матрицях для покращення операційних параметрів лактат-селективних біосенсорів» (№ДР:018U000297, обсяг фінансування – 2.693.100 грн.). Під його керівництвом захищено дві докторські (Товстюк К.К., Білинський І.В.) та десять кандидатських дисертацій. Наукові діти професора Бойчука продовжують свої дослідження не лише у Дрогобицькому педагогічному університеті, а й у Національному університеті «Львівська політехніка», у Львівському та Чернівецькому національних університетах. Василь Бойчук є автором більше 270 наукових праць. Серед них 123 статті у центральних вітчизняних та зарубіжних журналах, що індексуються в міжнародних науково-метричних базах. Є автором 12 навчальних посібників для студентів університетів.

Бойчук В.І. був не лише відомим вченим-фізиком, а й організатором та активним учасником різних наукових заходів. Він був постійним Головою Оргкомітету Міжнародної конференції «Актуальні проблеми фізики напівпровідників», яка кожні 2-3 роки, починаючи з 1997 року, проводиться НАН України, Міністерством освіти і науки України на базі Дрогобицького педагогічного університету. У червні 2018 року відбудеться вже десята така конференція. Заснована професором Бойчуком В.І наукова школа з кола співробітників, докторантів, аспірантів, магістрантів і студентів добре відома своїми працями серед наукових спільнот України та зарубіжжя. Успішно працює започаткований ним щотижневий науковий семінар «Фізика гетеросистем різної вимірності». Він засновник і головний редактор наукового журналу «Актуальні проблеми фізики, математики та інформатики».

Професор Василь Бойчук – член секції фізики Західного наукового центру НАН України, член Спеціалізованих Вчених рад із захисту кандидатських і докторських дисертацій у Чернівецькому національному університеті ім. Ю. Федьковича та у Львівському національному університеті ім. І. Франка. В навчально-науковому інституті, яким керував проф. Бойчук В.І., ліцензовано аспірантуру зі спеціальностей: фізика напівпровідників та діелектриків; математичний аналіз; прикладна фізика та наноматеріали; економіка; математичні методи, моделі та інформаційні технології в економіці; професійна освіта (за спеціальностями), а також ліцензовано 11 спеціальностей другого (магістерського) рівня вищої освіти.

Професор Бойчук В.І. в нашій пам'яті залишиться як відомий вчений, непересічна особистість, різнобічно освічена людина, викладач найвищої кваліфікації, талановитий педагог, внесок якого у підготовку фахівців у галузі освіти і науки важко переоцінити.

УДК 537.311.322(063)

ББК 22.379.431

T7

*The materials are recommended for publication by Scientific Advice
at the Ivan Franko Drohobych State Pedagogical University
(protocol №7 on 17 May 2018)*

Topical Problems of Semiconductor Physics. Materials of the X International Conference. Truskavets, 26-29 June, 2018: Publishing House "UKRPOL" Ltd., 2018. 216 p.

The present conference proceedings contain the materials of the X International Conference «Topical Problems of Semiconductor Physics».

The materials reflect the content of the conference reports, in which the novel results, state and perspectives of research in the field of semiconductor physics on principal problems are presented:

- 1. Quantum-size confinement phenomena.*
- 2. Effects of strong correlation in the systems with electronic and ionic conductivity.*
- 3. Electronic transport, optic, photoelectric and magnetic properties of semiconductor crystals.*
- 4. Impurity and impurity-structural complexes of technological and radiation origin.*
- 5. Structural disordering factor manifestations of basic semi-conductor properties. Semiconductor oxide ceramics.*
- 6. Semiconductor metrology, novel techniques and methods.*
- 7. Cluster phase: formation, properties and modeling.*

The materials edition is compiled from author's original copies prepared for printing by Program Committee and Editorial Board of the 2018 Conference.

УДК 537.311.322(063)

ББК 22.379.431

EDITORIAL BOARD:

Olexander BELYAEV,

Ivan BLONSKYL,

Vasyl BOICHUK,

Academician of NAS of Ukraine, Professor

Corresponding member of NAS of Ukraine, Professor

Professor

EDITed by Vitalij Holskyj, Roman Pazyuk

ISBN 978-966-8955-72-3

® Publishing House "UKRPOL" Ltd.